Forschungszentrum Karlsruhe
in der Helmholtz-Gemeinschaft

Wissenschaftliche Berichte
FZKA 7093

Final KARMEN-Results on Neutrino-Oscillations and Neutrino-Nucleus-Interactions in the Energy-Regime of Supernovae

J. Reichenbacher

Institut für Kernphysik

Juni 2005

Forschungszentrum Karlsruhe
in der Helmholtz-Gemeinschaft

Wissenschaftliche Berichte
FZKA 7093

Final KARMEN-Results on Neutrino-Oscillations and Neutrino-Nucleus-Interactions in the Energy-Regime of Supernovae

Jürgen Reichenbacher

Institut für Kernphysik

von der Fakultät für Physik
der Universität Karlsruhe (TH) genehmigte Dissertation

Forschungszentrum Karlsruhe GmbH, Karlsruhe
2005

Impressum der Print-Ausgabe:

Als Manuskript gedruckt

Forschungszentrum Karlsruhe GmbH
Postfach 3640, 76021 Karlsruhe

Mitglied der Hermann von Helmholtz-Gemeinschaft
Deutscher Forschungszentren (HGF)

ISSN 0947-8620

urn:nbn:de:0005-070939

Final KARMEN-Results on Neutrino-Oscillations and Neutrino-Nucleus-Interactions in the Energy-Regime of Supernovae

Zur Erlangung des akademischen Grades eines

DOKTORS DER NATURWISSENSCHAFTEN

der Fakultät für Physik der
Universität Karlsruhe (TH)

genehmigte
DISSERTATION

von

Dipl.–Phys. Jürgen Reichenbacher
aus Karlsruhe

Tag der mündlichen Prüfung:	5. November 2004
Referent:	Prof. Dr. J. Blümer
Korreferent:	Prof. Dr. K.–H. Kampert

ZUSAMMENFASSUNG

Endgültige KARMEN Resultate zu Neutrino-Oszillationen und Neutrino-Kern-Wechselwirkungen im Energiebereich von Supernovae

Das KARMEN Neutrinoexperiment untersuchte von 1990-2001 an der Spallationsneutronenquelle ISIS Neutrino-Kern-Wechselwirkungen im Energiebereich bis zu 53 MeV mit spektroskopischer Qualität. Myonanti-, Elektron- und Myonneutrinos entstehen im ISIS Target aus der Pion- und Myonzerfallskette in Ruhe. In Verbindung mit der einzigartigen Zeitstruktur des ISIS Beschleunigers und den jeweils charakteristischen Detektorsignaturen konnten geladene und neutrale Stromreaktionen an C-12, C-13 und Fe-56 mit einem Signal zu Untergrundverhältnis von bis zu 100:1 nachgewiesen werden.

Durch die erste kombinierte Analyse aller mit KARMEN beobachtbaren Neutrinokernreaktionen konnten diese erstmals modellunabhängig und konsistent im Energiebereich von Supernovae vermessen werden. Hierzu wurden erstmals die gesamten KARMEN2-Daten (mit einer stark unterdrückten kosmischen Untergrundrate durch den Upgrade) detailliert analysiert. Dabei wurde insbesondere für das Verhältnis der Neutrino-Wirkungsquerschnitte von neutraler zu geladener Stromreaktion an C-12 eine bislang einzigartige experimentelle Präzision von 5% erreicht. Im Rahmen dieser Genauigkeit konnte z.B. die μ-e-Universalität der schwachen Wechselwirkung verifiziert werden.

Aus den gemessenen Wirkungsquerschnitten, welche alle mit den theoretischen Erwartungen übereinstimmten, wurden darüberhinaus Obergrenzen für Neutrino-Oszillationen abgeleitet. Im Rahmen dieser Arbeit konnten somit weite Teile des LSND-Evidenzbereiches für Oszillationen von Myonanti- in Elektronantineutrinos mit 90% CL ausgeschlossen werden, insbesondere für Massenquadratsdifferenzen oberhalb von $1eV^2$. Auch die Oszillationssuchen Myon- in Elektronneutrinos, sowie Elektronneutrinos in sterile Neutrinos lieferten keinen Hinweis auf ein zusätzliches steriles schwereres Neutrino (LSND-Szenario).

Abschließend konnte im Rahmen dieser Arbeit gezeigt werden, daß neutroneninduzierter strahlkorrelierter Untergrund vom Beschleuniger mit hoher Wahrscheinlichkeit die KARMEN-Zeitanomalie erklären kann.

ABSTRACT

Over the period of time from 1990-2001, the KARMEN neutrino experiment at the neutron-spallation-source ISIS was investigating neutrino-nucleus-interactions with spectroscopic quality in the energy-regime of up to 53 MeV. Muon-anti-, electron- and muon-neutrinos were produced in the pion- and muon-decay-chain at rest. In connection with the unique time structure of the ISIS accelerator and the characteristic detection signatures, it was feasible to measure precisely neutral- and charged-current-reactions on C-12, C-13 and Fe-56 with a signal to background ratio of up to 100:1.

In the framework of this thesis, it was possible for the first time to derive the corresponding cross sections in the energy-regime of supernovae both model-independently and consistently from the first combined analysis of all neutrino-nucleus-interactions, which could be studied with KARMEN. For this, the entire KARMEN2 data, with a strongly suppressed cosmic background rate due to the upgrade, was evaluated for the first time. Hence, an unprecedented experimental precision for the ratio of the measured neutrino cross sections for the neutral-current- and the exclusive charged-current-reaction on C-12 was achieved. Within this accuracy, it was feasible to verify e.g. the μ-e-universality of weak interaction.

Furthermore, upper limits on neutrino-oscillations were deduced from the measured cross sections, which all met theoretical expectations. Thus, it was straightforward possible to exclude at 90%CL large parts of the LSND favored evidence region for the oscillation of muon-anti- to electron-anti-neutrinos, especially for squared-mass differences above $1eV^2$. The searches for oscillations of muon- to electron-neutrinos, as well as electron-neutrinos to sterile neutrinos provided likewise no evidence for an additional heavy sterile neutrino (LSND-scenario).

Last but not least, it was shown in the framework of this thesis that the KARMEN-time-anomaly can be explained with a high probability of occurrence by intermediate-energy neutrons inducing beam correlated background from the accelerator.

Zusammenfassung

Neutrinos spielen für das Verständnis der Teilchenphysik eine zentrale Rolle, da sie nach den Photonen die zweithäufigsten Elementarteilchen im Universum sind. 1930 zunächst als masseloses, neutrales Spin-1/2-Teilchen von Pauli postuliert, um die Energie- und Impulserhaltung beim β-Zerfall aufrechtzuerhalten, erfolgte ihr experimenteller Nachweis erst 1953 an einem Kernreaktor durch Reines und Cowan [Rei53]. Die äußerst kleinen Wirkungsquerschnitte von 10^{-44}–$10^{-38}\,cm^2$ dieser nur schwach wechselwirkenden Teilchen machen unseren Planeten nahezu transparent für solche Neutrinos im MeV-Energiebereich und es bedarf etwa einem Lichtjahr an Materie, um sie abzuschirmen. Reines und Cowan wurden 1995 für ihr Experiment mit dem Nobelpreis ausgezeichnet.

Die Neutrinoastrophysik begann in den späten 60er Jahren mit dem ersten Sonnenneutrinoexperiment: In einem riesigen, unterirdisch vor kosmischer Strahlung geschützten, Tank gelang es Davis mit Hilfe eines aufwendigen radiochemischen Verfahrens Neutrinos von der Sonne aufzuspüren. Die in der Folgezeit gemessene solare Neutrinorate dieses und aller weiteren unterschiedlichen Experimente entsprach jedoch nur etwa der Hälfte der erwarteten Rate und stellte das sogenannte Sonnenneutrinoproblem dar. Schnelle Čerenkov- bzw. Szintillationsdetektortypen waren zusätzlich in der Lage, die Richtung und Energie der solaren Neutrinos zu bestimmen und die Sonne als Ursprungsort zu verifizieren. Unter der Leitung von Koshiba gelang es dem Kamiokande-Experiment erstmals bei der Explosion der Supernova 1987A Neutrinos auch von einer anderen astronomischen Quelle als der Sonne nachzuweisen. 2002 wurden Davis und Koshiba für die Detektion von Sonnen- bzw. Supernovaneutrinos mit dem Nobelpreis ausgezeichnet.

Mit dem Nachfolgeexperiment SuperKamiokande konnte 1998 erstmals schlüssig gezeigt werden, daß Neutrinos eine von Null verschiedene Ruhemasse haben, aufgrund der zenithwinkelabhängigen *disappearance* (Verschwinden) von Myonneutrinos, welche gleichmässig verteilt in der Erdatmosphäre produziert werden [Fuk98]. Die bis dato im Standardmodell der elektroschwachen Wechselwirkung gemachte *ad hoc* Annahme, Neutrinos hätten keine Ruhemasse und wären maximal paritätsverletzend, mußte revidiert werden. Darüberhinaus ist die gängige Annahme, daß Neutrinooszillationen $\nu_\mu \rightarrow \nu_\tau$ die wahrscheinlichste Erklärung der beobachteten *disappearance* atmosphärischer Myonneutrinos sind. Wie im Quarksektor stellen die Neutrinoflavors jeweils eine Mischung aus den verschiedenen Neutrinomassen-Eigenzuständen dar und können somit ineinander oszillieren. Oszillationen $\nu_e \rightarrow \nu_{\mu,\,\tau}$ von solaren Elektronneutrinos, auf ihrem Flugweg zur Erde, liefern auch eine schlüssige Erklärung für das fast drei Jahrzehnte diskutierte Sonnenneutrinodefizit [Ahm02a]. Umgekehrt gelten damit die Fusionsreaktionen (verantwortlich für die Elektronneutrinoproduktion) im Sonneninneren als wohlverstanden.

Weiterhin ungeklärt ist, ob neben den bekannten drei aktiven Neutrinoflavors (ν_e, ν_μ, ν_τ) noch zusätzliche sterile Neutrinoarten auftreten. Unterscheiden sich Neutrinos und ihre Antineutrinos voneinander (Dirac-Teilchen wie die Quarks) oder sind sie mit ihnen identisch (Majorana-Teilchen)? Zudem können bislang nur Obergrenzen für die absoluten Neutrinomassen angegeben werden, da Neutrinooszillations-Experimente nur auf die Differenzen der Massenquadrate sensitiv sind. Aus dem genauen Studium der Kinematik des Tritium-β-Zerfalls folgt die bislang kleinste Obergrenze für eine der Neutrinomassen: $m_{\nu_e} < 2.2\,\mathrm{eV}$ [Wei03]. Die Oszillationen von atmosphärischen und solaren Neutrinos definieren bereits zwei unabhängige Δm^2-Bereiche ($\Delta m^2_{atm} \approx 3 \cdot 10^{-3}\,eV^2$ und $\Delta m^2_{sol} \approx 7 \cdot 10^{-5}\,eV^2$). Der dritte Bereich ist durch die anderen beiden festgelegt und liegt nahe am Größeren. Deshalb repräsentiert die Obergrenze für die Elektronneutrinomasse gleichzeitig, im Rahmen von Neutrinooszillationen, die Obergrenze für jedes der drei aktiven Neutrinoflavors. Es sind weiterhin sowohl hierarchische als auch quasi-degenerierte Massenskalenmodelle möglich. Das zukünftige Experiment KATRIN[1] wird in der Lage sein, die bestehende Obergrenze für die Elektronneutrinomasse auf einen Wert von $m_{\nu_e} < 0.2\,\mathrm{eV}$ deutlich zu verbessern [Wei03]. Kosmologische Beobachtungen der strukturierten Clusterung von Galaxien sowie der Anisotropie der kosmischen $2.7\,\mathrm{K}$ Hintergrundstrahlung aus dem Urknall weisen darauf hin, daß $\sum m_{\nu,\,aktiv} < 1 - 2\,\mathrm{eV}$ ist [Han03].

Bereits 1995 veröffentlichte das LSND-Experiment in der *New York Times* einen Hinweis auf eine $\bar{\nu}_\mu \rightarrow \bar{\nu}_e$ Oszillation [Ath95]. Diese Evidenz auf Neutrinooszillation wird jedoch seither äußerst kontrovers diskutiert [Hil95]. Der Hinweis des LSND-Experiments auf $\bar{\nu}_\mu \rightarrow \bar{\nu}_e$ Oszillationen paßt aktuell nicht in das Bild von drei massiven Neutrinozuständen. Atmosphärische und solare Neutrinoexperimente definieren zwei unabhängige Differenzen der Massenquadrate, welche von verschiedenen Experimenten bereits konsistent reproduziert werden konnten. Deshalb müßte mindestens ein weiterer schwererer Neutrinozustand eingeführt werden, um ein schlüssiges Gesamtbild ein-

---

[1] KArlsruhe-TRItium-Neutrino-experiment

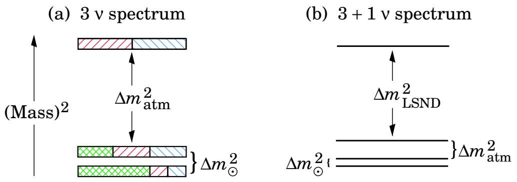

Abbildung 1: Aufspaltung der Neutrinomassen auf a) drei Neutrinoflavor und b) mit einem zusätzlichen sterilen Neutrino (LSND–Szenario)

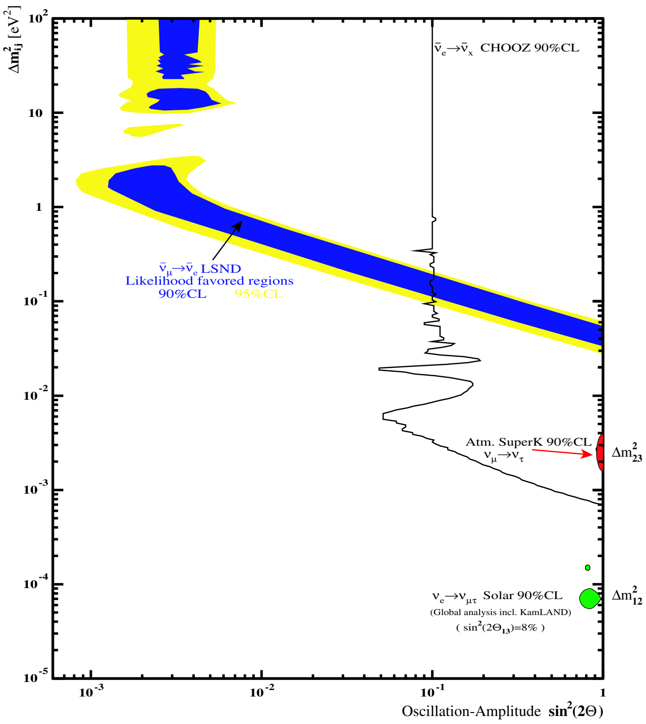

Abbildung 2: 2-Flavor-Oszillationsplot mit den Evidenzregionen (90%CL) der atmosphärischen ($\nu_\mu \rightarrow \nu_\tau$ in SuperK) und solaren Neutrinos ($\nu_e \rightarrow \nu_{\mu,\tau}$ in kombinierten Experimentdaten [Fog03]) sowie die Evidenz des LSND-Beschleunigerexperiments ($\bar{\nu}_\mu \rightarrow \bar{\nu}_e$). Vom CHOOZ–Reaktorexperiment können die Bereiche rechts der schwarzen Kurve für die Oszillation $\bar{\nu}_e \rightarrow \bar{\nu}_x$ mit 90%CL ausgeschlossen werden [Apo99].

schließlich LSND zu erhalten, welches im eV^2-Bereich für Differenzen der Massenquadrate sensitiv ist (*s. Abb.* 1 und *Abb.* 2). Aus dem unsichtbaren Anteil der Zerfallsbreite des Z^0-Bosons im LEPII-Colliderexperiment am CERN[2] weiß man allerdings, daß es genau drei aktive Neutrinoflavor gibt [PDG02]. Die LSND-Oszillation wäre somit nur über die Hinzunahme von mindestens einem sterilen schwereren Neutrino mit den existierenden Messungen kompatibel.
Sind Neutrinos Dirac-Teilchen wie die Quarks, d.h. ihre Teilchen und Antiteilchen unterscheiden sich voneinander, so müssen gleichzeitig die entsprechenden Neutrinopartner mit der entgegengesetzten Händigkeit existieren (Dirac-Massenterm $\neq 0$). Da diese aufgrund ihrer „falschen" Händigkeit nicht an der schwachen Wechselwirkung teilnehmen können, nennt man sie sterile Neutrinos. Im Gegensatz zu den Quarks können Neutrinos nur schwach wechselwirken, da sie elektrisch ungeladen sind und keine Farbladung tragen. Quarks mischen untereinander nur gering, während z.B. ν_μ mit ν_τ wahrscheinlich sehr stark miteinander mischen (*vgl. Abb.* 2). Das zukünftige Studium von CP-Verletzung bei Neutrinooszillationen könnte den Schlüssel zum Verständnis der Materie-Antimaterie-Asymmetrie im Universum bieten. Aufgrund der Unterschiede zum Quarksektor liegt es nahe zu untersuchen, ob Neutrinos keine Dirac-Teilchen sondern Majorana-Teilchen sind und sich nicht von ihren Antiteilchen unterscheiden. Über den sogenannten *Seesaw*[3]-Mechanismus wäre dann auch einsichtig, warum Neutrinos eine so winzige Ruhemasse besitzen: Die Masse eines linkshändigen Neutrinos wäre proportional zu der seines entsprechenden geladenen Fermions, aber umso kleiner je schwerer ein assoziiertes rechtshändiges Neutrino ist. Die Masse dieses neuen superschweren rechtshändigen Neutrinos läge etwas unterhalb der GUT[4]-Skala. Solche Energien übertreffen jedoch weit die bislang höchsten gemessenen Energien aus der kosmischen Strahlung. Ein möglicher direkter Nachweis eines superschweren Neutrinos ist damit unabsehbar. Daß Neutrinos Majorana-Teilchen sind, könnte nur durch die Beobachtung des neutrinolosen Doppel-Beta-Zerfalls gezeigt werden:
Das beim ersten β-Zerfall emittierte Neutrino könnte, falls es mit seinem Antiteilchen identisch ist, bei einem zweiten synchronen β-Zerfall im selben Atomkern sofort wieder absorbiert werden [Kla02].

---

[2] Europäisches Kernforschungszentrum (Centre Européen de Recherches Nucléaires)

[3] zu deutsch Wippe

[4] Grand-Unified-Theory

Die LSND-Oszillation wäre, wie erläutert, mit fundamentalen neuen Eigenschaften der Neutrinos verknüpft. Das Experiment der deutsch-britischen Kollaboration KARMEN[5] ist prinzipiell im selben Bereich sensitiv und kann LSND direkt verifizieren. Um die dazu benötigte Untergrundreduktion zu erreichen, wurde im Zeitraum von 1995-1997 ein umfangreicher Upgrade des KARMEN-Detektorsystems vorgenommen. Das KARMEN2 Endresultat für die $\bar{\nu}_\mu \rightarrow \bar{\nu}_e$ Oszillationssuche, wurde durch Auswertungen von wesentlichen Teilen der Daten gewonnen, die im Rahmen dieser Arbeit erhoben wurden, und schließt große Teile der LSND-Evidenzregion aus [Arm02]. In dieser Arbeit werden zwei ergänzende Methoden für die $\bar{\nu}_\mu \rightarrow \bar{\nu}_e$ Oszillationssuche im Detail vorgestellt, sowie die Oszillationssuchen $\nu_\mu \rightarrow \nu_e$ und $\nu_e \rightarrow \nu_{sterile}$.

Aufgrund der sehr guten Energie- und Zeitauflösung des KARMEN-Detektors war es erstmals möglich, geladene und neutrale Stromreaktionen von Neutrinos an Kernen in spektroskopischer Qualität im Energiebereich von Supernovae zu vermessen. Die Mechanismen, welche eine Supernova zur Explosion bringen, sind noch nicht verstanden. Bei einer Supernova des Typs II werden 99 % der freiwerdenden Energie in Neutrinos umgesetzt. Eine genaue Kenntnis der Wirkungsquerschnitte für die einzelnen Nachweisreaktionen ist für zukünftige Supernovaneutrinoexperimente wie KamLAND oder Borexino unerläßlich: Anhand der Raten für die einzelnen Neutrinoflavors wird eine Unterscheidung der diskutierten Supernovamodelle möglich. Desweiteren geben der zeitliche Verlauf und die Energiespektren ($\cong$ Temperatur) der Neutrinos Aufschluß über die Prozesse im Innern (Core) der Supernova kurz vor und während der Explosion. Der Core eines Supernova-Vorläufersterns besteht hauptsächlich aus Eisen, dem Endprodukt des letzten nuklearen Brennzykluses sehr massereicher Sterne. Deshalb wird die mittlere freie Weglänge von Neutrinos, welche während des Kollapses und der Explosion der Supernova erzeugt werden, durch deren Wirkungsquerschnitt an Eisenkernen bestimmt. Dieser kann im KARMEN-Experiment mit vergleichbar energetischen Neutrinos untersucht werden, welche im den Detektor umgebenden Stahl mit Eisenkernen wechselwirken.
Durch die Vermessung aller mit KARMEN beobachtbaren Neutrino-Kern-Reaktionen, insbesondere der neutralen und geladenen Stromreaktionen an ^{12}C, lassen sich fundamentale Tests der elektroschwachen Wechselwirkung durchführen, wie etwa die μ-e-Universalität der schwachen Wechselwirkung. Darüberhinaus lassen sich theoretische Kernmodelle sehr genau prüfen. Man unterscheidet hauptsächlich zwischen Elementarteilchenbehandlung (EPT) und mikroskopischen Modellen, welche der Struktur der Kerne gerechter werden. EPT-Modelle sind dagegen darauf angewiesen, Formfaktoren zu benutzen, die empirisch aus β-Zerfällen und μ-Einfangreaktionen gewonnen werden. Bei den mikroskopischen Modellen gibt es zwei Ansätze: Schalenmodelle (SM) welche besonders gut die Grundzustände im Kern beschreiben und Random-Phase-Approximationen (RPA), welche für angeregte Zustände geradzahliger Kerne geeigneter sind. Denn RPA-Modelle benutzen neben der Fermi-Verteilung für unkorrelierte Teilchen im mittleren Grundzustandspotential auch 1Teilchen-1Loch-Anregungen oberhalb der Fermikante.
Aktuell wurde auch vorgeschlagen, daß Neutrino-Kern-Reaktionen einen Beitrag zur Elementsynthese in Sternen leisten [Heg03]. Diese Neutrino-Nukleosynthese ist besonders im Bereich leichter Kerne (Nukleonenzahl $\approx$ 12) vielversprechend. Die mit KARMEN gemessenen Wirkungsquerschnitte dienen hier als Prüfstein, um die Güte der theoretischen Vorhersagen zu beurteilen.
Die erstmalige kombinierte Analyse aller mit KARMEN beobachtbaren Neutrinokernreaktionen repräsentiert ein weiteres Hauptziel dieser Arbeit. Hierfür wurden die gesamten KARMEN-Daten, welche von 1990-2001 aufgenommen wurden, zum ersten Mal global ausgewertet. Darüberhinaus war es die erste Untersuchung von Neutrinokernreaktionen, welche die gesamten KARMEN2-Daten benutzte (mit einer stark unterdrückten kosmischen Untergrundrate durch den Upgrade).

Aufgrund der hervorragenden Zeitauflösung ist KARMEN auf exotische Pionzerfälle sensitiv wie kein anderes Experiment. Für Zerfälle außerhalb des Standardmodells, bei denen massive schwach wechselwirkende Teilchen (WIMPs bzw. Neutralinos) entstehen, können kleinste Verzweigungsverhältnisse bis hinab zu 10^{-17} untersucht werden. In der hierzu benötigten Zeitverteilung der mit KARMEN gemessenen Neutrinos war eine Anomalie zu beobachten [Zei95], [Arm95]. Neben der Suche nach Neutrinooszillationen und der Vermessung von Neutrinokernreaktionen im Supernovaenergiebereich ist die Klärung dieser KARMEN-Zeitanomalie das dritte Hauptziel der Arbeit.

---

[5] KArlsruhe-Rutherford-interMediateEnergy-Neutrinoexperiment

Das KARMEN-Experiment hat im Zeitraum von 1990-2001 an der Spallationsneutronenquelle ISIS am Rutherford-Appleton-Laboratory bei Oxford (England) Neutrinos gemessen. ISIS ist ein *rapid-cycling* Synchrotron, welches Protonen auf eine kinetische Energie von 800 MeV beschleunigt (*s. Abb.* 3). Mit einer Frequenz von 50 Hz werden zeitlich parabelförmige Protonendoppelpulse extrahiert, die 100 ns breit und 325 ns zeitlich separiert sind (*s. Abb.* 4b). Diese werden zunächst über ein dünnes Vortarget schließlich auf ein massives Haupttarget aus Uran bzw. Tantal geleitet (dem sogenannten *beam-stop*). Dabei entstehen hauptsächlich Neutronen, aber auch Pionen aller drei Ladungszustände. Die π^0 zerfallen sehr schnell in zwei γ-Quanten ($\tau_{\pi^0} = 8.4 \cdot 10^{-17}\,\mathrm{s}$), während die geladenen Pionen vollständig im Target gestoppt werden. Die π^- werden anschließend von den umgebenden Kernen eingefangen. Deshalb ist für die Neutrinoproduktion nur die π^+-Zerfallskette relevant:

$$\begin{array}{lll} \pi^+ \longrightarrow & \mu^+ + \textcircled{\nu_\mu} & \qquad \tau = 2.6 \cdot 10^{-8} s \\ & \downarrow & \\ & e^+ + \textcircled{\nu_e} + \textcircled{\bar{\nu}_\mu} & \qquad \tau = 2.2 \cdot 10^{-6} s \end{array}$$

Aus dem Zerfall der π^+ in Ruhe entstehen monoenergetische ν_μ mit einer Energie von 29.8 MeV. Diese folgen zeitlich unmittelbar den Protonenpulsen, aufgrund der kurzen Lebensdauer der π^+ von 26 ns (*s. Abb.* 4a+b). Aus dem danach einsetzenden Dreikörperzerfall der entstandenen μ^+ werden desweiteren ν_e und $\overline{\nu_\mu}$ mit kontinuierlichen Energien bis 52.83 MeV produziert. Deren zeitliche Verteilung spiegelt die μ^+-Lebensdauer von 2.2 μs wider (*s. Abb.* 4a+c). Aufgrund der einzigartigen Zeitstruktur von ISIS und den beiden unterschiedlichen Lebensdauern von Myon und Pion können in zwei frühen Zeitfenstern (entsprechend dem Tastverhältnis der Protonpulse) fast ausschließlich ν_μ und in einem späten Zeitfenster auf einer μs-Skala rein ν_e und $\overline{\nu_\mu}$ untersucht werden. Die gesamte Länge einer Beamperiode bis zum nächsten Protonendoppelpuls beträgt 20 ms und kann dazu genutzt werden, den kosmischen Untergrund sehr genau zu vermessen (*duty-factor* bis zu $\approx 10^{-5}$). Bei einem Protonenstrahlstrom von 200 μA erzeugt ISIS isotrop $5.6 \cdot 10^{13}$ Neutrinos pro Flavor und Sekunde. Insgesamt wurden im Meßzeitraum von 1990-2001 mit KARMEN 18547 C Strahlladung akkumuliert. Dies entspricht einer gesamten Neutrinoproduktion von $5.2 \cdot 10^{21}$ pro Flavor. Die Energien, der von ISIS erzeugten Neutrinos, können analytisch berechnet werden aus dem 2-Körper- bzw. 3-Körper-Zerfall in Ruhe und liegen im astrophysikalisch interessanten Bereich von Supernovae des Typs II (*vgl. Abb.* 4a+d).

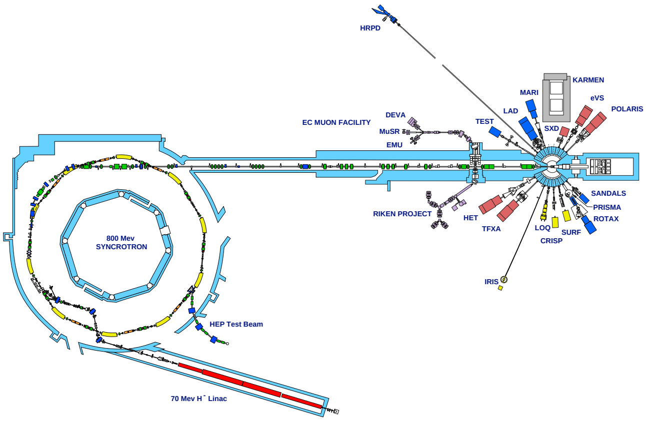

Abbildung 3: Anordnung ISIS und KARMEN

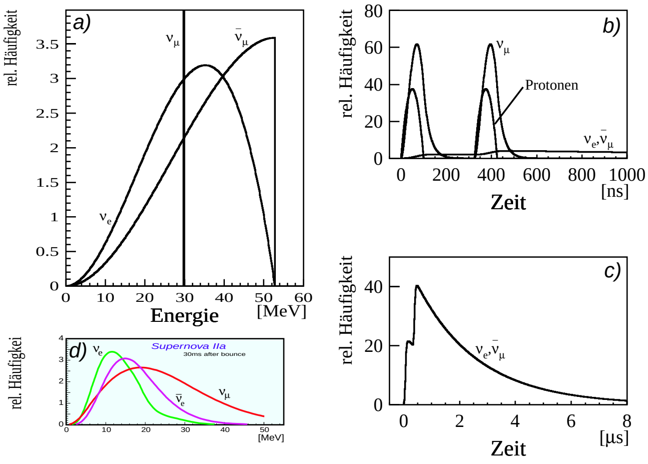

Abbildung 4: a) Energie- und b)+c) Zeitverteilungen der im ISIS-Target erzeugten Neutrinos. d) Zum Vergleich die Energieverteilungen von Neutrinos bei einer exemplarischen Supernova Typ IIa

Der KARMEN-Detektor ist ein 56 t Kalorimeter aus organischem Flüssigszintillator und segmentiert in 512 einzelne Module (*s. Abb.* 5) [Wol95]. Jedes dieser Module ist 353 cm lang, 18 cm breit und hoch. Entstandenes Szintillationslicht wird im Modul über Totalreflektion zu seinen beiden Stirnenden transportiert. Dort befinden sich jeweils zwei 3-inch-Photomultiplier zum Auslesen. Die Seitenwände der Module sind

doppelwandig konstruiert und beinhalten einen Luftspalt, der die Totalreflektion für den Lichttransport längs der Modulachse ermöglicht. Zusätzlich ist zwischen den Modulwänden Papier lose eingebracht, das mit Gadolinium beschichtet ist. Dies erhöht nicht nur den Nachweis thermischer Neutronen sondern verhindert auch das Überkoppeln von Licht in benachbarte Module. Der gesamte KARMEN-Detektor verfügt über eine hervorragende Energieauflösung von $\frac{\sigma(E)}{E} = \frac{11.5\%}{\sqrt{E(MeV)}}$ [Dod93] und eine sehr schnelle Zeitauflösung von 1 ns [Wol95]. Der 65 m^3 große Detektor deckt 0.5 % des vollen ISIS-Raumwinkels ab und befindet sich in einem mittleren Abstand von 17.7 m zum Haupttarget. Der Winkel zur *beam-line* beträgt 100° (*s. Abb.* 3). Der gesamte Detektor ist nochmals umgeben von einem 7000 t massiven und 10 m hohen Blockhaus aus Stahlbrammen (*s. Abb.* 6). Dies dient zur Abschirmung der kosmischen Höhenstrahlung und strahlkorrelierter Neutronen vom Target. Zwischen dem Haupttarget und dem Detektor befinden sich insgesamt 7 m Eisen. Diese Abschirmung entspricht mehr als 30 Abschwächlängen für Neutronen mit kinetischen Energien von über 10 MeV. Zu den Seiten beträgt die Eisenwand 2 m und auf dem Dach 3 m. Der Fluß der kosmischen Myonen wird dadurch auf ein Drittel reduziert. Zur weiteren Untergrundreduktion ist der Zentraldetektor umgeben von einer Lage aktiver Antizählermodule, einer 18 cm dicken passiven Eisenabschirmung und einem Shield aus 3 cm dicken Plastikszintillatormodulen (*s. Abb.* 5 und 6).
In den Jahren 1995-1997 wurde wie bereits erwähnt ein umfangreicher Upgrade des Detektorsystems vorgenommen [Rei98]. Dabei wurde innerhalb des Eisenblockhauses ein weiterer Vetozähler aus 5 cm dicken und bis zu 4 m langen Plastikszintillatormodulen installiert (*s. Abb.* 6). Dieser Vetozähler reduziert nochmals den kosmischen Untergrund. Er weist zudem diejenigen kosmischen Myonen nach, die den Detektor nicht treffen aber in der Eisenabschirmung hochenergetische Neutronen produzieren können, welche ungesehen das alte Shield- und Antizählersystem durchdringen (*vgl. Abb.* 6). Diese hochenergetischen Neutronen aus Myoneinfangreaktionen und tiefinelastischer Streuung an Eisenkernen des Blockhauses limitierten zuvor die Sensitivität für die Suche nach der LSND-Oszillation ($\bar{\nu}_\mu \rightarrow \bar{\nu}_e$) [Arm98].

Der Nachweis der Neutrinos erfolgt bei KARMEN hauptsächlich über Neutrino-Kern-Reaktionen am ^{12}C des organischen Szintillators (*s. Abb.* 7):
Zum einen kann beim $A = 12$ Isospin-Triplett die

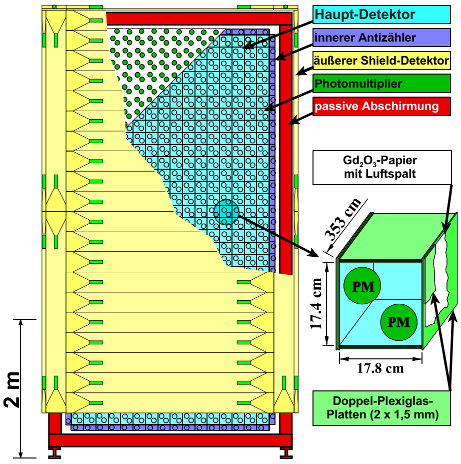

Abbildung 5: Der KARMEN–Detektor

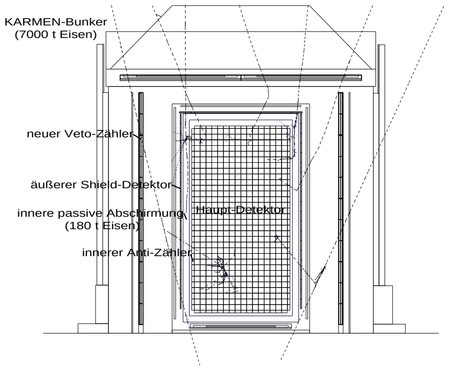

Abbildung 6: Schematische Darstellung des KARMEN-Detektors mit neuem Veto-Zähler innerhalb der Eisenabschirmung

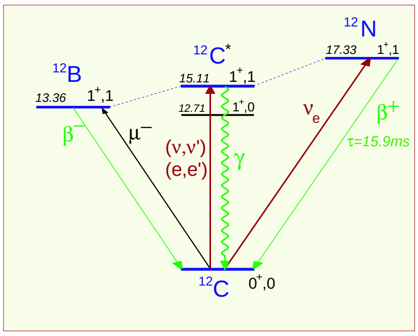

Abbildung 7: Das $A = 12$ Isospin-Triplett

neutrale Stromreaktion $^{12}\mathrm{C}\,(\,\nu\,,\nu'\,)\,^{12}\mathrm{C}^*$ benutzt werden, bei der das $^{12}\mathrm{C}^*(\,1^+\,,1\,)$-Niveau angeregt wird und ein 15.11 MeV γ-Quant beim Übergang zurück in den Grundzustand resultiert. Dieses kann als promptes Einzelereignis (*Single-Event*) im Detektor nachgewiesen werden. An dieser neutralen Stromreaktion (NC) nehmen alle Neutrinoflavors teil.

Zum anderen kann die geladene Stromreaktion $^{12}\mathrm{C}\,(\,\nu_e,\mathrm{e}^-\,)\,^{12}\mathrm{N}_{\mathrm{g.s.}}$ benutzt werden, bei der das $^{12}\mathrm{N}_{\mathrm{g.s.}}(\,1^+\,,1\,)$-Niveau durch einen inversen β-Zerfall erzeugt wird ($-$Q-Wert $= -17.33$ MeV). An einer geladenen Stromreaktion (CC) nehmen nur ν_e teil (für ν_μ und $\bar{\nu}_\mu$ aus π^+- bzw. dem μ^+-Zerfall in Ruhe sind die benötigten Neutrinoenergien $\geq m_\mu c^2$ nicht gegeben). Der Grundzustand von $^{12}\mathrm{N}$ zerfällt wiederum mit einer Lebensdauer von 15.9 ms über einen β^+-Zerfall in den Grundzustand von $^{12}\mathrm{C}$. Die exklusive CC-Reaktion $^{12}\mathrm{C}\,(\,\nu_e\,,\mathrm{e}^-\,)\,^{12}\mathrm{N}_{\mathrm{g.s.}}$ kann folglich im Detektor sehr klar über die Sequenz von einem prompten e^- sowie einem zeitlich verzögerten und räumlich korrelierten e^+ nachgewiesen werden. Die inklusive CC-Reaktion $^{12}\mathrm{C}\,(\,\nu_e\,,\mathrm{e}^-\,)\,^{12}\mathrm{N}^*$ in angeregte Zustände von $^{12}\mathrm{N}$ erzeugt dagegen nur ein einzelnes promptes *Single-Event* im Detektor (wie die NC-Reaktion). *Abb.* 8 zeigt die mit KARMEN gemessenen Sequenzen der exklusiven CC-Reaktion $^{12}\mathrm{C}\,(\,\nu_e\,,\mathrm{e}^-\,)\,^{12}\mathrm{N}_{\mathrm{g.s.}}$ für prompte sichtbare Energien über 10 MeV und im späten Zeitfenster ($\geq 0.6\,\mu$s): In der linken Spalte sind die sichtbare Energie sowie die Zeit- und Ortsverteilung der prompten e^- abgebildet, während in der rechten Spalte die sichtbare Energie sowie die Zeitdifferenz- und Ortsdifferenzverteilung der verzögerten sequentiellen e^+ dargestellt sind. Die gemessenen Spektren stimmen hervorragend mit der Erwartung aus MC-Simulationen (jeweils durchgezogene Linie) überein. Die Zeitverteilung der prompten Ereignisse spiegelt die Myonlebensdauer von 2.2 μs wider und die Zeitdifferenz der sequentiellen Ereignisse die des $^{12}\mathrm{N}_{\mathrm{g.s.}}$ von 15.9 ms (entsprechend elektronisch bedingter Korrekturen, wie z.B. die Ausleselücke am Ende einer Beamperiode). In der Ortsverteilung der prompten Ereignisse ist die $1/(\mathit{Abstand})^2$-Abhängigkeit der Neutrinos deutlich zu sehen. In dieser Arbeit konnten durch die exklusive CC-Reaktion $^{12}\mathrm{C}\,(\,\nu_e\,,\mathrm{e}^-\,)\,^{12}\mathrm{N}_{\mathrm{g.s.}}$ mit KARMEN 846 ν_e in spektroskopischer Qualität und nahezu untergrundfrei vermessen werden (Signal zu Untergrundverhältnis = 61). Die Anzahl der nachgewiesenen Reaktionen ($N = 846$) hängt mit der Anzahl der Targetatome ($N_T^{C12} = 2.54\cdot 10^{30}$) pro effektiver skalierter Fläche ($4\pi(17.7m)^2 = 1/\Omega$) sowie dem absoluten ν-Fluß ($\Phi = 5.2\cdot 10^{21}$) und der Nachweiseffizienz ($\epsilon_{ges} = 27.2\%$) folgendermaßen zusammen:

$$\langle\,\sigma\,\rangle = \frac{N}{N_T\cdot\Omega\cdot\epsilon_{ges}\cdot\Phi}$$

Damit ergibt sich ein über das ν_e-Energiespektrum gemittelter Wirkungsquerschnitt von:

$$\boxed{\begin{array}{c}\langle\sigma(^{12}\mathrm{C}\,(\,\nu_e\,,\mathrm{e}^-\,)\,^{12}\mathrm{N}_{\mathrm{g.s.}})\rangle = \\ (9.6\pm 0.3(stat.)\pm 0.7(syst.))\cdot 10^{-42}cm^2\end{array}}$$

Der systematische Fehler des Wirkungsquerschnitts wird dominiert durch die Unsicherheit im absoluten ISIS-ν-Fluß. Der mit KARMEN gemessene Wert ist in guter Übereinstimmung mit den theoretischen EPT, SM und (C)RPA Berechnungen ($7.9\ldots 10.1\cdot 10^{-42}cm^2$) sowie mit dem von LSND gemessenen Wert ($8.9\pm 0.3(stat.)\pm 0.9(syst.))\cdot 10^{-42}cm^2$ [Aue01]. Die Sequenzanalyse dieser exklusiven CC-Reaktion mit KARMEN verdeutlicht eindrucksvoll, wie gut die Eigenschaften des KARMEN-Detektors und ISIS verstanden sind. Es ist nun gerechtfertigt, im nächsten Schritt Obergrenzen für die *Disappearance* (Verschwinden) der ν_e anzugeben bzw. mit KARMEN nach weiteren ν-Oszillationen zu suchen.

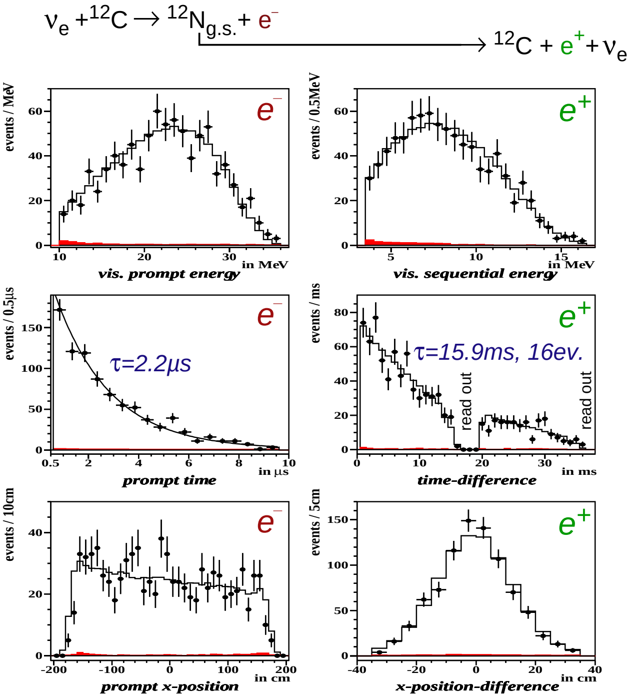

Abbildung 8: Mit KARMEN spektroskopisch gemessene Energie-, Zeit- und Ortsverteilungen der prompten und sequentiellen Ereignisse aus der exklusiven geladenen Stromreaktion $^{12}\mathrm{C}\,(\,\nu_e\,,\mathrm{e}^-\,)\,^{12}\mathrm{N}_{\mathrm{g.s.}}$

Die Analyse der prompten *Single-Events* in KARMEN erlaubt die Vermessung neutraler und geladener Stromreaktionen an ^{12}C, ^{13}C und ^{56}Fe. Mit einem konsistenten Schätzverfahren ist dies unabhängig von theoretischen Kernmodellen möglich. In *Abb.* 9 sind die Energie-, Orts- und Zeitverteilung der *Single-Event*-Reaktionen mit sichtbaren Energien über 10 MeV im späten Zeitfenster ($\geq 0.6\,\mu$s) dargestellt. Der kosmische Untergrund ist bei dem Energie- und Ortsspektrum entsprechend der Erwartung aus dem *pre-beam* abgezogen. Die Ortsverteilung weist in jedem der drei Bereiche die $1/(Abstand)^2$-Abhängigkeit der Neutrinos auf (Details s. Kapitel 3). In der Zeitverteilung ist dem flachverteilten kosmischen Untergrund eine Exponentialfunktion der Neutrinos überlagert, entsprechend der 2.2 μs-Myonlebensdauer.

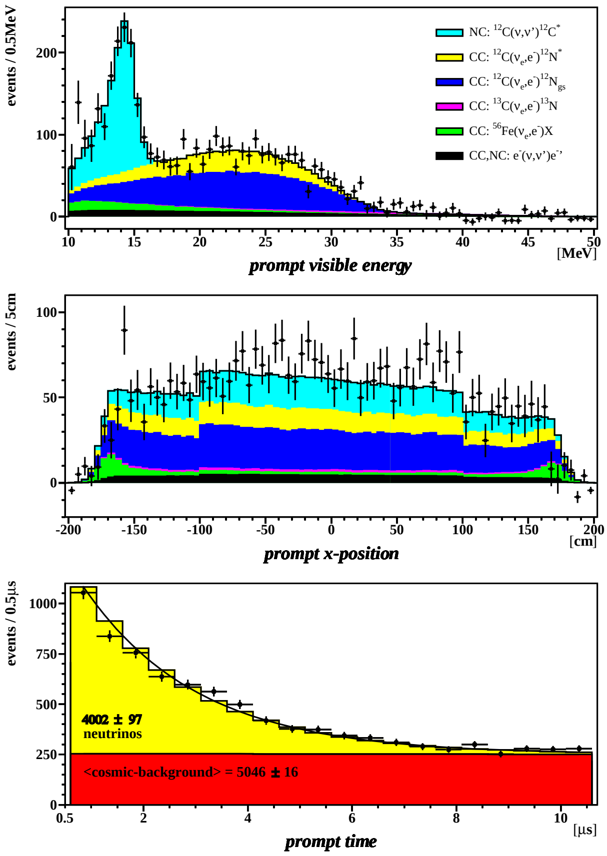

Abbildung 9: Energie-, Orts- und Zeitverteilung der *Single-Events* in KARMEN (der kosmische Untergrund ist bei dem Energie- und Ortsspektrum entsprechend der Erwartung aus dem *pre-beam* abgezogen)

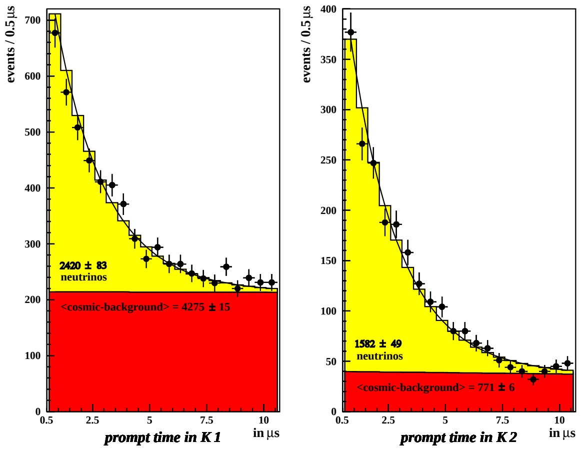

Abbildung 10: Zeitverteilung der *Single-Events* in KARMEN1 (K1) vor und KARMEN2 (K2) nach dem Upgrade. Der kosmische Untergrundanteil ist jeweils entsprechend der Erwartung aus dem *pre-beam* miteingezeichnet.

Abb. 10 zeigt getrennt die Zeitverteilungen für KARMEN1 (K1) vor und KARMEN2 (K2) nach dem Upgrade. Das Neutrino zu Untergrundverhältnis verbesserte sich von ca. 1/2 in K1 auf ca. 2/1 in K2. Zur Vermessung fast aller *Single-Event*-Neutrino-Kernreaktionen werden nur die K2-Daten benutzt (9425 C von insgesamt 18547 C), da bei einer Gesamtanalyse (K1 + K2) die statistischen Fehler größer wären oder Korrekturen durch die Ereignisse, welche die Zeitanomalie verursachen, nicht zu vernachlässigen sind. Aufgrund der sehr charakteristischen Peakstruktur in der Energie können einzig für die NC-Reaktion $^{12}\mathrm{C}\,(\,\nu\,,\nu'\,)\,^{12}\mathrm{C}^*$ die kompletten *Single-Event*-Daten ausgewertet werden. Die zu bestimmenden Neutrino-Kernreaktionen lassen sich am besten am Energiespektrum unterscheiden. Deshalb werden mit einer χ^2-Methode die unbekannten Wirkungsquerschnitte als freie Parameter gefittet. Als feste Größen gehen in den Fit ein: Der analytisch berechnete Wert für die ν-e^--Streuung ($\langle\sigma\rangle = (0.347 \pm 0.002) \cdot 10^{-42} cm^2$), desweiteren die in K1 bzw. K2 nahezu untergrundfrei gemessenen Werte für die exklusive CC-Reaktion $^{12}\mathrm{C}\,(\,\nu_e\,,\mathrm{e}^-\,)\,^{12}\mathrm{N}_{\mathrm{g.s.}}$ und schließlich der im *pre-beam* gemessene Erwartungswert des kosmischen Untergrunds. Zur Bestimmung der statistischen Fehler der Fitresultate und Kontrolle der Fitgüte wurden 1000 KARMEN–Experimente simuliert und analysiert. *Abb.* 11 zeigt das Ergebnis für die *Single-Events* in K2. Das gefittete Energiespektrum (durchgezogene Linie) stimmt gut mit den Meßpunkten im Rahmen deren Fehler überein ($\chi^2/ndf = 1.3$). In *Tabelle 1* sind die gemessenen bzw. erwarteten Ereigniszah-

Reaktion		*N*	$N_T[10^{30}]$	$\epsilon_{ges}[\%]$
$^{12}\mathrm{C}\,(\,\nu\,,\nu'\,)\,^{12}\mathrm{C}^{*}$	*K1*	604.2	2.54	36.2
$^{12}\mathrm{C}\,(\,\nu\,,\nu'\,)\,^{12}\mathrm{C}^{*}$	*K2*	451.7	2.54	26.0
$^{12}\mathrm{C}\,(\,\nu_e\,,\mathrm{e}^-\,)\,^{12}\mathrm{N}_{\mathrm{g.s.}}$	*K1*	⟨870.2⟩	2.54	54.7
$^{12}\mathrm{C}\,(\,\nu_e\,,\mathrm{e}^-\,)\,^{12}\mathrm{N}_{\mathrm{g.s.}}$	*K2*	⟨585.6⟩	2.54	36.9
$^{12}\mathrm{C}\,(\,\nu_e\,,\mathrm{e}^-\,)\,^{12}\mathrm{N}^{*}$	*K1*	⟨430.7⟩	2.54	55.5
$^{12}\mathrm{C}\,(\,\nu_e\,,\mathrm{e}^-\,)\,^{12}\mathrm{N}^{*}$	*K2*	313.2	2.54	37.3
$^{13}\mathrm{C}\,(\,\nu_e\,,\mathrm{e}^-\,)\,^{13}\mathrm{N}$	*K1*	⟨49.7⟩	0.0282	55.5
$^{13}\mathrm{C}\,(\,\nu_e\,,\mathrm{e}^-\,)\,^{13}\mathrm{N}$	*K2*	⟨35.1⟩	0.0282	36.2
$^{56}\mathrm{Fe}\,(\,\nu_e\,,\mathrm{e}^-\,)\,\mathrm{X}$	*K1*	⟨120.4⟩	2.34	0.37
$^{56}\mathrm{Fe}\,(\,\nu_e\,,\mathrm{e}^-\,)\,\mathrm{X}$	*K2*	88.7	2.34	0.25
$\mathrm{e}^-\,(\,\nu\,,\nu'\,)\,\mathrm{e}^{-\prime}$	*K1*	⟨158.6⟩	20.2	35.7
$\mathrm{e}^-\,(\,\nu\,,\nu'\,)\,\mathrm{e}^{-\prime}$	*K2*	⟨117.4⟩	20.2	24.4

Tabelle 1: Gemessene bzw. ⟨erwartete⟩ Ereigniszahl, effektive Targetkernanzahl und Nachweiseffizienz für die einzelnen *Single-Event*-Reaktionen

len für die einzelnen *Single-Event*-Reaktionen aufgelistet. Die Verteilungen der Fitresultate für 1000 simulierte K2–Experimente sind für die variierten Wirkungsquerschnitte gaussförmig und haben keinen *Bias* ($\overline{\sigma}_{fit} = \sigma_{input}$). Vergleicht man in *Abb.* 12 die feiner gebinnten Energiespektren der *Single-Events* in K1 und K2 mit den eingezeichneten Fitresultaten aus grober Binnung, so ist die Übereinstimmung im Rahmen der Fehler sehr gut. Dies gilt auch für die Energie-, Orts- und Zeitverteilung aller *Single-Events* in KARMEN (*s. Abb.* 9).

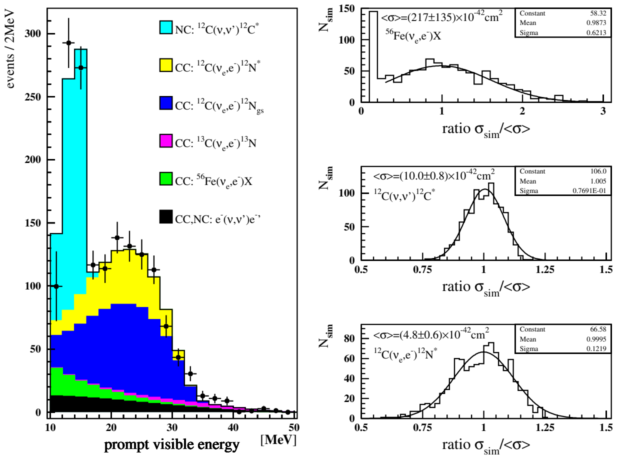

Abbildung 11: Aus den *Single-Events* in KARMEN2 mit einer χ^2-Methode bestimmte Neutrinowirkungsquerschnitte. Links das gefittete Energiespektrum abzüglich kosmischen Untergrunds. Rechts die Verteilungen der Fitresultate der variierten Wirkungsquerschnitte für 1000 simulierte KARMEN2–Experimente.

Für die weltweit erstmals von KARMEN beobachtete NC-Reaktion $^{12}\mathrm{C}\,(\,\nu\,,\nu'\,)\,^{12}\mathrm{C}^{*}(\,1^+\,,1\,;15.11\ \mathrm{MeV}\,)$ ergibt sich bei einer Gesamtanalyse (K1+K2) nach dieser Arbeit ein über das ν_e- und $\bar{\nu}_\mu$-Energiespektrum gemittelter Wirkungsquerschnitt von:

$$\boxed{\begin{array}{c}\langle\sigma(^{12}\mathrm{C}\,(\,\nu\,,\nu'\,)\,^{12}\mathrm{C}^{*})\rangle = \\ (10.2 \pm 0.4(stat.) \pm 0.8(syst.)) \cdot 10^{-42} cm^2\end{array}}$$

Die Werte von K1 und K2 wurden effizienz- und flußgewichtet addiert. Der systematische Fehler dieses und aller anderen bestimmten Wirkungsquerschnitte wird dominiert durch die Unsicherheit im absoluten ISIS-ν-Fluß. Der von KARMEN gemessene Wert wird von allen theoretischen Berechnungen bestätigt $(9.8 \ldots 11.9 \cdot 10^{-42} cm^2)$, ist jedoch systematisch kleiner als der frühere, in einem *Fiducial*-Volumen bestimmte, K1 Wert von $(10.9 \pm 0.7(stat.)) \cdot 10^{-42} cm^2$ [Sch96].

Bildet man nun den Quotienten aus dem Meßwert für die NC-Reaktion und dem Wert für die nahezu untergrundfrei nachgewiesene exklusive CC-Reaktion $^{12}\mathrm{C}\,(\,\nu_e\,,\mathrm{e}^-\,)\,^{12}\mathrm{N}_{\mathrm{g.s.}}$, so läßt sich damit die μ-e-Universalität neutraler und geladener schwacher Ströme präzise testen. Es ergibt sich ein über das ν_e- und $\bar{\nu}_\mu$-Energiespektrum gemitteltes Verhältnis $\frac{\langle\sigma^{NC}\rangle}{\langle\sigma^{CC}_{gs}\rangle}$:

$$\boxed{R = \frac{\langle\sigma^{NC}\rangle}{\langle\sigma^{CC}_{gs}\rangle} = 1.07 \pm 0.06(stat.) \pm 0.01(syst.)}$$

Die Unsicherheit im absoluten ISIS-ν-Fluß entfällt im systematischen Fehler dieses Verhältnisses. Der mit KARMEN gemessene Wert stimmt mit zwei der

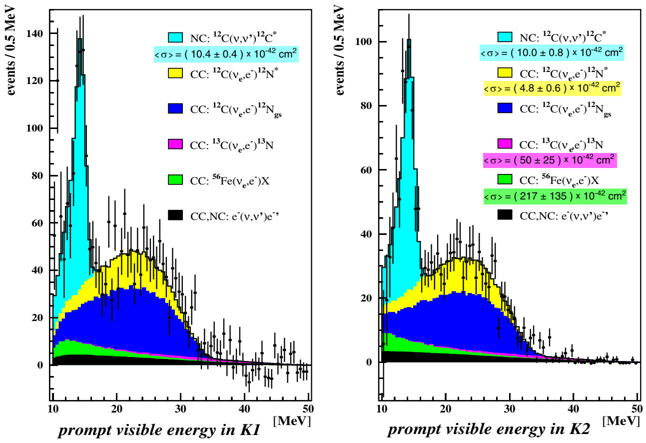

Abbildung 12: Sichtbares Energiespektrum der *Single-Events* in KARMEN1 (K1) vor und KARMEN2 (K2) nach dem Upgrade und die daraus gewonnenen Wirkungsquerschnitte. Der kosmische Untergrund ist jeweils entsprechend der Erwartung aus dem *pre-beam* abgezogen.

fünf theoretischen Berechnungen überein (1.07 ... 1.27) und liefert somit keinen Hinweis auf die Verletzung der μ-e-Universalität der schwachen Wechselwirkung im V-A Standardmodell. Durch die bislang einzigartige Präzision dieses gemessenen Verhältnisses R können umgekehrt Modellrechnungen geprüft werden. So z.B. die CRPA: Ein mikroskopisches Modell, welches eigentlich der Struktur der Kerne gerechter wird und auch zur Berechnung der Neutrino-Nukleosynthese in Sternen herangezogen wird (relevante Nukleonenzahl ≈ 12). Mit $R^{CRPA} = 1.18$ liefert diese jedoch keine hinreichende Beschreibung des neuen KARMEN-Wertes (früherer K1 Wert: $1.17 \pm 0.1(stat.)$ [Sch96]).

Für die inklusive CC-Reaktion ${}^{12}\mathrm{C}\,(\,\nu_e\,,\mathrm{e}^-\,)\,{}^{12}\mathrm{N}^*$ in angeregte Zustände von ${}^{12}\mathrm{N}$ ergibt sich ein über das ν_e-Energiespektrum gemittelter Wirkungsquerschnitt:

$$\boxed{\begin{array}{c}\langle\sigma({}^{12}\mathrm{C}\,(\,\nu_e\,,\mathrm{e}^-\,)\,{}^{12}\mathrm{N}^*)\rangle = \\ (4.8 \pm 0.6(stat.)\,{}^{+\,0.4}_{-\,0.5}(syst.)) \cdot 10^{-42} cm^2\end{array}}$$

Der mit KARMEN2 gemessene Wert ist in Übereinstimmung mit fast allen theoretischen Berechnungen ($3.7\ \ldots\ 8.3 \cdot 10^{-42} cm^2$) sowie mit dem von LSND gemessenen Wert $(4.3{\pm}0.4(stat.){\pm}0.6(syst.)){\cdot}10^{-42} cm^2$ [Aue01].

Für die weltweit erstmals beobachtete und im Rahmen dieser Arbeit detailliert analysierte CC-Reaktion ${}^{56}\mathrm{Fe}\,(\,\nu_e\,,\mathrm{e}^-\,)\,\mathrm{X}$ ergibt sich ein über das ν_e-Energiespektrum gemittelter Wirkungsquerschnitt von:

$$\boxed{\begin{array}{c}\langle\sigma({}^{56}\mathrm{Fe}\,(\,\nu_e\,,\mathrm{e}^-\,)\,\mathrm{X})\rangle = \\ (217 \pm 135(stat.)\,{}^{+\,27}_{-\,65}(syst.)) \cdot 10^{-42} cm^2\end{array}}$$

Der mit KARMEN2 gemessene Wert ist in Übereinstimmung mit allen theoretischen Berechnungen (214 ... $380 \cdot 10^{-42} cm^2$) und besagt, daß Ereignisse aus dieser Reaktion mit $90\% CL$ beobachtet wurden (ohne Berücksichtigung des systematischen Fehlers). Die mittlere freie Weglänge für Neutrinos im Core einer Typ-II-Supernova beträgt damit 40 km während des Kollapses und nur 20 m direkt danach [Sch97].

Für die weltweit erstmals im Rahmen dieser Arbeit gemessene CC-Reaktion ${}^{13}\mathrm{C}\,(\,\nu_e\,,\mathrm{e}^-\,)\,{}^{13}\mathrm{N}$ ergibt sich ein über das ν_e-Energiespektrum gemittelter Wirkungsquerschnitt von:

$$\boxed{\begin{array}{c}\langle\sigma({}^{13}\mathrm{C}\,(\,\nu_e\,,\mathrm{e}^-\,)\,{}^{13}\mathrm{N})\rangle = \\ (50 \pm 25(stat.)\,{}^{+\,4}_{-\,6}(syst.)) \cdot 10^{-42} cm^2\end{array}}$$

Dieser Wert wurde nach einer Fenstermethode im Energiebereich von 38 ... 50 MeV in einem *Fiducial*-Volumen bestimmt. Im selektierten Bereich tragen neben dem präzise meßbaren kosmischen Anteil nur noch die analytisch berechenbare ν-e^--Streuung als Komponente bei. Der so mit KARMEN2 gemessene Wert wird von den meisten theoretischen Berechnungen bestätigt ($29\ \ldots\ 113 \cdot 10^{-42} cm^2$). Da der größte berechnete Wert von der Messung ausgeschlossen werden kann, läßt dies darauf schließen, daß der Gamow-Teller-Übergang in das ${}^{13}\mathrm{N}^*(3/2^-)$-Niveau stark gequencht ist (wie bei den anderen Berechnungen, die zu deutlich kleineren Werten führen, angenommen).

Die Flavoreigenzustände der Neutrinos koppeln ausschließlich über die Vektorbosonen der schwachen Wechselwirkung ($W^{\pm}$, Z^0). Aufgrund der Tatsache, daß Neutrinos eine Ruhemasse haben, koppeln andererseits ihre Masseneigenzustände an Higgs-Felder. Die für Neutrinoexperimente relevanten Observablen sind jedoch die Flavoreigenzustände ($|\nu_\alpha\rangle$ mit $\alpha = e, \mu, \tau$). Diese lassen sich folglich jeweils als Linearkombination der Masseneigenzustände ($|\nu_i\rangle$ mit $i = 1, 2, 3$) darstellen:

$$|\nu_\alpha\rangle = \sum_i U_{\alpha i} |\nu_i\rangle$$

Die Flavoreigenzustände können somit bei Nichtdiagonalität von $U_{\alpha i}$ ineinander oszillieren aufgrund der unterschiedlichen Zeitentwicklung der Masseneigenzustände. Die unitäre Mischungsmatrix $U_{\alpha i}$ für diese Oszillationstransformation wird Maki-Nakagawa-Sakata-Matrix (MNS-Matrix) genannt. Dieser 3-Flavor-Formalismus kann zweckmäßig durch einen 2-Flavor-Formalismus ohne Berücksichtigung von CP-Verletzung approximiert werden:

$$\begin{pmatrix} |\nu_\alpha\rangle \\ |\nu_\beta\rangle \end{pmatrix} = \begin{pmatrix} \cos\Theta & \sin\Theta \\ -\sin\Theta & \cos\Theta \end{pmatrix} \cdot \begin{pmatrix} |\nu_1\rangle \\ |\nu_2\rangle \end{pmatrix}$$

Die Wahrscheinlichkeit $\mathcal{P}$ für die Oszillation $\nu_\alpha \to \nu_\beta$ ist dann gegeben durch:

$$\mathcal{P}(|\nu_\alpha\rangle \to |\nu_\beta\rangle) = \sin^2(2\Theta)\sin^2\left(\frac{1.27 \cdot \Delta m^2[eV^2] \cdot L[m]}{E_\nu[MeV]}\right) \tag{1}$$

$$mit \quad \Delta m^2 = |{m_1}^2 - {m_2}^2|$$

Bei gegebener Neutrinoenergie E_ν und festem Abstand L des Detektors von der Quelle sind $\sin^2(2\Theta)$ und Δm^2 die Variablen, welche den räumlichen und

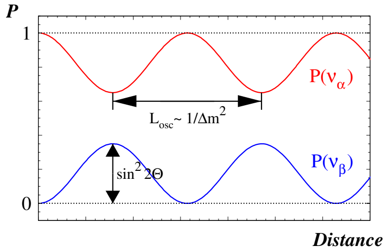

Abbildung 13: Schematische räumliche Entwicklung der Flavorwahrscheinlichkeit bei 2-Flavor-Oszillation $\nu_\alpha \longrightarrow \nu_\beta$

zeitlichen Verlauf der Oszillationswahrscheinlichkeit bestimmen. $\sin^2(2\Theta)$ entspricht dabei der Oszillationsamplitude während die Oszillationslänge von Δm^2 abhängt (*s. Abb.* 13). Zur graphischen Darstellung des Ergebnisses einer ν-Oszillationssuche wird deshalb praktischerweise Δm^2 über der Oszillationsamplitude $\sin^2(2\Theta)$ aufgetragen (*s. Abb.* 2 und 14). Bei $\Delta m^2 \simeq E_\nu/L$ ist die Oszillation maximal und somit ein Experiment am sensitivsten auf ν-Oszillationen (vgl. das 2. Argument in Glg. 1).

Der mit KARMEN gemessene Wirkungsquerschnitt der exklusiven CC-Reaktion $^{12}\mathrm{C}\,(\,\nu_e\,,\mathrm{e}^-\,)\,^{12}\mathrm{N}_{\mathrm{g.s.}}$ ist kompatibel mit den theoretischen Vorhersagen. Damit kann eine Obergrenze für die *Disappearance* (Verschwinden) von $\nu_e\!\longrightarrow\nu_{sterile}$ abgeleitet werden. Bei einer Erwartung von (806±66) ν_e (insgesamt 8 % Unsicherheit aus Theorie, ν-Fluß und Nachweiseffizienz) wurden (860±29) Sequenzen gemessen mit einem verschwindend kleinem Untergrundanteil von (14 ± 1) Ereignissen. Hieraus läßt sich ein mögliches Oszillationssignal von 53 verschwundenen ν_e mit 90%CL ausschließen. Das Verhältnis von $N_{90\%CL} = 53$ zu der Erwartung bei vollständiger Oszillation $N_{full} = 806$ ergibt die Obergrenze für die Oszillationswahrscheinlichkeit $\mathcal{P}_{90\%CL} = 6.5 \cdot 10^{-2}$. Eingesetzt in Glg. 1 läßt sich $\sin^2(2\Theta)$ als Funktion von Δm^2 abstands- und energiegewichtet berechnen:

$$\sin^2(2\Theta) = \frac{\mathcal{P}_{90\%CL}^{\nu_e\rightarrow\nu_{sterile}}}{\int_L w(L)\cdot\int_E w_{\Phi\,\sigma\,\epsilon}(E)\cdot\sin^2\left(\frac{1.27\cdot\Delta m^2\cdot L}{E_\nu}\right)\,dE\,dL}$$

In *Abb.* 14 ist diese 90%CL-Ausschlußkurve dargestellt. Bereiche rechts der Kurve sind mit 90%CL ausgeschlossen. Die größte Sensitivität erreicht KARMEN bei $2-3\,eV^2$ ($\simeq 44\,[MeV]/17.7\,[m]$). Für große Δm^2 ergibt sich folgende Obergrenze für die *Disappearance* von $\boxed{\nu_e\!\longrightarrow\nu_{sterile}}$:

$$\boxed{\sin^2(2\Theta)\ <\ 0.13\ (90\%CL)}$$

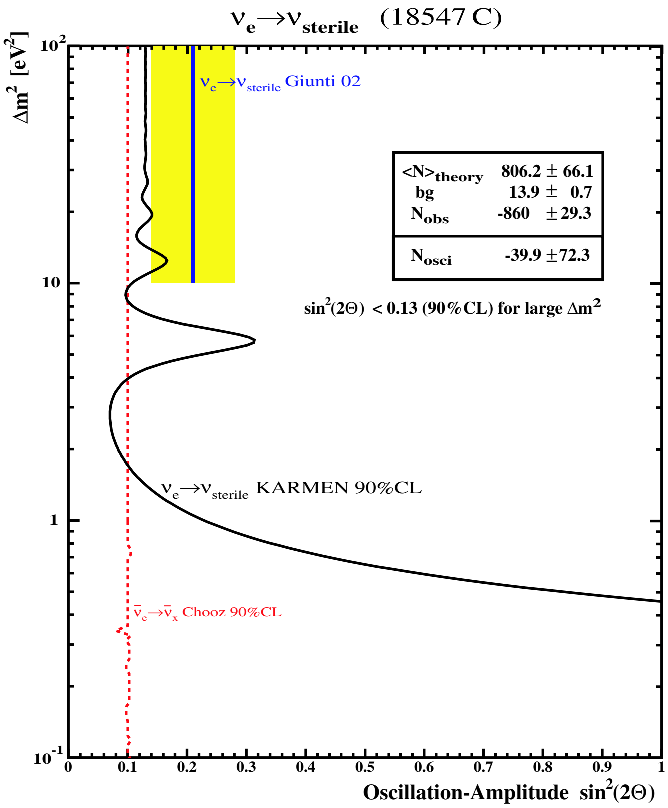

Abbildung 14: Ausschlußkurve für die *Disappearance* von $\nu_e\!\longrightarrow\nu_{sterile}$ abgeleitet aus dem gemessenen $^{12}\mathrm{C}\,(\,\nu_e\,,\mathrm{e}^-\,)\,^{12}\mathrm{N}_{\mathrm{g.s.}}$ Wirkungsquerschnitt mit KARMEN (Bereiche rechts der Kurve sind mit 90%CL ausgeschlossen). Zum Vergleich ist die Region miteingezeichnet, welche als mögliche Erklärung für die Weinbergwinkelanomalie des NuTeV–Experiments diskutiert wird [Giu02] sowie das Limit für die *Disappearance* von Reaktorantineutrinos im CHOOZ–Experiment [Apo99].

Damit kann die Region, welche als mögliche Erklärung für die Weinbergwinkelanomalie des NuTeV-Experiments diskutiert wird [Giu02], fast vollständig ausgeschlossen werden. Es findet sich dabei mit KARMEN kein Hinweis auf schwere sterile Neutrinos. Läßt man eine mögliche CP-Verletzung außer Betracht, so ist dieses Resultat konform mit dem Limit für die *Disappearance* von Reaktorantineutrinos ($\bar{\nu}_e$) im CHOOZ–Experiment [Apo99].

Bei KARMEN kann nicht nur die *Disappearance* (Verschwinden) von ν_e im späten Zeitfenster des μ^+-Zerfalls, sondern auch die *Appearance* (Erscheinen) von ν_e in den beiden frühen Zeitfenstern der π^+-Zerfälle untersucht werden. Dazu wird in zwei 100 ns breiten Zeitfenstern (entsprechend dem Tastverhältnis der Protondoppelpulse) nach der *Appearance* von $\nu_\mu \rightarrow \nu_e$ gesucht (*vgl. Abb.* 4). Diese ν_e können über die bereits in spektroskopischer Qualität studierte exklusive CC-Reaktion $^{12}\mathrm{C}\,(\,\nu_e\,,\mathrm{e}^-\,)\,^{12}\mathrm{N}_{\mathrm{g.s.}}$ nachgewiesen werden. Um verbleibende hochenergetische schnelle Neutronen ($E_{kin}>$ 10 MeV) abzuschneiden, werden jeweils nur die ersten 100 ns der beiden Pulse analysiert. Die Suche $\nu_\mu \rightarrow \nu_e$ findet 4 Sequenzen bei 3.2 erwarteten ν_e aus dem bereits einsetzenden μ^+-Zerfall. Die zusätzliche Erwartung aus kosmischem und zufälligem Untergrund beträgt 0.7 Ereignisse. Damit läßt sich ein mögliches Oszillationssignal von 4.8 erschienenen ν_e Bayesisch mit 90%CL ausschließen. Mit Hilfe des gemessenen und energiekorrigierten Wirkungsquerschitts $\langle\sigma(^{12}\mathrm{C}\,(\,\nu_e\,,\,\mathrm{e}^-\,)\,^{12}\mathrm{N}_{\mathrm{g.s.}})\rangle$ bestimmt sich die Erwartung für vollständige Oszillation zu 398 ν_e. Für große Δm^2 ergibt sich folgende Obergrenze für die *Appearance* von $\boxed{\nu_\mu \rightarrow \nu_e}$:

$$\boxed{\sin^2(2\Theta)\;<\;2.4\cdot 10^{-2}\;(90\%CL)}$$

Abb. 15 zeigt die 90%CL-Ausschlußkurve. KARMEN ist für $\Delta m^2 < 10\,eV^2$ das sensitivere Experiment.

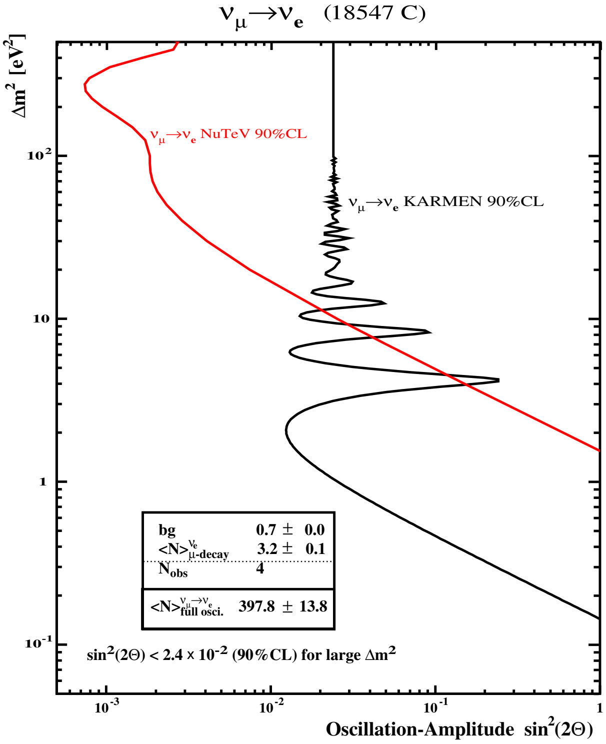

Abbildung 15: Ausschlußkurve für die *Appearance* von $\nu_\mu \rightarrow \nu_e$ in KARMEN und NuTeV [Avv02]. Bereiche rechts der Kurven sind jeweils mit 90%CL ausgeschlossen.

Die Suche nach der *Appearance* von $\bar{\nu}_\mu \rightarrow \bar{\nu}_e$ (LSND-Oszillation) kann in KARMEN2 mit einer dedizierten Sequenzanalyse durchgeführt werden: $\bar{\nu}_e$ werden über den inversen β-Zerfall p($\bar{\nu}_e$,e^+)n an den freien Protonen des organischen Szintillators nachgewiesen ($-Q= -1.8\,$MeV), indem zum prompten e^+ ein zeitlich verzögertes und räumlich korreliertes Neutron gesucht wird. Dazu werden jeweils die ersten 300 μs, nach einem prompten e^+ im späten Zeitfenster der μ^+-Zerfälle, auf ein sequentielles Neutron hin analysiert ($\tau\,=\,120\,\mu$s: Thermalisierungs- und Diffusionszeit). Die Neutroneneffizienz des (n,γ)-Nachweises an den freien Protonen des Szintillators und dem Gadolinium in den Modulwänden beträgt 42%. Bis auf die simulierte $\bar{\nu}_e$-Kontamination sind die Untergrundquellen für die (e^+,n)-Sequenzsuche mit KARMEN präzise meßbar: Der kosmische Untergrund, die exklusive CC-Reaktion $^{12}\mathrm{C}\,(\,\nu_e\,,\mathrm{e}^-\,)\,^{12}\mathrm{N}_{\mathrm{g.s.}}$ und der ν_e-induzierte zufällige Untergrund. Insgesamt erwartet man 15.8 Sequenzen. Die Analyse findet 15 Sequenzen und liefert somit keinen Hinweis auf Oszillation $\bar{\nu}_\mu \rightarrow \bar{\nu}_e$. Es läßt sich Bayesisch ein zusätzliches Signal von 7.4 $\bar{\nu}_e$ mit 90%CL ausschließen. Mit der Erwartung von 5826 $\bar{\nu}_e$ bei vollständiger Oszillation ergibt sich für große Δm^2 folgende Obergrenze für die *Appearance* von $\boxed{\bar{\nu}_\mu \rightarrow \bar{\nu}_e}$ aus der Sequenzsuche:

$$\boxed{\sin^2(2\Theta)\;<\;2.5\cdot 10^{-3}\;(90\%CL)}$$

In *Abb.* 16b) ist die entsprechende 90%CL-Ausschlußkurve eingezeichnet. Für $\Delta m^2\,>\,1\,eV^2$ lassen sich weitere Teile der LSND-Evidenzregion ausschließen. Eine nochmals stringentere Ausschlußgrenze mit KARMEN2 erhält man aus der Sequenzanalyse über ein Maximum-Likelihood-Verfahren, das ausführlich in [Arm02] beschrieben ist und zusätzlich die volle verfügbare spektrale Information benützt (*vgl. Abb.* 16a). Für große Δm^2 ergibt sich daraus im *Unified Approach* eine Obergrenze von $\sin^2(2\Theta)\,<\,1.7\cdot 10^{-3}$ (90%CL) für die *Appearance* von $\bar{\nu}_\mu \rightarrow \bar{\nu}_e$.

Die Suche nach der *Appearance* von $\bar{\nu}_\mu \rightarrow \bar{\nu}_e$ kann in KARMEN2 auch mit einer Analyse der *Single-Events* durchgeführt werden: In einem *Fiducial*-Volumen mit sichtbaren Energien oberhalb von 38 MeV tragen, neben dem präzise meßbaren kosmischen Untergrund, nur noch die analytisch berechenbare ν-e^--Streuung, sowie die CC-Reaktion $^{13}\mathrm{C}\,(\,\nu_e\,,\mathrm{e}^-\,)\,^{13}\mathrm{N}$ als Komponenten zu den *Single-Events* bei. $\bar{\nu}_e$ würden somit über die Reaktion p($\bar{\nu}_e$,e^+)n eine zusätzliche Untergrundkomponente darstellen. Nimmt man konservativ für $\langle\sigma(^{13}\mathrm{C}\,(\,\nu_e\,,\mathrm{e}^-\,)\,^{13}\mathrm{N})\rangle$ den kleinsten theoretischen Wert der mikroskopischen Modelle ($\sigma_{theo} = 52.8\cdot10^{-42}cm^2$), so erwartet man insgesamt 14.4 Ereignisse. Bei 14 beobachteten Ereignissen läßt sich hieraus Bayesisch ein zusätzliches Signal von 7.4 $\bar{\nu}_e$ mit 90%CL ausschließen. Mit der vollständigen Oszillationserwartung von 5313 $\bar{\nu}_e$ (trotz höherer Energieschwelle im Vgl. zur Sequenzmethode *s. Tabelle 2*) ergibt sich für große Δm^2 folgende Obergrenze für die *Appearance* von $\boxed{\bar{\nu}_\mu\!\rightarrow\bar{\nu}_e}$ aus den *Single-Events*:

$$\boxed{\sin^2(2\Theta)\;<\;2.8\cdot10^{-3}\;(90\%CL)}$$

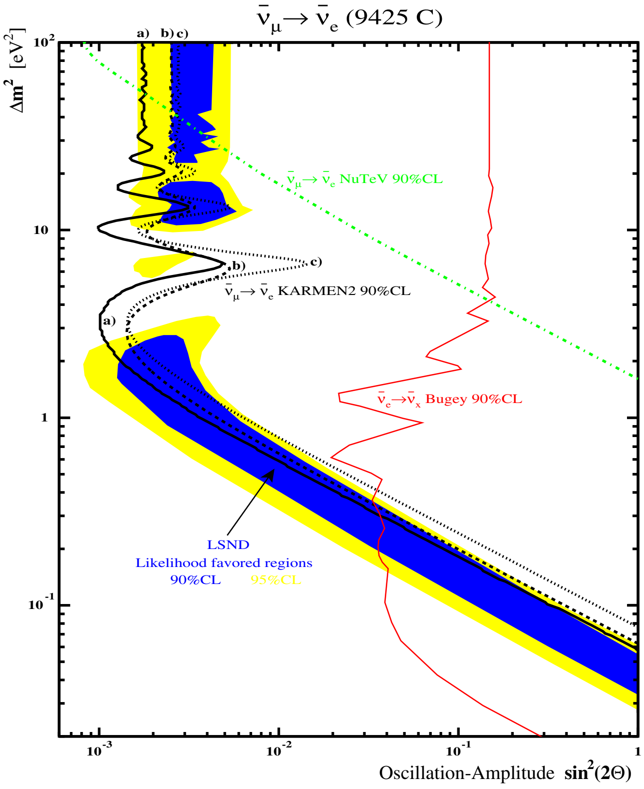

Abbildung 16: Oszillationsplot mit der LSND-Evidenzregion für $\bar{\nu}_\mu\!\rightarrow\bar{\nu}_e$ und Ausschlußkurven: a) Finale KARMEN2 Likelihood-Methode [Arm02], b) KARMEN2 sequentielle Fenstermethode, c) KARMEN2 Single-Event-Analyse, sowie die Resultate von NuTeV [Avv02] und Bugey ($\bar{\nu}_e\!\rightarrow\bar{\nu}_x$) [Ach95]. Bereiche rechts der Kurven sind jeweils mit 90%CL ausgeschlossen.

In *Abb.* 16c) ist die 90%CL-Ausschlußkurve dargestellt. Wieder lassen sich für $\Delta m^2 > 1\,eV^2$ weite Teile der LSND-Evidenzregion ausschließen, aufgrund dieses neuen, unabhängigen KARMEN2 Resultats. KARMEN liefert folglich in keiner der drei Analysemethoden einen Hinweis auf die Existenz eines zusätzlichen sterilen schwereren Neutrinos (LSND–Szenario). In einer weiteren Untersuchung mit KARMEN können die $\bar{\nu}_e$-Emission aus Leptonflavor-verletzenden μ^+-Zerfällen als mögliche Erklärung für das LSND-Signal ausgeschlossen werden [Arm03].

Reaktion	$\sigma[10^{-42}cm^2]$	N_{full}	$N_T[10^{30}]$
p($\bar{\nu}_e$,e^+)n $\rightarrow$ (n,γ)	93.5	5576	4.52
p($\bar{\nu}_e$,e^+)n	93.5	5313	4.52
^{12}C($\bar{\nu}_e$,e^+n)^{11}B$\rightarrow$ (n,γ)	8.5	250	2.54

Tabelle 2: Für vollständige Oszillation $\bar{\nu}_\mu\!\rightarrow\bar{\nu}_e$ erwartete $\bar{\nu}_e$-Anzahl, Wirkungsquerschnitte der prompten Nachweisreaktionen (Sequenz- bzw. *Single-Event*-Methode) und effektive Targetkernanzahl.

Eine Anomalie in der Zeitverteilung der *Single-Events* ist in KARMEN1 zwischen 3μs und 4μs zu beobachten (*vgl. Abb.* 10). Als mögliche Erklärung dieser KARMEN-Zeitanomalie wurde der Pionzerfall außerhalb des Standardmodells ($\pi^+\rightarrow\mu^+ + X$) in ein neues schwach wechselwirkendes 33.9 MeV massives X-Teilchen intensiv diskutiert [Zei95], [Oeh99]. In dieser Arbeit wird gezeigt, daß die Zeitanomalie mit hoher Wahrscheinlichkeit durch intermediäre Neutronen erklärt werden kann, welche strahlkorrelierten Untergrund verursachen.

In *Abb.* 17a) ist der energieabhängige totale Wirkungsquerschnitt von Neutronen an Eisen im Resonanzbereich (1 keV - 2 MeV) dargestellt. Deutlich erkennbar sind die scharfen Wirkungsquerschnittsminima, die teilweise unter 100 mbarn hinabreichen. In *Abb.* 17b) ist der energieabhängige Wirkungsquerschnitt der Neutronen als Funktion ihrer mittleren Flugzeit vom Haupttarget aufgetragen. Betrachtet man das tiefe Doppelminimum im Wirkungsquerschnitt (Nr.3 + 4), so erreichen diese Neutronen mit 129 keV bzw. 137 keV kinetischer Energie den KARMEN-Detektor nach etwa 3.5 μs: Im Zeitbereich der Anomalie. Über eine prompte Fe(n,γ)-Reaktion im unmittelbar den Detektor umgebenden Stahl könnten diese intermediären Neutronen indirekt eine *Single-Event*-

Signatur erzeugen. Die γ-Quanten aus z.B. ^{57}Fe(n,γ)-Reaktionen haben eine Energie von 10 MeV und können bis zu 0.5 m tief in den Detektor eindringen (2.2 % Isotopenanteil von ^{57}Fe). Durch die endliche Energieauflösung des Detektors sind höhere sichtbare Energien möglich. In KARMEN1 ist im sichtbaren Energiespektrum der *Single-Events* deutlich ein Überschuß an der unteren Schwelle zwischen 10 MeV und 12 MeV zu erkennen (*s. Abb.* 12). Durch den Einbau der 5 cm dicken Vetozähler aus Plastikszintillator mit zusätzlich 4 cm dicken borierten PE-Platten wurde ein Großteil dieser intermediären Neutronen moderiert und über eine ^{10}B(n,α)-Reaktion dort eingefangen. Die Zeitanomalie zwischen 3μs und 4μs ist in K2 nicht mehr zu beobachten (*vgl. Abb.* 10). Allerdings war in K2 das Vortarget von ISIS mit bis zu 10 mm im Mittel fast doppelt so dick wie in K1. Die seitliche Eisenabschirmung in Richtung des Vortargets beträgt lediglich 2 m im Vergleich zu den 7 m Abschirmung zum Haupttarget. Entsprechend der größeren Entfernung des Vortargets von 29.1 m (Haupttarget 17.7 m) erreichen dort produzierte Neutronen mit 129 keV bzw. 137 keV kinetischer Energie den Detektor erst nach etwa 5.8μ s (*s. Nr.*$3+4$ *in Abb.* 17c).

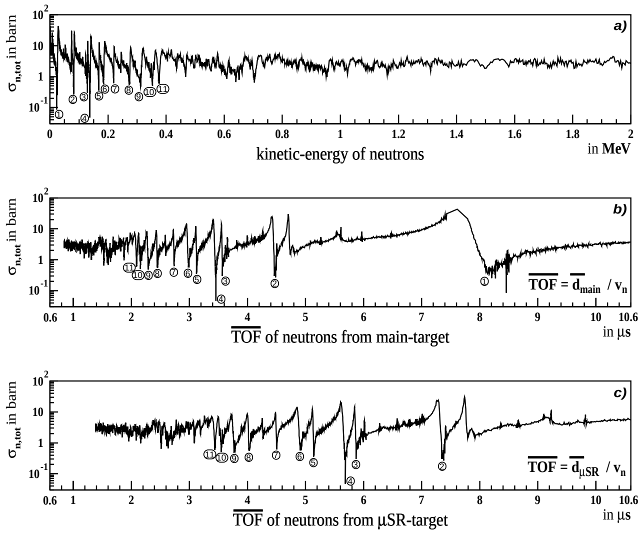

Abbildung 17: Totaler Wirkungsquerschnitt von Neutronen an Eisen im Resonanzbereich (1 keV - 2 MeV) [Har84]. Dargestellt in Abhängigkeit a) der kinetischen Energie der Neutronen, b) der mittleren Flugzeit vom Haupttarget und c) der mittleren Flugzeit vom μSR-Vortarget. Zur Orientierung sind die 11 tiefsten Wirkungsquerschnittminima markiert.

In einer dedizierten Geschwindigkeitsanalyse der *Single-Events* läßt sich mit einer Maximum-Likelihood-Methode die Interpretation der KARMEN-Zeitanomalie als strahlkorrelierter Neutronenuntergrund untermauern und quantifizieren. Hierfür wird für K1 und K2 jeweils die Zahl der (n,γ)-Ereignisse in den *Single-Events* über der Neutronengeschwindigkeit variiert. Die intermediären Neutronen werden entsprechend der Zeitverteilung der parabelförmigen Protonendoppelpulse im Haupt- bzw. Vortarget generiert (unter Berücksichtigung der unterschiedlichen Protonenflugzeit in der *beam-line*). *Abb.* 18 zeigt das Ergebnis dieser Likelihood-Analyse. Mit Hilfe der Likelihood-Funktion $\mathcal{L}$ können für K1 (vom Haupttarget aus betrachtet) die tiefen Doppelminima im Neutronenwirkungsquerschnitt (Nr.$3+4$ in A1) den gefundenen Neutronengeschwindigkeiten statistisch signifikant zugeordnet werden. Diese der Zeitanomalie entsprechenden Minima sind in K2 nach dem Upgrade nicht mehr signifikant (Nr.3+ 4 in A2). Dafür wird in K2 jetzt vom dickeren Vortarget aus betrachtet das Wirkungsquerschnittsminimum (Nr.3 in B2) bei der gleichen Neutronenge-

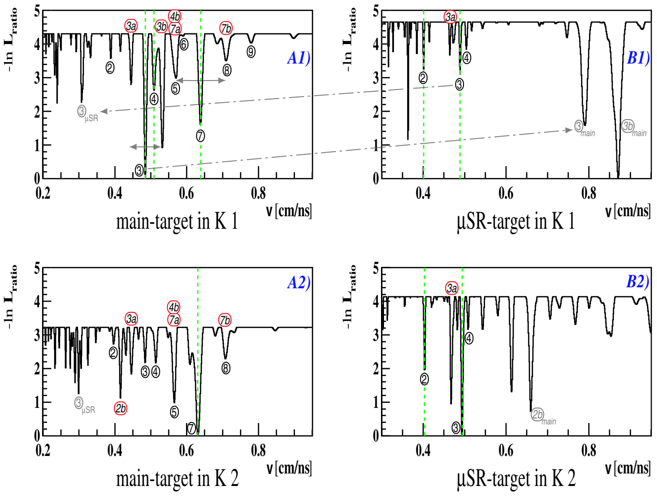

Abbildung 18: Geschwindigkeitsanalyse der *Single-Events* in KARMEN: Vergleich der Minima des geschwindigkeitsabhängigen Neutronenwirkungsquerschnitts in Eisen mit den Likelihood-Funktionen A1),B1) vor dem Upgrade und A2),B2) danach. Links die Likelihood-Funktionen A1),A2) sind auf das Haupttarget bezogen sowie rechts B1),B2) auf das μSR-Vortarget. Eineindeutig zugeordnete signifikante Minima in den Likelihood-Funktionen sind jeweils mit einer senkrechten gestrichelten Linie hervorgehoben. Zudem visualisiert sind in den Likelihood-Funktionen die Mehrdeutigkeiten welche durch jeweils zwei vorhandene Nebenminima (Doppelpulsstruktur) und zwei Produktionstargets entstehen.

schwindigkeit gefunden wie in K1 vom Haupttarget. Unter Beachtung der Mehrdeutigkeiten in $\mathcal{L}$, aufgrund der Doppelpulsstruktur in zwei Produktionstargets, können weitere statistisch signifikante Minima zugeordnet werden (*benchmark*: $68\% CL$ bzw. $1.15\,|\Delta ln\mathcal{L}|$). Für die Hypothese des strahlkorrelierten Neutronenuntergrunds ergibt sich im Vergleich zur Nullhypothese bei einer Gesamtanalyse (K1+K2) eine Gesamtwahrscheinlichkeit von etwa $1\,Mrd.:1$ ($\cong -20\,ln\mathcal{L}_{ratio}$ im Vgl. zu $-7.3\,ln\mathcal{L}_{ratio}$ für die X-Teilchen Hypothese [Oeh99]). Die neutroneninduzierten strahlkorrelierten (n,γ)-Ereignisse in den *Single-Events* liefern folglich eine sehr plausible Erklärung der KARMEN-Zeitanomalie. Anschaulich wirkt die massive Eisenabschirmung als Filter für spezielle intermediäre Neutronenenergien vom Target.
Es bleibt zu erwähnen, daß nicht verstanden ist, wie die sichtbare Energie der in der Geschwindigkeitsanalyse bestimmten (n,γ)-Ereignisse Werte von über 16 MeV annehmen kann (was v.a. in K2 zu einem Teil passiert sein muß). Nur etwa die Hälfte aller Überschuß-Ereignisse der Zeitanomalie weisen sichtbare Energien an der unteren Schwelle zwischen 10 MeV und 13 MeV auf [Oeh99].

Der Pionzerfall ($\pi^+ \rightarrow \mu^+ + X$) in ein neues schwach wechselwirkendes 33.9 MeV massives X-Teilchen (WIMP, Neutralino) kann Bayesisch bis zu einem Verzweigungsverhältnis von $6 \cdot 10^{-17}$ ($90\% CL$) ausgeschlossen werden (bei einer Lebensdauer im μs-Bereich).

In *Abb.* 19 sind in die beiden Zeitverteilungen der *Single-Events* (K1/K2) die Anteile aller in der Geschwindigkeitsanalyse bestimmten (n,γ)-Ereignisse miteingezeichnet. Relativ zur Anzahl der Neutrinos beträgt deren Anteil in K1: 5% sowie in K2: 3%. Die statistischen Fehler der aus den *Single-Events* bestimmten ν-Wirkungsquerschnitte sind in K2 deutlich größer. Eventuelle Korrekturen sind in K2 vernachlässigbar, nicht aber in K1 für die Reaktionen $^{56}\mathrm{Fe}\,(\,\nu_e\,,\mathrm{e}^-\,)\,\mathrm{X}$ und $^{12}\mathrm{C}\,(\,\nu_e\,,\mathrm{e}^-\,)\,^{12}\mathrm{N}^*$, für welche die relativ große Anzahl von (n,γ)-Ereignissen größere Korrekturen erfordern würde. Aufgrund der sehr charakteristischen Peakstruktur in der sichtbaren Energie können in K1 einzig für die NC-Reaktion $^{12}\mathrm{C}\,(\,\nu\,,\nu'\,)\,^{12}\mathrm{C}^*$ Korrekturen ebenfalls vernachlässigt werden.

LSND hat eine vergleichbar dicke Eisenabschirmung zum Target. Strahlkorrelierte intermediäre Neutronen könnten dort direkt die sequentielle zufällige Untergrundrate für die (e^+,n)-Sequenzsuche erhöhen.
Wird diese jedoch entsprechend dem *duty-factor* zu etwa 90 % aus den *beam-off* Daten bestimmt, könnte der Untergrund für die Suche nach der *Appearance* von $\bar{\nu}_\mu \rightarrow \bar{\nu}_e$ (LSND-Oszillation) unterschätzt sein.

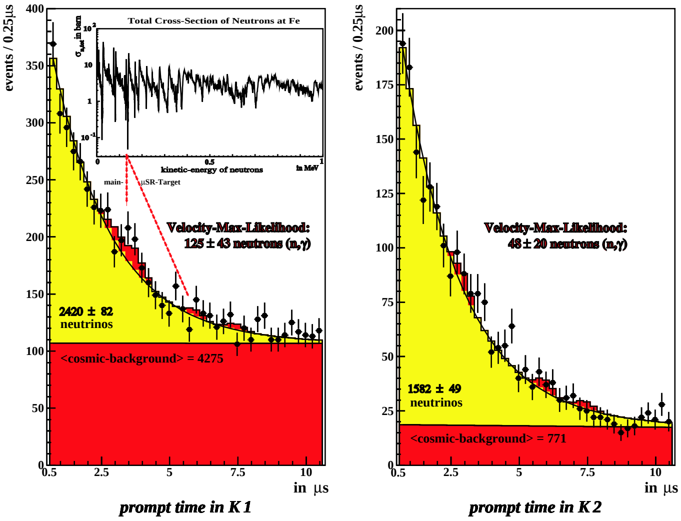

Abbildung 19: Zeitverteilung der *Single-Events* in KARMEN1 (K1) vor und KARMEN2 (K2) nach dem Upgrade. Neben der fast flachen kosmischen Untergrunderwartung aus dem pre-beam sind auch der Anteil miteingezeichnet, der in der Geschwindigkeitsanalyse bestimmten neutroneninduzierten strahlkorrelierten (n,γ)-Ereignisse. In K1 ist exemplarisch die Verknüpfung eines Minimums im Neutronenwirkungsquerschnitt mit dieser Zeitverteilung dargestellt (für Haupt- und μSR-Vortarget).

Im Rahmen dieser Arbeit konnten mit dem KARMEN2-Experiment nach dem Upgrade weite Teile des Evidenzbereiches der LSND-Oszillation ($\bar{\nu}_\mu \rightarrow \bar{\nu}_e$) mit $90\% CL$ ausgeschlossen werden. Dies gilt insbesondere für Massenquadratsdifferenzen Δm^2 oberhalb von $1\,eV^2$. Sowohl die detailliert vorgestellte Suche nach $\bar{\nu}_e$-Sequenzen mit einer Fenstermethode, als auch die ausführliche Analyse der *Single-Events*, bestätigten das KARMEN2 Endresultat für die $\bar{\nu}_\mu \rightarrow \bar{\nu}_e$ Oszillationssuche und lieferten keinen Hinweis auf ein zusätzliches steriles schwereres Neutrino (LSND-Szenario).
Die Suche mit den KARMEN-Gesamtdaten (K1+K2) nach der *Appearance* von $\nu_\mu \rightarrow \nu_e$ lieferte im LSND-Bereich von Massenquadratsdifferenzen keinen Hinweis auf ν-Oszillation (und CP-Verletzung) sowie damit verbundene zusätzliche sterile schwerere Neutrinos. Bestehende Ausschlußgrenzen konnten für den $\nu_\mu \rightarrow \nu_e$ Oszillationskanal im Bereich $0.1\,eV^2 < \Delta m^2 < 10\,eV^2$ verbessert werden.
Desweiteren konnte die Suche mit den KARMEN-Gesamtdaten (K1+K2) nach der *Disappearance* von $\nu_e \rightarrow \nu_{sterile}$ im LSND-Bereich von Massenquadratsdifferenzen zeigen, daß die NuTeV-Anomalie im Weinbergwinkel nicht mit sterilen Neutrinos erklärbar ist.

Neutrinoinduzierte neutrale und geladene Stromreaktionen an ^{12}C, ^{13}C und ^{56}Fe konnten erstmals durch eine kombinierte Analyse aller mit KARMEN beobachtbaren Neutrinokernreaktionen modellunabhängig und konsistent im Energiebereich von Supernovae vermessen werden. Hierzu wurden erstmals die gesamten K2-Daten (mit einer stark unterdrückten kosmischen Untergrundrate durch den Upgrade), sowie die globalen KARMEN-Daten (K1+K2), detailliert analysiert.
Dabei wurde insbesondere für das Verhältnis ($R = \frac{\langle \sigma^{NC} \rangle}{\langle \sigma^{CC}_{gs} \rangle}$) der ν-Wirkungsquerschnitte von neutraler zu geladener Stromreaktion an ^{12}C eine bislang einzigartige experimentelle Präzision von 5% erreicht. Im Rahmen dieser Genauigkeit wurde die μ-e-Universalität neutraler und geladener schwacher Ströme verifiziert und die Annahme des V-A Standardmodells bestätigt. Trotz guter Ergebnisse der CRPA, welches das meistbenutzte mikroskopische Modell bei Berechnungen zur Neutrino-Nukleosynthese und Supernovaexplosionen ist, bleibt eine Diskrepanz in R.
Desweiteren ist die genaue Kenntnis, der in dieser Arbeit gemessenen ν-Wirkungsquerschnitte an ^{12}C und ^{13}C für zukünftige Supernovaneutrinoexperimente wie KamLAND und Borexino unerläßlich, um zwischen den diskutierten Modellen anhand der beobachteten Raten unterscheiden zu können.
Mit dem gemessenen ν-Wirkungsquerschnitt an ^{56}Fe kann die mittlere freie Weglänge von Neutrinos im Core einer Typ-II-Supernova berechnet werden.

Abschließend konnte im Rahmen dieser Arbeit gezeigt werden, daß neutroneninduzierter strahlkorrelierter Untergrund vom Beschleuniger mit hoher Wahrscheinlichkeit die KARMEN-Zeitanomalie erklären kann.

Contents

1 Introduction 1

2 KARMEN–Experiment 5

2.1 ISIS–Neutrino–Source and KARMEN–Detector 5

2.2 Time Structure of Beam-Periods in the Data Acquisition 11

2.3 Physics with KARMEN and Goals 12

3 Neutrino–Nucleus–Interactions 14

3.1 Sequential Detection: Exclusive Charged–Current–Reaction $^{12}\mathrm{C}\,(\,\nu_e\,,\mathrm{e}^-\,)\,^{12}\mathrm{N}_{\mathrm{g.s.}}$ 16

3.1.1 Search for Sequences from $^{12}\mathrm{C}\,(\,\nu_e\,,\mathrm{e}^-\,)\,^{12}\mathrm{N}_{\mathrm{g.s.}}$ 17

3.1.2 Reduction of Stopped Cosmic Muons and Refinement of Energy-Calibration 18

3.1.3 Remaining Cosmic Induced and Random Background 20

3.1.4 Measurement of Cross Section for $^{12}\mathrm{C}\,(\,\nu_e\,,\mathrm{e}^-\,)\,^{12}\mathrm{N}_{\mathrm{g.s.}}$ 20

3.2 Single–Events: Inclusive Charged–Current– and Neutral–Current–Reactions 27

3.2.1 Window–Method for Inclusive CC–Reaction $^{13}\mathrm{C}\,(\,\nu_e\,,\mathrm{e}^-\,)\,^{13}\mathrm{N}$ 28

3.2.2 χ^2–Method for $^{12}\mathrm{C}\,(\,\nu\,,\nu'\,)\,^{12}\mathrm{C}^*$, $^{12}\mathrm{C}\,(\,\nu_e\,,\mathrm{e}^-\,)\,^{12}\mathrm{N}^*$ and $^{56}\mathrm{Fe}\,(\,\nu_e\,,\mathrm{e}^-\,)\,\mathrm{X}$ 33

3.2.2.1 Inclusive NC–Reaction $^{12}\mathrm{C}\,(\,\nu\,,\nu'\,)\,^{12}\mathrm{C}^*$ 44

3.2.2.2 Inclusive CC–Reaction $^{12}\mathrm{C}\,(\,\nu_e\,,\mathrm{e}^-\,)\,^{12}\mathrm{N}^*$ 46

3.2.2.3 Inclusive CC–Reaction $^{56}\mathrm{Fe}\,(\,\nu_e\,,\mathrm{e}^-\,)\,\mathrm{X}$ 47

3.2.2.4 Ratio $R = \langle\sigma^{NC}\rangle/\langle\sigma_{gs}^{CC}\rangle$ 49

4 Neutrino–Oscillations **52**

4.1 Formalism of Neutrino–Oscillations 53

4.1.1 Overview of Experimental Status 57

4.2 Search for $\nu_e \rightarrow \nu_{sterile}$ Disappearance 60

4.2.1 Calculating the Oscillation–Amplitude $\sin^2(2\Theta)$ as Function of Δm^2 60

4.2.2 Exclusion Limit for $\nu_e \rightarrow \nu_{sterile}$ Disappearance 63

4.3 Search for $\nu_\mu \rightarrow \nu_e$ Appearance 65

4.3.1 Background Expectation for $\nu_\mu \rightarrow \nu_e$ Appearance 66

4.3.2 Full $\nu_\mu \rightarrow \nu_e$ Oscillation Expectation and Measurement of ${}^{12}\mathrm{C}\,(\,\nu_e\,,\mathrm{e}^-\,)\,{}^{12}\mathrm{N}_{\mathrm{g.s.}}$ Cross Section at 29.8 MeV . . . 68

4.3.3 Exclusion Limit for $\nu_\mu \rightarrow \nu_e$ Appearance with Bayesian Method . . . 70

4.4 Search for $\bar{\nu}_\mu \rightarrow \bar{\nu}_e$ Appearance (LSND–Oscillation) 73

4.4.1 Method using Sequences for $\bar{\nu}_\mu \rightarrow \bar{\nu}_e$ Appearance Search 73

4.4.1.1 Background for Sequential $\bar{\nu}_\mu \rightarrow \bar{\nu}_e$ Appearance Search . . . 75

4.4.1.2 Exclusion Limit for $\bar{\nu}_\mu \rightarrow \bar{\nu}_e$ Appearance 79

4.4.2 Method using Single–Events for $\bar{\nu}_\mu \rightarrow \bar{\nu}_e$ Appearance Search 83

4.4.2.1 Background in Single–Events for $\bar{\nu}_\mu \rightarrow \bar{\nu}_e$ Appearance Search 83

4.4.2.2 Result from Single–Events for $\bar{\nu}_\mu \rightarrow \bar{\nu}_e$ Appearance Search . 85

5 Time–Anomaly **87**

5.1 Hypothesis of Intermediate–Energy Neutrons Inducing Beam Correlated Background 88

5.2 Velocity Analysis 90

5.2.1 Maximum Likelihood Approach 90

5.2.2 Results of Maximum Likelihood Analyses 92

5.2.3 Interpretation of Results 95

5.2.4 Implications on ν Cross Sections Determined from Single-Events . . 96

5.2.5 Implications on $\bar{\nu}_\mu \rightarrow \bar{\nu}_e$ Appearance and LSND 98

5.3 Exclusion Limit for a Weakly-Interacting 33.9 MeV Massive X-Particle from $\pi^+ \rightarrow \mu^+ + X$ 99

6 Conclusion **102**

A Refinement of Energy–Calibration **106**

B Buzzing–Modules 111

C Rejection of Events in Outer Regions of Defective Modules (X-Cut) 115

D Efficiencies 118

E Single–Events Excluding Sequences from CC–Reaction $^{12}\mathrm{C}\,(\,\nu_e\,,\mathrm{e}^-\,)\,^{12}\mathrm{N}_{\mathrm{g.s.}}$ 125

References 133

Chapter 1

Introduction

Neutrinos play a major part in the understanding of particle physics, due to the fact that they are, after the photons, the second most common elementary particles in the universe. The neutrino particle was postulated in 1930 by Pauli, as a massless and neutral spin-1/2-particle, in order to maintain the energy- and momentum-conservation for the β-decay. However, the first experimental detection of neutrinos occurred not until 1953, when Reines and Cowan performed an experiment close to a nuclear reactor [Rei53]. The extremely small values of the corresponding cross sections from $10^{-44} - 10^{-38}\, cm^2$ make our whole planet almost transparent for such neutrinos with energies in the few MeV-range. It would take roughly one light-year of matter in order to shield them entirely. Reines and Cowan were awarded for their experiment with the Nobel prize in 1995.

The field of neutrino astrophysics originated from the first solar neutrino experiment, which was set up in the late sixties: With a huge tank, protected underground from cosmic rays, Davis managed to trace neutrinos from the sun by utilizing a sophisticated radiochemical method. The solar neutrino rate, which has been measured from then on by this experiment, as well as the rate found later by all different types of detectors, always came out as roughly half of the theoretical expected rate and therefore constituted the so-called solar neutrino problem. In the following fast Čerenkov- and scintillation detectors were additionally capable to determine the energy and the direction of the incident solar neutrinos. Such types of detectors have given proof that the measured neutrinos are really coming from the sun. During the explosion of supernova 1987A, the Kamiokande-experiment, under the leadership of Koshiba, managed for the first time to detect neutrinos from another astronomical source than the sun. In 2002, Davis and Koshiba were awarded the Nobel prize in physics for the detection of solar and supernova neutrinos, respectively.

In 1998 the successor experiment SuperKamiokande showed conclusively that neutrinos must possess a nonzero rest mass, due to the observed zenith angle dependent disappearance of muon-neutrinos, which are produced uniformly in the atmosphere of the earth [Fuk98]. The *ad hoc* assumption within the standard model of electroweak interaction, that neutrinos are massless and maximal parity violating, had to be revised since then. Now, it is accepted that neutrino-oscillations $\nu_\mu \rightarrow \nu_\tau$ are the most likely explanation of the observed disappearance of atmospheric muon-neutrinos. In analogy to the quark sector, the neutrino-flavors are constituted of a mixture of the different neutrino-mass eigenstates and hence can oscillate into each other. $\nu_e \rightarrow \nu_{\mu,\tau}$ oscillations of the solar neutrinos give as well a conclusive solution to the solar neutrino deficit, which has been discussed for almost three decades. The SNO-experiment, which was designed to measure also the flavor independent rate of solar neutrinos, observed on the one hand the well-known deficit of electron-neutrinos from the sun, but confirmed on the other hand the theoretical predicted solar neutrino rate by looking at the flavor independent neutral current reaction channel [Ahm02a]. Thus, the standard solar model, which describes the fusion reactions being responsible for the electron-neutrino production in the core of the sun, is well understood in the framework of neutrino oscillations.

Apart from the known three active neutrino-flavors ($\nu_e,\ \nu_\mu,\ \nu_\tau$), it is still unresolved whether additional sterile neutrinos are existing or not. Are neutrinos and anti-neutrinos distinguishable (Dirac particles like quarks) or are they identical (Majorana particles)? It is still only possible to derive upper limits on the absolute neutrino masses, because neutrino oscillations are just driven by the squared-mass differences. However, the precise study of the kinematics of the tritium β-decay delivers the most stringent limit on any of the neutrino masses so far:

$$m_{\nu_e} < 2.2\,\mathrm{eV} \quad \text{[Wei03]}$$

The oscillations of atmospheric and solar neutrinos define already two independent Δm^2 scales ($\Delta m^2_{atm} \approx 3 \cdot 10^{-3}\,eV^2$ and $\Delta m^2_{sol} \approx 7 \cdot 10^{-5}\,eV^2$). The third scale is fixed by the other two and is close to the larger one. Hence, in the framework of neutrino-oscillations, the upper boundary on the electron-neutrino mass represents an upper limit for all of the three active neutrino-flavors. Both hierarchical and quasi-degenerated mass scale models are still possible. The future experiment KATRIN[1] will be capable to improve the upper boundary on the electron-neutrino mass down to a value of $m_{\nu_e} < 0.2\,\mathrm{eV}$ [Wei03]. Cosmological observations of the structured clustering of galaxies and the anisotropy of the cosmic 2.7 K background radiation from Big Bang indicate that $\sum m_{\nu,\,active} < 1 - 2\,\mathrm{eV}$ [Han03].

Already 1995, the LSND-experiment published in the *New York Times* evidence for neutrino-oscillations ($\bar{\nu}_\mu \rightarrow \bar{\nu}_e$) [Ath95]. Since then, it has been discussed very controversially [Hil95]. The evidence of the accelerator-based LSND-experiment for $\bar{\nu}_\mu \rightarrow \bar{\nu}_e$ oscillations does not fit in the framework assuming three massive neutrino states. Atmospheric and solar neutrino experiments define already two independent squared-mass differences, which were consistently reproduced by various experiments. Therefore, at least one other heavier neutrino state needs to be introduced in order to present a coherent picture of neutrino-oscillations including LSND, which is sensitive in the eV^2-range of squared-mass differences. Those extra neutrino states would have to be sterile, i.e. they are not taking part in weak interactions because of their "wrong" handedness (e.g. right-handed neutrinos). This is due to the fact that the invisible decay-width of the Z^0-boson, measured precisely with the LEPII collider experiment at CERN[2], shows that there are exactly three active neutrino states [PDG02].

If neutrinos are Dirac particles like quarks, i.e. particle and anti-particle are distinguishable, then the corresponding sterile neutrino partners with the opposite handedness must exist as well (Dirac mass-term $\neq 0$). Neutrinos are only weakly-interacting in contrast

---

[1] KArlsruhe-TRItium-Neutrino-experiment

[2] European Organization for Nuclear Research (Centre Européen de Recherches Nucléaires)

to the quarks, which possess electric and color charge. The mixing between quarks is minimal, whereas the mixing of e.g. ν_μ with ν_τ seems to be almost maximal. The future study of CP-violation with neutrino-oscillations could provide a key in the understanding of the matter-antimatter-asymmetry in the universe. The described differences from the quark sector trigger further investigations of neutrinos, in order to see if they are not Dirac but Majorana particles instead, and thus being indistinguishable from their own anti-particles. Via the so-called seesaw mechanism it would then be understandable why neutrinos have such a tiny rest mass: On the one hand the mass of a left-handed neutrino would be proportional to its corresponding charged fermion, but on the other hand it would be even lighter the heavier an associated right-handed neutrino is. The mass of this new superheavy right-handed neutrino would be just below the GUT[3]-scale. Such energies exceed by far the highest measured energies from cosmic rays. Thus, a possible direct detection of such a superheavy neutrino is unrealistic. Showing that neutrinos are Majorana particles would only be feasible by the observation of the neutrinoless double β-decay: If the neutrino is identical to its anti-particle, the neutrino, being emitted in the first β-decay, could be immediately absorbed again from the same nucleus in a second, synchronous β-decay [Kla02].

The LSND-oscillation ($\bar{\nu}_\mu \rightarrow \bar{\nu}_e$) scenario would be concatenated with fundamental new properties of neutrinos, as already discussed. The experiment of the British-German collaboration KARMEN[4] has been principally sensitive to neutrino-oscillations in an assimilable region of squared-mass differences as LSND. In order to meet the necessary background reduction, an extensive upgrade of the KARMEN-detector-system was under commission during the period of 1995-1997. The final KARMEN2 result for the $\bar{\nu}_\mu \rightarrow \bar{\nu}_e$ oscillation search has been gained by analysis of substantial parts of the data, that has been taken within the framework of this thesis. It excludes major parts of the LSND evidence region [Arm02]. In this thesis two other complementary methods for the $\bar{\nu}_\mu \rightarrow \bar{\nu}_e$ oscillation search will be introduced in detail, as well as the oscillation searches $\nu_\mu \rightarrow \nu_e$ and $\nu_e \rightarrow \nu_{sterile}$.

Due to the very good energy and time resolution of the KARMEN-detector, it was possible for the first time to measure precisely charged- and neutral-current-reactions of neutrinos on nuclei with spectroscopic quality in the energy regime of supernovae. The mechanisms, which cause a supernova explosion, are not fully understood, yet. About 99 % of the energy, which is set free during a supernova of type II, is transferred to neutrinos. The exact knowledge of the cross sections for the corresponding detection reactions is essential for future supernova-neutrino-experiments like KamLAND or Borexino: The observed rates for each neutrino-flavor will enable a discrimination between different supernova-models. Moreover, the time distribution and the energy spectra ($\cong$ temperature) of neutrinos give testimony to the hidden processes deep inside the core of a supernova, just before and during the explosion. The core of a supernova predecessor star predominantly consists of iron, the final product of the last nuclear burning cycle of very massive stars. Hence, the

---

[3] Grand-Unified-Theory

[4] KArlsruhe-Rutherford-interMediateEnergy-Neutrinoexperiment

mean free path-length of neutrinos, produced during the collapse and the explosion of a supernova, is governed by their cross section on iron nuclei. The KARMEN-experiment can investigate this cross section with assimilable energetic neutrinos, which interact with iron nuclei of the steel-shielding, that closely surrounds the detector.
Via the measurement of all neutrino-nucleus-reactions accessible to KARMEN, especially the neutral- and charged-current-reactions on $^{12}\mathrm{C}$, it is feasible to perform fundamental tests of the electroweak interaction, like e.g. the μ-e-universality of weak interactions. Moreover, theoretical nuclear models can be checked very precisely. These can be grouped into the elementary particle treatment (EPT) and microscopic models, which account more for the structure of nuclei. EPT-models require form-factors instead, which are empirically derived from β-decays and μ-capture reactions. There are two approaches for microscopic models: Shell-Models (SM), giving especially a good description of the ground states of nuclei and random phase approximations (RPA), which are more suitable for excited states of even-numbered nuclei. RPA-models utilize, apart from the Fermi distribution for uncorrelated particles in the mean potential of ground state, 1particle-1hole-excitations above the Fermi-edge.
Recently, it was suggested that neutrino-nucleus-reactions are contributing to the synthesis of elements in stars [Heg03]. This neutrino-nucleus-synthesis is especially promising in the range of light nuclei (number of nucleons ≈ 12). Hence, the measured cross sections with KARMEN serve as a figure of merit, in order to judge the theoretical predictions.

The first combined analysis of all neutrino-nucleus-interactions, which can be studied with KARMEN, represents another major goal of this thesis. For this, the entire KARMEN data, which was acquired from 1990-2001 and corresponds to 18547 C of accumulated proton-on-target charge, has been evaluated globally for the first time. Additionally, this thesis is the first investigation of neutrino-nucleus-reactions using the entire KARMEN2 data (with a strongly suppressed cosmic background rate due to the upgrade).

KARMEN is sensitive to exotic pion-decays like no other experiment, due to the excellent time resolution. For decays beyond the standard model, which produce weakly-interacting massive particles (WIMPs and neutralinos, respectively), tiny branching ratios down to 10^{-17} can be investigated. The corresponding time distributions of neutrinos measured with KARMEN, showed indeed an anomaly [Zei95], [Arm95]. Beside of the search for neutrino-oscillations and the measurement of neutrino-nucleus-reactions in the energy regime of supernovae, the solution to this KARMEN-Time-Anomaly represents the third major goal of this thesis.

Chapter 2

KARMEN–Experiment

2.1 ISIS–Neutrino–Source and KARMEN–Detector

ISIS-Neutrino-Source

The KARMEN-experiment was measuring neutrinos over the period of time from 1990-2001 at the pulsed neutron-spallation-source ISIS of the Rutherford-Appleton-Laboratory near Oxford (England). ISIS is a rapid-cycling synchrotron, which accelerates protons to a kinetic energy of 800 MeV with a design beam current of 200 μA (*see Fig.* 2.1). The

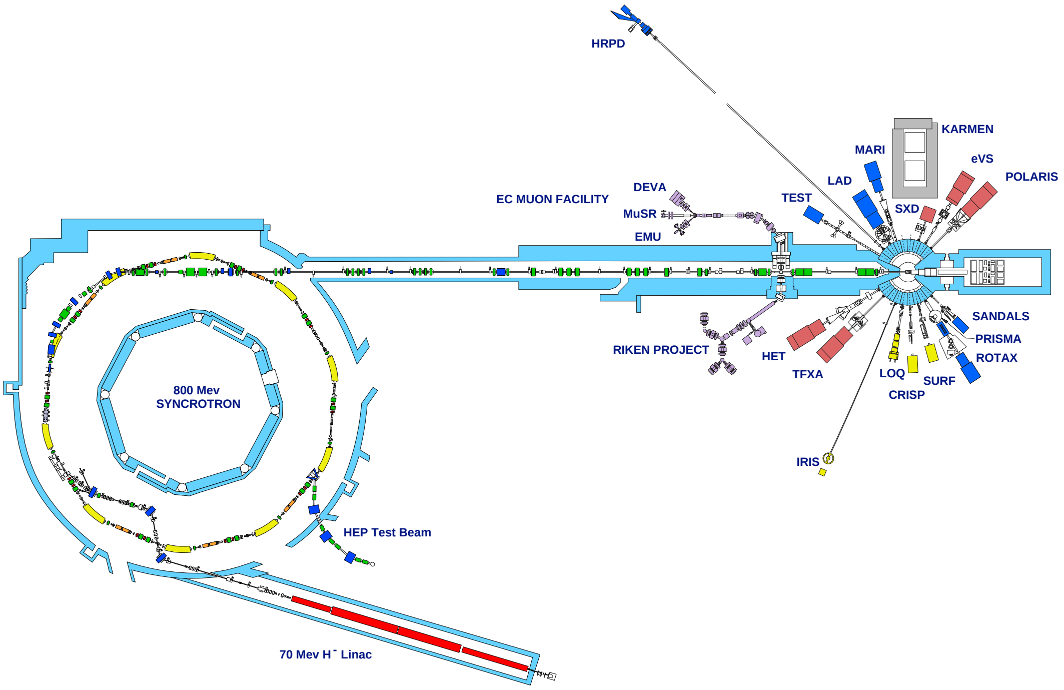

Figure 2.1: Layout of ISIS and KARMEN.

protons are extracted from the synchrotron with a repetition frequency of 50 Hz as a double pulse, consisting of two in time parabolic pulses, with a width of 100 ns and being separated by 325 ns (*see Fig.* 2.2b). In the beam-line these protons are guided through a thin pre-target up to a massive water cooled main-target (the beam-stop), which consists of uranium- and tantalum-D_2O, respectively. Thereby, mainly neutrons are produced but also pions of all three states of charge (e.g. 0.0448 ± 0.0030 π^+ per incident proton). The π^0 decay very rapidly into two γ-rays ($\tau_{\pi^0} = 8.4 \cdot 10^{-17}$ s), whereas the charged pions are stopped entirely inside the main-target. After this, the π^- undergo nuclear capture in the surrounding nuclei. Therefore, only the π^+-decay-chain is relevant for the production of neutrinos:

$$\begin{array}{llcl} \pi^+ \longrightarrow & \mu^+ + \textcircled{ν_μ} & \qquad & \tau = 2.6 \cdot 10^{-8} s \\ & \downarrow & & \\ & e^+ + \textcircled{ν_e} + \textcircled{$\bar{\nu}_\mu$} & & \tau = 2.2 \cdot 10^{-6} s \end{array}$$

Mono-energetic ν_μ with an energy of 29.8 MeV are resulting from the 2-body-decay of π^+ at rest. These ν_μ follow closely the proton pulses, due to the short π^+-lifetime of 26 ns (*see Fig.* 2.2a+b). Moreover, ν_e and $\overline{\nu_\mu}$ are produced with continuous energies up to 52.83 MeV from the subsequent 3-body-decay of μ^+ at rest (*see Fig.* 2.2a). The time distribution of these subsequent neutrinos reflects the μ^+-lifetime of 2.2 μs (*see Fig.* 2.2c).

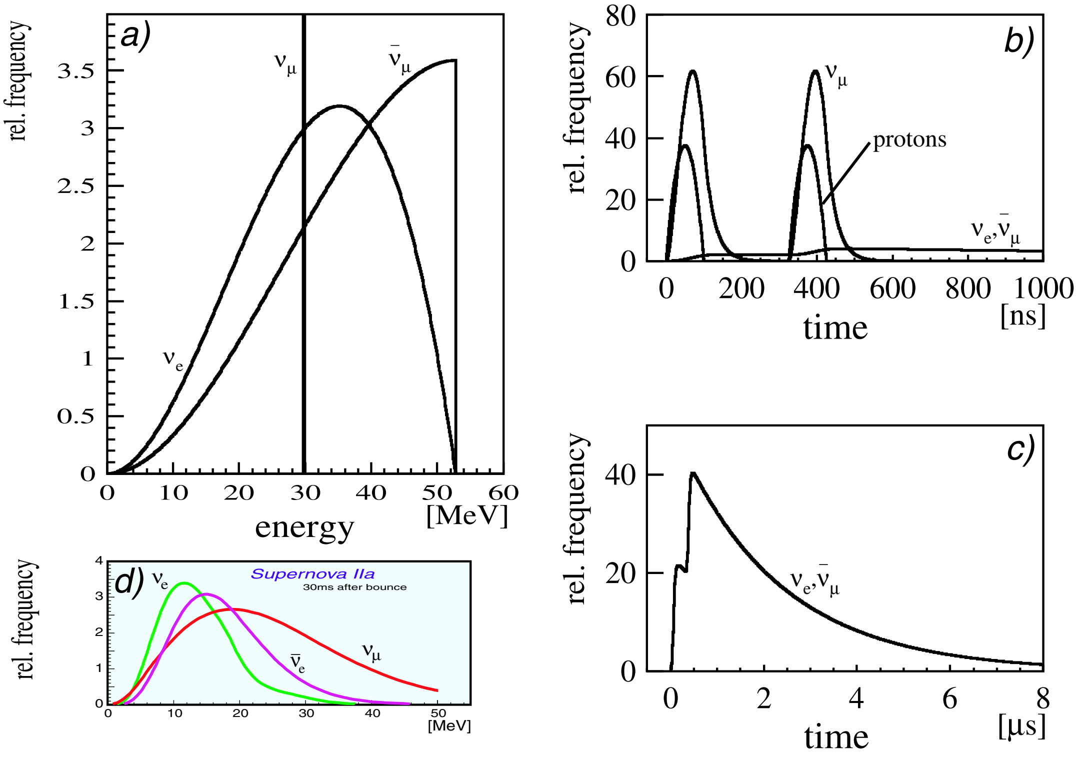

Figure 2.2: a) Energy- and b)+c) time distributions of the neutrinos produced inside the target of ISIS. d) For comparison: The energy distributions of neutrinos from an exemplary supernova type IIa.

Due to the unique time structure of ISIS and the different lifetimes of muon and pion, it is feasible to investigate almost exclusively ν_μ in two early time windows (corresponding to the proton double pulses). It is furthermore possible to scrutinize almost exclusively ν_e and $\overline{\nu_\mu}$ in a late time window on a μs-scale. The entire duration of a beam-period, until the next proton double pulse arises, amounts to 20 ms and can be utilized for measuring very precisely the cosmic background (duty-factor up to $\approx 10^{-5}$). At a proton beam current of $200\,\mu$A, ISIS produces isotropically $5.6 \cdot 10^{13}\,s^{-1}$ neutrinos per flavor. Over the entire measuring period from 1990-2001 a total beam charge of 18547 C was accumulated with KARMEN. This corresponds to an entire neutrino production of $5.2 \cdot 10^{21}$ per flavor. The energies of neutrinos, being produced at ISIS, can be calculated analytically from the kinematics of 2-body- and 3-body-decay at rest (simple V-A structure of μ^+-decay[1]) and match with the energy regime of neutrinos from supernovae of type II (*compare Fig.* 2.2a+d). Thus, the investigations of the properties of neutrinos from ISIS are of special interest for astrophysics.

KARMEN-Detector

The KARMEN-detector [Dre90] was a segmented high resolution liquid scintillation calorimeter, located at a mean distance of 17.7 m from the ISIS main-target and positioned at an angle of 100 degrees relative to the proton beam-line (*see Fig.* 2.1). The $65\,m^3$ of liquid scintillator covered 0.5% of the entire solid angle and were furthermore enclosed by a multilayer active veto-system and a 7000 t steel shielding (*see Fig.* 2.3).

The iron blockhouse, which was 10 m in height and built out of steel slabs in a modular way, shielded drastically both the cosmic ray and beam correlated neutrons from the ISIS target. Between the ISIS main-target and the liquid scintillator there were in total 7 m of iron. This shielding corresponded to more than 30 attenuation-lengths for neutrons with kinetic energies above 10 MeV. Towards the sides the iron wall amounted to roughly 2 m, whereas on the roof it came out at 3 m. Thus, the flux of cosmic muons was reduced to a third.

The 56 t of liquid scintillator consisted of a mixture of paraffin oil (75 vol%), pseudocumene (25 vol%) and 2 g/l of the scintillating additive 1-phenyl-3-mesityl-2-pyrazoline (PMP). The hydrocarbon acted as active target for neutrino-nucleus-reactions (^{12}C , ^{13}C , ^{1}H).

The volume of the liquid scintillator was optically separated into independent modules by an optical segmentation of double-lucite-sheets (*see Fig.* 2.4). A small airgap between the double-lucite-sheets of the segmentation caused optical total-reflection and thus a very efficient transport of scintillation light to the ends of the modules, where the scintillation light was read-out by a pair of (3" VALVO XP 3462) photomultiplier tubes (PMT). Furthermore, gadolinium-coated paper had been put between the acrylic walls for an efficient detection of thermal neutrons and to prevent scintillation light from coupling into neighboring modules.

The segmentation consisted of 608 modules in total, which were placed inside a rectangular tank with the dimensions of 3.53 m × 3.20 m × 5.96 m in length, width and height (*see again Fig.* 2.4). The central detector consisted of the inner 512 modules (each with

---

[1] Energy distribution: $N(\epsilon)d\epsilon = 4\epsilon^2[3(1-\epsilon) + \frac{2}{3}\rho(4\epsilon-3)]d\epsilon$ with $\epsilon = \frac{E_\nu}{E_{max}}$; $E_{max} = 52.83\,\text{MeV}$ and the Michel-parameter $\rho = 0$ for ν_e , $\rho = 0.75$ for $\bar{\nu}_\mu$

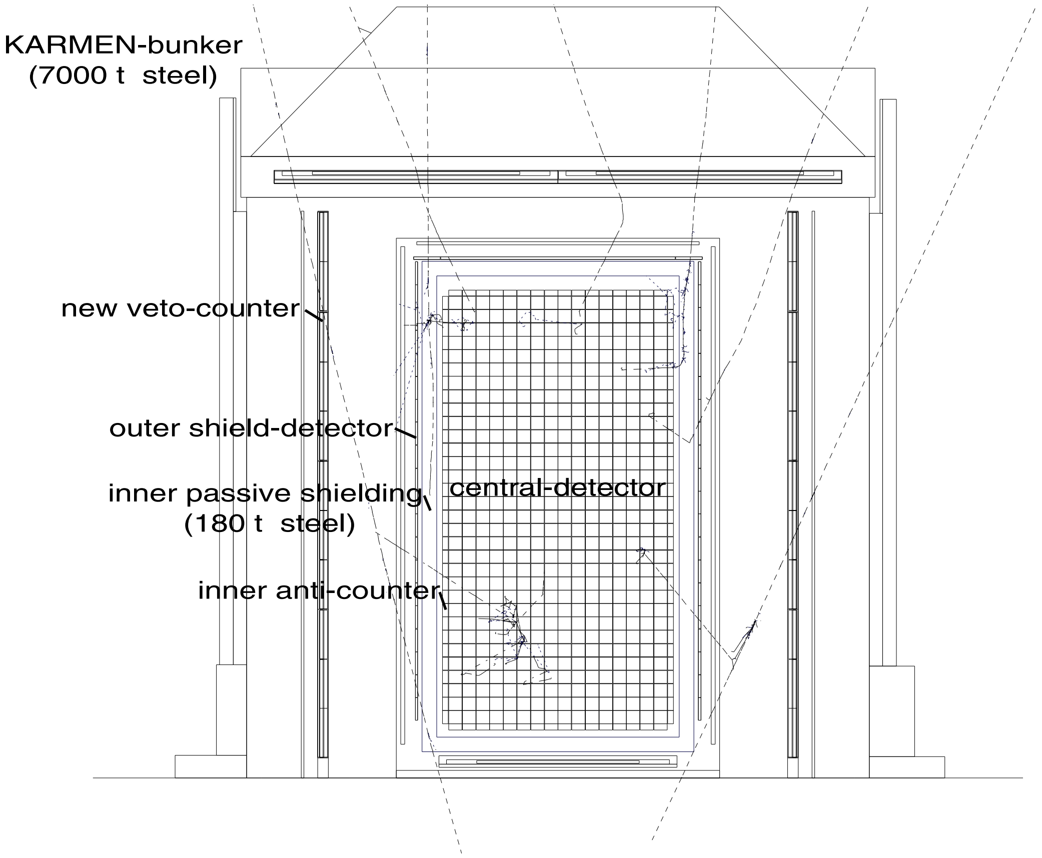

Figure 2.3: Schematic view of the KARMEN-detector inside the steel shielding.

the dimensions of 353 cm × 17.7 cm × 18.1 cm in length, width and height), arranged in 32 rows and 16 columns. A surrounding layer of modules with half the cross section of a central detector module defined the inner anti-counter. An inner passive shielding of 18 cm thick steel slabs surrounded the scintillator tank, providing passive shielding and mechanical stability. The second layer of active shielding (outer shield-detector) consisted of 136 plastic scintillator bars (NE-110) with thickness of 3 cm and lengths ranging from 2.4 m to 3.1 m, which were mounted onto the passive shielding on all sides but the bottom side.

As already mentioned, the surrounding steel shielding was built in a modular way out of layers of steel slabs. This structure of layers allowed the later integration of an outer veto-system inside the steel shielding (*see Fig.* 2.5 *and* 2.3). In total, 136 bars of 5 cm thick and up to 4 m long plastic scintillator (BICRON BC-412) had been used for the outer veto system, which provided also active shielding under the detector [Rei98]. This additional outer veto system was under commission during the period of 1995-1997, marking the beginning of the KARMEN2-experiment. The extensive upgrade of the experimental configuration was performed in order to meet the necessary cosmic background reduction for the sequential $\bar{\nu}_\mu \rightarrow \bar{\nu}_e$ appearance search (LSND-oscillation), as will be outlined in *Chapter* 4.4.1. This new veto system tagged grazing cosmic muons, which did not hit the central detector but who could produce high-energy neutrons (inside the iron shielding), which penetrated the central detector, unrecognized by the old shield- and anti-counter system (*see Fig.* 2.3). Such neutrons (with kinetic energies above 10 MeV) from muon capture reactions and deep inelastic scattering on iron nuclei of the blockhouse were limiting the sensitivity for the $\bar{\nu}_\mu \rightarrow \bar{\nu}_e$ oscillation search [Arm98].

The KARMEN-detector was a calorimeter, consisting of liquid organic scintillator, which was optimized for a high energy resolution of $\sigma(E)/E = 11.5\%/\sqrt{E(MeV)}$ [Dod93]. An event information comprised the energy-, time- and position information, as well as the number of addressed modules and their relative time differences. A scintillator module hit was accepted if there was a coincidence of signals of the photomultipliers at both ends

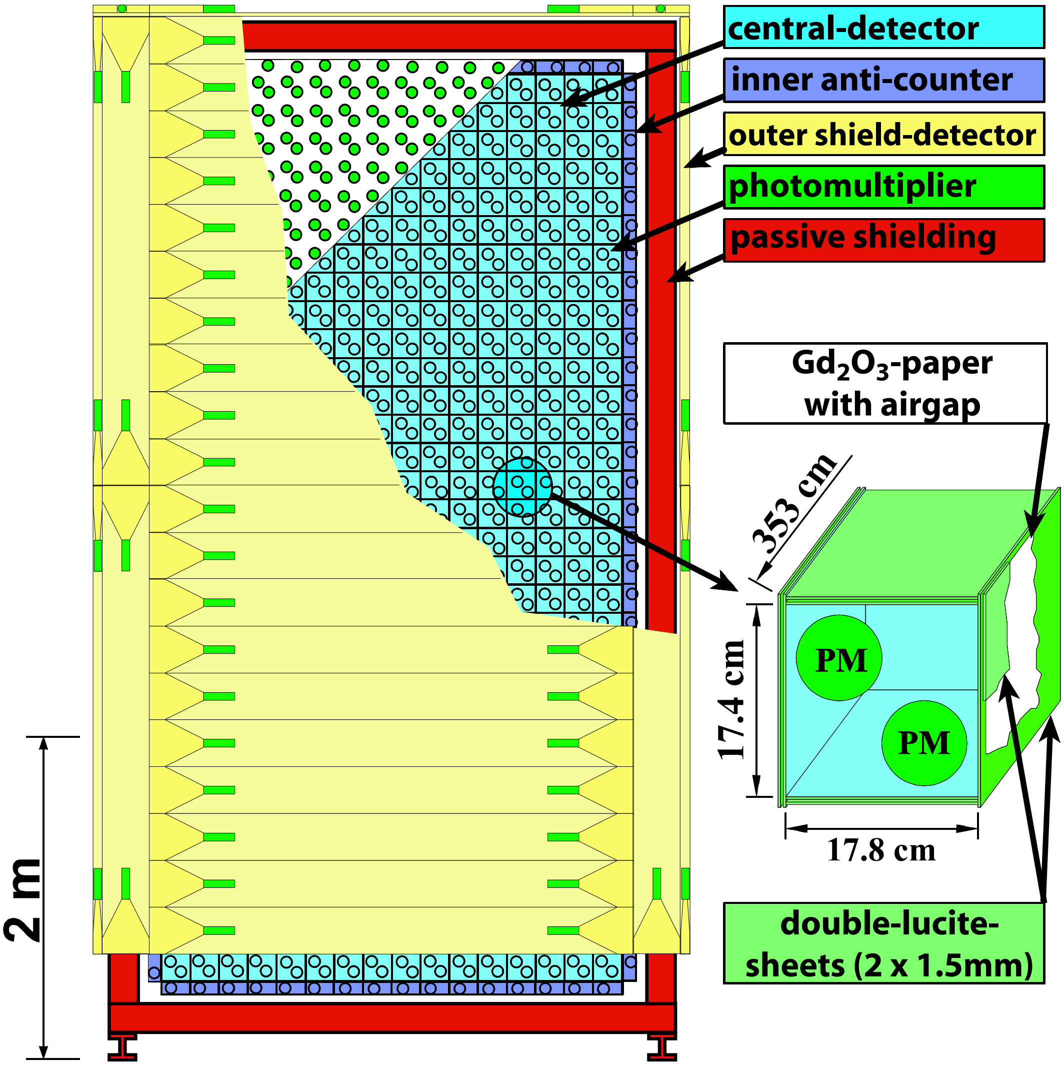

Figure 2.4: The KARMEN-detector

within a coincidence time of $\Delta T_{C1} = 190\,\mathrm{ns}$ (first level trigger). The position of the event along the module-axis (x-direction) is obtained by the time difference between the signals, whereas the energy information is derived from the integrated PMT pulses. The absolute energy-calibration of the detector is fixed by the analysis of the Michel energy spectrum of electrons from the decay of stopped cosmic ray muons. The energy-calibration is performed for each single module and takes into account the individual light-output curves of the modules. Module hits within a coincidence time of $\Delta T_C < 90\,\mathrm{ns}$ are combined to one event. The analysis of through-going muons makes it feasible to calibrate the relative times of module hits T_{REL} with an accuracy of $\delta T_{REL} = 0.8\,\mathrm{ns}$ (FWHM) [Wol95]. In case of events with more than one module hit, the 3-dimensional position information (x,y,z) corresponding to module-axis, row and column is constructed by the energy-weighted average of the single module information. Finally, the event time T relative to the ISIS proton beam is recorded. Individual KARMEN modules are synchronized to the ISIS beam with an accuracy of $\delta T < 2\,\mathrm{ns}$, allowing to exploit the ISIS time structure in detail. A beam reference time of $T = 0$ is attributed to the time, when the first neutrino enters the KARMEN-detector. A full description of the detector energy- and timing calibration is given in [Wol95].

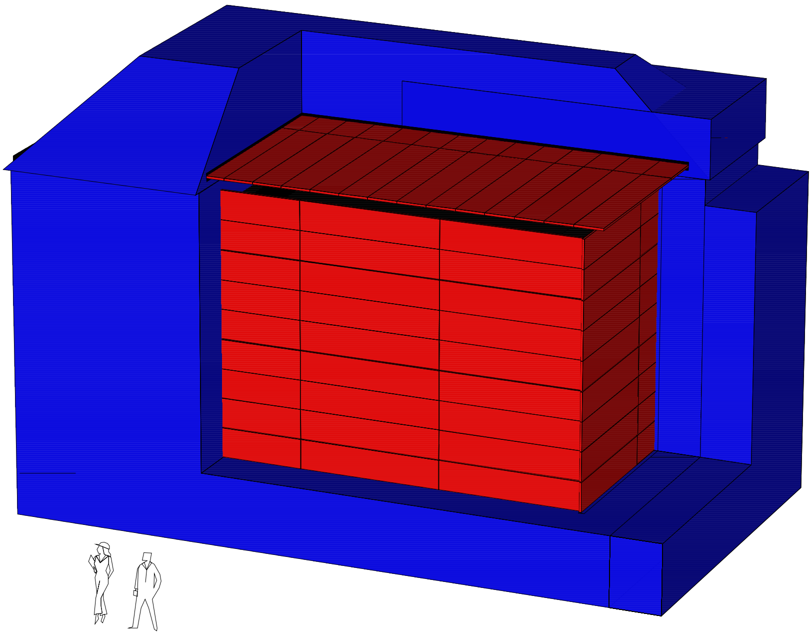

Figure 2.5: The upgrade of the KARMEN-experiment with a new system of veto-counters, being mounted inside the iron blockhouse.

2.2 Time Structure of Beam-Periods in the Data Acquisition

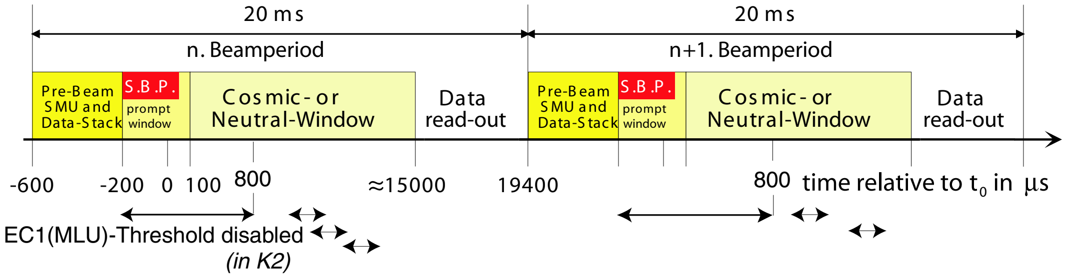

Figure 2.6: Time structure of two contiguous beam-periods in the data acquisition. If an event occurred in the prompt time window between $-200\,\mu$s and $+50\,\mu$s, the following beam-period is recorded as *Second Beam-Period*, i.e. the *Cosmic* calibration mode is not enabled for both the current and the next beam-period, in order to be able to record sequential events from ^{12}C (ν_e ,-e$^-$) ^{12}N$_{\text{g.s.}}$ ($\tau_{N12gs} = 15.9$ ms).

The basis of the time structure of KARMEN-data is the beam-period, i.e. the time between two following ISIS proton double pulses (20 ms, corresponding to a synchrotron extraction rate of 50 Hz). The time $T = 0 - 53ns$ marks the time, when the proton beam hits the ISIS main-target. From $-600\,\mu$s until $-200\,\mu$s (before beam-on-target) only SMU (Stopped cosmic MUons inside the KARMEN-detector) and stack-entries (by the Memory Lookup Unit MLU processed events) are recorded for the recognition of background. Then the *Hardware Prompt Time Window* for *Neutral* events starts at $T = -200\,\mu$s and lasts until $+100\,\mu$s after beam-on-target. If a *Neutral* event occurred in the *Software Prompt Time Window* between $-200\,\mu$s and $+50\,\mu$s, the following beam-period is recorded as *Second Beam-Period*, i.e. the *Cosmic* calibration mode is not enabled for both the current and the next beam-period, in order to be able to record sequential events from ^{12}C (ν_e , e$^-$) ^{12}N$_{\text{g.s.}}$ ($\tau_{N12gs} = 15.9$ ms). If no *Neutral* event occurred in the entire *Hardware Prompt Time Window*, the matrix of the TRIP (TRIgger Processor) is switched to the *Calibration Cosmic Matrix* for the remaining beam-period. Through-going horizontal and vertical cosmic muons can be utilized for the later calibration of the detector-modules (energy, relative time and x-position). After approximately 15 ms the data acquisition is stopped[2]. The acquired data of the CAMAC-units is read-out by two ACCs (Auxiliary Crate Controllers), then gets analyzed by the software-trigger and is finally transferred to the LSI 11/73 computer, where it is stored on tape or harddisk. The average amount of data per day is of the order of 1GByte.

In KARMEN2 the threshold of the MLU (EC1) is disabled from $-200\,\mu$s until $+800\,\mu$s after beam-on-target, in order to increase the neutron detection efficiency for the sequential $\bar{\nu}_\mu \rightarrow \bar{\nu}_e$ appearance search (*see Chapter* 4.4.1). In order to be able to determine precisely

---

[2] Maximal time was reduced in later RUNs with lower thresholds, which caused that the maximal recordable number of 16 events per beam-period was reached too quickly.

the overall neutron detection efficiency from decays of stopped cosmic ray muons (SMUs), the EC1-threshold is variably switched off for 600 μs whenever an event above this MLU-threshold occurred in the following cosmic- or neutral-window of the beam-period.

2.3 Physics with KARMEN and Goals

The unique time structure of the ISIS-neutrino-source and the well-defined energy distributions of the three produced neutrino flavors combined with the excellent time- and energy resolution of the KARMEN-calorimeter allow for investigation of a variety of interesting topics in nuclear-, particle and astrophysics:

- *Neutrino-Nucleus-Interactions:* Neutrino-induced neutral- and charged-current-reactions on ^{12}C, ^{13}C and ^{56}Fe nuclei can be measured for the first time by utilizing neutrinos from μ^+-decays at rest in the energy regime of supernovae. The unique signature of the ν_e-induced exclusive CC-reaction $^{12}\mathrm{C}\,(\,\nu_e\,,\mathrm{e}^-\,)\,^{12}\mathrm{N}_{\mathrm{g.s.}}$ makes a sequential detection feasible, which is almost free of background. Thus, from the exact shape of the unfolded energy spectrum of the ν_e, it is feasible to derive implications on the Lorentz structure of the weak interaction via the Michel-shape-parameter ω_L [Arm98b]. Furthermore, the flux-independent ratio $R = \langle\sigma^{NC}\rangle/\langle\sigma^{CC}_{gs}\rangle$ of the measured ν cross sections for the neutral-current- and the exclusive charged-current reaction on ^{12}C allows for more fundamental tests of the electroweak interaction, like e.g. the μ-e-universality of weak interaction.
  The value of the cross section for the weak neutral-current-reaction $^{12}\mathrm{C}\,(\,\nu_\mu\,,\nu_\mu{}'\,)\,^{12}\mathrm{C}^*$ $(\,1^+\,,1\,;15.11\ \mathrm{MeV}\,)$ measured by KARMEN, utilizing mono-energetic ν_μ from π^+-decays at rest ($\langle\sigma\rangle^{K1} = (3.2 \pm 0.5(stat.) \pm 0.4(syst.)) \cdot 10^{-42} cm^2$ [Arm98c]), is in good agreement with the standard model. The isovector-axialvector coupling constant of weak hadronic current deduced from this experiment is $|\beta| = 1.11 \pm 0.13$.

- Decay- and capture reactions on ^{12}C and ^{13}C of cosmic muons, which are stopping inside the detector, can be studied precisely [Jan95].

- *Neutrino-Oscillations:* Most notably it can be searched for neutrino-oscillations $\bar{\nu}_\mu\!\rightarrow\bar{\nu}_e$, $\nu_\mu\!\rightarrow\nu_e$ and $\nu_e\!\rightarrow\nu_{sterile}$. For each oscillation channel an appropriate neutrino nucleus interaction is consulted and investigated with KARMEN. Hereby it is distinguished between the *appearance* of $\bar{\nu}_e$ from $\bar{\nu}_\mu\!\rightarrow\bar{\nu}_e$ oscillations (or ν_e from $\nu_\mu\!\rightarrow\nu_e$) and the *disappearance* of ν_e from $\nu_e\!\rightarrow\nu_{sterile}$ oscillations. It is generally accepted that neutrinos do have a rest mass and that neutrino-oscillations are the most likely explanation of the observed neutrino deficits from atmospheric, solar and very long baseline reactor neutrino experiments [Fuk98], [Ahm02a], [Egu02]. The evidence of the other accelerator based LSND-experiment for $\bar{\nu}_\mu\!\rightarrow\bar{\nu}_e$ oscillations does not fit in the framework assuming three massive neutrino states. Atmospheric and solar neutrino experiments define already two independent squared-mass differences. Therefore, at least one additional heavier neutrino state needs to be introduced in

order to present a coherent picture of neutrino-oscillations including LSND. Thus, it is also crucial, in the more dimensional context of neutrino-oscillations, to check if other neutrino-oscillations occur in the LSND-region of squared-mass differences. Especially since it was proposed to interpret the Weinberg-angle discrepancy, measured by the NuTeV-experiment, as $\nu_e \rightarrow \nu_{sterile}$ oscillations in the LSND-region of squared-mass differences [Giu02]. In addition, the searches for $\nu_e \rightarrow \nu_{sterile}$ disappearance and $\nu_\mu \rightarrow \nu_e$ appearance with KARMEN could give rise to possible CP-violation in the neutrino sector.
Moreover, it has been feasible to derive upper limits on lepton number violating π^+- and μ^+-decays like $\pi^+ \rightarrow \mu^+ + \bar{\nu}_e$, $\pi^+ \rightarrow \mathrm{e}^+ + \bar{\nu}_e$ [Eit95] or $\mu^+ \rightarrow \mathrm{e}^+ + \bar{\nu}_e + \nu_\mu$ [Arm03]. For Majorana-oscillations like e.g. $\nu_e \rightarrow \bar{\nu}_e$ an upper limit has been deduced as well [Ste99].
In principle, KARMEN facilitates a direct measurement of the rest mass of monoenergetic ν_μ from π^+-decays by measuring their time-diletation via a velocity analysis (analogous to *Chapter* 5). But the sensitivity on the rest mass comes out in the few MeV-range and is thus an order of magnitude larger than the existing best upper limit of $m_{\nu_\mu} < 0.19\,\mathrm{MeV}$ [PDG02], being deduced from the kinematic of π^+-decay.

- *Time-Anomaly:* Last but not least, in KARMEN1 an anomaly in the time distribution of single-events was observed between 3μs and 4μs. As possible explanation of this KARMEN-Time-Anomaly the pion-decay beyond standard model ($\pi^+ \rightarrow \mu^+ + X$) into a new weakly-interacting 33.9 MeV massive X-particle was intensely discussed [Zei95], [Oeh99].

Chapter 3

Neutrino–Nucleus–Interactions

Neutrino-induced neutral- and charged-current-reactions on ^{12}C , ^{13}C and ^{56}Fe nuclei will be measured precisely with neutrinos from μ^+-decay at rest in the energy regime of supernovae. The unique signature of the ν_e-induced exclusive CC-reaction $^{12}\mathrm{C}\,(\,\nu_e\,,\mathrm{e}^-\,)\,^{12}\mathrm{N}_{\mathrm{g.s.}}$ makes a sequential detection feasible, which is almost free of background. Therefore, this will be the first neutrino-nucleus-reaction being investigated, in order to test how well the properties of the KARMEN-detector and the ISIS-neutrino-source are understood. Moreover, the measured cross section for $^{12}\mathrm{C}\,(\,\nu_e\,,\mathrm{e}^-\,)\,^{12}\mathrm{N}_{\mathrm{g.s.}}$ will serve as an independent input parameter for the subsequent analysis of the inclusive neutrino-nucleus-reactions. Together with the strongly suppressed cosmic background rate in KARMEN2, it will then be feasible to measure the inclusive neutrino-nucleus-reactions for the first time consistently and model-independently via a combined analysis of the single-events. In order to reduce the degrees of freedom for this combined analysis, the cross section for the inclusive CC-reaction $^{13}\mathrm{C}\,(\,\nu_e\,,\mathrm{e}^-\,)\,^{13}\mathrm{N}$ will be derived from an appropriate window-method in KARMEN2, where this reaction can be studied solely with well-known background.

The best opportunity, for comparing the results with theoretical calculations, will be provided by the flux-independent ratio $R = \langle\sigma^{NC}\rangle/\langle\sigma_{gs}^{CC}\rangle$ of the measured ν cross sections for the neutral-current- and the exclusive charged-current reaction on ^{12}C . Thus, even fundamental tests of the electroweak interaction, like e.g. the μ-e-universality of weak interaction can be performed.
Hence, theoretical nuclear models can be checked very precisely. These models can be grouped into elementary particle treatment (EPT) and microscopic models, which account more for the structure of nuclei. EPT-models require form-factors instead, which are empirically derived from β-decays and μ-capture reactions. There are two approaches for microscopic models: Shell-Models (SM), giving a good description especially of the ground states of nuclei and random phase approximations (RPA), which are more suitable for excited states of even-numbered nuclei. RPA-models utilize, apart from the Fermi distribution for uncorrelated particles in the mean potential of ground state, 1particle-1hole-excitations above the Fermi-edge. Moreover, the continuum-RPA (CRPA) is especially suitable for transitions into states of the continuum, above the threshold for particle emission.

For the calculation of the neutrino cross sections on nuclei, the corresponding semi-leptonic transition matrix element $\mathcal{M}$ is relevant ($|q^2| \ll m_W^2$). In Fermi's current-current-approach it is given by:

$$\mathcal{M} = \frac{G_F}{\sqrt{2}}\, j^l\, J^h \tag{3.1}$$

with G_F the Fermi-coupling-constant (which is additionally multiplied by $\cos\Theta_C$ of the Cabibbo-angle in case of CC-reactions). The leptonic current $j^l = \overline{\psi_\nu}\gamma_\alpha(1-\gamma_5)\psi_\nu$ can be calculated straightforward, whereas for the hadronic weak current J^h the inner structure of the nucleon has to be taken into account by the nuclear models. The charged hadronic current is purely left-handed. It can be split into vector- and axial-vector components ($J^h_{CC} = V - A$), which are usually treated separately for the theoretical investigation of semi-leptonic weak processes. The neutral hadronic current possesses both left-handed and right-handed components. The admixture of the right-handed components is determined by the Weinberg-angle Θ_W: $J^h_{NC} = (1 - 2\sin^2\Theta_W)V - A$ [Fuk88].

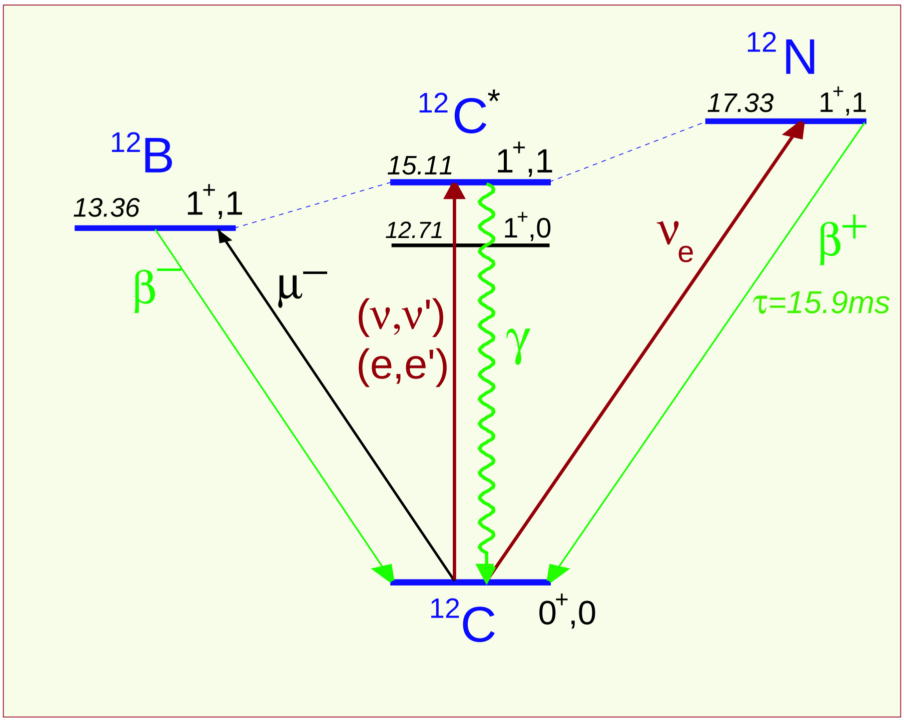

Figure 3.1: The $A = 12$ isospin-triplet

In KARMEN the neutrinos interact predominantly on ^{12}C nuclei of the organic scintillator. The ^{12}C nucleus is part of the $A = 12$ isospin-triplet ^{12}B – ^{12}C* – ^{12}N with $J^\pi T = 1^+1$ (*see Fig.* 3.1). The excitation of the ground state of ^{12}C ($J^\pi T = 0^+0$) into one of the three isospin states ($T = 1, T_z = 0, \pm 1$) does always involve a defined change of the nuclear spin J and the isospin T. Therefore, the ^{12}C nucleus acts as spin-isospin-filter for the investigation of ν-induced nuclear transitions and gives rise to especially the isovector

($\Delta T = 1$) and axialvector ($\Delta J = 1$) components of the weak hadronic current.
The NC-excitation of the ground state of ^{12}C into the 15.11 MeV-level of the ^{12}C$^*(1^+1)$ can be induced by neutrinos of all flavors. This isovector-axialvector excitation can be detected in KARMEN via a prompt single-event, resulting from the γ, which is emitted whilst the transition back into the ground state of the ^{12}C nucleus (*see Section* 3.2.2.1).

The CC-excitation of the ground state of ^{12}C(0^+0) into the ground state of ^{12}N(1^+1) can be solely induced by ν_e (inverse β-decay with $E_{el,max} = E_{\nu_e} - 17.33 MeV$). ν_μ and $\bar{\nu}_\mu$ from π^+- and μ^+-decays at rest, respectively, do not possess the necessary energy ($\geq m_\mu c^2$) for this CC-excitation. The ground state of ^{12}N decays back into the ground state of ^{12}C, according to the lifetime of $\tau = 15.9$ ms for this β^+-decay. Hence, the exclusive CC-reaction $^{12}\mathrm{C}\,(\,\nu_e\,,\mathrm{e}^-\,)\,^{12}\mathrm{N}_{\mathrm{g.s.}}$ can be very clearly detected in KARMEN via the sequence of a prompt e^- followed by a delayed and spatially correlated e^+ (*see Section* 3.1).
By contrast, the inclusive CC-reaction $^{12}\mathrm{C}\,(\,\nu_e\,,\mathrm{e}^-\,)\,^{12}\mathrm{N}^*$ into excited states of ^{12}N produces just a prompt single-event in the detector (*see Section* 3.2.2.2).

Moreover, the inclusive CC-reaction $^{13}\mathrm{C}\,(\,\nu_e\,,\mathrm{e}^-\,)\,^{13}\mathrm{N}$ can also produce prompt single-events in KARMEN, as the organic scintillator contains ^{13}C nuclei to a small fraction, according to the natural abundance of 1.1%. (*see Section* 3.2.1).

With KARMEN it is furthermore feasible to investigate the CC-reaction $^{56}\mathrm{Fe}\,(\,\nu_e\,,\mathrm{e}^-\,)\,\mathrm{X}$ by utilizing neutrinos, which interact with iron nuclei of the steel, that closely surrounds the detector. This is of special interest for astrophysics, as the mean free path-length of neutrinos, being produced with assimilable energies during the collapse and the explosion of a supernova type II, is ruled by their cross section on iron nuclei. The ν_e-induced CC-reaction $^{56}\mathrm{Fe}\,(\,\nu_e\,,\mathrm{e}^-\,)\,\mathrm{X}$ into excited or particle unstable states of ^{56}Co can be detected in KARMEN via an inclusive single-event (*see Section* 3.2.2.3).

3.1 Sequential Detection: Exclusive Charged–Current–Reaction $^{12}\mathrm{C}\,(\,\nu_e\,,\mathrm{e}^-\,)\,^{12}\mathrm{N}_{\mathrm{g.s.}}$

As already pointed out, the unique signature of the ν_e-induced exclusive CC-reaction $^{12}\mathrm{C}\,(\,\nu_e\,,\mathrm{e}^-\,)\,^{12}\mathrm{N}_{\mathrm{g.s.}}$ makes a sequential detection feasible, which is almost free of background:

$$\begin{array}{llll} \nu_e + {}^{12}\mathrm{C} & \longrightarrow {}^{12}\mathrm{N}_{\mathrm{g.s.}} + \textcircled{\mathrm{e}^-} & & -17.33\,\mathrm{MeV} \\ & \quad \llcorner\!\!\longrightarrow {}^{12}\mathrm{C} + \textcircled{\mathrm{e}^+} + \nu_e & & \tau = 15.9\,ms \end{array}$$

In the following, it will be described how the corresponding sequence sample is obtained from the KARMEN data, with a minimal fraction of remaining background. This will lead to a precise test of the understanding of the KARMEN-detector and the ISIS-neutrino-source. Finally, the value of the cross section for the exclusive CC-reaction $^{12}\mathrm{C}\,(\,\nu_e\,,\mathrm{e}^-\,)\,^{12}\mathrm{N}_{\mathrm{g.s.}}$ will be determined and compared with results from theoretical calculations.

3.1.1 Search for Sequences from $^{12}\mathrm{C}\,(\,\nu_e\,,\mathrm{e}^-\,)\,^{12}\mathrm{N}_{\rm g.s.}$

In a dedicated sequence analysis one searches for a prompt e^- followed in time by a spatially correlated e^+ induced by the CC-reaction above. The prompt e^- possesses continuous visible energies up to roughly 36 MeV, due to the Q-value of 17.33 MeV for the inverse β-decay on ^{12}C and the maximum ν-energy of 52.83 MeV from μ^+-decay at rest. Moreover, the lifetime of the muons ($\tau_\mu = 2.2\,\mu$s) determines the exponentially decreasing time distribution of the prompt electrons. A delayed signal can be observed in the vicinity of the prompt e^-, with a time distribution according to the lifetime of $^{12}\mathrm{N}_{\rm g.s.}$ ($\tau = 15.9$ ms). The delayed e^+ from β^+-decays of $^{12}\mathrm{N}_{\rm g.s.}$ possess continuous visible energies up to roughly 17 MeV. The unique signature of the sequential detection of ν_e via $^{12}\mathrm{C}\,(\,\nu_e\,,\mathrm{e}^-\,)\,^{12}\mathrm{N}_{\rm g.s.}$ strongly suppresses background reactions and it is possible to set the lower boundary on the prompt visible e^--energy down to 10 MeV. For the visible sequential e^+-energy a lower boundary of 3.5 MeV is feasible. In order to search for sequences from $^{12}\mathrm{C}\,(\,\nu_e\,,\mathrm{e}^-\,)\,^{12}\mathrm{N}_{\rm g.s.}$ two contiguous 20 ms long beam-periods, corresponding to more than two lifetimes of $^{12}\mathrm{N}_{\rm g.s.}$ ($\tau = 15.9$ ms), can be scrutinized in the KARMEN data. After an event occurred in the software prompt time window ($-200\,\mu\mathrm{s} \leq T_{pr} \leq 50\,\mu$s), the following beam-period is enabled as a second beam-period, which uses only the neutral matrix in the trigger processor (TRIP) and not the one for calibration cosmics (*see Fig.* 2.6 *and* [Wol95]). Thus, two full beam-periods are available for the detection of a sequential e^+ from β^+-decay of $^{12}\mathrm{N}_{\rm g.s.}$.

In order to minimize the cosmic background for prompt and sequential events from $^{12}\mathrm{C}\,(\,\nu_e\,,\mathrm{e}^-\,)\,^{12}\mathrm{N}_{\rm g.s.}$, optimized software dead-times are applied after every stack-entry (and veto-only VO in K2). This stack-reduction minimizes the background from unrecognized muons stopping and decaying ($\overline{\tau} \approx 2.2\,\mu$s) close or inside the central detector and thus mainly producing delayed Michel electrons or positrons with an energy up to $E_{max} = 52.83$ MeV. Although, the efficiency of the anti-counter-system for tagging stopped muons is approximately 99.8%, a background rate for single events remains, which is 10^5 times higher than the neutrino rate. Therefore, after every event, being processed by the MLU (Memory Lookup Unit) and thus obtaining a stack-entry, an optimized software dead-time of the order of 20 μs is applied [Arm98]. On the one hand this reduces drastically the cosmic background rate, but on the other hand the stack-reduction for prompt and sequential events from $^{12}\mathrm{C}\,(\,\nu_e\,,\mathrm{e}^-\,)\,^{12}\mathrm{N}_{\rm g.s.}$ is together causing an efficiency loss of 13% in K1 and 25% in K2, respectively (*see Fig.* D.1 *and Table* 3.2).

In order to search for sequences from $^{12}\mathrm{C}\,(\,\nu_e\,,\mathrm{e}^-\,)\,^{12}\mathrm{N}_{\rm g.s.}$, all following cuts and general event requirements for the prompt and the delayed event, respectively, are applied to the KARMEN data:

$$\begin{array}{lllll}
0.6\ \mu\mathrm{s} & \leq & T_{pr} & \leq & 9.6\ \mu\mathrm{s} \qquad \textit{; prompt time} \\
500\ \mu\mathrm{s} & \leq & \Delta T & \leq & 36\ \mathrm{ms} \qquad \textit{; time-difference} \\
10\ \mathrm{MeV} & < & E_{pr,\,vis} & \leq & 36\ \mathrm{MeV} \qquad \textit{; prompt visible energy} \\
3.5\ \mathrm{MeV} & < & E_{seq,\,vis} & \leq & 16.5\ \mathrm{MeV} \qquad \textit{; sequential vis. energy} \\
-200\ \mathrm{cm} & < & X_{pr} & \leq & 200\ \mathrm{cm} \qquad \textit{; prompt x-position} \\
0.5 & < & ROW_{pr} & \leq & 32.5 \qquad \textit{; prompt row} \\
0.5 & < & COL_{pr} & \leq & 16.5 \qquad \textit{; prompt column}
\end{array}$$

$\|\Delta X\|$	$\leq$	35 cm	*; x-position-difference*
$\|\Delta ROW\|$	$\leq$	1.5	*; row-difference*
$\|\Delta COL\|$	$\leq$	1.5	*; column-difference*
no Veto hit			*; pr. and seq. event*
M_{pr}	$\leq$	10	*; prompt multiplicity*
M_{seq}	$\leq$	5	*; sequential multiplicity*
Thresh	$=$	30 chn.	*; prompt threshold cut (if* $M_{pr} = 1$*)*
		15 μs	*; pr. K2 dead-time after stack-entry*
		10 μs	*; pr. K2 dead-time after veto-only VO*
		20 μs	*; pr. K1 dead-time after stack-entry*
		10 μs	*; seq. dead-time after stack-entry*
T_{REL}	$\leq$	50 ns	*; rel. time between modules*
SMU-reduction			*; see following Section 3.1.2*

The sequence analysis of the KARMEN data, which was acquired from the year 1990 until 2001, delivers 860 candidate sequences (503 in K1 + 357 in K2), which satisfy all cuts and general event requirements for the exclusive CC-reaction $^{12}\mathrm{C}\,(\,\nu_e\,,\mathrm{e}^-\,)\,^{12}\mathrm{N}_{\mathrm{g.s.}}$. *Fig.* 3.2 shows the visible energy, time and spatial distributions of the prompt events and the concatenated delayed events, respectively (*see also Fig.* 3.3 for K1 and 3.4 for K2). The remaining background components will be introduced in the following two sections, before the value of the cross section for $^{12}\mathrm{C}\,(\,\nu_e\,,\mathrm{e}^-\,)\,^{12}\mathrm{N}_{\mathrm{g.s.}}$ will be determined.

3.1.2 Reduction of Stopped Cosmic Muons and Refinement of Energy-Calibration

Stopped cosmic muons (SMU) inside the central detector can cause spatially correlated events on the time scale of a few microseconds up to several milliseconds. Whereas all μ^+ stopping in the detector will decay, a fraction of $\alpha_c = 7.8\%$ of the stopped μ^- undergo nuclear capture reactions in the scintillator. The muon-decay produces a spatially correlated Michel electron or positron with an energy up to $E_{max} = 52.83$ MeV. The time correlation is defined by the lifetime of μ^+ ($\tau = 2.197\,\mu$s) and μ^- ($\tau = 2.026\,\mu$s). The energy distribution of the Michel electrons or positrons can be calculated analytically from the 3-body-decay of muons at rest. Hence, the stopped muons being recorded every beam-period (since RUN 31), give rise to an *in situ* refinement of the energy-calibration. For each recorded RUN the measured Michel energy spectrum is compared with the corresponding MC-simulation, which accounts for the detector response and calibration. Despite of the excellent energy-calibration, small mismatches occurred up to a 5% level, especially towards the end of KARMEN, when the number of defective modules increased drastically. The small mismatches are corrected by adjusting the 50%-value of the falling edge near the endpoint of the visible Michel energy spectrum of each RUN. Thus, scaling factors for the visible energy of each RUN are deduced. Herewith, it is feasible to refine the energy-calibration RUN-wise (*see Appendix* A).

The small fraction of stopped μ^-, which undergo nuclear capture reactions in the scintillator, can involve neutron production with a branching ratio of $\Gamma_{\mu^-} = 0.82$:

$$\mu^- + {}^{12}\mathrm{C} \rightarrow {}^{12-x}\mathrm{B} + \mathrm{x} \cdot \mathrm{n} + \nu_\mu \tag{3.2}$$

The neutrons are detected by the typical neutron capture events of p(n,γ) or Gd(n,γ) with $E_0 = 8\,\mathrm{MeV}$ and $\tau_{capture} \approx 120\,\mu\mathrm{s}$. This process leads to a contribution to the cosmic induced background, especially for the sequential $\bar{\nu}_\mu \rightarrow \bar{\nu}_e$ oscillation search (*see Chapter* 4.4.1), which arises from unvetoed muons with short track lengths, stopping in the central detector and depositing less than 51 MeV.
Long-lived background arises from muon capture reactions of μ^-

$$\mu^- + {}^{12}\mathrm{C} \rightarrow {}^{12}\mathrm{B} + \nu_\mu \tag{3.3}$$

to the ^{12}B ground state or γ-unstable levels, through the subsequent β-decay:

$$^{12}\mathrm{B}_{\mathrm{g.s.}} \rightarrow {}^{12}\mathrm{C} + \mathrm{e}^- + \bar{\nu}_e \tag{3.4}$$

with $\tau = 29.1\,\mathrm{ms}$ and an endpoint energy of $E_{max} = 13.3\,\mathrm{MeV}$ for the beta-electron. Hence, this reaction has an overlap in its signature with ν_e-induced sequences from $^{12}\mathrm{C}\,(\,\nu_e\,,\mathrm{e}^-\,)\,^{12}\mathrm{N}_{\mathrm{g.s.}}$. Therefore, each event arising in the main detector is checked (within a coincidence volume) for preceding stopped muons for time differences up to $\Delta T < 100\,\mathrm{ms}$ to suppress the β-decay, whose electrons otherwise give also rise to random coincidences. In order to eliminate most of the background originating from stopped muons, events are rejected if a preceding stopped muon is found within the following time-differences and coincidence volumes (SMU-reduction):

$^{12}\mathrm{B}_{\mathrm{g.s.}} \rightarrow {}^{12}\mathrm{C} + \mathrm{e}^- + \bar{\nu}_e$

$500\ \mu\mathrm{s} \leq \Delta T < 100$ ms ; *time-difference*
$|\Delta X| < 60$ cm ; *x-position-difference*
$|\Delta ROW| < 0.5$; *row-difference*
$|\Delta COL| < 0.5$; *column-difference*

$\mu^- + {}^{12}\mathrm{C} \rightarrow {}^{12-x}\mathrm{B} + \mathrm{x} \cdot \mathrm{n} + \nu_\mu$

$40\ \mu\mathrm{s} \leq \Delta T < 500\ \mu\mathrm{s}$; *time-difference*
$|\Delta X| < 80$ cm ; *x-position-difference*
$|\Delta ROW| < 2.5$; *row-difference*
$|\Delta COL| < 2.5$; *column-difference*

$\Delta T < 40\ \mu\mathrm{s}$; *time-difference*
entire detector

3.1.3 Remaining Cosmic Induced and Random Background

The random background expectation for the exclusive CC-reaction $^{12}\mathrm{C}\,(\,\nu_e\,,\mathrm{e}^-\,)\,^{12}\mathrm{N}_{\mathrm{g.s.}}$ can be determined at high precision from the entire data. A prompt event satisfying all cuts is simulated for every recorded beam-period. The data search for a sequential event is then performed for each beam-period as well, in order to measure the random probability for observing a ν_e-like sequence. Hence, the number of expected random background sequences for the exclusive CC-reaction $^{12}\mathrm{C}\,(\,\nu_e\,,\mathrm{e}^-\,)\,^{12}\mathrm{N}_{\mathrm{g.s.}}$ is given by the product of the measured random probability and the measured number of prompt single-events[1].

The cosmic background expectation for the exclusive CC-reaction $^{12}\mathrm{C}\,(\,\nu_e\,,\mathrm{e}^-\,)\,^{12}\mathrm{N}_{\mathrm{g.s.}}$ can be measured very precisely as well by analyzing the pre-beam time window ($-191\,\mu\mathrm{s} \leq T_{pr} \leq -1\,\mu\mathrm{s}$), which is more than 21 times longer than the $9\,\mu$s short neutrino time window ($0.6\,\mu\mathrm{s} \leq T_{pr} \leq 9.6\,\mu\mathrm{s}$). The portion of cosmic background being due to random sequences is subtracted thereby.

Table 3.1 lists all numbers of expected cosmic induced and random background for KARMEN1 and KARMEN2. The global cosmic induced and random background expectation $\langle N_{cos,\,rnd}\rangle_{CC}^{K1+K2}$ for the exclusive CC-reaction $^{12}\mathrm{C}\,(\,\nu_e\,,\mathrm{e}^-\,)\,^{12}\mathrm{N}_{\mathrm{g.s.}}$ in K1+K2 comes out as:

$$\langle N_{cos,\,rnd}\rangle_{CC}^{K1+K2} = 13.9 \pm 0.7$$

Hence, the sequential detection of ν_e via the exclusive CC-reaction $^{12}\mathrm{C}\,(\,\nu_e\,,\mathrm{e}^-\,)\,^{12}\mathrm{N}_{\mathrm{g.s.}}$ is almost free of background in KARMEN. The corresponding signal to background ratio amounts to 61 : 1 (48 : 1 in K1 and 96 : 1 in K2, respectively).

$\langle background\rangle$	K1	K2	K1+K2
$\langle N_{cos}\rangle$	5.9 ± 0.6	1.0 ± 0.3	6.9 ± 0.7
$\langle N_{rnd}\rangle$	4.4 ± 0.1	2.7 ± 0.1	7.1 ± 0.1

Table 3.1: In KARMEN1 and KARMEN2 measured numbers of expected ν_e-like sequences from cosmic- and random background for the exclusive CC-reaction $^{12}\mathrm{C}\,(\,\nu_e\,,\mathrm{e}^-\,)\,^{12}\mathrm{N}_{\mathrm{g.s.}}$.

3.1.4 Measurement of Cross Section for $^{12}\mathrm{C}\,(\,\nu_e\,,\mathrm{e}^-\,)\,^{12}\mathrm{N}_{\mathrm{g.s.}}$

Fig. 3.2 illustrates the sequences measured in KARMEN for the exclusive CC-reaction $^{12}\mathrm{C}\,(\,\nu_e\,,\mathrm{e}^-\,)\,^{12}\mathrm{N}_{\mathrm{g.s.}}$ (*see also Fig.* 3.3 for K1 and 3.4 for K2). Shown in the left column are the visible energy, time and spatial distribution of the prompt e^-, whereas in the right column the visible energy, as well as the time- and spatial-difference of the delayed

---

[1] Number of prompt single-events (neutrinos and cosmic background) with respect to different cuts and corrected according to different dead-times for single-events and CC-sequences (*see Appendix* D).

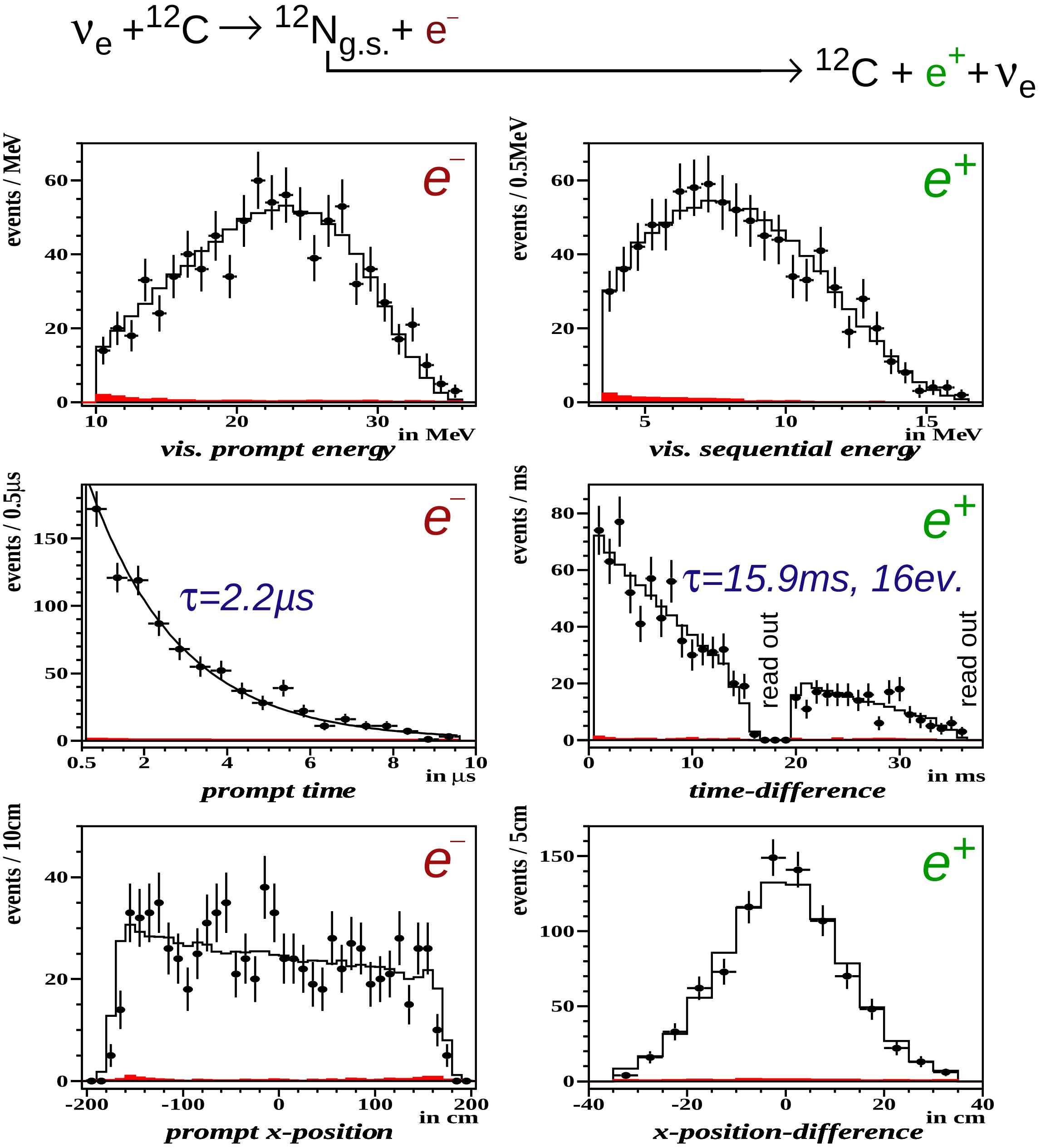

Figure 3.2: With KARMEN (K1+K2) spectroscopically measured energy-, time- and spatial distributions of prompt and sequential events from the exclusive CC-reaction $^{12}\mathrm{C}\,(\,\nu_e\,,\mathrm{e}^-\,)\,^{12}\mathrm{N}_{\mathrm{g.s.}}$. Plotted into each spectrum is the expectation from the MC-simulation (solid line) and from the background measurement (filled red area).

e^+ are displayed. The measured spectra are in excellent agreement with the expectation from MC-simulations (solid line in each spectrum). The spatial distribution of the prompt events possesses the $1/(distance)^2$-dependence of the neutrinos and the time distribution of the prompt events reflects clearly the muon-lifetime ($\tau = 2.2\,\mu$s). Thus, it is demonstrated impressively that ν_e originate from μ^+-decays inside the ISIS main-target. Furthermore, the visible energies of the prompt electrons give rise to the original ν_e-energy spectrum. Moreover, from the exact shape of the unfolded energy spectrum of ν_e from muon-decay at rest, it is feasible to derive implications on the Lorentz structure of the weak interaction via the Michel-shape-parameter ω_L [Arm98b].
The time-difference distribution of the sequential events gives rise to the lifetime of $^{12}\mathrm{N}_{\mathrm{g.s.}}$ ($\tau = 15.9\,$ms), with respect to corrections caused by the electronics. These corrections are due to: a) the read-out gap at the end of every beam-period, b) the maximum number of 16 events, which can be recorded every beam-period (*compare Fig.* D.3), c) the variable EC1-threshold in K2 (for $T > 800\mu$s), which switches again to a $600\,\mu$s long period of low threshold (EC1 off) after an event above MLU-threshold occurred (*see Fig.* 2.6) as well as d) failures of the enabling of the second beam-period mode for the following beam-period. All of these corrections, modifying the observed sequential time spectrum of positrons from β^+-decays of $^{12}\mathrm{N}_{\mathrm{g.s.}}$ ($\tau = 15.9\,$ms), can be derived precisely from the recorded data. For this, the only input parameters in K2 are the simulated values of the MC-efficiencies with EC1-threshold on and off (*see Fig.* D.4).
With the exclusive CC-reaction $^{12}\mathrm{C}\,(\,\nu_e\,,\mathrm{e}^-\,)\,^{12}\mathrm{N}_{\mathrm{g.s.}}$ in KARMEN, it is feasible to study precisely 846 ν_e in spectroscopic quality and almost free of background (signal to background ratio of 61 : 1). The cross section $\langle\,\sigma\,\rangle$, averaged over the ν-energy spectrum, depends on a) the number of detected reactions ($N = 846$), b) the effective number of target-nuclei ($N_{target}^{C12} = 2.54\cdot 10^{30}$), c) the inverse effective scaled area ($\Omega_{eff} = 1/[4\pi(17.72m)^2]$), d) the absolute ν-flux Φ_ν and e) the overall detection efficiency $\epsilon_{overall}$ as follows:

$$\langle\,\sigma\,\rangle = \frac{N}{N_{target}\cdot\Omega_{eff}\cdot\epsilon_{overall}\cdot\Phi_\nu} \tag{3.5}$$

The overall detection efficiencies $\epsilon_{overall}^{K1}$ for K1 and $\epsilon_{overall}^{K2}$ for K2, respectively, are given by:

$$\begin{aligned}
\epsilon_{overall}^{K1} &= \epsilon_{MC}^{K1}\cdot\epsilon_{t_{pr},\tau_\mu}\cdot\epsilon_{t_{seq}}^{K1}\cdot\epsilon_{stack,\,pr,\,\tau_\mu}^{K1}\cdot\epsilon_{stack,\,seq}^{K1}\cdot\epsilon_{SMU}^{K1}\cdot\epsilon_{PPP}^{K1}\\
\epsilon_{overall}^{K2} &= \epsilon_{MC,\,ECoff}^{K2}\cdot\epsilon_{t_{pr},\tau_\mu}\cdot\epsilon_{t_{seq}}^{K2}(\epsilon_{MC,\,ECon/off})\cdot\epsilon_{stack,\,pr,\,\tau_\mu}^{K2}\cdot\epsilon_{stack,\,seq}^{K2}\cdot\epsilon_{SMU}^{K2}
\end{aligned}$$

With the values listed in *Table* 3.2, the overall detection efficiency comes out as $\epsilon_{overall}^{K1} = 30.98\%$ for K1 and $\epsilon_{overall}^{K2} = 22.23\%$ for K2, respectively. The absolute ν-flux amounts to $\Phi_\nu^{K1} = 2.52\cdot 10^{21}$ for K1 and $\Phi_\nu^{K2} = 2.71\cdot 10^{21}$ for K2, respectively. Hence, with the number of detected reactions $N^{K1} = 492.8$ in K1 and $N^{K2} = 353.3$ in K2, the following

		K1 [%]	K2 [%]
MC-efficiency (ECoff in K2)	ϵ_{MC}	58.18	58.72
prompt time efficiency	$\epsilon_{t_{pr},\tau_\mu}$	83.85	83.85
sequential time efficiency ($\epsilon_{MC,\,ECon/off}$ in K2)	$\epsilon_{t_{seq}}$	73.81	61.37
stack efficiency for pr. event ($\tau_\mu = 2.2\,\mu$s weighted)	$\epsilon_{stack,\,pr,\,\tau_\mu}$	91.19	80.34
stack efficiency for seq. event	$\epsilon_{stack,\,seq}$	95.96	93.10
SMU-efficiency	ϵ_{SMU}	98.30	98.34
protons-per-pulse efficiency ($PPP > 60$)	ϵ_{PPP}	99.62	100.00
overall efficiency	$\epsilon_{overall}$	30.98	22.23

Table 3.2: Values of the efficiencies for the sequential detection of events from the exclusive CC-reaction $^{12}\mathrm{C}\,(\,\nu_e\,,\mathrm{e}^-\,)\,^{12}\mathrm{N}_{\rm g.s.}$ in KARMEN1 and KARMEN2. Apart from the MC-efficiency, any other value for the efficiency can be determined precisely from the recorded data in KARMEN. The different time dependence for each measured efficiency is illustrated in *Appendix* D. The stack efficiency for the prompt event needs to be weighted additionally with an exponential curve according to the lifetime of the muons ($\tau_\mu = 2.2\,\mu$s), especially since K2 (intelligible efficiency-dip in the prompt time window, due to longer dead-times and a higher rate of events).

cross section values, averaged over the ν_e-energy spectrum, are derived for the exclusive CC-reaction $^{12}\mathrm{C}\,(\,\nu_e\,,\mathrm{e}^-\,)\,^{12}\mathrm{N}_{\rm g.s.}$:

$$\langle\sigma(^{12}\mathrm{C}\,(\,\nu_e\,,\mathrm{e}^-\,)\,^{12}\mathrm{N}_{\rm g.s.})\rangle^{K1} = (9.9 \pm 0.5(stat.) \pm 0.7(syst.)) \cdot 10^{-42} cm^2$$

$$\langle\sigma(^{12}\mathrm{C}\,(\,\nu_e\,,\mathrm{e}^-\,)\,^{12}\mathrm{N}_{\rm g.s.})\rangle^{K2} = (9.1 \pm 0.5(stat.) \pm 0.7(syst.)) \cdot 10^{-42} cm^2$$

In order to obtain the global KARMEN cross section $\langle\sigma\rangle^{K1+K2}$ for the exclusive CC-reaction $^{12}\mathrm{C}\,(\,\nu_e\,,\mathrm{e}^-\,)\,^{12}\mathrm{N}_{\rm g.s.}$, the values for the cross section $\langle\sigma\rangle^{K1}$ in K1 and $\langle\sigma\rangle^{K2}$ in K2 are added flux- and efficiency-weighted:

$$\langle\sigma\rangle^{K1+K2} = \frac{\epsilon^{K1}_{overall}\cdot\Phi^{K1}_\nu\cdot\langle\sigma\rangle^{K1} \;+\; \epsilon^{K2}_{overall}\cdot\Phi^{K2}_\nu\cdot\langle\sigma\rangle^{K2}}{\epsilon^{K1}_{overall}\cdot\Phi^{K1}_\nu \;+\; \epsilon^{K2}_{overall}\cdot\Phi^{K2}_\nu} \tag{3.6}$$

Thus, the following global (K1+K2) cross section value, averaged over the ν_e-energy spectrum, is determined for the exclusive CC-reaction $^{12}\mathrm{C}\,(\,\nu_e\,,\mathrm{e}^-\,)\,^{12}\mathrm{N}_{\rm g.s.}$ in KARMEN (corresponding to a number of $N = 846.1$ detected reactions, an absolute ν-flux of $\Phi_\nu = 5.23{\cdot}10^{21}$ and an effective overall detection efficiency of $\langle\epsilon_{overall}\rangle = 27.2\%$):

$$\boxed{\langle\sigma(^{12}\mathrm{C}\,(\,\nu_e\,,\mathrm{e}^-\,)\,^{12}\mathrm{N}_{\rm g.s.})\rangle = (9.6 \pm 0.3(stat.) \pm 0.7(syst.)) \cdot 10^{-42} cm^2}$$

The systematic error of the cross section is dominated by the 7% uncertainty of the absolute ν-flux from ISIS (*see Table* 3.3). The value of the cross section, measured

by KARMEN, is well in agreement with all theoretical EPT, SM and (C)RPA calculations ($7.9 \ldots 10.1 \cdot 10^{-42} cm^2$). There is no particular type of model to be preferred (*see Table* 3.4). Moreover, the KARMEN value is well in agreement with the value of $(8.9 \pm 0.3(stat.) \pm 0.9(syst.)) \cdot 10^{-42} cm^2$ measured by the LSND-experiment [Aue01]. LSND possesses a correlated systematic uncertainty of the ν-flux, due to the usage of the same MC-program for the flux-calculations [Bur95].
The former K1 value of $(9.4 \pm 0.4(stat.) \pm 0.8(syst.)) \cdot 10^{-42} cm^2$ is 5% smaller than the value for $\langle\sigma(^{12}\mathrm{C}\,(\,\nu_e\,,\mathrm{e}^-\,)\,^{12}\mathrm{N}_{\mathrm{g.s.}})\rangle^{K1}$ derived in the framework of this thesis. The discrepancy arises mainly from a less accurate determination of various efficiencies in [Arm98b] (*compare Table* 3.2).

The sequence analysis of the exclusive CC-reaction $^{12}\mathrm{C}\,(\,\nu_e\,,\mathrm{e}^-\,)\,^{12}\mathrm{N}_{\mathrm{g.s.}}$ in KARMEN demonstrates impressively, how well the properties of the KARMEN-detector and the ISIS-neutrino-source are understood. It is now justified to derive in the next step an upper limit on $\nu_e \rightarrow \nu_{sterile}$ disappearance. But before that, the inclusive neutrino-nucleus-reactions in KARMEN will be studied in detail.

	Parameter	*Relative Uncertainty [%]*
ν-flux	$\Delta\Phi_\nu$ [Bur95]	6.7
MC-efficiency	$\Delta\epsilon_{MC}$	3.0
inverse effective scaled area	$\Delta\Omega$ ($\Delta X = 10\,\mathrm{cm}$)	1.1
effective no. of target nuclei	ΔN_{target}	1.0
further efficiencies	$\Delta\epsilon$ ($\Delta\epsilon_{single} = 0.1\%$)	0.3
cross section	$\Delta\sigma(syst.)$	7.5

Table 3.3: Relative uncertainties of all parameters accounting for the systematic error of the measured cross section for the exclusive CC-reaction $^{12}\mathrm{C}\,(\,\nu_e\,,\mathrm{e}^-\,)\,^{12}\mathrm{N}_{\mathrm{g.s.}}$.

Author		*Type of Model*	$\langle\sigma(^{12}\mathrm{C}\,(\,\nu_e\,,\mathrm{e}^-\,)\,^{12}\mathrm{N}_{\mathrm{g.s.}})\rangle$ $[10^{-42}\,cm^2]$
Kolbe	[Kol99]	CRPA	8.9
Auerbach(SIII)	[Aue97]	RPA	10.1
Vogel	[Vog96]	SM	9.1
Volpe	[Vol01]	SM	8.1
Hayes	[Hay00]	SM	7.9
Donnelly	[Don91]	SM	9.4
Fukugita	[Fuk88]	EPT	9.1(9)
Mintz	[Min93]	EPT	8.0

Table 3.4: Comparison of theoretical calculations of the cross section $\langle\sigma\rangle$ for the exclusive CC-reaction $^{12}\mathrm{C}\,(\,\nu_e\,,\mathrm{e}^-\,)\,^{12}\mathrm{N}_{\mathrm{g.s.}}$.

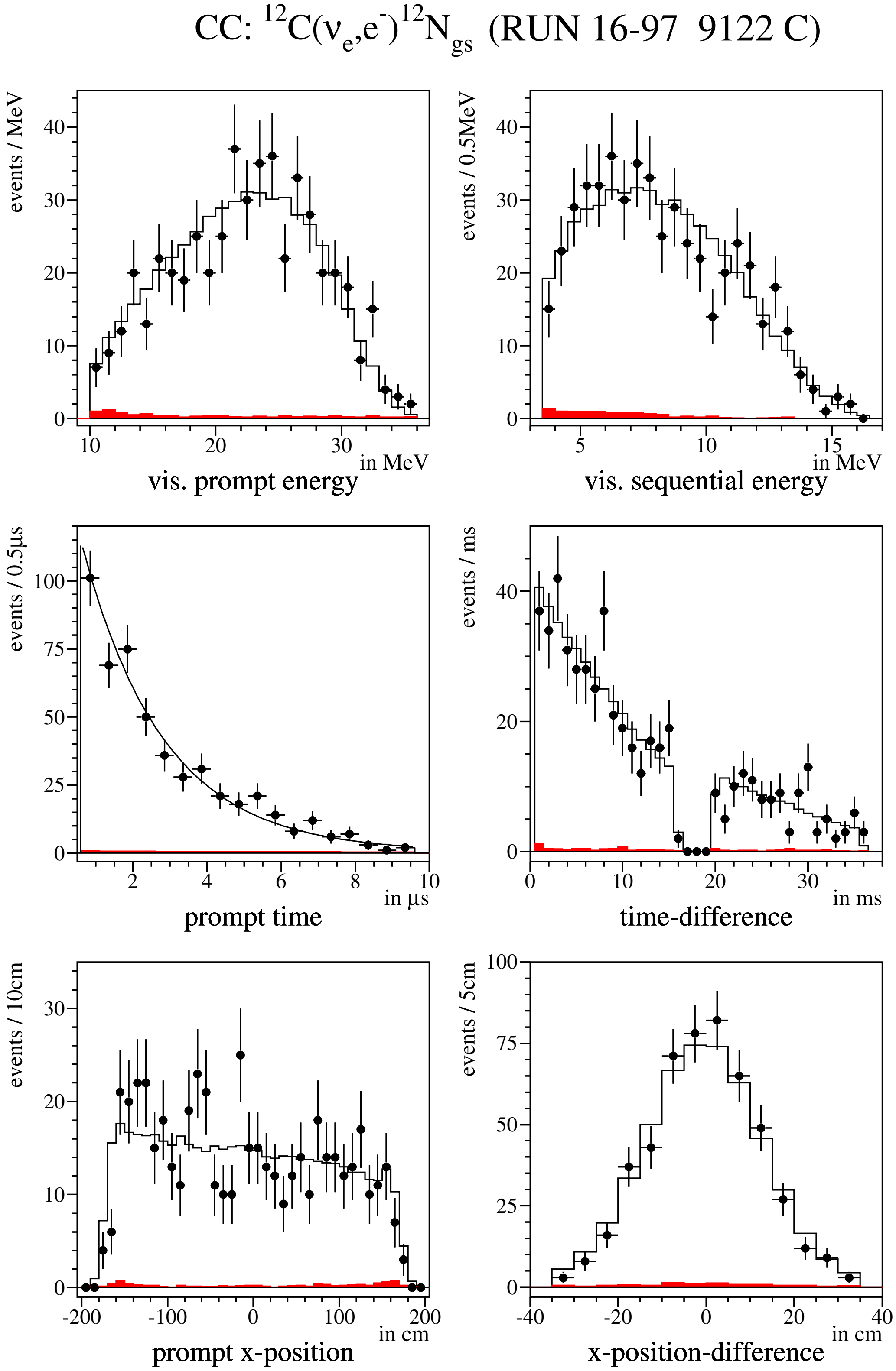

Figure 3.3: With KARMEN1 spectroscopically measured energy-, time- and spatial distributions of prompt and sequential events from the exclusive CC-reaction $^{12}\mathrm{C}\,(\,\nu_e\,,\mathrm{e}^-\,)\,^{12}\mathrm{N}_{\mathrm{g.s.}}$. Plotted into each spectrum is the expectation from the MC-simulation (solid line) and from the background measurement (filled red area).

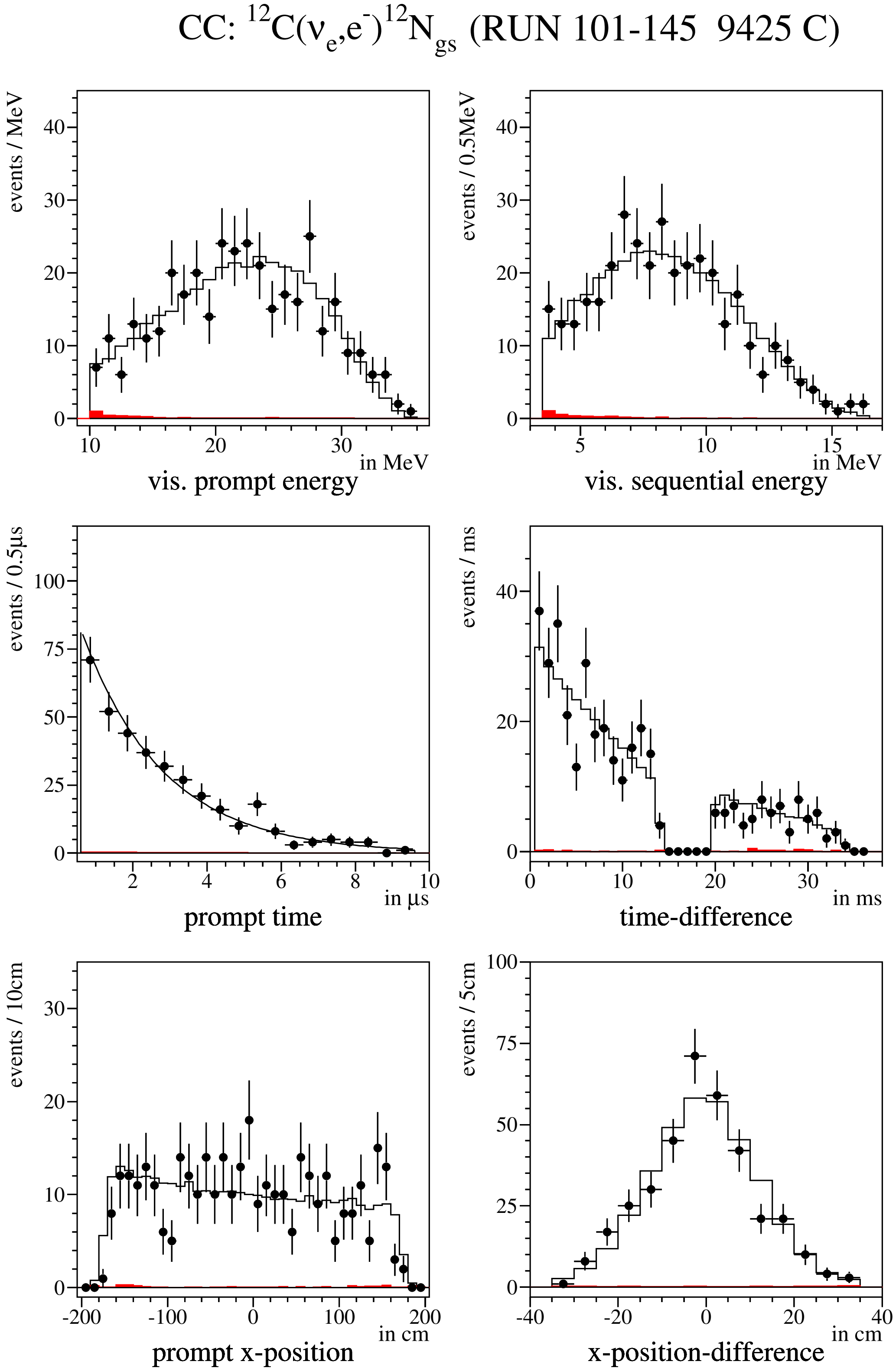

Figure 3.4: With KARMEN2 spectroscopically measured energy-, time- and spatial distributions of prompt and sequential events from the exclusive CC-reaction $^{12}\mathrm{C}\,(\,\nu_e\,, \mathrm{e}^-\,)\,^{12}\mathrm{N}_{\mathrm{g.s.}}$. Plotted into each spectrum is the expectation from the MC-simulation (solid line) and from the background measurement (filled red area).

3.2 Single–Events: Inclusive Charged–Current– and Neutral–Current–Reactions

Neutrino-induced inclusive charged- and neutral-current-reactions on ^{12}C, ^{13}C and ^{56}Fe nuclei will be measured precisely with neutrinos from μ^+-decay at rest in the energy regime of supernovae. Due to the KARMEN-upgrade, the cosmic background rate for single-events is strongly suppressed in KARMEN2 (*see Fig.* 3.5). Therefore, it is feasible to measure the inclusive neutrino-nucleus-reactions for the first time consistently and model-independently via a combined analysis of the single-events. For this, the previously measured cross section for the exclusive CC-reaction $^{12}\mathrm{C}\,(\,\nu_e\,,\mathrm{e}^-\,)\,^{12}\mathrm{N}_{\mathrm{g.s.}}$ will serve as an independent input parameter. In order to reduce more degrees of freedom for the combined analysis, the cross section for the inclusive CC-reaction $^{13}\mathrm{C}\,(\,\nu_e\,,\mathrm{e}^-\,)\,^{13}\mathrm{N}$ will be derived first in KARMEN2 from an appropriate window-method, where this reaction can be studied solely with well-known background. Finally, the undetermined cross sections for the inclusive neutrino-nucleus-reactions $^{12}\mathrm{C}\,(\,\nu\,,\nu'\,)\,^{12}\mathrm{C}^*$, $^{12}\mathrm{C}\,(\,\nu_e\,,\mathrm{e}^-\,)\,^{12}\mathrm{N}^*$ and $^{56}\mathrm{Fe}\,(\,\nu_e\,,\mathrm{e}^-\,)\,\mathrm{X}$ will be derived from a χ^2-fit to the visible energy of the single-events in

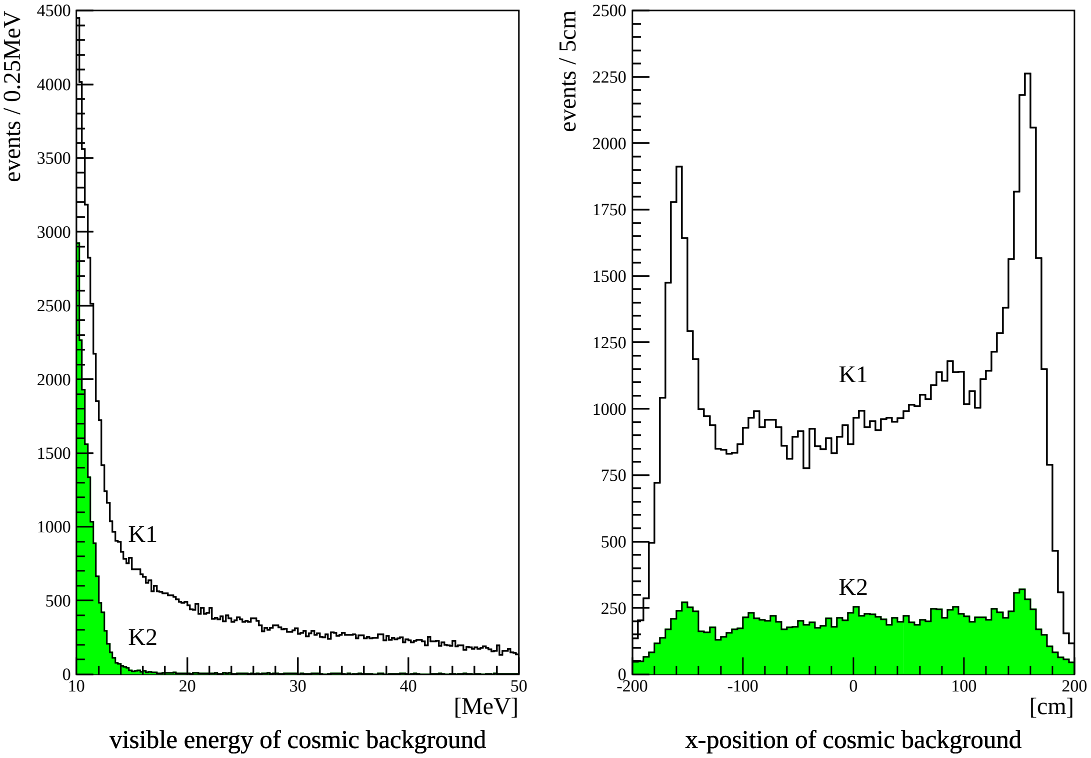

Figure 3.5: Energy- and spatial distribution of the cosmic induced background for the single-events in KARMEN1 (K1) before and KARMEN2 (K2) after the upgrade. The spectra are derived from the pre-beam time window ($-191\,\mu\mathrm{s} \leq T_{pr} \leq -1\,\mu\mathrm{s}$), using the cuts and general event requirements from *Section* 3.2.2.

KARMEN2. Hence, no theoretical calculation for a neutrino-nucleus cross section will be needed and all measurements will be performed consistently. Due to the very characteristic peak structure in the visible energy of the NC-reaction $^{12}\mathrm{C}\,(\,\nu\,,\nu'\,)\,^{12}\mathrm{C}^*$, a further improvement will be achieved for this reaction by combining the fit-results from KARMEN2 with KARMEN1. The flux-independent ratio $R = \langle\sigma^{NC}\rangle / \langle\sigma^{CC}_{gs}\rangle$ of the measured ν cross sections for the NC- and the exclusive CC-reaction on $^{12}\mathrm{C}$ will deliver the most accurate result for the comparison with theoretical calculations. Thus, the μ-e-universality of the weak interaction will be tested.

3.2.1 Window–Method for Inclusive CC–Reaction $^{13}\mathrm{C}\,(\,\nu_e\,,\mathrm{e}^-\,)\,^{13}\mathrm{N}$

The organic scintillator of KARMEN contains $^{13}\mathrm{C}$ nuclei just to a small fraction, according to the natural abundance of 1.1%. But its contribution to the inclusive neutrino-nucleus-reactions is not negligible, as theoretical calculations suggest that the cross section for the inclusive CC-reaction $^{13}\mathrm{C}\,(\,\nu_e\,,\mathrm{e}^-\,)\,^{13}\mathrm{N}$ is almost by one order of magnitude larger than the cross sections for neutrino-induced reactions on $^{12}\mathrm{C}$. In order to reduce a further degree of freedom for the combined analysis, this cross section for the inclusive CC-reaction $^{13}\mathrm{C}\,(\,\nu_e\,,\mathrm{e}^-\,)\,^{13}\mathrm{N}$ will be derived in the following from KARMEN2 with an appropriate window-method, where this reaction can be studied solely with well-known background. The inclusive CC-reaction $^{13}\mathrm{C}\,(\,\nu_e\,,\mathrm{e}^-\,)\,^{13}\mathrm{N}$ can produce prompt single-events in KARMEN with visible energies up to roughly 50 MeV, due to the small Q-value of 2.22 MeV for the ground state transition and the maximum ν-energy of 52.83 MeV from μ^+-decay at rest:

$$\nu_e \quad + \quad ^{13}\mathrm{C} \quad \longrightarrow \quad ^{13}\mathrm{N}^{(*)} \quad + \quad \enclose{circle}{\mathrm{e}^-} \quad (\; + \enclose{circle}{\gamma} \;) \qquad -Q < -2.22\,\mathrm{MeV}$$

Moreover, the lifetime of the muons ($\tau_\mu = 2.2\,\mu$s) determines the exponentially decreasing time distribution of the prompt signal. The two transitions into the states $^{13}\mathrm{N}_{\mathrm{g.s.}}$ and $^{13}\mathrm{N}(3/2^-)$ account for 85% of the prompt visible events from $^{13}\mathrm{C}\,(\,\nu_e\,,\mathrm{e}^-\,)\,^{13}\mathrm{N}$ (*see Fig.* 3.7) [Ara89]. A sequential detection of events from subsequent decays is not feasible, due to the corresponding lifetimes and the timing of KARMEN (e.g. $\tau_{N13gs} = 14.4\,\mathrm{min}$).
Above 38 MeV prompt visible energy, only events from $^{56}\mathrm{Fe}\,(\,\nu_e\,,\mathrm{e}^-\,)\,\mathrm{X}$, ν-e^--scattering and cosmic background are contributing to the single-events. Restricting additionally the fiducial volume to the inner region of the modules ($|X_{pr}| < 130\,\mathrm{cm}$), eliminates Bremsstrahlung γ-rays from reactions $^{56}\mathrm{Fe}\,(\,\nu_e\,,\mathrm{e}^-\,)\,\mathrm{X}$ occurring within the steel, that closely surrounds the detector. Hence, the contribution from the inclusive CC-reaction $^{56}\mathrm{Fe}\,(\,\nu_e\,,\mathrm{e}^-\,)\,\mathrm{X}$ to the single-events is negligible, due to the applied window-method (*see Table* 3.5). Only the analytically calculable ν-e^--scattering and the precisely measurable cosmic background remain as background for the study of the inclusive CC-reaction $^{13}\mathrm{C}\,(\,\nu_e\,,\mathrm{e}^-\,)\,^{13}\mathrm{N}$. Data, recorded before the KARMEN-upgrade, are not evaluated for this analysis, because the cosmic background rate for single-events is strongly suppressed in KARMEN2 (*see Fig.* 3.5). In order to reduce the cosmic background for single-events

further, optimized software dead-times are applied after every stack-entry and veto-only VO (*see Section* 3.2.2). The necessary stack-reduction for single-events in K2 is causing an efficiency loss of 31% (*see Fig.* D.1 *and Table* 3.7).
In order to search for prompt single-events from ${}^{13}\mathrm{C}\,(\,\nu_e\,,\mathrm{e}^-\,)\,{}^{13}\mathrm{N}$, all following cuts and general event requirements are applied to the KARMEN2 data:

$0.6\,\mu\mathrm{s} \leq T_{pr} \leq 10.6\,\mu\mathrm{s}$ *; prompt time*
$38\,\mathrm{MeV} < E_{pr,\,vis} \leq 50\,\mathrm{MeV}$ *; prompt visible energy*
$-130\,\mathrm{cm} < X_{pr} \leq 130\,\mathrm{cm}$ *; prompt x-position*
$0.5 < ROW_{pr} \leq 32.5$ *; prompt row*
$0.5 < COL_{pr} \leq 16.5$ *; prompt column*

no Veto hit *; pr. event*

$M_{pr} \leq 4$ *; prompt multiplicity*
Thresh = 30 chn. *; prompt threshold cut (if $M_{pr} = 1$)*

$28\,\mu\mathrm{s}$ *; pr. K2 dead-time after stack-entry*
$17\,\mu\mathrm{s}$ *; pr. K2 dead-time after veto-only VO*

$T_{REL} \leq 50\,\mathrm{ns}$ *; rel. time between modules*

SMU-reduction *; see Section 3.1.2*

The analysis of the KARMEN2 data, which was acquired from the year 1997 until 2001, delivers 14 single-events, which satisfy all cuts and general event requirements for the inclusive CC-reaction ${}^{13}\mathrm{C}\,(\,\nu_e\,,\mathrm{e}^-\,)\,{}^{13}\mathrm{N}$. *Fig.* 3.6 shows the visible energy, time, and spatial distributions of the 14 single-events. The remaining background components will be determined in the following, before the value of the cross section for ${}^{13}\mathrm{C}\,(\,\nu_e\,,\mathrm{e}^-\,)\,{}^{13}\mathrm{N}$ will be deduced.

Cosmic Induced Background

The cosmic background expectation for the inclusive CC-reaction ${}^{13}\mathrm{C}\,(\,\nu_e\,,\mathrm{e}^-\,)\,{}^{13}\mathrm{N}$ can be measured very precisely by analyzing the pre-beam time window ($-191\,\mu\mathrm{s} \leq T_{pr} \leq -1\,\mu\mathrm{s}$), which is 19 times longer than the $10\,\mu\mathrm{s}$ short neutrino time window ($0.6\,\mu\mathrm{s} \leq T_{pr} \leq 10.6\,\mu\mathrm{s}$). Corrections, due to the time dependence of the stack-efficiency, are in the order of a few percent and not marginal anymore, because of the longer applied dead-times and a higher rate of events in K2 (*see Fig.* D.1). The cosmic induced background expectation $\langle N_{cos}\rangle^{K2}_{C13}$ for the inclusive CC-reaction ${}^{13}\mathrm{C}\,(\,\nu_e\,,\mathrm{e}^-\,)\,{}^{13}\mathrm{N}$ in K2 comes out as:

$$\langle N_{cos}\rangle^{K2}_{C13} = 2.1 \pm 0.3$$

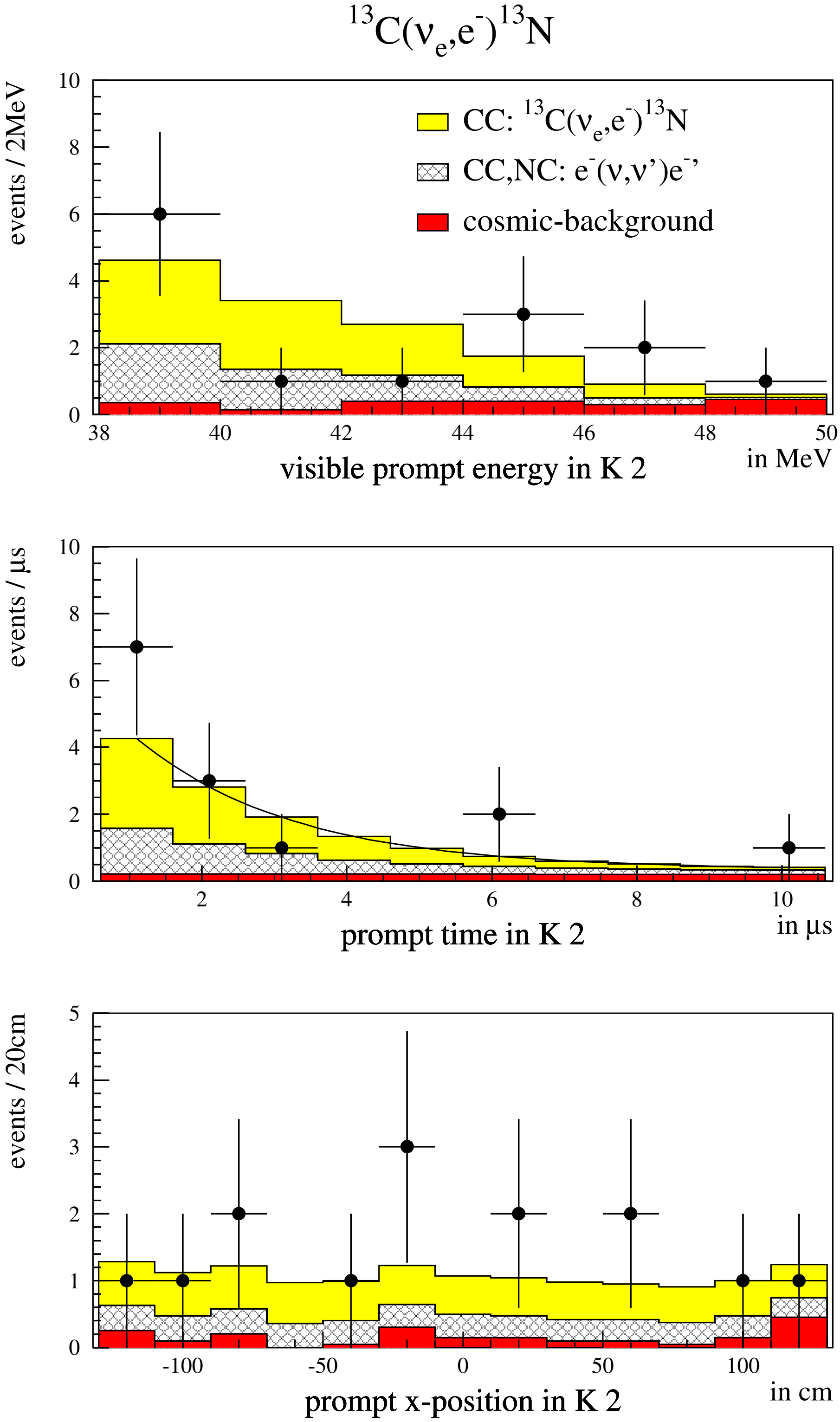

Figure 3.6: Energy-, time- and spatial distributions of the 14 single-events in KARMEN2 (K2), derived from an optimized window-method for the inclusive CC-reaction ^{13}C (ν_e , e$^-$) ^{13}N. The determined contributions from cosmic background, ν-e^--scattering and the inclusive CC-reaction ^{13}C (ν_e , e$^-$) ^{13}N are plotted additionally into each spectrum, according to expectations from MC-simulations and pre-beam measurements, respectively.

Background from ν-e^--Scattering

As already pointed out, the ν-e^--scattering is analytically calculable. The cross section value of $\langle\sigma\rangle = (0.347 \pm 0.002) \cdot 10^{-42} cm^2$, averaged over the ν_e- and $\bar{\nu}_\mu$-energy spectrum, is derived in the framework of the standard model [Ebe92].

Moreover, the overall detection efficiency $\epsilon^{K2}_{overall}$ for K2 is given by:

$$\epsilon^{K2}_{overall} = \epsilon^{K2}_{MC} \cdot \epsilon_{t_{pr},\,\tau_\mu} \cdot \epsilon^{K2}_{stack,\,pr,\,\tau_\mu} \cdot \epsilon^{K2}_{SMU} \tag{3.7}$$

With the values listed in *Table* 3.7 and the corresponding MC-efficiency of $\epsilon^{K2}_{MC} = 1.61\%$ the overall detection efficiency for ν-e^--scattering amounts to $\epsilon^{K2}_{overall} = 0.92\%$. Together with *Eq.* 3.5 and an effective number of electrons of $N^{el}_{target} = 20.2 \cdot 10^{30}$ as well as an absolute ν-flux in K2 of $\Phi^{K2}_\nu = 2.71 \cdot 10^{21}$ the expected background from ν-e^--scattering is calculated to be:

$$\langle N_{ES}\rangle^{K2}_{C13} = 4.4 \pm 0.0$$

Cross Section for ^{13}C (ν_e , e$^-$) ^{13}N

Finally, with the number of 14 single-events, which satisfy all cuts and general event requirements, the measured number of events from the inclusive CC-reaction ^{13}C (ν_e , e$^-$) ^{13}N amounts to (*see Table* 3.5):

$$N^{K2}_{C13} = 7.5 \pm 3.8$$

With the values listed in *Table* 3.7 and the corresponding MC-efficiency of $\epsilon^{K2}_{MC} = 13.52\%$ the overall detection efficiency for ^{13}C (ν_e , e$^-$) ^{13}N amounts to $\epsilon^{K2}_{overall} = 7.75\%$. Together with *Eq.* 3.5 and an effective number of ^{13}C target-nuclei of $N^{C13}_{target} = 0.0282 \cdot 10^{30}$ as well as an absolute ν-flux of $\Phi^{K2}_\nu = 2.71 \cdot 10^{21}$, the following total cross section value, averaged over the ν_e-energy spectrum, is determined for the inclusive CC-reaction ^{13}C (ν_e , e$^-$) ^{13}N in K2:

$$\boxed{\langle\sigma(^{13}\mathrm{C}\,(\,\nu_e\,,\mathrm{e}^-\,)\,^{13}\mathrm{N})\rangle = (50 \pm 25(stat.)\,^{+4}_{-6}(syst.)) \cdot 10^{-42} cm^2}$$

Thus, the cross section for the inclusive CC-reaction ^{13}C (ν_e , e$^-$) ^{13}N has been measured (within $2\sigma_{stat}$) for the first time in the world. The overall error is still dominated by the low statistics, so that the systematic error[2], which is considerably caused by the 7% uncer-

---

[2] An additional systematic arises from the applied fiducial volume, causing that the value of the cross section is overestimated by roughly 8%, due to the MC-simulation of the efficiency (*see Table* 3.13).

tainty of the absolute ν-flux from ISIS (*see Table* 3.3), does hardly contribute. The value of the cross section, measured by KARMEN, is confirmed by most of the theoretical EPT, SM and RPA calculations ($29 \ldots 113 \cdot 10^{-42} cm^2$). But the largest value of $113 \cdot 10^{-42} cm^2$, derived from a SM not considering Gamow-Teller quenching, can be excluded (*see Table* 3.6 *and Fig.* 3.7). This delivers first evidence that the Gamow-Teller transition from the ground state ^{13}C$(1/2^-)$ into the excited state ^{13}N$(3/2^-)$ is strongly quenched, as assumed in the other SM-calculation leading to a cross section value of $52.(8) \cdot 10^{-42} cm^2$ [Kub93].

Moreover, due to the fact that the derived cross section value for the inclusive CC-reaction $^{13}\mathrm{C}\,(\,\nu_e\,,\mathrm{e}^-\,)\,^{13}\mathrm{N}$ does not exceed any of the theoretical expectations, no evidence for $\bar{\nu}_\mu \rightarrow \bar{\nu}_e$ appearance (LSND-oscillation) is delivered. Additional single-events from e.g. processes p($\bar{\nu}_e$,e^+)n would increase the value of the determined cross section instead (*see Chapter* 4.4.2).

Reaction		*N*	$N_{target}[10^{30}]$	$\epsilon_{overall}[\%]$
$^{13}\mathrm{C}\,(\,\nu_e\,,\mathrm{e}^-\,)\,^{13}\mathrm{N}$	*K2*	7.5 ± 3.8	0.0282	7.75
$\mathrm{e}^-\,(\,\nu\,,\nu'\,)\,\mathrm{e}^{-\prime}$	*K2*	$\langle 4.4 \pm 0.0 \rangle$	20.2	0.92
$^{56}\mathrm{Fe}\,(\,\nu_e\,,\mathrm{e}^-\,)\,\mathrm{X}$	*K2*	$\langle 0.0 \pm 0.0 \rangle$	2.34	0.000
⟨cosmic background⟩	*K2*	$\langle 2.1 \pm 0.3 \rangle$		
in total observed events	*K2*	14		

Table 3.5: Window-method for $^{13}\mathrm{C}\,(\,\nu_e\,,\mathrm{e}^-\,)\,^{13}\mathrm{N}$: Measured (or ⟨expected⟩) number of events, effective number of target-nuclei and overall detection efficiency for each of the contributing single-event-reactions. In addition, the expected number of cosmic induced events is given, as well as the total number of observed events.

Author		*Type of Model*	$\langle\sigma(^{13}\mathrm{C}\,(\,\nu_e\,,\mathrm{e}^-\,)\,^{13}\mathrm{N})\rangle\ [10^{-42}\,cm^2]$
Kubodera	[Kub93]	SM (GT-quenching)	52.(8)
Arafune	[Ara89]	SM (no GT-quenching)	113
Singh	[Sin98]	RPA	73
Mintz	[Min00]	EPT	29

Table 3.6: Comparison of theoretical calculations of the cross section $\langle\sigma\rangle$ for the inclusive CC-reaction $^{13}\mathrm{C}\,(\,\nu_e\,,\mathrm{e}^-\,)\,^{13}\mathrm{N}$.

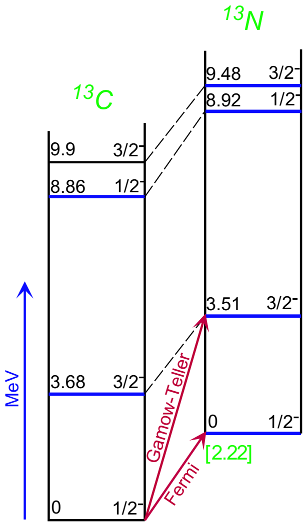

Figure 3.7: Energy levels for ^{13}C and ^{13}N nuclei. The Fermi transition into the ground state ^{13}N($1/2^-$) and the Gamow-Teller transition into the excited state ^{13}N($3/2^-$) account for 85% of the prompt visible events from $^{13}\mathrm{C}\,(\,\nu_e\,,\mathrm{e}^-\,)\,^{13}\mathrm{N}$ [Ara89].

3.2.2 χ^2–Method for $^{12}\mathrm{C}\,(\,\nu\,,\nu'\,)\,^{12}\mathrm{C}^*$, $^{12}\mathrm{C}\,(\,\nu_e\,,\mathrm{e}^-\,)\,^{12}\mathrm{N}^*$ and $^{56}\mathrm{Fe}\,(\,\nu_e\,,\mathrm{e}^-\,)\,\mathrm{X}$

Due to the strongly suppressed cosmic background rate for single-events in KARMEN2, it will be feasible to measure the inclusive neutrino-nucleus-reactions for the first time model-independently and consistently by using a single estimation procedure. The undetermined cross sections for the inclusive neutrino-nucleus-reactions $^{12}\mathrm{C}\,(\,\nu\,,\nu'\,)\,^{12}\mathrm{C}^*$, $^{12}\mathrm{C}\,(\,\nu_e\,,\mathrm{e}^-\,)\,^{12}\mathrm{N}^*$ and $^{56}\mathrm{Fe}\,(\,\nu_e\,,\mathrm{e}^-\,)\,\mathrm{X}$ will be derived from a χ^2-fit to the visible energy of the single-events in KARMEN2. For this, the previously measured cross sections for the exclusive CC-reaction $^{12}\mathrm{C}\,(\,\nu_e\,,\mathrm{e}^-\,)\,^{12}\mathrm{N}_{\mathrm{g.s.}}$ and the inclusive CC-reaction $^{13}\mathrm{C}\,(\,\nu_e\,,\mathrm{e}^-\,)\,^{13}\mathrm{N}$ will serve as independent input parameters. Hence, no theoretical calculation for a neutrino-nucleus cross section will be needed and all measurements will be performed consistently. Due to the very characteristic peak structure in the visible energy of the NC-reaction $^{12}\mathrm{C}\,(\,\nu\,,\nu'\,)\,^{12}\mathrm{C}^*$, a further improvement will be achieved for this reaction by combining the fit-results from KARMEN2 with KARMEN1. The flux-independent ratio $R = \langle\sigma^{NC}\rangle/\langle\sigma^{CC}_{gs}\rangle$ of the measured ν cross sections for the NC- and the exclusive CC-reaction on ^{12}C, will deliver the most accurate result for the comparison with theoretical calculations. Thus, the μ-e-universality of the weak interaction will be tested.

Deriving the Sample of Single-Events and Selection Criteria

Neutrinos from μ^+-decays at rest can produce single-events with prompt visible energies up to roughly 50 MeV. A lower boundary on the prompt visible energy of 10 MeV is set, in order to limit the cosmic background, which is steeply rising towards low energies (*see Fig.* 3.5). The lifetime of muons ($\tau_\mu = 2.2\,\mu$s) determines the exponentially decreasing time distribution of the neutrino induced single-events, whereas the cosmic induced background for single-events possesses an almost flat time distribution.

Stack-Reduction (Software Dead-Time Applied after Stack-Entries):
In order to minimize the cosmic background for single-events, optimized software dead-times have to be applied after every stack-entry (and veto-only VO in K2). This stack-reduction minimizes the background from unrecognized muons stopping and decaying ($\overline{\tau} \approx 2.2\,\mu$s) close or inside the central detector and thus mainly producing delayed Michel electrons or positrons with an energy up to 52.83 MeV. Although, the efficiency of the anti-counter-system for tagging stopped muons is approximately 99.8%, a background rate for single-events remains, which is 10^5 times higher than the neutrino rate. Therefore, after every event, being processed by the MLU[3] and thus obtaining a stack-entry, an optimized software dead-time of the order of $20\,\mu$s is applied *see Appendix* D [Arm98]. On the one hand this reduces drastically the cosmic background rate, but on the other hand the stack-reduction for single-events is causing an efficiency loss of 9% in K1 and 31% in K2, respectively (*see Fig.* D.1 *and Table* 3.7). The immensely increased efficiency loss in K2 is caused by the higher rate of events and the longer dead-time, which is to be applied, in order to obtain the optimal reduction of the cosmic background in K2.

Rejection of Events in Outer Regions of Defective Modules (X-Cut):
Especially after the upgrade, the number of defective detector modules increased and consecutively the description of the energy resolution became less accurate, predominantly in the outer regions of bad modules (due to the lightoutput-curves that are exponentially rising towards the ends of the modules, which makes the correction of light-leakage more difficult). In addition, the statistics for vertical and horizontal calibration cosmic muons are not sufficient enough for the correction of light-leakage in the outer 76.5 cm of defective modules. Therefore, a spatial X-cut is always applied to defective modules: Single-Events in the outer regions of defective modules ($|X_{pr}| > 100\,\mathrm{cm}$) are rejected, in order to keep up the quality of the energy-calibration. This is essential for a χ^2-fit to the visible energy of the single-events (*see Appendix* C). For statistical reasons, it is not possible to evaluate only good modules, because the fraction of single-events, occurring in defective modules, amounts to roughly a third in K2.

In order to search for prompt single-events in the late time window ($T_{pr} \geq 0.6\,\mu$s) for neutrinos from μ^+-decays at rest, all following cuts and general event requirements are applied to the KARMEN data:

$$\begin{array}{llcll}
0.6\ \mu\mathrm{s} & \leq & T_{pr} & \leq & 10.6\ \mu\mathrm{s} & ;\ \textit{prompt time} \\
10\ \mathrm{MeV} & < & E_{pr,\,vis} & \leq & 50\ \mathrm{MeV} & ;\ \textit{prompt visible energy} \\
-200\ \mathrm{cm} & < & X_{pr} & \leq & 200\ \mathrm{cm} & ;\ \textit{prompt x-position} \\
 & & \mathrm{if}\ \ |X_{pr}| & > & 100\ \mathrm{cm} & ;\ \textit{only good modules} \\
0.5 & < & ROW_{pr} & \leq & 32.5 & ;\ \textit{prompt row} \\
0.5 & < & COL_{pr} & \leq & 16.5 & ;\ \textit{prompt column}
\end{array}$$

---

[3] Memory Lookup Unit

no Veto hit			*; pr. event*
M_{pr}	$\leq$	4	*; prompt multiplicity*
Thresh	$=$	30 chn.	*; prompt threshold cut (if $M_{pr} = 1$)*
		20 μs	*; pr. K1 dead-time after stack-entry*
		28 μs	*; pr. K2 dead-time after stack-entry*
		17 μs	*; pr. K2 dead-time after veto-only VO*
T_{REL}	$\leq$	50 ns	*; rel. time between modules*
SMU-reduction			*; see Section 3.1.2*

The analysis of the KARMEN data, which was acquired from the year 1990 until 2001, delivers 9048 single-events (6695 in K1 + 2353 in K2), which satisfy all cuts and general event requirements for neutrino-nucleus-reactions in the late time window of neutrinos from μ^+-decays at rest. The portion of cosmic background will be evaluated in the following, before the unknown cross sections for the inclusive neutrino-nucleus-reactions $^{12}\mathrm{C}\,(\,\nu\,,\nu'\,)\,^{12}\mathrm{C}^*$, $^{12}\mathrm{C}\,(\,\nu_e\,,\mathrm{e}^-\,)\,^{12}\mathrm{N}^*$ and $^{56}\mathrm{Fe}\,(\,\nu_e\,,\mathrm{e}^-\,)\,\mathrm{X}$ will be derived from a χ^2-fit to the visible energy of the single-events.

Cosmic Induced Background

The expected number of single-events, being due to cosmic background, can be measured very precisely by analyzing the pre-beam time window ($-191\,\mu\mathrm{s} \leq T_{pr} \leq -1\,\mu\mathrm{s}$), which is 19 times longer than the $10\,\mu$s short neutrino time window ($0.6\,\mu\mathrm{s} \leq T_{pr} \leq 10.6\,\mu\mathrm{s}$). Corrections, due to the time dependence of the stack-efficiency, are in the order of a few percent for K2 and not marginal anymore, because of the longer applied dead-times and a higher rate of events in K2 (*see Fig.* D.1). The expected number $\langle N_{cos}\rangle$ of cosmic induced background for the single-events in K1 and K2, respectively, amounts to:

$$\langle N_{cos}\rangle^{K1} = 4275.1 \pm 15.0$$
$$\langle N_{cos}\rangle^{K2} = 770.9 \pm 6.2$$

The remaining number $\langle N_\nu\rangle$ of neutrino induced single-events in K1 and K2, respectively, is:

$$\langle N_\nu\rangle^{K1} = 2419.9 \pm 83.2$$
$$\langle N_\nu\rangle^{K2} = 1582.2 \pm 48.9$$

Fig. 3.8 shows separately the time distributions for K1 before the upgrade and K2 afterwards.

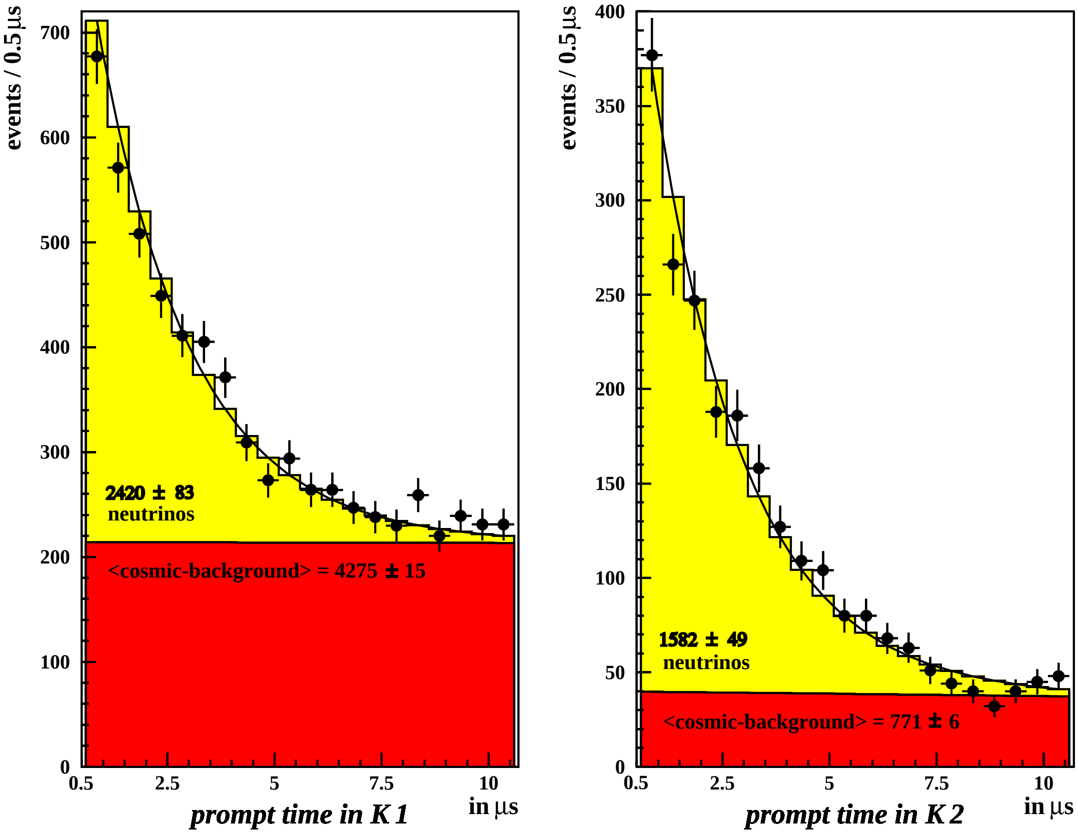

Figure 3.8: Time distribution of single-events in KARMEN1 (K1) before the upgrade and KARMEN2 (K2) afterwards. The portion of cosmic background is drawn-in for each (according to expectation from pre-beam).

χ^2 -Fit

The inclusive neutrino-nucleus-reactions ^{12}C (ν , ν') ^{12}C* , ^{12}C (ν_e , e$^-$) ^{12}N* and ^{56}Fe (ν_e ,-e$^-$) X , which are to be determined, can be best distinguished by their visible energy spectrum. Hence, the unknown cross sections will be fitted as free parameters in a χ^2 -method applied to the binned energy spectrum from 10 MeV to 50 MeV. For this, the known values are fixed to their expectation value and the errors are incorporated for every measured point of the spectrum. Furthermore, the cosmic background is subtracted according to the expectation from pre-beam.

A maximum likelihood method has not been chosen with respect to computing-time, given the size of sample and the number of free parameters.

The neutrino to background ratio has improved from approximately 1 : 2 in K1 to approximately 2 : 1 in K2. Therefore, most of the unknown cross sections for the inclusive neutrino-nucleus-reactions are derived only from the K2 data (9425 C of the entire 18547 C), because a global analysis (K1 + K2) would increase the statistical error for the reaction ^{56}Fe (ν_e , e$^-$) X and require non-negligible corrections for the reaction

$^{12}\mathrm{C}\,(\,\nu_e\,,\mathrm{e}^-\,)\,^{12}\mathrm{N}^*$ in K1, due to the number of events causing the time-anomaly (*see Chapter* 5.2.4). The very characteristic peak structure in the visible energy of the NC-reaction $^{12}\mathrm{C}\,(\,\nu\,,\nu'\,)\,^{12}\mathrm{C}^*$, gives rise to a further improvement solely for this reaction by combining the fit-results from K2 with K1.

Input Parameters for the Fit in K2:

- cosmic background being precisely measurable:
  $\langle N_{cos}\rangle^{K2} = (770.9 \pm 6.2)$ single-events
  (visible energy spectrum of cosmic background, being displayed in *Fig.* 3.5, is subtracted according to expectation from pre-beam – the size of the error-bars does still reflect the energy spectrum)
- ν-e^--scattering being analytically calculable (NC: $\bar{\nu}_\mu$, ν_e + CC: ν_e):
  $\langle\sigma(\mathrm{e}^-\,(\,\nu\,,\,\nu'\,)\,\mathrm{e}^{-\prime})\rangle = (0.347 \pm 0.002)\cdot 10^{-42} cm^2$ [Ebe92]
  (visible backscattering spectrum decreases strongly with increasing energy.)
- sequential CC-reaction $^{12}\mathrm{C}\,(\,\nu_e\,,\mathrm{e}^-\,)\,^{12}\mathrm{N}_{\mathrm{g.s.}}$ being measured almost free of background
  $\langle\sigma(^{12}\mathrm{C}\,(\,\nu_e\,,\mathrm{e}^-\,)\,^{12}\mathrm{N}_{\mathrm{g.s.}})\rangle^{K2} = (9.1 \pm 0.5)\cdot 10^{-42} cm^2$
  (visible energy spectrum of electrons reflects roughly the ν_e-energy from μ^+-decay at rest. $E_{max} = 52.8MeV - 17.3MeV \approx 36MeV$)
- inclusive CC-reaction $^{13}\mathrm{C}\,(\,\nu_e\,,\mathrm{e}^-\,)\,^{13}\mathrm{N}$ being measured in an appropriate window-method
  $\langle\sigma(^{13}\mathrm{C}\,(\,\nu_e\,,\mathrm{e}^-\,)\,^{13}\mathrm{N})\rangle^{K2} = (50 \pm 25)\cdot 10^{-42} cm^2$
  (visible energy spectrum of electrons reflects roughly the ν_e-energy from μ^+-decay at rest. $E_{max} = 52.8MeV - 2.2MeV \approx 51MeV$)

Free Parameters for the Fit in K2:

- cross section for the NC-reaction $^{12}\mathrm{C}\,(\,\nu\,,\nu'\,)\,^{12}\mathrm{C}^*(\,1^+\,,1\,;15.11\text{ MeV}\,)$
  with $\nu = \bar{\nu}_\mu\,,\nu_e$
  (visible energy spectrum of γ-rays consists of a peak around 15 MeV)
- cross section for the inclusive CC-reaction $^{12}\mathrm{C}\,(\,\nu_e\,,\mathrm{e}^-\,)\,^{12}\mathrm{N}^*$
  (visible energy spectrum of electrons reflects roughly the ν_e-energy from μ^+-decay at rest, like for the exclusive CC-reaction but with 2MeV quenching loss per average. $E_{max} = 52.8MeV - 17.3MeV - E_{quench} \approx 34MeV$)
- cross section for the inclusive CC-reaction $^{56}\mathrm{Fe}\,(\,\nu_e\,,\mathrm{e}^-\,)\,\mathrm{X}$
  (visible energy spectrum of the Bremsstrahlung γ-rays decreases strongly with increasing energy. $E_{max} = 52.8MeV - 1.5MeV \approx 51MeV$)

Contributions from other neutrino-nucleus-reactions are negligible (like e.g. the NC-reaction $^{13}\mathrm{C}\,(\,\nu\,,\nu'\,)\,^{13}\mathrm{C}^*$, where the excited 15 MeV level decays primarily via α- or neutron-emission and only 0.4% via γ-emission).

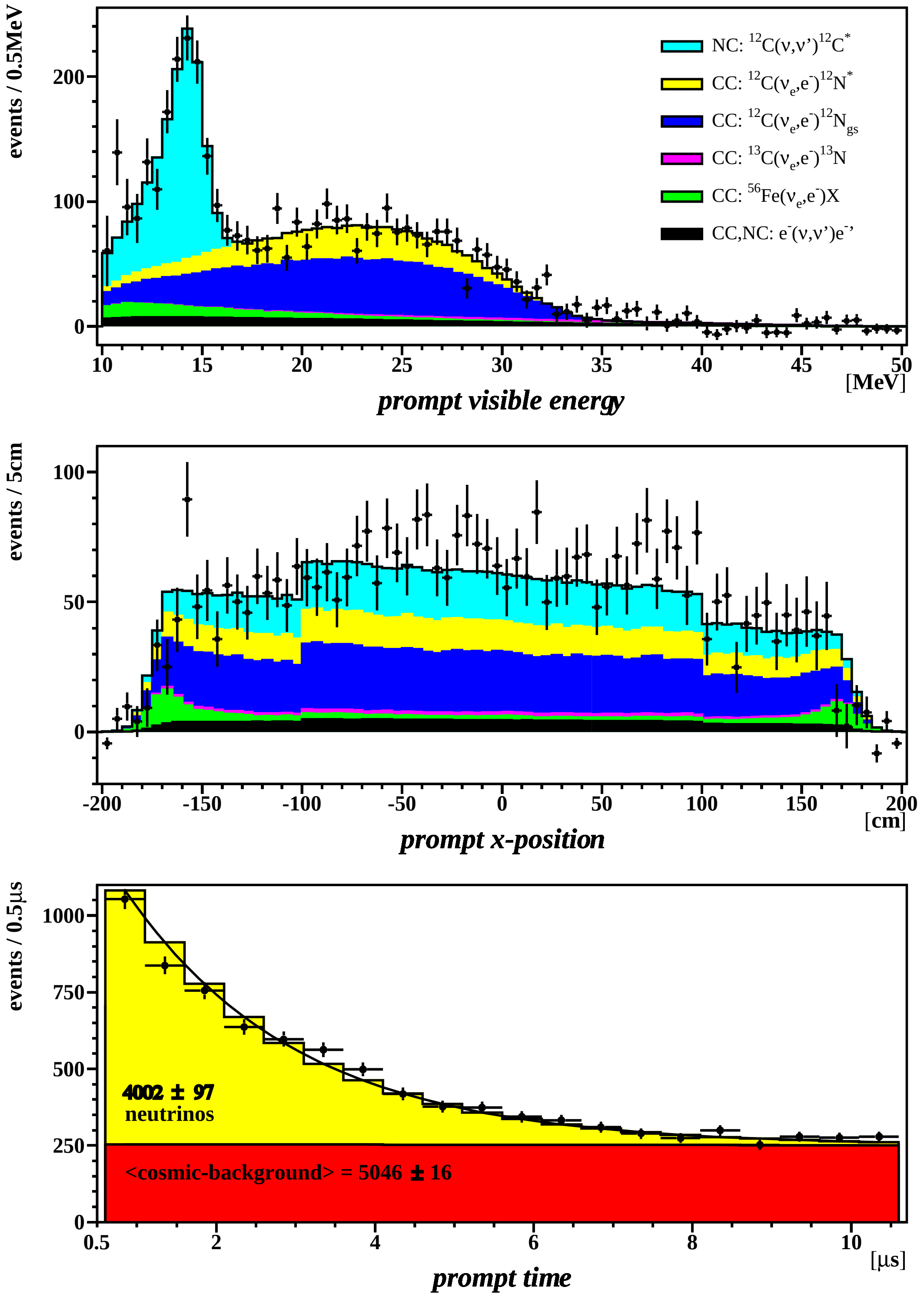

Figure 3.9: In KARMEN (K1 + K2) measured energy-, spatial- and time distribution of single-events. The portion of cosmic background is already subtracted in the energy- and spatial spectrum (according to the expectation from pre-beam). Plotted into the measured energy- and spatial spectrum are the expected portions for each single-event reaction derived from the combined analysis and MC-simulations (solid line for overall expectation).

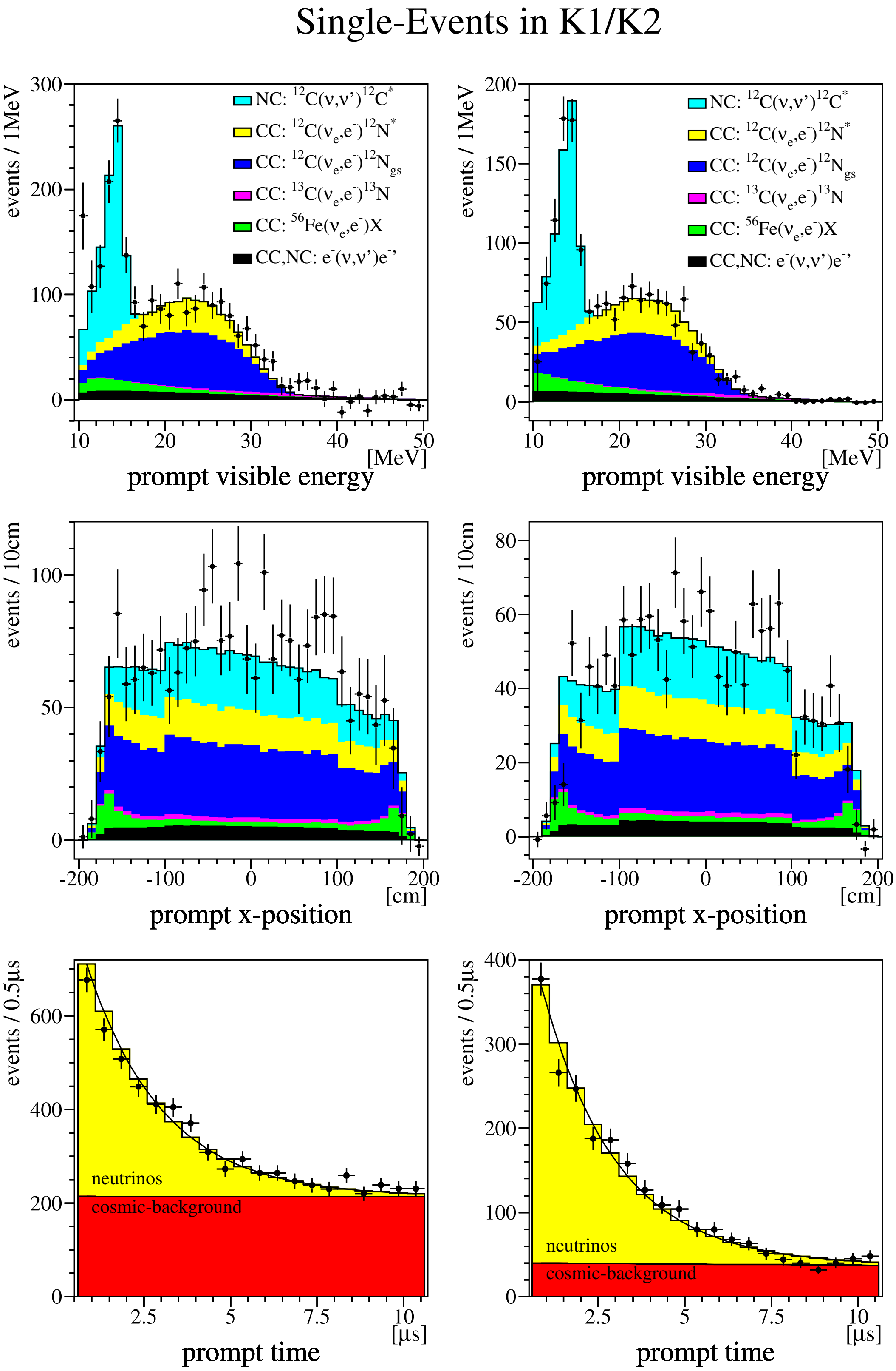

Figure 3.10: Measured energy-, spatial- and time distributions of single-events in KARMEN1 (left) and KARMEN2 (right). The portion of cosmic background is already subtracted in the energy- and spatial spectra (according to the corresponding expectation from pre-beam). Plotted into the measured energy- and spatial spectra are the expected portions for each single-event reaction derived from the combined analysis and MC-simulations (solid line for overall expectation).

		K1 [%]	K2 [%]
prompt time efficiency	$\epsilon_{t_{pr},\tau_\mu}$	84.37	84.37
stack efficiency for pr. event ($\tau_\mu = 2.2\,\mu$s weighted)	$\epsilon_{stack,\,pr,\,\tau_\mu}$	91.19	69.12
SMU-efficiency	ϵ_{SMU}	98.30	98.34
protons-per-pulse efficiency ($PPP > 60$)	ϵ_{PPP}	99.62	100.00
absolute ν-flux	Φ_ν	$2.52 \cdot 10^{21}$	$2.71 \cdot 10^{21}$

Table 3.7: Measured values of the efficiencies for the detection of prompt single-events from inclusive CC- and NC-reactions in KARMEN1 and KARMEN2. The absolute ν-flux for K1 and for K2 is given as well. Apart from the MC-efficiency, which is not listed above, any other value for the efficiency can be determined precisely from the recorded data in KARMEN. The different time dependence for each measured efficiency is illustrated in *Appendix* D. The stack efficiency for the prompt event needs to be weighted additionally with an exponential curve according to the lifetime of the muons ($\tau_\mu = 2.2\,\mu$s), especially since K2 (intelligible efficiency-dip in the prompt time window, due to longer dead-times and a higher rate of events).

Reaction		N	$N_{target}[10^{30}]$	$\epsilon_{overall}[\%]$
$^{12}\mathrm{C}\,(\nu\,,\nu')\,^{12}\mathrm{C}^*$	*K1*	604.2 ± 20.9	2.54	36.2
$^{12}\mathrm{C}\,(\nu\,,\nu')\,^{12}\mathrm{C}^*$	*K2*	451.7 ± 34.7	2.54	26.0
$^{12}\mathrm{C}\,(\nu_e\,,\mathrm{e}^-)\,^{12}\mathrm{N}_{\mathrm{g.s.}}$	*K1*	$\langle 870.2 \pm 40.0\rangle$	2.54	54.7
$^{12}\mathrm{C}\,(\nu_e\,,\mathrm{e}^-)\,^{12}\mathrm{N}_{\mathrm{g.s.}}$	*K2*	$\langle 585.6 \pm 31.6\rangle$	2.54	36.9
$^{12}\mathrm{C}\,(\nu_e\,,\mathrm{e}^-)\,^{12}\mathrm{N}^*$	*K1*	$\langle 430.7 \pm 52.5\rangle$	2.54	55.5
$^{12}\mathrm{C}\,(\nu_e\,,\mathrm{e}^-)\,^{12}\mathrm{N}^*$	*K2*	313.2 ± 38.2	2.54	37.3
$^{13}\mathrm{C}\,(\nu_e\,,\mathrm{e}^-)\,^{13}\mathrm{N}$	*K1*	$\langle 49.7 \pm 24.9\rangle$	0.0282	55.5
$^{13}\mathrm{C}\,(\nu_e\,,\mathrm{e}^-)\,^{13}\mathrm{N}$	*K2*	$\langle 35.1 \pm 17.6\rangle$	0.0282	36.2
$^{56}\mathrm{Fe}\,(\nu_e\,,\mathrm{e}^-)\,\mathrm{X}$	*K1*	$\langle 120.4 \pm 74.8\rangle$	2.34	0.37
$^{56}\mathrm{Fe}\,(\nu_e\,,\mathrm{e}^-)\,\mathrm{X}$	*K2*	88.7 ± 55.1	2.34	0.25
$\mathrm{e}^-\,(\nu\,,\nu')\,\mathrm{e}^{-\prime}$	*K1*	$\langle 158.6 \pm 1.0\rangle$	20.2	35.7
$\mathrm{e}^-\,(\nu\,,\nu')\,\mathrm{e}^{-\prime}$	*K2*	$\langle 117.4 \pm 0.7\rangle$	20.2	24.4

Table 3.8: Fitted (or $\langle$expected$\rangle$) number of events, effective number of target-nuclei and overall detection efficiency for either of the single-event reactions in K1 and K2.

The overall detection efficiencies $\epsilon^{K1}_{overall}$ and $\epsilon^{K2}_{overall}$ for either of the single-event reactions in K1 and K2, respectively, are given by:

$$\begin{aligned}
\epsilon^{K1}_{overall} &= \epsilon^{K1}_{MC} \cdot \epsilon_{t_{pr},\,\tau_\mu} \cdot \epsilon^{K1}_{stack,\,pr,\,\tau_\mu} \cdot \epsilon^{K1}_{SMU} \cdot \epsilon^{K1}_{PPP} \\
\epsilon^{K2}_{overall} &= \epsilon^{K2}_{MC} \cdot \epsilon_{t_{pr},\,\tau_\mu} \cdot \epsilon^{K2}_{stack,\,pr,\,\tau_\mu} \cdot \epsilon^{K2}_{SMU}
\end{aligned}$$

With the measured efficiency values listed in *Table* 3.7 and the simulated MC-efficiency for each reaction in K1 and K2, the overall detection efficiencies $\epsilon^{K1}_{overall}$ and $\epsilon^{K2}_{overall}$ can be calculated separately for every neutrino-induced reaction (*see Table* 3.8). According to *Eq.* 3.5, the number of single-events from each reaction in K1 and K2 is then always given by a) the corresponding effective number of target-nuclei, b) the absolute ν-flux in K1 ($\Phi^{K1}_{\nu} = 2.52 \cdot 10^{21}$) and K2 ($\Phi^{K2}_{\nu} = 2.71 \cdot 10^{21}$), c) the just calculated corresponding overall detection efficiency in K1 and K2, d) the inverse effective scaled area, as well as e) the corresponding cross section value, which is averaged over the appropriate ν-energy spectrum. *Table* 3.8 lists all expected or fitted numbers of single-events for the neutrino-induced reactions in K1 and K2, respectively.

Due to limited statistics, it is necessary to use a bin-width of 2 MeV for the visible energy spectrum, in order to derive an unbiased χ^2-fit. The merit of the fit is checked by simulating and analyzing 1000 KARMEN-experiments. Thus, the statistical errors of the fitted parameters are determined. *Fig.* 3.11 shows the result of the χ^2-fit to the visible energy spectrum in K2. The fitted energy spectrum (solid line) is well in agreement with the measured points and the corresponding errors ($\chi^2/ndf = 1.3$). *Table* 3.8 lists the fitted numbers of single-events for either of the determined neutrino-nucleus-reactions. The

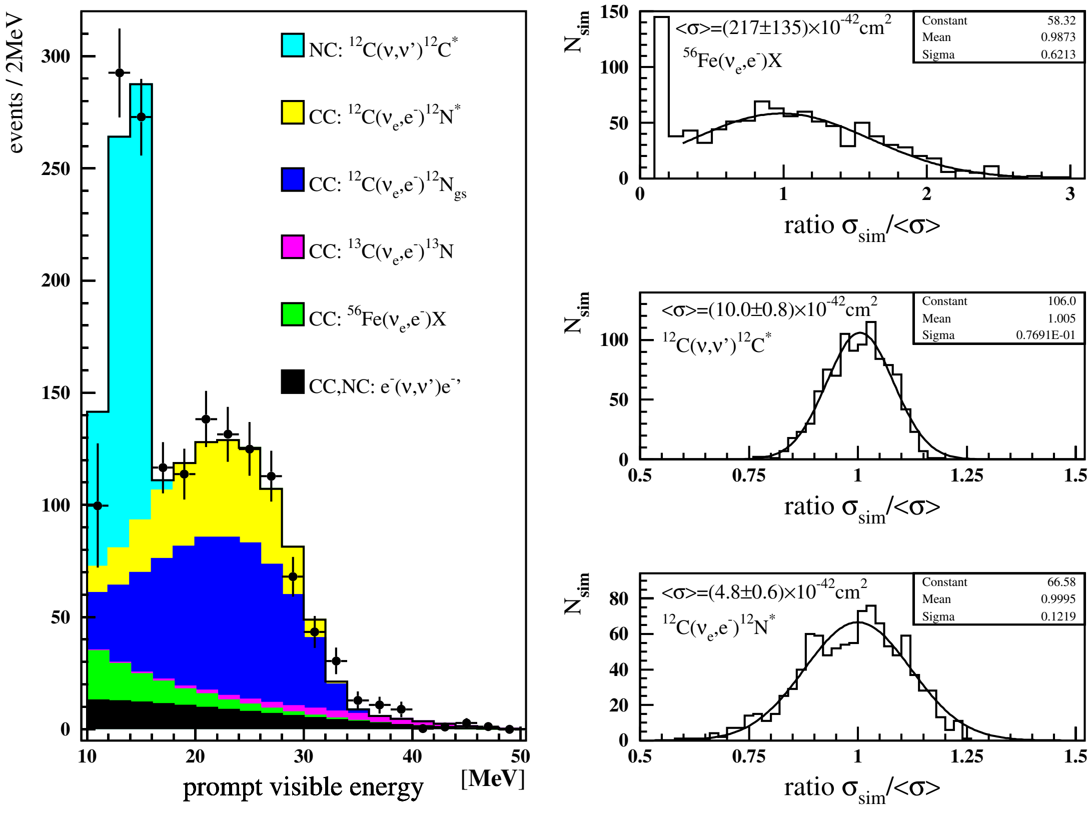

Figure 3.11: Via a χ^2-method from the single-events in KARMEN2 determined neutrino cross sections. On the left: The fitted energy spectrum with the cosmic background being subtracted. On the right: The distributions of fit-results for the varied cross sections in 1000 simulated KARMEN2-experiments.

distributions of the fit-results for 1000 simulated K2-experiments are Gaussian-shaped for the varied cross sections and do not possess a bias ($\overline{\sigma}_{fit} = \sigma_{input}$).

The number of cosmic induced single-events in K1 is more than five times larger than in K2. An analogous χ^2-fit to the visible energy spectrum in K1 does not converge with three free parameters. The visible energy spectrum of the cosmic background, which is reflected in the errors of the measured points, can be hardly distinguished from Bremsstrahlung γ-rays caused by the inclusive CC-reaction $^{56}\mathrm{Fe}\,(\,\nu_e\,,\mathrm{e}^-\,)\,\mathrm{X}$. Therefore, the fit-result for the cross section $\langle\sigma(^{56}\mathrm{Fe}\,(\,\nu_e\,,\mathrm{e}^-\,)\,\mathrm{X})\rangle^{K2}$ from K2 is utilized as input parameter for the fit in K1. Moreover, the cross section $\langle\sigma(^{12}\mathrm{C}\,(\,\nu_e\,,\mathrm{e}^-\,)\,^{12}\mathrm{N}_{\mathrm{g.s.}})\rangle^{K1} = (9.9 \pm 0.5)\cdot 10^{-42} cm^2$ for the sequential CC-reaction $^{12}\mathrm{C}\,(\,\nu_e\,,\mathrm{e}^-\,)\,^{12}\mathrm{N}_{\mathrm{g.s.}}$, which has been measured almost free of background in K1, is chosen as input parameter for the fit in K1. *Fig.* 3.12 shows the result of the χ^2-fit to the visible energy spectrum in K1. The fitted energy spectrum (solid line) is in agreement with the measured points and the corresponding errors ($\chi^2/ndf = 1.6$). *Table* 3.8 lists the determined numbers of single-events for either of the neutrino-induced reactions. The distributions of the fit-results for 1000 simulated K1-experiments are also Gaussian-shaped for the varied cross sections and do not possess a bias.

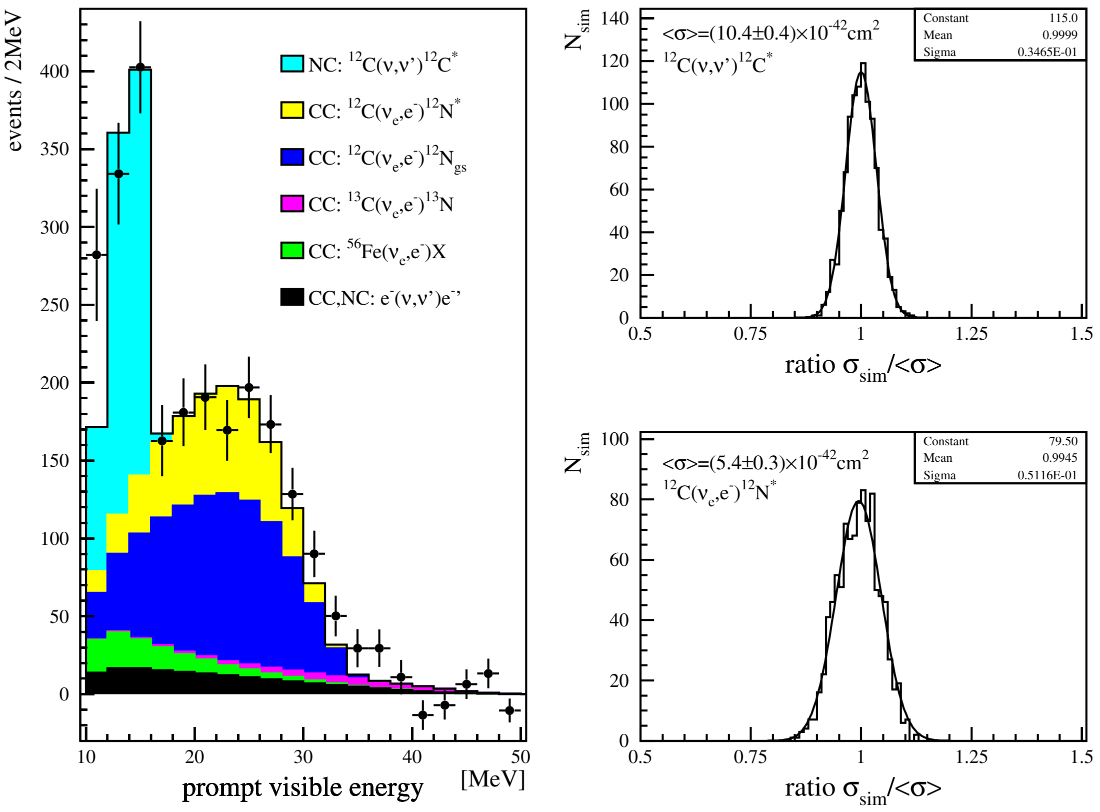

Figure 3.12: Via a χ^2-method from the single-events in KARMEN1 derived neutrino cross sections. On the left: The fitted energy spectrum with the cosmic background being subtracted. On the right: The distributions of fit-results for the varied cross sections in 1000 simulated KARMEN1-experiments.

Fig. 3.13 demonstrates that finer binned energy spectra for the single-events in K1 and K2 are in excellent agreement (within the errors) with the drawn-in final fit-results from rougher binning. This is also the case for the energy-, spatial- and time distribution of all single-events in KARMEN, being displayed in *Fig.* 3.9. The spatial distribution possesses the expected $1/(distance)^2$-dependance in each of the three regions (separation due to the rejection of defective modules in the outer 76.5 cm). The time distribution reflects clearly the sum of the almost flat cosmic background expectation and the expected exponential function of the neutrinos according to the lifetime of muons ($\tau = 2.2\,\mu$s).

By combining the results from the sequential detection of $^{12}\mathrm{C}\,(\,\nu_e\,,\mathrm{e}^-\,)\,^{12}\mathrm{N}_{\mathrm{g.s.}}$ and the result from the window-method for $^{13}\mathrm{C}\,(\,\nu_e\,,\mathrm{e}^-\,)\,^{13}\mathrm{N}$ with the χ^2-method for the single-events, no theoretical calculation for a neutrino-nucleus cross section was needed and all measurements were performed consistently. Thus, it was feasible to measure precisely all neutrino-nucleus-reactions, which are observable in KARMEN, with neutrinos from μ^+-decays at rest in the energy regime of supernovae. In the following, the results from the χ^2-method for the inclusive neutrino-nucleus-reactions $^{12}\mathrm{C}\,(\,\nu\,,\nu'\,)\,^{12}\mathrm{C}^*$, $^{12}\mathrm{C}\,(\,\nu_e\,,\mathrm{e}^-\,)\,^{12}\mathrm{N}^*$

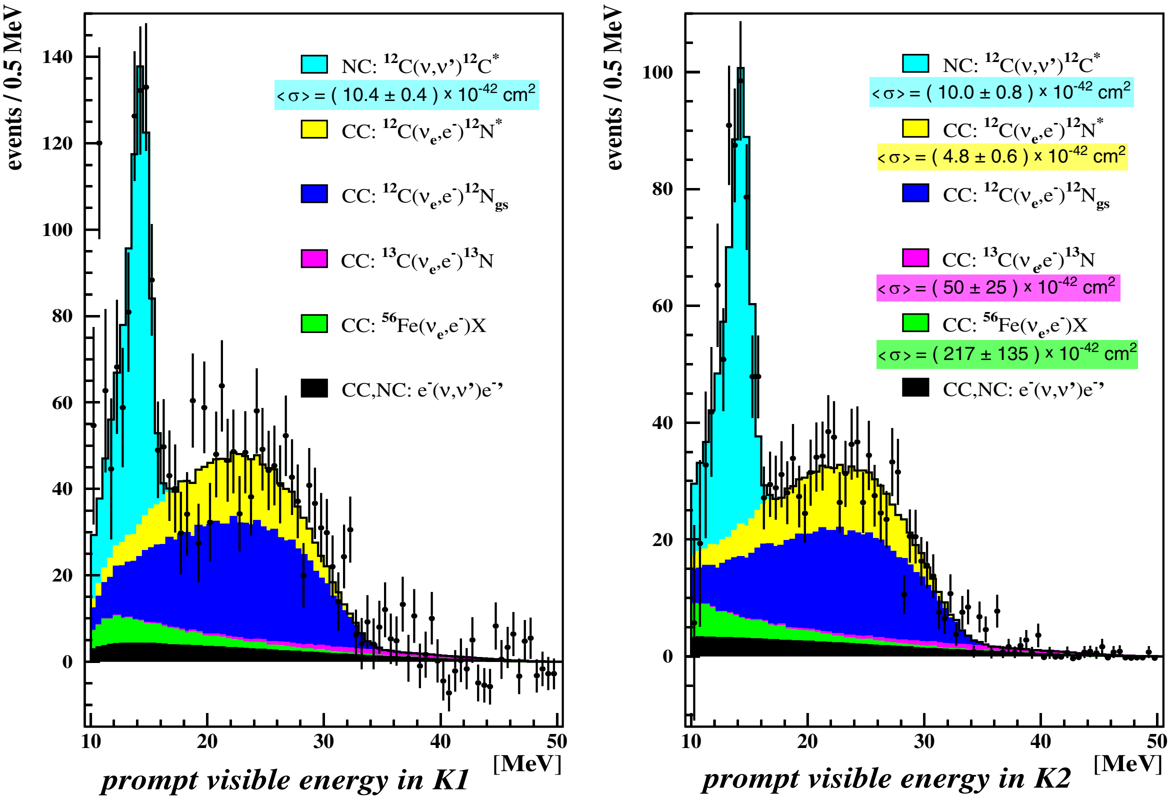

Figure 3.13: Measured visible energy spectra of single-events in KARMEN1 (K1) before the upgrade and KARMEN2 (K2) afterwards. The portion of cosmic background is already subtracted in the energy spectra (according to the corresponding expectation from pre-beam). Also drawn-in are either the fitted or the expected portions for each single-event reaction in accordance with the fitted cross section values and the MC-simulations (solid line for overall fit). From each spectrum derived final cross section values are given as well.

and ${}^{56}\mathrm{Fe}\,(\,\nu_e\,,\mathrm{e}^-\,)\,\mathrm{X}$ will be presented and the obtained value for the flux-independent ratio $R = \langle\sigma^{NC}\rangle/\langle\sigma^{CC}_{gs}\rangle$ will be discussed.

3.2.2.1 Inclusive NC–Reaction ${}^{12}\mathrm{C}\,(\,\nu\,,\nu'\,)\,{}^{12}\mathrm{C}^*$

With KARMEN it was possible to observe the neutrino-induced NC-reaction ${}^{12}\mathrm{C}\,(\,\nu\,,\nu'\,)\,{}^{12}\mathrm{C}^*$ $(\,1^+\,,1\,;15.11\ \mathrm{MeV}\,)$ for the first time in the world [Ebe92]. The isovector-axialvector excitation of the 15.11 MeV-level of ${}^{12}\mathrm{C}$, with $\bar{\nu}_\mu$ and ν_e from μ^+-decays at rest, can be detected via the following inclusive single-event reaction (*see also Fig.* 3.1):

$$\nu \;+\; {}^{12}\mathrm{C} \;\longrightarrow\; {}^{12}\mathrm{C}^*\;(\,1^+\,,1\,;15.11\ \mathrm{MeV}\,) \;+\; \nu' \qquad \nu = \bar{\nu}_\mu\,,\,\nu_e$$

$$\hookrightarrow\; {}^{12}\mathrm{C}_{\mathrm{g.s.}} \;+\; \text{\textcircled{γ}}\;(\,15.11\ \mathrm{MeV}\,)$$

${}^{12}\mathrm{C}^*(\,1^+\,,1\,;15.11\ \mathrm{MeV}\,)\rightarrow$	Fraction [%]	γ-Energy [MeV]
${}^{12}\mathrm{C}_{\mathrm{g.s.}}$	88.2 (92)	15.11
${}^{12}\mathrm{C}$(4.44 MeV) → 100% γ-decay	2.2 (2.3)	10.67 4.44
${}^{12}\mathrm{C}$(7.65 MeV) → 100% α-decay	2.5 (2.6)	7.46 –
${}^{12}\mathrm{C}$(10.3 MeV) → 100% α-decay	1.5 (1.6)	4.81 –
${}^{12}\mathrm{C}$(12.71 MeV) → 2% γ-decay → 98% α-decay	1.3 (1.4)	2.40 12.71 –
${}^{8}\mathrm{Be} + \alpha$	4.1 ± 0.9	–

Table 3.9: Decay channels of the 15.11 MeV-level of ${}^{12}\mathrm{C}$ [Ajz90], [Wol95]. The fraction given in brackets equals the branching ratio referring to the pure γ-transitions, whereas the first number equals the branching ratio referring to all decays.

In 92% of all observable decays of ${}^{12}\mathrm{C}^*(\,1^+\,,1\,;15.11\ \mathrm{MeV}\,)$, a single γ results with an energy of 15.11 MeV. *Table* 3.9 lists all branching ratios. Only decays with γ production can be tagged by the detector, because α-particles with energies in the few MeV-range undergo strong quenching-effects in the organic scintillator and thus cannot be observed. With respect to the calorimetric properties of the detector, the decays of the 15.11 MeV-level of ${}^{12}\mathrm{C}$ produce prompt visible energies with a peak at 14 MeV and a tail towards lower energies, due to the decays with α-production (*compare Fig.* 3.9). The isoscalar-axialvector NC-excitation of the 12.71 MeV-level $(\,1^+\,,0\,)$ of ${}^{12}\mathrm{C}$ is forbidden by the standard model. Nevertheless, with a small fraction of 0.5% this forbidden transition can still occur, due to a small isovector admixture of 6% [Don79]. But the 12.71 MeV-level decays in 98% of all cases into an α and ${}^{8}\mathrm{Be}$, which bursts again into two α's. Therefore, the forbidden

NC-excitation of the 12.71 MeV-level $(1^+, 0)$ of ^{12}C cannot be observed in KARMEN. Moreover, $(4 \pm 1)\,\%$ of the permitted NC-excitations into the 15.11 MeV-level $(1^+, 1)$ of ^{12}C result in three α's as well and thus are excluded from observation either.

As already demonstrated, the very characteristic peak structure in the visible energy of the NC-reaction $^{12}\mathrm{C}\,(\nu, \nu')\,^{12}\mathrm{C}^*$, makes it feasible to derive the value of the cross section from a χ^2-fit to the visible energy, both for K1 and K2 (*see Section* 3.2.2). Moreover, the events causing the time-anomaly can be separated well enough for this reaction and are therefore negligible, due to the applied χ^2-method (*see Chapter* 5.2.4).
The overall detection efficiency for the NC-reaction $^{12}\mathrm{C}\,(\nu, \nu')\,^{12}\mathrm{C}^*$ comes out as $\epsilon^{K1}_{overall} = 36.2\%$ for K1 and $\epsilon^{K2}_{overall} = 26.0\%$ for K2, respectively (*see Table* 3.8). The absolute ν-flux amounts to $\Phi^{K1}_\nu = 2.52 \cdot 10^{21}$ for K1 and $\Phi^{K2}_\nu = 2.71 \cdot 10^{21}$ for K2, respectively. Hence, with the fitted number of detected reactions $N^{K1} = 604.2$ in K1 and $N^{K2} = 451.7$ in K2, the following total cross section values, averaged over the $\bar{\nu}_\mu$- and ν_e-energy spectrum, are derived for the NC-reaction $^{12}\mathrm{C}\,(\nu, \nu')\,^{12}\mathrm{C}^*$ (*see Eq.* 3.5 *and Fig.* 3.11 + 3.12):

$$\langle\sigma(^{12}\mathrm{C}\,(\nu, \nu')\,^{12}\mathrm{C}^*)\rangle^{K1} = (10.4 \pm 0.4(stat.) \pm 0.8(syst.)) \cdot 10^{-42} cm^2$$

$$\langle\sigma(^{12}\mathrm{C}\,(\nu, \nu')\,^{12}\mathrm{C}^*)\rangle^{K2} = (10.0 \pm 0.8(stat.) \pm 0.8(syst.)) \cdot 10^{-42} cm^2$$

A further improvement is achieved for this NC-reaction by combining the results from K2 and K1. In order to obtain the global KARMEN cross section $\langle\sigma\rangle^{K1+K2}$, the values for the cross section $\langle\sigma\rangle^{K1}$ in K1 and $\langle\sigma\rangle^{K2}$ in K2 are added flux- and efficiency-weighted (*see Eq.* 3.6). Thus, the following global (K1+K2) total cross section value, averaged over the $\bar{\nu}_\mu$- and ν_e-energy spectrum, is determined for the NC-reaction $^{12}\mathrm{C}\,(\nu, \nu')\,^{12}\mathrm{C}^*(1^+, 1;$ 15.11 MeV$)$ in KARMEN (corresponding to a fitted number of $N = 1055.9$ detected reactions, an absolute ν-flux of $\Phi_\nu = 5.23 \cdot 10^{21}$ and an effective overall detection efficiency of $\langle\epsilon_{overall}\rangle = 31.7\%$):

$$\boxed{\langle\sigma(^{12}\mathrm{C}\,(\nu, \nu')\,^{12}\mathrm{C}^*)\rangle = (10.2 \pm 0.4(stat.) \pm 0.8(syst.)) \cdot 10^{-42} cm^2}$$

The systematic error[4] of the cross section is dominated by the 7% uncertainty of the absolute ν-flux from ISIS (*see Table* 3.3). The value of the cross section, measured by KARMEN, is well in agreement with all theoretical EPT, SM and (C)RPA calculations ($9.8 \ldots 11.9 \cdot 10^{-42} cm^2$). There is no particular type of model to be preferred (*see Table* 3.10).
The cross section value, measured in the framework of this thesis, is roughly 7% smaller than the former K1 value of $(10.9 \pm 0.7(stat.)) \cdot 10^{-42} cm^2$ [Sch96] (independently of the errors and the data set). This is mainly due to the formerly applied fiducial volume, which had caused extra systematics for the MC-efficiency (*see Table* 3.13).

---

[4] An additional systematic error arises from the 0.9% uncertainty of the branching ratio of the $^{12}\mathrm{C}^*(1^+, 1; 15.11$ MeV$)$ decay into an α and ^{8}Be, resulting in three α's and thus being excluded from observation (*see Table* 3.9).

Author		*Type of Model*	$\langle\sigma({}^{12}\text{C}\,(\,\nu\,,\nu'\,)\,{}^{12}\text{C}^*)\rangle\ [10^{-42}\,cm^2]$
Kolbe	[Kol99]	CRPA	10.5
Vogel	[Vog96]	SM	9.8
Parthasarathy	[Par94]	SM	9.9
Donnelly	[Don91]	SM	11.9
Fukugita	[Fuk88]	EPT	9.8(7)
Mintz	[Min93]	EPT	9.8

Table 3.10: Comparison of theoretical calculations of the cross section $\langle\sigma\rangle$ for the NC-reaction ${}^{12}\text{C}\,(\,\nu\,,\nu'\,)\,{}^{12}\text{C}^*(\,1^+\,,1\,;15.11\text{ MeV}\,)$.

3.2.2.2 Inclusive CC–Reaction ${}^{12}\text{C}\,(\,\nu_e\,,\text{e}^-\,)\,{}^{12}\text{N}^*$

The ν_e-induced CC-reaction ${}^{12}\text{C}\,(\,\nu_e\,,\text{e}^-\,)\,{}^{12}\text{N}^*$ into the excited states of ${}^{12}\text{N}$ can be detected in KARMEN via the following inclusive single-event reaction:

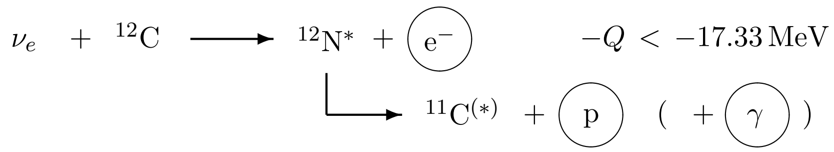

$$\nu_e \;+\; {}^{12}\text{C} \;\longrightarrow\; {}^{12}\text{N}^* \;+\; \text{e}^- \qquad\qquad -Q \;<\; -17.33\,\text{MeV}$$
$$\hookrightarrow\; {}^{11}\text{C}^{(*)} \;+\; \text{p} \quad (\;+\;\gamma\;)$$

In addition to the prompt electron from the inverse β-decay, a proton results from the transition into the particle unstable states of ${}^{12}\text{N}^*$ (occurring on the very short time scale of the strong interaction). If the proton emission leads to an excited state of ${}^{11}\text{C}$, γ-radiation is produced as well (occurring on the short time scale of the electromagnetic interaction). Consequently, the CC-reaction ${}^{12}\text{C}\,(\,\nu_e\,,\text{e}^-\,)\,{}^{12}\text{N}^*$ is inclusive in KARMEN and the proton as well as the γ-ray contribute to the prompt visible energy of the observed single-event. A sequential detection of events from subsequent decays is not feasible, due to the corresponding lifetimes and the timing of KARMEN (e.g. $\tau_{C11} = 41\,\text{min}$). The visible energy spectrum is almost the same as for the exclusive CC-reaction ${}^{12}\text{C}\,(\,\nu_e\,,\text{e}^-\,)\,{}^{12}\text{N}_{\text{g.s.}}$. It is slightly shifted towards lower energies, mainly due to the approximately 2MeV quenching loss E_{quench} for protons ($E_{max} = 52.8MeV - 17.3MeV - E_{quench} \approx 34MeV$).

The overall detection efficiency for the inclusive CC-reaction ${}^{12}\text{C}\,(\,\nu_e\,,\text{e}^-\,)\,{}^{12}\text{N}^*$ comes out as $\epsilon^{K1}_{overall} = 55.5\%$ for K1 and $\epsilon^{K2}_{overall} = 37.3\%$ for K2, respectively (*see Table* 3.8). The absolute ν-flux amounts to $\Phi^{K1}_{\nu} = 2.52 \cdot 10^{21}$ for K1 and $\Phi^{K2}_{\nu} = 2.71 \cdot 10^{21}$ for K2, respectively. Hence, with the fitted number of detected reactions $N^{K1} = 479.5$ in K1 and $N^{K2} = 313.2$ in K2, the following total cross section values, averaged over the ν_e-energy spectrum, are derived for the CC-reaction ${}^{12}\text{C}\,(\,\nu_e\,,\text{e}^-\,)\,{}^{12}\text{N}^*$ (*see Eq.* 3.5 *and Fig.* 3.11 + 3.12):

$$\langle\sigma({}^{12}\text{C}\,(\,\nu_e\,,\text{e}^-\,)\,{}^{12}\text{N}^*)\rangle^{K1} \;=\; (5.4 \pm 0.3(stat.)\,{}^{+\,0.4}_{-\,0.6}(syst.)) \cdot 10^{-42}cm^2$$

$$\langle\sigma({}^{12}\text{C}\,(\,\nu_e\,,\text{e}^-\,)\,{}^{12}\text{N}^*)\rangle^{K2} \;=\; (4.8 \pm 0.6(stat.)\,{}^{+\,0.4}_{-\,0.5}(syst.)) \cdot 10^{-42}cm^2$$

But it has to be pointed out, that the (n,γ)-events assumed to cause the time-anomaly cannot be separated well enough for this reaction, due to the applied χ^2-method (*see Chapter* 5.2.4). The visible energy spectrum of single-events from the inclusive CC-reaction $^{12}\mathrm{C}\,(\,\nu_e\,,\mathrm{e}^-\,)\,^{12}\mathrm{N}^*$ is not as unique as the very characteristic peak structure in the visible energy of the NC-reaction $^{12}\mathrm{C}\,(\,\nu\,,\nu'\,)\,^{12}\mathrm{C}^*$. Considering a worst case scenario, in which the entire (n,γ)-events are associated in the χ^2-fit solely with the inclusive CC-reaction $^{12}\mathrm{C}\,(\,\nu_e\,,\mathrm{e}^-\,)\,^{12}\mathrm{N}^*$, it has to be concluded that the reaction $^{12}\mathrm{C}\,(\,\nu_e\,,\mathrm{e}^-\,)\,^{12}\mathrm{N}^*$ cannot be evaluated reliably enough for K1. The statistical error of the cross section for $^{12}\mathrm{C}\,(\,\nu_e\,,\mathrm{e}^-\,)\,^{12}\mathrm{N}^*$ in K1 is intelligibly exceeded by the systematic error due to 125 (n,γ)-events in the worst case: 480 ± 27 events are fitted, corresponding to the value of the cross section for $^{12}\mathrm{C}\,(\,\nu_e\,,\mathrm{e}^-\,)\,^{12}\mathrm{N}^*$ in K1 of $(5.4 \pm 0.3) \cdot 10^{-42}\,cm^2$. In contrast, the number of 48 ± 20 (n,γ)-events in K2 does not exceed the order of the statistical error of the 313 ± 38 events being fitted in K2 for the reaction $^{12}\mathrm{C}\,(\,\nu_e\,,\mathrm{e}^-\,)\,^{12}\mathrm{N}^*$. Therefore, the total cross section value from K2, averaged over the ν_e-energy spectrum, is chosen for the final KARMEN result on the inclusive CC-reaction $^{12}\mathrm{C}\,(\,\nu_e\,,\mathrm{e}^-\,)\,^{12}\mathrm{N}^*$ into excited states of $^{12}\mathrm{N}$:

$$\boxed{\langle\sigma(^{12}\mathrm{C}\,(\,\nu_e\,,\mathrm{e}^-\,)\,^{12}\mathrm{N}^*)\rangle = (4.8 \pm 0.6(stat.)\,^{+0.4}_{-0.5}(syst.)) \cdot 10^{-42} cm^2}$$

The systematic error of the cross section is considerably caused by the 7% uncertainty of the absolute ν-flux from ISIS (*see Table* 3.3). In addition, the cross section would be overestimated by maximal 15% in the worst case scenario, in which the entire (n,γ)-events causing the time-anomaly are associated in the χ^2-fit solely with the inclusive CC-reaction $^{12}\mathrm{C}\,(\,\nu_e\,,\mathrm{e}^-\,)\,^{12}\mathrm{N}^*$ and neither with the reaction $^{56}\mathrm{Fe}\,(\,\nu_e\,,\mathrm{e}^-\,)\,\mathrm{X}$ nor with the cosmic background, whose energy distribution is expected to be most similar to the visible (n,γ)-energies (*see Fig.* 3.5 *and Table* 5.1). It is therefore assumed that at least half of the (n,γ)-events are not associated in the χ^2-fit with the reaction $^{12}\mathrm{C}\,(\,\nu_e\,,\mathrm{e}^-\,)\,^{12}\mathrm{N}^*$.
The value of the cross section, measured by KARMEN, is well in agreement with almost all of the theoretical SM and (C)RPA calculations ($3.7 \ldots 8.3 \cdot 10^{-42} cm^2$). There is no particular type of model to be preferred (*see Table* 3.11). EPT models are not utilized for calculating the cross section into the excited states of $^{12}\mathrm{N}$, because the necessary number of form-factors would become too large.
The KARMEN value is furthermore well in agreement with the value of $(4.3 \pm 0.4(stat.) \pm 0.6(syst.)) \cdot 10^{-42} cm^2$ measured by the LSND-experiment [Aue01]. As already pointed out, LSND possesses a correlated systematic uncertainty of the ν-flux, due to the usage of the same MC-program for the flux-calculations [Bur95].

3.2.2.3 Inclusive CC–Reaction $^{56}\mathrm{Fe}\,(\,\nu_e\,,\mathrm{e}^-\,)\,\mathrm{X}$

With KARMEN it was feasible to investigate the CC-reaction $^{56}\mathrm{Fe}\,(\,\nu_e\,,\mathrm{e}^-\,)\,\mathrm{X}$ for the first time in the world by utilizing neutrinos, which interact with iron nuclei of the steel, that closely surrounds the detector [Ruf95]. This is of special interest for astrophysics, as the mean free path-length of neutrinos, being produced with assimilable energies during the collapse and the explosion of a supernova type II, is ruled by their cross section on iron nu-

Author		*Type of Model*	$\langle\sigma({}^{12}\mathrm{C}\,(\,\nu_e\,,\mathrm{e}^-\,)\,{}^{12}\mathrm{N}^*)\rangle$ $[10^{-42}\,cm^2]$
Kolbe	[Kol99]	CRPA	5.4
Auerbach(SIII)	[Aue97]	RPA	6.4
Volpe	[Vol01]	SM	8.3
Hayes	[Hay00]	SM	4.1
Donnelly	[Don91]	SM	3.7

Table 3.11: Comparison of theoretical calculations of the cross section $\langle\sigma\rangle$ for the inclusive CC-reaction ${}^{12}\mathrm{C}\,(\,\nu_e\,,\mathrm{e}^-\,)\,{}^{12}\mathrm{N}^*$.

clei. The ν_e-induced CC-reaction ${}^{56}\mathrm{Fe}\,(\,\nu_e\,,\mathrm{e}^-\,)\,\mathrm{X}$ into excited or particle unstable states of ${}^{56}\mathrm{Co}$ can be detected in KARMEN via the following inclusive single-event reaction:

$$\nu_e \;+\; {}^{56}\mathrm{Fe} \longrightarrow \mathrm{X} \;+\; \mathrm{e}^- \qquad\qquad \mathrm{X}={}^{56}\mathrm{Co}+\gamma,\ {}^{55}\mathrm{Fe}+p,\ \ldots$$
$$\xrightarrow{+{}^{56}\mathrm{Fe}} \mathrm{e}^{-\prime} \;+\; {}^{56}\mathrm{Fe}' \;+\; \textcircled{γ}$$

In addition to the electron from the inverse β-decay, a γ, proton, neutron or α results from the transition into the excited or particle unstable states of ${}^{56}\mathrm{Co}$. The prompt electrons from inverse β-decays[5] possess energies up to approximately 51 MeV, due to the small minimal Q-value of 1.5 MeV for the CC-reaction ${}^{56}\mathrm{Fe}\,(\,\nu_e\,,\mathrm{e}^-\,)\,\mathrm{X}$. Within the massive iron shielding these electrons produce predominantly Bremsstrahlung γ-rays with energies up to roughly 51 MeV as well. It is the Bremsstrahlung γ-rays, which can pass through the remaining steel and even penetrate the outer regions of the central detector, without being tagged by the system of anti-counters. These rare incidents, which can produce a single-event in the central detector, occur with a small probability of roughly 0.5%. Nevertheless, it is feasible to measure this inclusive CC-reaction ${}^{56}\mathrm{Fe}\,(\,\nu_e\,,\mathrm{e}^-\,)\,\mathrm{X}$ via the observed single-events in KARMEN (due to the value of the ν_e-induced cross section on ${}^{56}\mathrm{Fe}$, which is expected to be more than an order of magnitude larger than the cross sections on ${}^{12}\mathrm{C}$). The prompt visible energy spectrum of the Bremsstrahlung γ-rays declines strongly with increasing energy. A sequential detection of events from e.g. subsequent decays of ${}^{56}\mathrm{Co}$ is not feasible with respect to the corresponding energy and lifetime ($\tau_{Co^{56}} = 113.6\,\mathrm{d}$).

The number of cosmic induced single-events in K1 is more than five times larger than in K2. As already discussed for the χ^2-method, the visible energy spectrum of the cosmic background in K1 can be hardly distinguished in the χ^2-fit from the Bremsstrahlung γ-rays caused by the inclusive CC-reaction ${}^{56}\mathrm{Fe}\,(\,\nu_e\,,\mathrm{e}^-\,)\,\mathrm{X}$ (*compare Fig.* 3.5 *and* 3.9). In addition, the (n,γ)-events assumed to cause the time-anomaly cannot be separated well enough for this reaction either (*see Chapter* 5.2.4). Considering again a worst case scenario, in which the entire (n,γ)-events are associated in the χ^2-fit solely with the inclusive CC-reaction ${}^{56}\mathrm{Fe}\,(\,\nu_e\,,\mathrm{e}^-\,)\,\mathrm{X}$, it has to be concluded again that the reaction ${}^{56}\mathrm{Fe}\,(\,\nu_e\,,\mathrm{e}^-\,)\,\mathrm{X}$ cannot be evaluated reliably enough for K1. There are only 120 events expected in K1 from ${}^{56}\mathrm{Fe}\,(\,\nu_e\,,\mathrm{e}^-\,)\,\mathrm{X}$. This is less than the 125 (n,γ)-events in K1. In contrast, the number of 48 ± 20 (n,γ)-events in K2 does not exceed the order of the statistical error of the

---

[5] In [Ruf95] a wrong correlation of angles was utilized for this inelastic scattering process ${}^{56}\mathrm{Fe}\,(\,\nu_e\,,\mathrm{e}^-\,)\,\mathrm{X}$.

89 ± 55 fitted events for the reaction $^{56}\mathrm{Fe}\,(\,\nu_e\,,\mathrm{e}^-\,)\,\mathrm{X}$ in K2. Therefore, the fit-result from K2 is chosen for the final KARMEN result on the inclusive CC-reaction $^{56}\mathrm{Fe}\,(\,\nu_e\,,\mathrm{e}^-\,)\,\mathrm{X}$.

The effective number of iron target-nuclei amounts to $N_{target}^{Fe56} = 2.34 \cdot 10^{30}$. For the iron the inverse effective scaled area ($\Omega_{eff} = 1/[4\pi(17.68m)^2]$) is slightly larger than for the detector. The overall detection efficiency for the inclusive CC-reaction $^{56}\mathrm{Fe}\,(\,\nu_e\,,\mathrm{e}^-\,)\,\mathrm{X}$ comes out as $\epsilon_{overall}^{K2} = 0.25\%$ for K2 (*see Table* 3.8) and the absolute ν-flux in K2 amounts to $\Phi_\nu^{K2} = 2.71 \cdot 10^{21}$. Hence, with the fitted number of detected reactions $N^{K2} = 88.7$ in KARMEN2, the following total cross section value, averaged over the ν_e-energy spectrum, is derived for the inclusive CC-reaction $^{56}\mathrm{Fe}\,(\,\nu_e\,,\mathrm{e}^-\,)\,\mathrm{X}$ (*see Eq.* 3.5 *and Fig.* 3.11):

$$\boxed{\langle\sigma(^{56}\mathrm{Fe}\,(\,\nu_e\,,\mathrm{e}^-\,)\,\mathrm{X})\rangle = (217 \pm 135(stat.)\,^{+\,27}_{-\,65}(syst.)) \cdot 10^{-42}cm^2}$$

Consequently, events from this neutrino-nucleus-reaction on iron were observed at $90\%CL$ in KARMEN2 (disregarding the systematic error). With the derived value for the ν cross section σ on iron nuclei, the mean free path-length l of neutrinos inside the core of a type II supernova predecessor star amounts to 40 km during the collapse ($l = m_{Fe}/\rho\,\sigma$ with $m_{Fe} \approx A \cdot m_N \approx 9.3 \cdot 10^{-23}g$ and a core-matter density ρ of roughly $10^{11}g/cm^3$ [Sch97]). Right at the beginning of the explosion, the mean free path-length l of neutrinos inside the core is then reduced to just 20 m (core-matter density $\rho \approx 2.5 \cdot 10^{14}g/cm^3$). The opacity κ in core-matter is thereby defined as $\kappa = 1/(l \cdot \rho) = \sigma/m_{Fe}$.

The value of the cross section, measured by KARMEN, is well in agreement with all of the theoretical SM, (C)RPA and EPT calculations ($214 \,\ldots\, 380 \cdot 10^{-42}cm^2$). There is no particular type of model to be preferred (*see Table* 3.12).
As for previous reactions the systematic error of the cross section is considerably caused by the 7% uncertainty of the absolute ν-flux from ISIS (*see Table* 3.3). Because some of the Bremsstrahlung γ's being detected in the very outer regions of the detector, an extra uncertainty of 10% arises from the MC-simulation.
It has to be pointed out again, that the cross section would be overestimated by maximal 54% in the worst case scenario, in which the entire (n,γ)-events causing the time-anomaly are associated in the χ^2-fit solely with the inclusive CC-reaction $^{56}\mathrm{Fe}\,(\,\nu_e\,,\mathrm{e}^-\,)\,\mathrm{X}$ and neither with the reaction $^{12}\mathrm{C}\,(\,\nu_e\,,\mathrm{e}^-\,)\,^{12}\mathrm{N}^*$ nor with the cosmic background, whose energy distribution is expected to be most similar to the visible (n,γ)-energies (*see Fig.* 3.5 *and Table* 5.1). It is therefore assumed that at least half of the (n,γ)-events are not associated in the χ^2-fit with the reaction $^{56}\mathrm{Fe}\,(\,\nu_e\,,\mathrm{e}^-\,)\,\mathrm{X}$.

3.2.2.4 Ratio $R = \langle\sigma^{NC}\rangle/\langle\sigma_{gs}^{CC}\rangle$

The uncertainty of the ν-flux, dominating the systematic errors of the ν cross sections on carbon nuclei, can be eliminated by determining the ratio $R = \langle\sigma^{NC}\rangle/\langle\sigma_{gs}^{CC}\rangle$ of the measured ν cross sections for the inclusive neutral-current- and the sequential charged-current reaction on ^{12}C (*see Sections* 3.1 *and* 3.2.2.1). Thus, the following global (K1+K2) value,

Author		*Type of Model*	$\langle\sigma(^{56}\mathrm{Fe}\,(\,\nu_e\,,\mathrm{e}^-\,)\,\mathrm{X})\rangle$ $[10^{-42}\,cm^2]$
Kolbe	[Kol01]	CRPA	240
Bruenn	[Bru85]	SM	255
Bugaev	[Bug79]	SM	380
Mintz	[Min02]	EPT	214

Table 3.12: Comparison of theoretical calculations of the cross section $\langle\sigma\rangle$ for the inclusive CC-reaction $^{56}\mathrm{Fe}\,(\,\nu_e\,,\mathrm{e}^-\,)\,\mathrm{X}$.

averaged over the $\bar{\nu}_\mu$- and ν_e-energy spectrum, is determined for the flux-independent ratio $R = \langle\sigma(^{12}\mathrm{C}\,(\,\nu\,,\nu'\,)\,^{12}\mathrm{C}^*)\rangle\,/\,\langle\sigma(^{12}\mathrm{C}\,(\,\nu_e\,,\mathrm{e}^-\,)\,^{12}\mathrm{N}_{\mathrm{g.s.}})\rangle$ in KARMEN:

$$\boxed{R = \langle\sigma^{NC}\rangle/\langle\sigma^{CC}_{gs}\rangle = 1.07 \pm 0.06(stat.) \pm 0.01(syst.)}$$

A small systematic error remains from the 0.9% uncertainty of the branching ratio of the $^{12}\mathrm{C}^*(\,1^+\,,1\,;15.11\ \mathrm{MeV}\,)$ decay into an α and $^8\mathrm{Be}$, resulting in three α's and thus being excluded from observation (*see Table* 3.9).

The value of the ratio R, measured in the framework of this thesis, is more than 10% smaller compared to the former K1 value of $1.17 \pm 0.1(stat.)$ [Sch96]. There are two reasons for this:

a) The value of $(10.2 \pm 0.4(stat.)) \cdot 10^{-42}cm^2$ of the cross section for the NC-reaction $^{12}\mathrm{C}\,(\,\nu\,,\nu'\,)\,^{12}\mathrm{C}^*$, measured in the framework of this thesis, is roughly 7% smaller than the former K1 value of $(10.9 \pm 0.7(stat.)) \cdot 10^{-42}cm^2$ [Sch96] (independently of the errors and the data set). This is mainly due to the formerly applied fiducial volume, which had caused extra systematics for the MC-efficiency (*see Table* 3.13). In [Sch96] the fiducial volume was applied for single-events from the inclusive NC-reaction but not for sequences from the exclusive CC-reaction. This inconsistency increased artificially the ratio R by roughly 8%. If the fiducial cut is consistently applied to both reaction analyses, the ratio R remains unaffected in K1, K2 and K1+K2 (*see again Table* 3.13).

b) The K1 value of $(9.9 \pm 0.5(stat.)) \cdot 10^{-42}cm^2$ of the cross section for the exclusive CC-reaction $^{12}\mathrm{C}\,(\,\nu_e\,,\mathrm{e}^-\,)\,^{12}\mathrm{N}_{\mathrm{g.s.}}$, measured in the framework of this thesis, is roughly 5% larger than the former K1 value of $(9.4 \pm 0.4(stat.)) \cdot 10^{-42}cm^2$ [Arm98b]. The discrepancy arises mainly from a less accurate determination of various efficiencies in [Arm98b] (*see Section* 3.1).

a+b) Altogether, the former K1 value of the ratio R was systematically overestimated by approximately 13% ($\cong 2.5\sigma_{stat}$).

The final KARMEN value of $R = 1.07 \pm 0.055(stat.)$, measured in the framework of this thesis, is well in agreement with two out of five theoretical EPT, SM and (C)RPA calculations (1.07 ... 1.27 *see Table* 3.14). Hence, within the achieved experimental accuracy of 5%, the μ-e-universality of neutral and charged weak currents is verified in the intermediate-energy range. Thus, the general assumption of the V-A standard model is confirmed. Furthermore, the unprecedented accuracy of the ratio R has given rise to a more stringent comparison of various theoretical models for ν-interactions with light and medium-heavy nuclei. Despite of the good results from the CRPA, which is also one of the most utilized microscopic models in calculations for neutrino-nucleus-syntheses and supernova-explosions, there remains a discrepancy in R ($R^{CRPA} = 1.18$).

Last but not least it has to be pointed out, that the ratio $R = \langle\sigma^{NC}\rangle / \langle\sigma^{CC}_{gs}\rangle$ gives rise to one of the fundamental constants of the V-A standard model: The value of $\sin^2 \Theta_W$ of the Weinberg-angle Θ_W could be derived from the measured ratio R in the intermediate-energy range, depending on the theoretical model for the neutrino-nucleus-interactions. For this, the models would have to provide an accurately-enough description of the energy dependent cross section values for both ν and $\overline{\nu}$. There are still existing uncertainties of various input-parameters (like e.g. c_A/c_V).

	Cut	K1	K2	K1 + K2
$\langle\sigma(^{12}\mathrm{C}\,(\,\nu\,,\nu'\,)\,^{12}\mathrm{C}^*)\rangle\ [10^{-42}\,cm^2]$	standard	10.4 ± 0.4	10.0 ± 0.8	10.2 ± 0.4
$\langle\sigma(^{12}\mathrm{C}\,(\,\nu\,,\nu'\,)\,^{12}\mathrm{C}^*)\rangle\ [10^{-42}\,cm^2]$	full fid.	11.1 ± 0.4	10.7 ± 0.4	10.9 ± 0.3
$\langle\sigma(^{12}\mathrm{C}\,(\,\nu_e\,,\mathrm{e}^-\,)\,^{12}\mathrm{N}_{\mathrm{g.s.}})\rangle\ [10^{-42}\,cm^2]$	standard	9.9 ± 0.5	9.1 ± 0.5	9.6 ± 0.3
$\langle\sigma(^{12}\mathrm{C}\,(\,\nu_e\,,\mathrm{e}^-\,)\,^{12}\mathrm{N}_{\mathrm{g.s.}})\rangle\ [10^{-42}\,cm^2]$	full fid.	10.8 ± 0.6	9.9 ± 0.6	10.4 ± 0.4
$R = \langle\sigma^{NC}\rangle / \langle\sigma^{CC}_{gs}\rangle$	standard	1.05 ± 0.06	1.09 ± 0.10	1.07 ± 0.06
$R = \langle\sigma^{NC}\rangle / \langle\sigma^{CC}_{gs}\rangle$	full fid.	1.04 ± 0.07	1.08 ± 0.08	1.05 ± 0.05

Table 3.13: Measured values of the cross sections for the inclusive NC-reaction $^{12}\mathrm{C}\,(\,\nu\,,\nu'\,)\,^{12}\mathrm{C}^*$, the exclusive CC-reaction $^{12}\mathrm{C}\,(\,\nu_e\,,\mathrm{e}^-\,)\,^{12}\mathrm{N}_{\mathrm{g.s.}}$ and the corresponding ratio $R = \langle\sigma^{NC}\rangle / \langle\sigma^{CC}_{gs}\rangle$ in dependence of the applied cuts (standard cuts for each of the two reactions as introduced in this thesis and moreover a full fiducial cut with $|X_{pr}| < 150\,cm$, $1.5 < ROW_{pr} \leq 31.5$, $1.5 < COL_{pr} \leq 15.5$ and only good modules if $|X_{pr}| > 100\,\mathrm{cm}$). The values for K1 and K2 are always added flux- and efficiency-weighted in order to derive the corresponding global value for KARMEN (K1 + K2).

Author		*Type of Model*	$R = \langle\sigma^{NC}\rangle / \langle\sigma^{CC}_{gs}\rangle$
Kolbe	[Kol99]	CRPA	1.18
Vogel	[Vog96]	SM	1.08
Donnelly	[Don91]	SM	1.27
Fukugita	[Fuk88]	EPT	1.07
Mintz	[Min93]	EPT	1.23

Table 3.14: Comparison of theoretical calculations for the flux-independent ratio $R = \langle\sigma^{NC}\rangle / \langle\sigma^{CC}_{gs}\rangle$ of the cross sections for the NC-reaction $^{12}\mathrm{C}\,(\,\nu\,,\nu'\,)\,^{12}\mathrm{C}^*$ and the exclusive CC-reaction $^{12}\mathrm{C}\,(\,\nu_e\,,\mathrm{e}^-\,)\,^{12}\mathrm{N}_{\mathrm{g.s.}}$.

Chapter 4

Neutrino–Oscillations

The evaluated neutrino cross sections on carbon and iron nuclei demonstrate that the KARMEN-detector is very well understood. The experimental cross sections are all in agreement with theoretical calculations. In the following we will search for neutrino-oscillations $\bar{\nu}_\mu \rightarrow \bar{\nu}_e$, $\nu_\mu \rightarrow \nu_e$ and $\nu_e \rightarrow \nu_{sterile}$. For each oscillation channel an appropriate neutrino-nucleus-interaction is consulted and investigated with KARMEN. Hereby it is distinguished between the *appearance* of $\bar{\nu}_e$ from $\bar{\nu}_\mu \rightarrow \bar{\nu}_e$ oscillations (or ν_e from $\nu_\mu \rightarrow \nu_e$) and the *disappearance* of ν_e from $\nu_e \rightarrow \nu_{sterile}$ oscillations.

It is accepted that neutrinos do have a rest mass and that neutrino-oscillations are the most likely explanation of the observed neutrino deficits from atmospheric, solar and very long baseline reactor neutrino experiments [Fuk98], [Ahm02a], [Egu02]. Most recently, the actual sinusoidal oscillation pattern has been observed as well [Neu04a], [Neu04b]. Already the combination of the results from atmospheric, solar and reactor neutrino experiments forms a convincing picture under the assumption of neutrino-oscillations. The evidence of the accelerator-based LSND-experiment for $\bar{\nu}_\mu \rightarrow \bar{\nu}_e$ oscillations does not fit in this framework assuming three massive neutrino states. Atmospheric and solar neutrino experiments define already two independent squared-mass differences. Therefore, at least one other heavier neutrino state needs to be introduced in order to present a coherent picture of neutrino-oscillations including LSND (*see Fig.* 4.1 *and* 4.2). Those extra neutrino states would have to be sterile, i.e. they are not taking part in weak interactions because of their "wrong" handedness (e.g. right-handed neutrinos). This is due to the fact that the invisible decay-width of the Z^0-boson, measured precisely with the LEPII collider experiment at CERN, shows that there are exactly three active neutrino states [PDG02]. The KARMEN-experiment is sensitive to neutrino-oscillations in an assimilable region of squared-mass differences as LSND. The final KARMEN result for the $\bar{\nu}_\mu \rightarrow \bar{\nu}_e$ oscillation search, gained by analysis of substantial parts of the data, taken within the framework of this thesis, excludes major parts of the LSND evidence region [Arm02]. In the following the results from two other complementary methods for the $\bar{\nu}_\mu \rightarrow \bar{\nu}_e$ oscillation search will be introduced in detail. Moreover, it is crucial, in the multi-dimensional context of neutrino-oscillations, to check if other neutrino-oscillations occur in the LSND-region of squared-mass differences. Especially since it was proposed to interpret the Weinberg-angle discrepancy, measured by the NuTeV-experiment, as $\nu_e \rightarrow \nu_{sterile}$ oscillations in the LSND-region of squared-mass differences [Giu02]. In addition, the searches for $\nu_e \rightarrow \nu_{sterile}$ disappearance and $\nu_\mu \rightarrow \nu_e$ appearance with KARMEN could give rise to possible CP-violation in the neutrino sector.

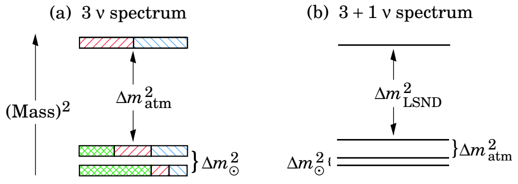

Figure 4.1: Splitting of neutrino-masses for a) three neutrino generations and b) with an extra sterile neutrino (LSND–scenario)

4.1 Formalism of Neutrino–Oscillations

The flavor eigenstates of neutrinos are coupling exclusively via the vector bosons of weak interaction ($W^{\pm}$, Z^0). Given that neutrinos do have a rest mass, the mass eigenstates are contrariwise coupling to the Higgs-fields. However, for neutrino experiments the relevant observables are the flavor eigenstates ($|\nu_\alpha\rangle$ with $\alpha = e, \mu, \tau$). Each of those flavor eigenstates can then be constituted as linear combination of the mass eigenstates ($|\nu_i\rangle$ with $i = 1, 2, 3$; *see Fig.* 4.1):

$$|\nu_\alpha\rangle = \sum_i U_{\alpha i} |\nu_i\rangle \tag{4.1}$$

For non-diagonality of $U_{\alpha i}$ each flavor eigenstate is linked to a mixture of mass eigenstates. If the mass eigenstates have a different time- and space-evolution ($\Delta m^2 > 0$), the flavor eigenstates are consequently oscillating into each other, analogous to the quark sector. The unitary mixing matrix $U_{\alpha i}$ for this oscillation transformation is named Maki-Nakagawa-Sakata-matrix (MNS-matrix analogous to CKM-matrix for quarks). It is often parametrized as follows:

$$U_{MNS} = \begin{pmatrix} U_{e1} & U_{e2} & U_{e3} \\ U_{\mu 1} & U_{\mu 2} & U_{\mu 3} \\ U_{\tau 1} & U_{\tau 2} & U_{\tau 3} \end{pmatrix} =$$

$$\begin{pmatrix} 1 & & \\ & c_{23} & s_{23} \\ & -s_{23} & c_{23} \end{pmatrix} \cdot \begin{pmatrix} c_{13} & & s_{13}e^{-i\delta} \\ & 1 & \\ -s_{13}e^{i\delta} & & c_{13} \end{pmatrix} \cdot \begin{pmatrix} c_{12} & s_{12} & \\ -s_{12} & c_{12} & \\ & & 1 \end{pmatrix} \tag{4.2}$$

c_{23} in the factor on the left hand side defines $\cos(\Theta_{23})$ (and s_{23} defines $\sin(\Theta_{23})$, respectively). Θ_{23} is the almost maximal mixing angle from the oscillation $\nu_\mu \rightarrow \nu_\tau$ of atmospheric neutrinos (*see Fig.* 4.2 *and Fig.* 4.1). So far, no hint for the oscillation $\nu_e \!\rightarrow \nu_\tau$ is observed by long baseline reactor experiments being sensitive in the same Δm^2-region. The corresponding small mixing angle Θ_{13} appears in the factor in the middle. The oscillation $\nu_e \!\rightarrow \nu_\mu$ requires the mixing angle Θ_{12} in the factor on the right hand side. The disappearance of solar neutrinos ($\nu_e \!\rightarrow \nu_x$) travelling from the sun to the earth is driven by the large mixing angle Θ_{12} and the almost maximal mixing angle Θ_{23}. This is because the *very* long baseline reactor experiment KamLAND has observed the oscillation $\bar{\nu}_e \!\rightarrow \bar{\nu}_x$ as

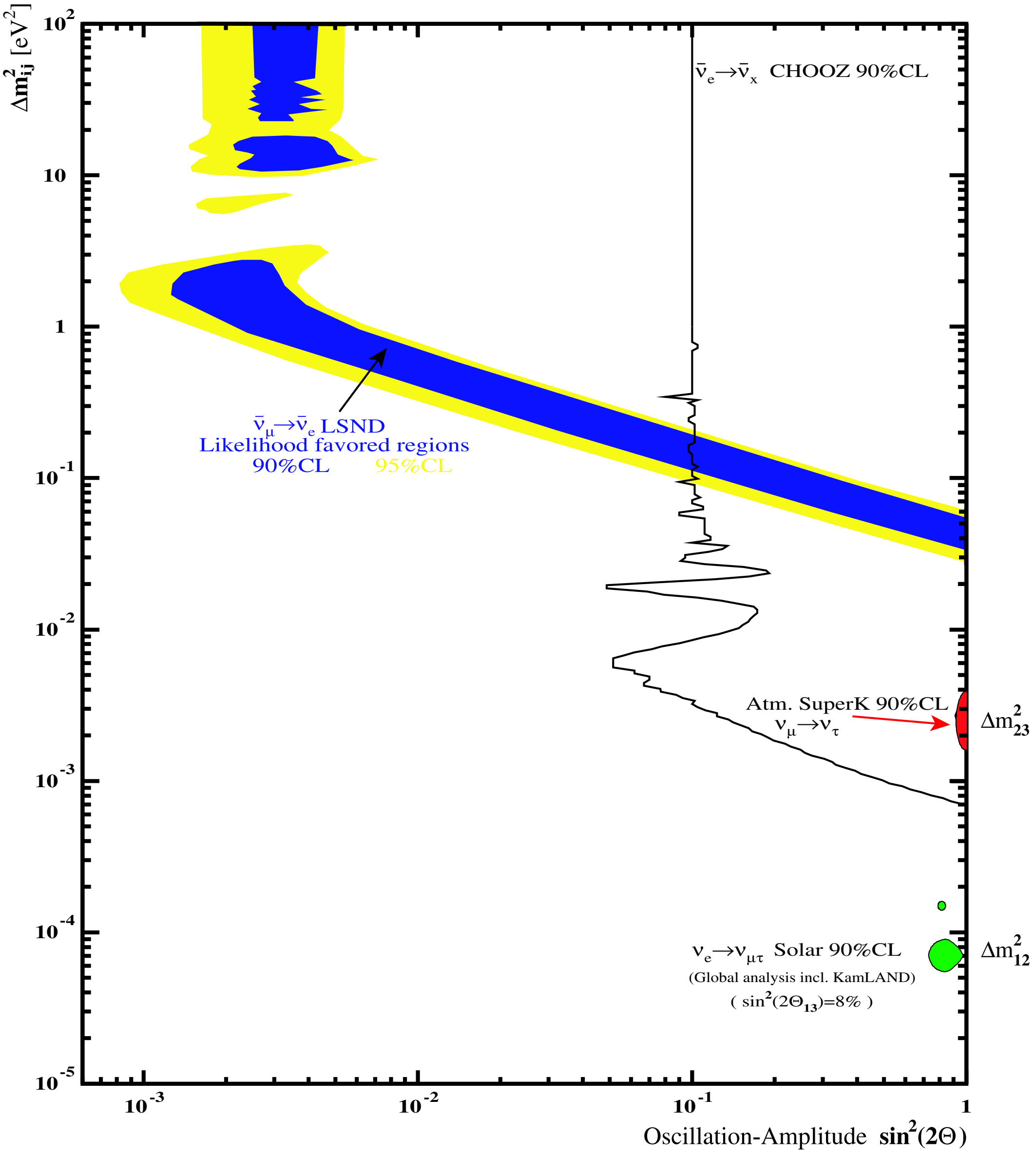

Figure 4.2: 2-flavor-oscillation plot with the evidence regions (90%CL) of atmospheric ($\nu_\mu \!\rightarrow \nu_\tau$ in SuperK) and solar neutrinos ($\nu_e \!\rightarrow \nu_{\mu,\tau}$ in combined experiment data [Fog03]) as well as the evidence of the LSND accelerator experiment ($\bar{\nu}_\mu \!\rightarrow \bar{\nu}_e$). From the CHOOZ reactor experiment the oscillation $\bar{\nu}_e \!\rightarrow \bar{\nu}_x$ can be excluded at $90\% CL$ for regions right hand side of the black curve.

well, in the Δm^2-region of the large mixing angle (LMA) solar solution (*see Fig.* 4.2). From this, no hint for CP-violation in the neutrino sector is given yet.
δ in the factor in the middle of *Eq.* 4.2 characterizes the CP-violating phase for the Dirac case (another two phases are required for the Majorana case).
Because two mixing angles of the MNS-matrix being large or almost maximal, the MNS-matrix itself is distinctly different from the CKM-matrix of the quark sector. The mixing of quarks is just a small effect. Quarks are definitely Dirac-particles and can be easily distinguished from their own anti-particles by their electric charge.

The transition probability $\mathcal{P}$ of measuring the neutrino flavor eigenstate ν_β with a neutrino detector at distance $x = L$ from a ν_α-source is given by [Mak62], [Alt03]:

$$\mathcal{P}(|\nu_\alpha\rangle \rightarrow |\nu_\beta\rangle) = \left| \sum_i U_{\beta i} \, \exp[-i(E_i t - p_i x)] \, U^*_{\alpha i} \right|^2 \tag{4.3}$$

For fixed neutrino energy, one can express p_i and t in terms of $E_i = E_\nu$, m_i and $x = L$. Without CP-violation (i.e. MNS-matrix U is assumed real) *Eq.* 4.3 can be simplified to:

$$\mathcal{P}(|\nu_\alpha\rangle \rightarrow |\nu_\beta\rangle) = \delta_{\alpha\beta} - 4 \sum_{i=1}^{n} \sum_{j=i+1}^{n} U_{\alpha i} U_{\beta i} U_{\alpha j} U_{\beta j} \sin^2\left(\frac{\Delta m^2_{ij} \cdot L}{2E_\nu}\right) \tag{4.4}$$

Thus, the MNS-matrix U defines the amplitudes of the resulting oscillations, while the oscillation frequencies are determined by the differences between the squared-masses Δm^2_{ij} for the mass eigenstates.
On the one hand, *Eq.* 4.4 can be extended straightforward to more than three neutrino states ($n > 3$ in *Eq.* 4.4). On the other hand it is often useful for practical purposes to consider the simplified case, where only two neutrino flavor eigenstates α and β take part in the oscillations. Neglecting again CP-violation, the approximation of the 3-flavor-formalism by a 2-flavor-formalism yields:

$$\begin{pmatrix} |\nu_\alpha\rangle \\ |\nu_\beta\rangle \end{pmatrix} = \begin{pmatrix} \cos\Theta & \sin\Theta \\ -\sin\Theta & \cos\Theta \end{pmatrix} \cdot \begin{pmatrix} |\nu_1\rangle \\ |\nu_2\rangle \end{pmatrix} \tag{4.5}$$

The probability $\mathcal{P}$ for the oscillation $\nu_\alpha \rightarrow \nu_\beta$ in vacuum is then given by:

$$\begin{aligned} \mathcal{P}(|\nu_\alpha\rangle \rightarrow |\nu_\beta\rangle) &= |\langle \nu_\beta | \nu_\alpha(x = L, t)\rangle|^2 \\ &= \sin^2(2\Theta) \cdot \sin^2\left(\frac{1.27 \cdot \Delta m^2[eV^2] \cdot L[m]}{E_\nu[MeV]}\right) \end{aligned} \tag{4.6}$$

$$with \quad \Delta m^2 = |{m_1}^2 - {m_2}^2|$$

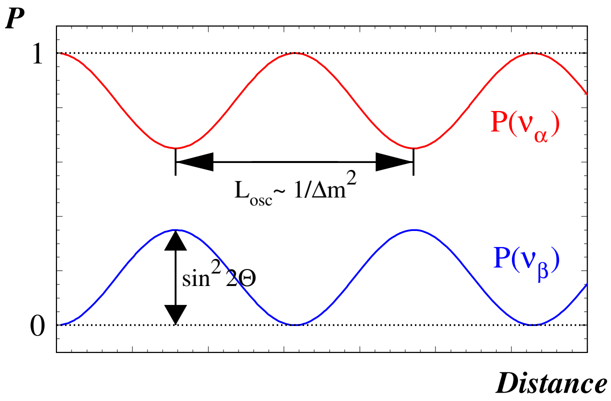

Figure 4.3: Schematic evolution in space of the flavor eigenstate probability for 2-flavor-oscillation $\nu_\alpha \rightarrow \nu_\beta$

For a given ν-energy E_ν and a fix distance L of the detector from the source, $\sin^2(2\Theta)$ and Δm^2 are the variables driving the space-time-evolution of the oscillation. $\sin^2(2\Theta)$ defines the oscillation-amplitude within the 2-flavor-formalism, bearing in mind that $\sin^2(2\Theta)$ depends generally on various matrix elements of U, while the oscillation-frequency is given by Δm^2 (*see Fig.* 4.3). For practical purposes the result of a ν-oscillation search is visualized by plotting Δm^2 versus the oscillation-amplitude $\sin^2(2\Theta)$ (*see Fig.* 4.2). At $\Delta m^2 \approx E_\nu/L$ the oscillation effect is maximal and consequently an experiment most sensitive to ν-oscillations (*compare the 2. argument in Eq.* 4.6).
Three kinematical ranges can be distinguished:

- $L/E \ll 1/\Delta m^2$ (E large or L small): The sine function can be approximated by a linear function, and the "oscillation" effect is small even if the mixing angle is large.

- $L/E \approx 1/\Delta m^2$: The actual sinusoidal oscillation pattern is accessible to observation, as already mentioned above.

- $L/E \gg 1/\Delta m^2$ (E small or L large): The sinusoidal oscillations become so fast that they will be unmeasurable. In this case, only an average oscillation effect, proportional to $\sin^2(2\Theta)$, can be observed. The factor $\sin^2\left(\frac{1.27\cdot\Delta m^2\cdot L}{E_\nu}\right)$ averages out at $\frac{1}{2}$. This case is referred to as large Δm^2-region.

4.1.1 Overview of Experimental Status

Δm^2_{atm}-Region of Atmospheric Neutrinos:

- **SuperKamiokande (Successor of Kamiokande)**:
  A water-Čerenkov-detector using 50 kt of pure water (sited 1000 m underground at Kamioka mine in Japan). SuperK has measured the disappearance of atmospheric ν_μ in dependence of the zenith angle, while the distributions of atmospheric ν_e meet expectations [Fuk98]. With the energy of atmospheric neutrinos being on a GeV-scale and typical distances through the earth being on a 1000 km-scale, the corresponding Δm^2_{atm}-region is roughly $10^{-3}\,eV^2$. The latest result for the assumed $\nu_\mu \rightarrow \nu_\tau$ oscillation restricts the range of Δm^2_{atm} from $1.6\cdot10^{-3}\,eV^2$ to $3.9\cdot10^{-3}\,eV^2$ at $90\%CL$ and the almost maximal oscillation-amplitude to $\sin^2(2\Theta) \geq 0.92$ [Kan02]. The alternative oscillation of ν_μ into $\nu_{sterile}$ is disfavored at $99\%CL$, which is mainly due to results from NC-interactions and the absence of matter effects in the energy dependence of the oscillation.
  The KEK-to-Kamioka long baseline accelerator neutrino experiment (K2K), using 98% pure ν_μ with a mean energy of 1.3 GeV and a flight-length of 250 km, is probing the Δm^2_{atm}-region with the SuperK-detector, but with artificial neutrinos instead [Kat03]. Initial results indicate a deficit of ν_μ of the right order.

- **CHOOZ**:
  5 t of Gd-loaded scintillator were used for this detector, which was located at a distance of 1 km from a nuclear power plant in France. $\bar{\nu}_e$ from β-decays occurring inside the reactor can be measured with the CHOOZ-detector via the prompt reaction $\mathrm{p}(\bar{\nu}_e, e^+)\mathrm{n}$ and the delayed correlated $\mathrm{Gd}(\mathrm{n},\gamma)$-reaction. With the long baseline of 1 km and the energy of $\bar{\nu}_e$ reactor neutrinos on a MeV-scale, a corresponding Δm^2-region down to $10^{-3}\,eV^2$ is accessible as well. CHOOZ has not observed the disappearance of $\bar{\nu}_e$ (in accordance with Palo Verde, a similar reactor neutrino experiment). For the oscillation $\bar{\nu}_e \rightarrow \bar{\nu}_x$ an oscillation-amplitude of $\sin^2(2\Theta) > 10\%$ is excluded at $90\%CL$ for large Δm^2 [Apo99]. Consequently the mixing angle Θ_{13} in *Eq.* 4.2 must be small, in contrast to the almost maximal mixing angle Θ_{23} from the observed $\nu_\mu \rightarrow \nu_\tau$ disappearance of atmospheric neutrinos.

$\Delta m^2_\odot$-Region of Solar Neutrinos:

- **Solar Neutrino Deficit**:
  A deficit in the measured flux of solar ν_e has been observed by all solar neutrino experiments over the last three decades. Ray Davis' deep underground radiochemical chlorine experiment at Homestake Mine utilized the reaction $^{37}\mathrm{Cl}(\nu_e, e^-)^{37}\mathrm{Ar}$, in order to tag solar neutrinos via the extraction and decay of produced $^{37}\mathrm{Ar}$ ($T_{1/2} = 35\,\mathrm{d}$). The measured solar neutrino flux amounts to just a third of the prediction by the standard solar model (SSM). Later, other radiochemical experiments using Gallium like Gallex, GNO and SAGE have been sensitive to lower solar neutrino energies, but still measured just half of the expected solar neutrino flux. Real-time water-Čerenkov experiments like Kamiokande and SuperK confirmed the

discrepancy as well. Neutrino-oscillations $\nu_e \rightarrow \nu_x$, causing the disappearance of solar neutrinos, have been proposed in order to solve this solar neutrino problem.

- **SNO**:
  The 2 km underground Solar Neutrino Observatory (SNO), at Sudbury mine in Canada, consists of a 1 kt heavy-water (D_2O) Čerenkov-detector. This detector is sensitive to all three active neutrino flavor eigenstates via the NC-reaction $D(\nu_x, \nu_x{}'n)p$. In contrast, the CC-reaction $D(\nu_e, e^- p)p$ is sensitive only to ν_e , like all previous radiochemical solar neutrino experiments. The contribution of the flavor ν_μ and ν_τ to neutrino-electron-scattering (ES) amounts to just a sixth, as well as for real-time water-Čerenkov-detectors. With the solar neutrino flux derived from the CC-reaction, SNO has observed the solar-neutrino-deficit too, while the flux determined from the NC-reaction is in good agreement with the prediction from SSM. So far, this is the most compelling evidence for neutrino flavor transformation [Ahm02a]. The solar neutrino flux derived from ES fits statistically significantly to the $\nu_e \rightarrow \nu_x$ oscillation hypothesis as well.

- **KamLAND**:
  The KamLAND-detector contains 1 kt of liquid scintillator and is sited at Kamioka mine in Japan. It is a very long baseline reactor neutrino experiment with an average distance of 140 km from all nuclear power plants in Japan and Korea. Therefore, it has full sensitivity for $\Delta m^2 > 10^{-5}\, eV^2$. KamLAND confirmed the $\bar{\nu}_e \rightarrow \bar{\nu}_x$ disappearance in the region of the large mixing angle (LMA) solar solution, while all other solar solutions are excluded. This beautiful concordance with the solar neutrino oscillation hypothesis by a completely different technique, based on artificial reactor neutrinos, is really a triumph for both neutrino physics and solar astrophysics. Combining the results from KamLAND with all results from solar, atmospheric and long baseline reactor experiments, the most likely value of $\Delta m^2_\odot$ is currently $7 \cdot 10^{-5}\, eV^2$ with an oscillation-amplitude of $\sin^2(2\Theta) = 0.8$ (*see Fig.* 4.2) [Fog03].

- **MSW-Effect**:
  The observed LMA solar solution embraces the Mikheyev-Smirnov-Wolfenstein-effect (MSW-effect) [Wol78]. Active massive neutrinos passing matter will undergo the MSW-effect. Their momentum is modified proportional to $G_F \cdot N_e$ due to a "refractive index" in matter (with G_F being the Fermi constant and N_e the electron density). Hence, the effective neutrino masses and the effective mixing angles will change in an energy (momentum) dependent way, when entering matter. At a particular value of N_e the neutrinos can change their flavor resonantly. With a continuously varying electron density in the sun, the outgoing ν_e , produced in fusion reactions inside the core, will ultimately reach the resonance value of N_e and thus transform largely into ν_μ and ν_τ . $\nu_\mu \rightarrow \nu_\tau$ oscillations are not affected by matter effects, since ν_μ and ν_τ have the same interaction (NC) in ordinary matter and thus the same interaction potential. In contrast, $\nu_\mu \rightarrow \nu_{sterile}$ oscillations interfere with matter effects, because the MSW-potential of $\nu_{sterile}$ is zero and therefore differs from the MSW-potential of ν_μ .

Δm^2_{LSND}-Region of the Accelerator Based LSND-Experiment:

- **Δm^2_{atm} and $\Delta m^2_{\odot}$**:
  The oscillation of atmospheric and solar neutrinos define already two independent Δm^2 scales. The third scale is fixed by the other two and is close to the larger one (*compare Eq.* 4.4).

- **LSND**:
  Based at the LAMPF-accelerator in Los Alamos in the US, the LSND-experiment took data during the period of 1993 - 1998. The LSND-hybrid-detector consisted of 167 t of mineral oil with a small admixture of scintillant. This dilute mixture allowed the detection of both Čerenkov light and isotropic scintillation light [Ath96]. The Čerenkov light resulted in robust particle identification (PID) for $e^\pm$ and the ability to measure the direction of $e^\pm$, in contrast to KARMEN. The linear accelerator LAMPF produced 800 MeV protons with a repetition rate of 120 Hz and a beam current of 1 mA. Neutrinos were produced inside the water main-target, via π^+-decay at rest (DAR), analogous to ISIS, but with an additional small fraction of higher energetic neutrinos from π^+-decay in flight (DIF). Due to the 600 μs long proton bunches, no timing resolution of the π^+- and μ^+-decay was possible. The distance of the LSND-detector from the main-target averaged out at 30 m (KARMEN 17.7 m), resulting in a slightly different L/E and hence Δm^2 sensitivity of both experiments.

LSND claims evidence for $\bar{\nu}_\mu \rightarrow \bar{\nu}_e$ oscillation in the region of squared-mass differences $\Delta m^2_{LSND} > 3 \cdot 10^{-2} eV^2$ with oscillation-amplitudes from 1 down to $\sin^2(2\Theta) = 10^{-3}$ (*see Fig.* 4.2) [Agu01]. The KARMEN2 results for $\bar{\nu}_\mu \rightarrow \bar{\nu}_e$ oscillations in [Arm02] and within the framework of this thesis exclude major parts of the LSND evidence region. In the following the results from the other two complementary methods for the $\bar{\nu}_\mu \rightarrow \bar{\nu}_e$ oscillation search will be introduced in detail. Furthermore, it is crucial, in the more dimensional context of neutrino-oscillations, to check if other neutrino-oscillations occur in the LSND-region of squared-mass differences. To explain LSND, at least one additional heavier sterile neutrino state needs to be introduced in order to present a coherent picture of neutrino-oscillations and particle physics including LSND (*see Fig.* 4.1 *and* 4.2).
E.g. in a (3+1) scenario, there is a "one mass scale dominance": $\Delta m^2 = \Delta m^2_{41} \simeq \Delta m^2_{42} \simeq \Delta m^2_{43}$. The oscillation-amplitudes for the oscillation searches performed in the framework of this thesis are then given by (*compare Eq.* 4.4) [Sor03]:

$$\bar{\nu}_\mu \rightarrow \bar{\nu}_e \text{ appearance } (\nu_\mu \rightarrow \nu_e \text{ assuming } CP\text{-invariance}): \quad \sin^2(2\Theta) = 4 \cdot U^2_{e4} \cdot U^2_{\mu 4}$$

$$\nu_e \rightarrow \nu_{sterile} \text{ disappearance:} \quad \sin^2(2\Theta) = 4 \cdot U^2_{e4} \cdot (1 - U^2_{e4})$$

- **Future Experiment MiniBooNE**:
  The MiniBooNE Čerenkov-detector, using 776 t of mineral oil, is sited 500 m away from the neutrino production point at Fermilab (Chicago/US). MiniBooNE utilizes the 8 GeV booster at Fermilab's main injector in order to produce ν_μ with energies above 500 MeV. The expected experimental sensitivity for $\nu_\mu \rightarrow \nu_e$ appearance will reach $\sin^2(2\Theta) \approx 7 \cdot 10^{-4}$ for large Δm^2 and $\Delta m^2 \approx 2 \cdot 10^{-2} eV^2$ for $\sin^2(2\Theta) = 1$ [Baz02]. Hence, the entire LSND evidence region will be ultimately covered. The data taking is currently underway. After switching the polarity of the magnetic horn, the proximate search for $\bar{\nu}_\mu \rightarrow \bar{\nu}_e$ appearance will reach a sensitivity, likewise sufficient enough to test the LSND-region (without assuming CP-invariance).

4.2 Search for $\nu_e \rightarrow \nu_{sterile}$ Disappearance

The cross section of the exclusive CC-reaction $^{12}\mathrm{C}\,(\,\nu_e\,,\mathrm{e}^-\,)\,^{12}\mathrm{N}_{\mathrm{g.s.}}$, measured precisely with KARMEN, is in good agreement with theoretical predictions (*see Chapter* 3.1). There is no evidence for the *disappearance* of ν_e . Consequently an upper exclusion limit for $\nu_e \rightarrow \nu_{sterile}$ oscillations in the Δm^2_{LSND}-region will be derived in the following.
The exclusion limit for $\nu_e \rightarrow \nu_{sterile}$ oscillations will at least be equivalent to exclusion limits for $\nu_e \rightarrow \nu_\mu$ and $\nu_e \rightarrow \nu_\tau$ oscillations in the same Δm^2_{LSND}-region. This is because the even more precisely measured flux-independent ratio $R = \langle\sigma^{NC}\rangle / \langle\sigma^{CC}_{gs}\rangle$ is not larger than anticipated (*see Chapter* 3.2), as would be the case if $\nu_e \rightarrow \nu_\mu$ or $\nu_e \rightarrow \nu_\tau$ oscillations occurred. Such oscillations into active neutrino states would just decrease $\langle\sigma^{CC}_{gs}\rangle$ but leave $\langle\sigma^{NC}\rangle$ unaffected instead and hence increase the ratio $R = \langle\sigma^{NC}\rangle / \langle\sigma^{CC}_{gs}\rangle$, which is clearly in contrast to the observation.

4.2.1 Calculating the Oscillation–Amplitude $\sin^2(2\Theta)$ as Function of Δm^2

Once the upper limit for the oscillation-probability $\mathcal{P}^{\nu_e \rightarrow \nu_{sterile}}_{90\%CL}$ is known, the oscillation-amplitude $\sin^2(2\Theta)$ can be easily calculated within the 2-flavor-formalism as function of Δm^2 according to *Eq.* 4.6. Additionally, a distance- and an energy-weight-function need to be incorporated, due to the geometric size of the detector as well as the energy dependence of the ν_e-flux, cross section and detection efficiency:

$$\sin^2(2\Theta) = \frac{\mathcal{P}^{\nu_e \rightarrow \nu_{sterile}}_{90\%CL}}{\int\limits_{L'} w_L(L) \cdot \int\limits_{E'_\nu} w_{\Phi,\sigma,\epsilon}(E_\nu) \cdot \sin^2\left(\frac{1.27 \cdot \Delta m^2 \cdot L}{E_\nu}\right) dE_\nu \, dL} \tag{4.7}$$

The distance-weight-function $w_L(L)$ and the energy-weight-function $w_{\Phi,\sigma,\epsilon}(E_\nu)$ are normalized:

$$\int\limits_{L'} w_L(L)\, dL = 1 \tag{4.8}$$

$$\int\limits_{E'_\nu} w_{\Phi,\sigma,\epsilon}(E_\nu)\, dE_\nu = 1 \tag{4.9}$$

Furthermore, the energy-weight-function $w_{\Phi,\sigma,\epsilon}(E_\nu)$ is proportional to a) $f_\Phi(E_\nu)$ the effective differential ν_e-flux from μ^+-decay at rest (DAR), b) $f_\sigma(E_\nu)$ the effective differential cross section for $^{12}\mathrm{C}\,(\,\nu_e\,,\mathrm{e}^-\,)\,^{12}\mathrm{N}_{\mathrm{g.s.}}$ and c) $f_\epsilon(E_\nu)$ the relative detection efficiency:

$$w_{\Phi,\sigma,\epsilon}(E_\nu) \;=\; const\,\cdot\, f_\Phi(E_\nu)\cdot f_\sigma(E_\nu)\cdot f_\epsilon(E_\nu) \tag{4.10}$$

All these energy dependent functions are illustrated in *Fig.* 4.4 a)-d) on the left hand side. The lower boundary on the ν-energy reflects the Q-value of 17.33 MeV for the exclusive CC-reaction $^{12}\mathrm{C}\,(\,\nu_e\,,\mathrm{e}^-\,)\,^{12}\mathrm{N}_{\mathrm{g.s.}}$ as well as event cuts on the prompt visible energy ($>10\,\mathrm{MeV}$).

Moreover, the distance L distribution is derived by simulating events inside the entire volume of the segmented main-detector, according to the $1/L^2$ dependence of the ν-flux. The convolution of the obtained distance distribution w'_L with a Gaussian distribution delivers the final distance distribution w_L including the detector response:

$$w_L(L) \;=\; \int\limits_{-\infty}^{+\infty} w'_L(L')\cdot e^{-\frac{(L-L')^2}{2\cdot\overline{\sigma}^2_{smear}}}\;dL' \tag{4.11}$$

For this, the overall spatial resolution $\overline{\sigma}_{smear}$ is given by the spatial resolution in the x-position of the modules ($\sigma_x = 5\,\mathrm{cm}$) and the uncertainty of the transversal π^+ stopping point inside the production target ($\sigma_{target} = 5\,\mathrm{cm}$):

$$\overline{\sigma}_{smear} = \sqrt{\sigma^2_{target}+\sigma^2_x} \;=\; 7\,cm \tag{4.12}$$

The resulting distance distribution is shown in *Fig.* 4.4 e) and reflects clearly the $1/L^2$ dependence. The effective distance of the detector from the main-target amounts to 1767.5 cm.

There is an additional minor contribution to the ν-production originating from the μSR-pre-target. This ratio $r_{\mu SR}$ depends on its mean thickness $\overline{d}_{\mu SR}$ and can be calculated as follows [Bur95]:

$$r_{\mu SR} = \frac{\frac{8\cdot 10^{-4}\cdot \overline{d}_{\mu SR}}{5\,mm}}{\frac{8\cdot 10^{-4}\cdot \overline{d}_{\mu SR}}{5\,mm}+0.0448} \tag{4.13}$$

With $\overline{d}_{\mu SR} = 6.32\,\mathrm{mm}$ in K1+K2 (added flux-weighted), the ratio of neutrinos produced inside the μSR-pre-target amounts to:

$$r_{\mu SR} = 1 - r_{main} = 2.21\,\% \tag{4.14}$$

The distance distribution, regarding the μSR-pre-target, does not reflect the $1/L^2$ dependence anymore and possesses the shape of a triangle, as shown in *Fig.* 4.4 f). This is due to the geometric position of the rectangular detector that points towards the main-target and not towards the μSR-pre-target (*see Fig.* 2.1). The effective distance of the detector from the μSR-pre-target amounts to 2914 cm.

After having deduced the energy-weight-function $w_{\Phi,\sigma,\epsilon}(E_\nu)$, the distance-weight-functions $w_{L,main}$ and $w_{L,\mu SR}$ as well as the ratio $r_{\mu SR}$ of neutrinos from the μSR-pre-target, the oscillation-amplitude $\sin^2(2\Theta)$ can be finally calculated as function of Δm^2 as follows:

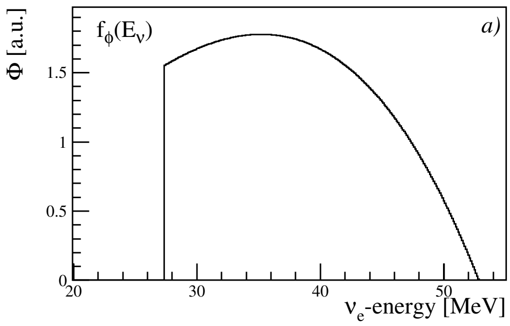

effective diff. ν_e-flux from DAR

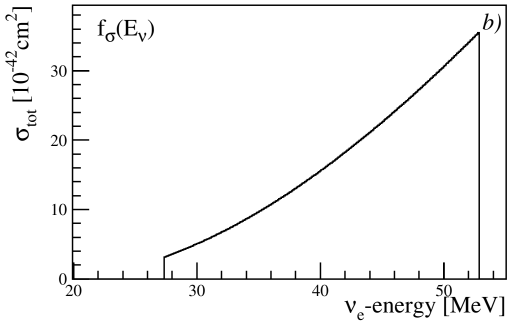

eff. diff. cross section $^{12}C(\nu_e,e^-)^{12}N_{gs}$

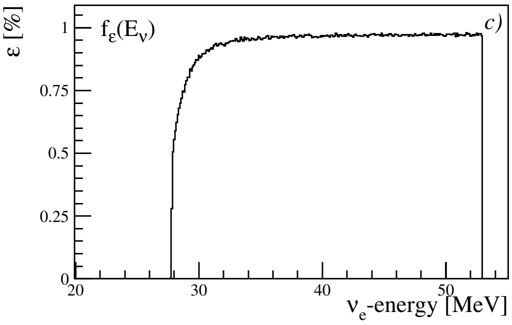

rel. efficiency

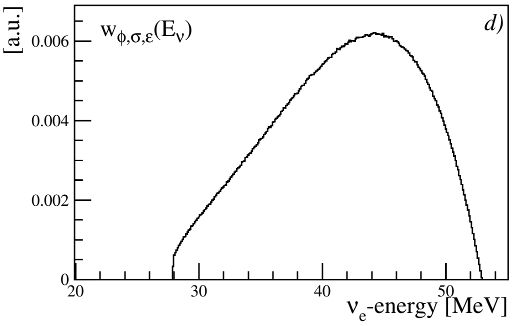

weighted energy spectrum

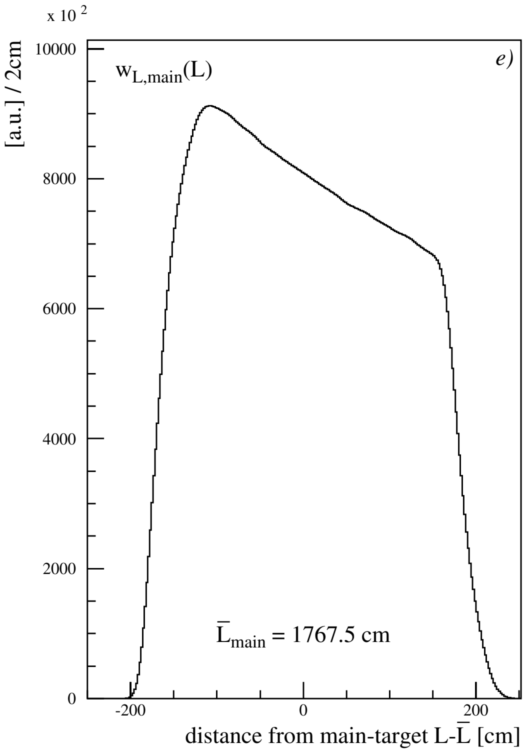

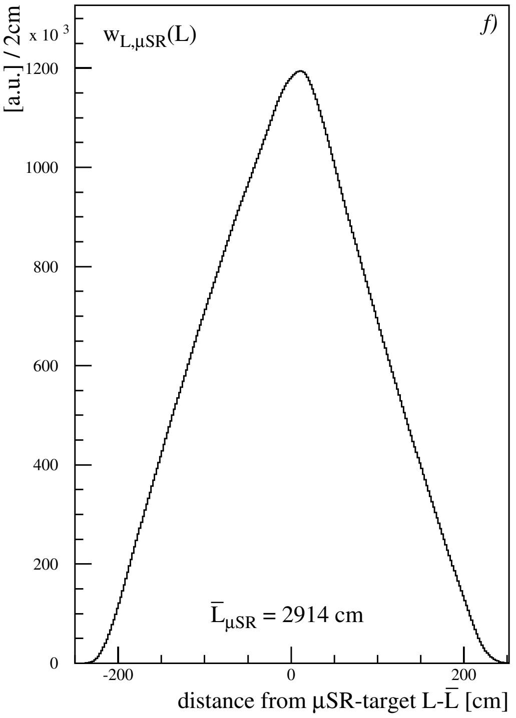

Figure 4.4: Neutrino energy and distance dependent input distributions needed for the calculation of the oscillation-amplitude $\sin^2(2\Theta)$ as function of Δm^2 (for $\nu_e \rightarrow \nu_{sterile}$ disappearance in KARMEN): a) effective differential ν_e-flux from μ^+-decay at rest (DAR), b) effective differential cross section for $^{12}C\,(\,\nu_e\,, e^-\,)\,^{12}N_{g.s.}$, c) relative detection efficiency, d) overall energy-weight-function, e) distance distribution regarding the main-target and f) the μSR-pre-target.

$$\begin{aligned}\mathcal{P}_{90\%CL}^{\nu_e\rightarrow\nu_{sterile}} \quad = \quad & \sin^2(2\Theta)\cdot\Bigg[\, r_{main}\cdot\int\limits_{L'} w_{L,main}(L)\cdot\int\limits_{E'_\nu} w_{\Phi,\sigma,\epsilon}(E_\nu)\cdot\sin^2\left(\frac{1.27\cdot\Delta m^2\cdot L}{E_\nu}\right)\, dE_\nu\, dL \\ & + r_{\mu SR}\cdot\int\limits_{L'} w_{L,\mu SR}(L)\cdot\int\limits_{E'_\nu} w_{\Phi,\sigma,\epsilon}(E_\nu)\cdot\sin^2\left(\frac{1.27\cdot\Delta m^2\cdot L}{E_\nu}\right)\, dE_\nu\, dL\Bigg]\end{aligned} \tag{4.15}$$

Fig. 4.5 shows the resulting $90\%CL$ exclusion curve. Regions on the right hand side of the curve are excluded at $90\%CL$. KARMEN attains maximal sensitivity for $\nu_e\rightarrow\nu_{sterile}$ disappearance at $2-3\,eV^2$ ($\simeq 44\,[MeV]/17.7\,[m]$ *compare Fig.* 4.4 d+e).

4.2.2 Exclusion Limit for $\nu_e\rightarrow\nu_{sterile}$ Disappearance

(806.2 ± 66.1) electron-neutrinos are expected to be measured with KARMEN (K1+K2) via the exclusive CC-reaction $^{12}\mathrm{C}\,(\,\nu_e\,,\mathrm{e}^-\,)\,^{12}\mathrm{N}_{\mathrm{g.s.}}$ according to theoretical predictions ($\overline{\sigma}_{theo}=(9.1\pm 0.3)\cdot 10^{-42}cm^2$ [Dre02]). The overall relative uncertainty of 8.2 % evolves from the relative error in theory (3.3 %), neutrino flux (6.7 %) and detection efficiency (3.4 %). The vanishing small background expectation amounts to (13.9 ± 0.7) sequences (7 sequences from cosmic background and 7 random sequences, respectively). (860 ± 29.3) sequences have been observed with KARMEN, i.e. even more ν_e have been measured via the exclusive CC-reaction than expected (-39.9 ± 72.3). Hence, a possible oscillation signal of 52.6 disappeared ν_e can be excluded at $90\%CL$ (corresponds to $1.28\,\sigma$ of the assumed Gaussian distribution of errors). The ratio of $N_{90\%CL}=52.6$ to the full oscillation expectation $N_{full}=806.2$ constitutes the upper limit for the oscillation probability $\mathcal{P}_{90\%CL}=6.5\cdot 10^{-2}$. Consequently, the oscillation-amplitude $\sin^2(2\Theta)$ can be calculated distance- and energy-weighted as a function of Δm^2 utilizing *Eq.* 4.15 (within the 2-flavor-formalism). *Fig.* 4.5 shows the resulting $90\%CL$ exclusion curve. Regions on the right hand side of the curve are excluded at $90\%CL$. For large Δm^2 the following upper limit is derived for $\boxed{\nu_e\rightarrow\nu_{sterile}}$ disappearance:

$$\boxed{\sin^2(2\Theta)\ <\ 0.13\ (90\%CL)}$$

In a (3+1) scenario ($\Delta m^2=\Delta m^2_{41}\simeq\Delta m^2_{42}\simeq\Delta m^2_{43}$) this oscillation-amplitude $\sin^2(2\Theta)$ for $\nu_e\rightarrow\nu_{sterile}$ disappearance is then given by $\sin^2(2\Theta)=4\cdot U^2_{e4}\cdot(1-U^2_{e4})$ (*compare Eq.* 4.4) [Sor03].

With the derived KARMEN result on $\nu_e\rightarrow\nu_{sterile}$ disappearance, it is feasible to exclude almost the entire region that has been proposed as possible explanation of the Weinberg-angle-anomaly reported by the NuTeV-experiment [Giu02]. KARMEN does not show evidence for such heavy sterile neutrinos being suggested. Neglecting possible CP-violation, this result conforms with the limit for disappearance of reactor anti-neutrinos ($\bar{\nu}_e\rightarrow\bar{\nu}_x$) from the CHOOZ-experiment [Apo99] (*see Fig.* 4.5).

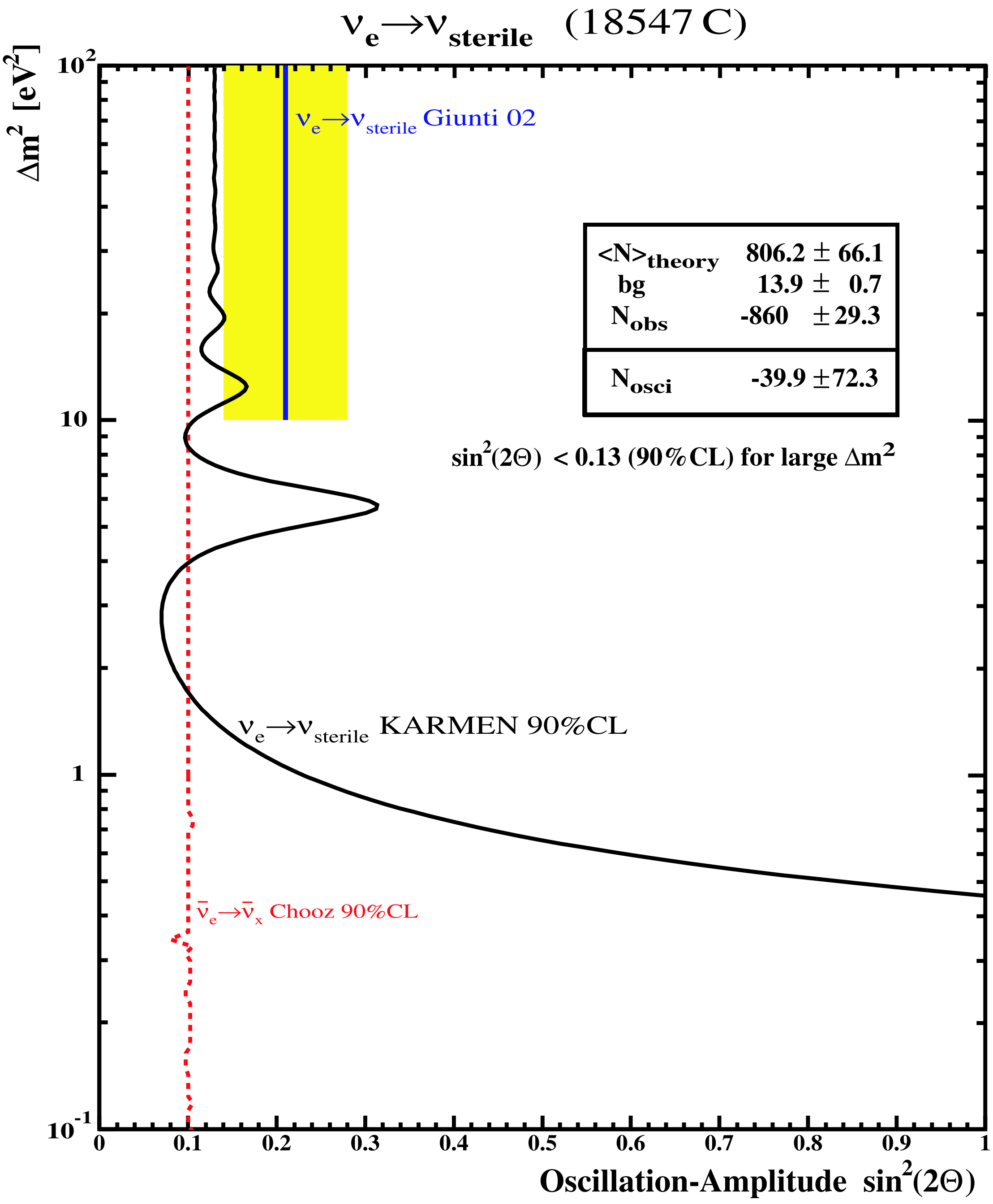

Figure 4.5: Exclusion curve for $\nu_e \rightarrow \nu_{sterile}$ disappearance deduced from the measured $^{12}\mathrm{C}\,(\,\nu_e\,,\mathrm{e}^-\,)\,^{12}\mathrm{N}_{\mathrm{g.s.}}$ cross section in KARMEN (areas on the right hand side of the curve are excluded at $90\% CL$). Drawn-in for comparison is the region discussed as possible explanation of the Weinberg-angle-anomaly reported by the NuTeV–experiment [Giu02], as well as the limit for disappearance of reactor anti-neutrinos ($\bar{\nu}_e \rightarrow \bar{\nu}_x$) from the CHOOZ–experiment [Apo99].

4.3 Search for $\nu_\mu \rightarrow \nu_e$ Appearance

In the KARMEN-experiment it is not only possible to search for the *disappearance* of ν_e by analyzing the late time window of μ^+-decay (as performed previously), but also to search for the *appearance* of ν_e by investigating the two early time windows of π^+-decays. ν_μ from π^+-decays oscillating into ν_e in the LSND-region of squared-mass differences would require at least one additional heavier sterile neutrino state, in order to present a coherent picture of neutrino-oscillations and particle physics including LSND (*see Fig.* 4.1 *and* 4.2). Such evidence for $\nu_\mu \rightarrow \nu_e$ oscillation in the Δm^2_{LSND}-region could as well give rise to leptonic CP-violation.
In the following the number of candidate sequences for $\nu_\mu \rightarrow \nu_e$ oscillation will be compared with the precisely measured expectation of all contributing background components. Finally, a Bayesian method of limiting the oscillation-probability at a given confidence level will be introduced.

Performing the search for $\nu_\mu \rightarrow \nu_e$ appearance, two 100 ns narrow time windows (according to the timing of the proton double pulses) are scrutinized for ν_e (*see Fig.* 4.6 and 2.2). Again, ν_e can be detected via the sequential CC-reaction $^{12}\mathrm{C}\,(\,\nu_e\,,\mathrm{e}^-\,)\,^{12}\mathrm{N}_{\mathrm{g.s.}}$ which has already been studied in spectroscopic quality for ν_e from μ^+-decay. Now, only the first 100 ns of both early time windows are scrutinized, in order to minimize beam-correlated background from neutron sequences. Herewith, this rare background, which is induced by high-energetic fast neutrons ($E_{kin} > 10\,\mathrm{MeV}$), can be neglected [Eit95]. But the restriction on the time causes a small efficiency loss for neutrinos from π^+-decays, as for these neutrinos the two in time parabolic shaped and 100 ns long proton pulses are folded with an exponential curve according to the 26 ns short lifetime of π^+. *Fig.* 4.6 visualizes the prompt time distributions of the proton double pulse and of the neutrinos from π^+-decays following the protons in time. Drawn-in as well, is the prompt time distribution of ν_e and $\overline{\nu_\mu}$ from already starting subsequent μ^+-decays. ν_e from μ^+-decays constitute the major

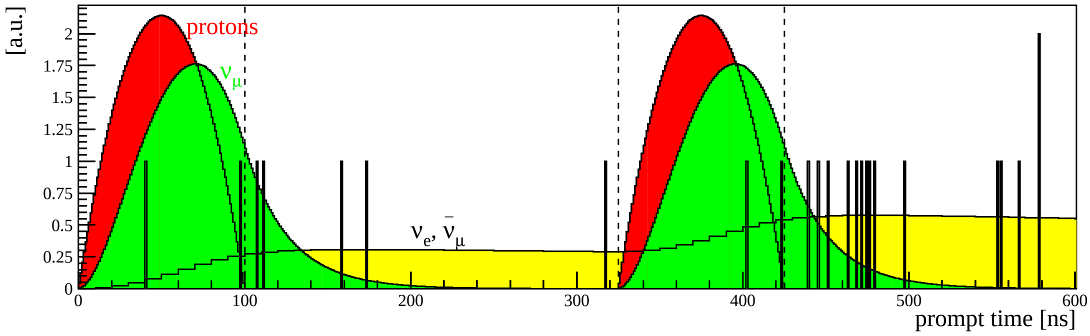

Figure 4.6: Prompt time distributions of **i)** $\nu_\mu \rightarrow \nu_e$ oscillation candidate sequences (black bars), **ii)** the two in time parabolic shaped proton pulses (defining the two analyzed 100 ns narrow time windows), **iii)** ν_μ from π^+-decays as well as **iv)** ν_e and $\overline{\nu_\mu}$ from already starting subsequent μ^+-decays (heights of histograms in arbitrary units).

background for $\nu_\mu\!\rightarrow\nu_e$ appearance. Contrary to these ν_e from μ^+-decays, neutrinos from π^+-decays have a fixed energy at 29.8 MeV. Therefore, the upper threshold on the prompt visible energy is reduced to 14 MeV for the $\nu_\mu\!\rightarrow\nu_e$ appearance search, in consideration of the large Q-value of 17.33 MeV for the CC-reaction ${}^{12}\mathrm{C}\,(\,\nu_e\,,\mathrm{e}^-\,)\,{}^{12}\mathrm{N}_{\mathrm{g.s.}}$. This reduces the background from μ^+-decays by more than an order of magnitude, together with the 100 ns narrow time windows. Apart from the cuts on the prompt visible energy (10 MeV $< E_{pr,\,vis} \leq$ 14 MeV) and on the prompt time ($0ns \ldots 100ns$, $325ns \ldots 425ns$), all other cuts remain identical to the ones applied for the spectroscopic measurement of the exclusive CC-reaction ${}^{12}\mathrm{C}\,(\,\nu_e\,,\mathrm{e}^-\,)\,{}^{12}\mathrm{N}_{\mathrm{g.s.}}$ in the late time window of μ^+-decay (*see Chapter* 3.1). The search for $\nu_\mu\!\rightarrow\nu_e$ appearance finds 4 ν_e-like sequences satisfying all cuts. *Fig.* 4.6 includes the prompt time distribution of $\nu_\mu\!\rightarrow\nu_e$ oscillation candidate sequences in the range from 0 ns to 600 ns after beam-on-target.

4.3.1 Background Expectation for $\nu_\mu\!\rightarrow\nu_e$ Appearance

There are three different background components taken into account for $\nu_\mu\!\rightarrow\nu_e$ appearance:

- ν_e produced by subsequent μ^+-decays
- cosmic induced background
- random background

All numbers required for calculating each background expectation for $\nu_\mu\!\rightarrow\nu_e$ appearance can be measured precisely by re-performing a slightly modified analysis of the exclusive CC-reaction ${}^{12}\mathrm{C}\,(\,\nu_e\,,\mathrm{e}^-\,)\,{}^{12}\mathrm{N}_{\mathrm{g.s.}}$ (*see Chapter* 3.1): For this, each of the two 100 ns narrow time windows is evaluated separately (1.pulse: $0ns \ldots 100ns$, 2.pulse: $325ns \ldots 425ns$), with the reduced upper threshold cut on the prompt visible energy being applied (10 MeV $<$ $E_{pr,\,vis} \leq$ 14 MeV).

Background from ν_e Produced by Subsequent μ^+-Decays

The overall detection efficiencies $\epsilon^{Kn}_{CC,\,n.pulse}$ for the exclusive CC-reaction ${}^{12}\mathrm{C}\,(\,\nu_e\,,\mathrm{e}^-\,)\,{}^{12}\mathrm{N}_{\mathrm{g.s.}}$ can be deduced for the first evaluation window in K1 and in K2, as well as for the second evaluation window in K1 and in K2. These numbers are compared with the standard overall detection efficiencies $\epsilon^{Kn}_{CC,\,std}$ for the exclusive CC-reaction ${}^{12}\mathrm{C}\,(\,\nu_e\,,\mathrm{e}^-\,)\,{}^{12}\mathrm{N}_{\mathrm{g.s.}}$ in K1 and K2, respectively. The entire number N^{global}_{CC} of ν_e from μ^+-decays, measured in the late time window in K1+K2 via the exclusive CC-reaction ${}^{12}\mathrm{C}\,(\,\nu_e\,,\mathrm{e}^-\,)\,{}^{12}\mathrm{N}_{\mathrm{g.s.}}$, is known, as well as the required flux- and efficiency-weight-factors w^{K1}_{std} for K1 and w^{K2}_{std} for K2. Consequently, the expected numbers $\langle N_{CC}\rangle^{Kn}_{\nu_\mu\rightarrow\,\nu_e}$ of ν_e from μ^+-decays can be calculated for the $\nu_\mu\!\rightarrow\nu_e$ appearance search in K1 and K2 as follows:

$$
\begin{aligned}
\langle N_{CC}\rangle^{K1}_{\nu_\mu\rightarrow\,\nu_e} &= N^{global}_{CC}\cdot w^{K1}_{std}\cdot\frac{\epsilon^{K1}_{CC,\,1.pulse}+\epsilon^{K1}_{CC,\,2.pulse}}{\epsilon^{K1}_{CC,\,std}} = \\
&= 846.07\cdot 0.56\cdot\frac{2.52\cdot 10^{-4}+8.80\cdot 10^{-4}}{0.31} = 1.74\pm 0.06 \\
\langle N_{CC}\rangle^{K2}_{\nu_\mu\rightarrow\,\nu_e} &= N^{global}_{CC}\cdot w^{K2}_{std}\cdot\frac{\epsilon^{K2}_{CC,\,1.pulse}+\epsilon^{K2}_{CC,\,2.pulse}}{\epsilon^{K2}_{CC,\,std}} = \\
&= 846.07\cdot 0.44\cdot\frac{1.97\cdot 10^{-4}+6.88\cdot 10^{-4}}{0.22} = 1.47\pm 0.05
\end{aligned}
$$

Hence, the global background expectation $\langle N_{CC}\rangle^{K1+K2}_{\nu_\mu\rightarrow\,\nu_e}$ for $\nu_\mu \rightarrow \nu_e$ appearance from ν_e from μ^+-decays, measured via the exclusive CC-reaction $^{12}\mathrm{C}\,(\,\nu_e\,,\mathrm{e}^-\,)\,^{12}\mathrm{N}_{\mathrm{g.s.}}$ in K1+K2 amounts to:

$$\langle N_{CC}\rangle^{K1+K2}_{\nu_\mu\rightarrow\,\nu_e} = 3.21\pm 0.11$$

Cosmic Induced and Random Background

The random background expectation for $\nu_\mu \rightarrow \nu_e$ appearance can be determined at high precision from the entire data (*see Chapter* 3.1). A prompt event satisfying all cuts is simulated for every recorded beam-period. The data search for a sequential event is then performed for each beam-period as well, in order to measure the random probability for observing a ν_e-like sequence. Hence, the number of expected random background sequences for $\nu_\mu \rightarrow \nu_e$ appearance is given by the product of the measured random probability and the measured number of prompt single-events[1].

The cosmic background expectation for $\nu_\mu \rightarrow \nu_e$ appearance can be measured very precisely as well by analyzing the pre-beam time window, which is almost one thousand times longer than the two 100 ns short neutrino time windows. The portion of cosmic background being due to random sequences is subtracted thereby.

Table 4.1 lists all numbers of expected cosmic induced and random background for the first 100 ns narrow time window and the second, respectively. The global cosmic induced and random background expectation $\langle N_{cos,\,rnd}\rangle^{K1+K2}_{\nu_\mu\rightarrow\,\nu_e}$ for $\nu_\mu \rightarrow \nu_e$ appearance in K1+K2 comes out as:

$$\langle N_{cos,\,rnd}\rangle^{K1+K2}_{\nu_\mu\rightarrow\,\nu_e} = 0.72\pm 0.03$$

$\langle background \rangle$	1. pulse ($0ns \ldots 100ns$)	2. pulse ($325ns \ldots 425ns$)	Σ pulses
$\langle N_{cos} \rangle$	$3.0 \cdot 10^{-2} \pm 0.5 \cdot 10^{-2}$	$3.0 \cdot 10^{-2} \pm 0.5 \cdot 10^{-2}$	0.06 ± 0.01
$\langle N_{rnd} \rangle$	0.32 ± 0.02	0.34 ± 0.02	0.66 ± 0.03

Table 4.1: Cosmic induced and random background expectation for $\nu_\mu \!\rightarrow \nu_e$ appearance (numbers derived by analyzing the first pulse and the second pulse, respectively).

Thus, the cosmic induced and random background components are almost negligible compared to ν_e from μ^+-decays which constitute the major background for $\nu_\mu \!\rightarrow \nu_e$ appearance. Finally, the overall global background expectation $\langle N_{CC,\,cos,\,rnd} \rangle^{K1+K2}_{\nu_\mu \rightarrow \nu_e}$ for $\nu_\mu \!\rightarrow \nu_e$ appearance amounts to:

$$\langle N_{CC,\,cos,\,rnd} \rangle^{K1+K2}_{\nu_\mu \rightarrow \nu_e} = 3.93 \pm 0.12$$

This is in excellent agreement with the 4 ν_e-like sequences found by searching for $\nu_\mu \!\rightarrow \nu_e$ appearance (*see Fig.* 4.6).

4.3.2 Full $\nu_\mu \!\rightarrow \nu_e$ Oscillation Expectation and Measurement of ^{12}C (ν_e , e$^-$) ^{12}N$_{\text{g.s.}}$ Cross Section at 29.8 MeV

In order to determine the number of ν_e sequences, which are expected under the assumption of full $\nu_\mu \!\rightarrow \nu_e$ oscillation, the cross section for the $^{12}\mathrm{C}\,(\,\nu_e\,,\mathrm{e}^-\,)\,^{12}\mathrm{N}_{\text{g.s.}}$ at 29.8 MeV ν_e-energy must be known. This cross section at fixed ν_e-energy can be derived straightforward from the already measured cross section $\langle \sigma(^{12}\mathrm{C}\,(\,\nu_e\,,\mathrm{e}^-\,)\,^{12}\mathrm{N}_{\text{g.s.}}) \rangle$ which is averaged over the energy spectrum of ν_e from μ^+-decay at rest (*see Chapter* 3.1). Both the energy spectrum $\Phi_{\nu_e}(E)$ of these ν_e and the energy dependence $\sigma_{theo}(E)$ of the cross section $\sigma(^{12}\mathrm{C}\,(\,\nu_e\,,\mathrm{e}^-\,)\,^{12}\mathrm{N}_{\text{g.s.}})$ are known well enough (*see Fig.* 4.4 a+b). Hence, the cross section at 29.8 MeV ν_e-energy can be calculated as follows:

$$\sigma(^{12}\mathrm{C}\,(\,\nu_e\,,\mathrm{e}^-\,)\,^{12}\mathrm{N}_{\text{g.s.}})_{@29.8\,MeV} = \frac{\langle \sigma(^{12}\mathrm{C}\,(\,\nu_e\,,\mathrm{e}^-\,)\,^{12}\mathrm{N}_{\text{g.s.}}) \rangle \;\cdot\; \{\sigma_{theo}(29.8\,MeV) \cdot \Phi_{\nu_e}(29.8\,MeV)\}}{\frac{\int_{E_{min}}^{E_{max}} \sigma_{theo}(E) \cdot \Phi_{\nu_e}(E)\,dE}{(E_{max} - E_{min})}} \tag{4.16}$$

---

[1] Number of prompt single-events (neutrinos and cosmic background) with respect to different cuts and corrected according to different dead-times for single-events and CC-sequences (*see Appendix* D).

The denominator equals the mean value of the product $\sigma_{theo}(E) \cdot \Phi_{\nu_e}(E)$ and is thereby computed for ν_e-energies greater than $E_{min} = 17.33\,\text{MeV}$ (Q-value) and less than $E_{max} = 52.83\,\text{MeV}$ $(0.5 \cdot m_\mu c^2)$. Thus, the measured cross section for the exclusive CC-reaction $^{12}\text{C}\,(\,\nu_e\,,\text{e}^-\,)\,^{12}\text{N}_{\text{g.s.}}$ at 29.8 MeV ν_e-energy amounts to:

$$\boxed{\sigma(^{12}\text{C}\,(\,\nu_e\,,\text{e}^-\,)\,^{12}\text{N}_{\text{g.s.}})_{@29.8\,MeV} = (5.6 \pm 0.2(stat.) \pm 0.4(syst.)) \cdot 10^{-42} cm^2}$$

Now, in analogy to *Chapter* 3.1 the definition of the cross section for $^{12}\text{C}\,(\,\nu_e\,,\text{e}^-\,)\,^{12}\text{N}_{\text{g.s.}}$ can be rewritten hereby as:

$$\begin{aligned}\langle N \rangle^{\nu_\mu \rightarrow \nu_e}_{full\,oscillation} \;=\;& \sigma(^{12}\text{C}\,(\,\nu_e\,,\text{e}^-\,)\,^{12}\text{N}_{\text{g.s.}})_{@29.8\,MeV} \cdot \Omega_{eff} \cdot N_{target} \cdot \\ & \cdot \Big[\, \epsilon^{K1}_{MC} \cdot \epsilon_{t_{pr},\,\tau_\pi} \cdot \epsilon^{K1}_{t_{seq}} \cdot \epsilon^{K1}_{stack,\,pr,\,\tau_\pi} \cdot \epsilon^{K1}_{stack,\,seq} \cdot \epsilon^{K1}_{SMU} \cdot (\epsilon^{K1}_{PPP} \cdot \Phi^{K1}_\nu) + \\ & + \epsilon^{K2}_{MC,\,ECoff} \cdot \epsilon_{t_{pr},\,\tau_\pi} \cdot \epsilon^{K2}_{t_{seq}}(\epsilon_{MC,\,ECon/off}) \cdot \epsilon^{K2}_{stack,\,pr,\,\tau_\pi} \cdot \epsilon^{K2}_{stack,\,seq} \cdot \epsilon^{K2}_{SMU} \cdot \Phi^{K2}_\nu \Big]\end{aligned}$$

Thus, the number $\langle N \rangle^{\nu_\mu \rightarrow \nu_e}_{full\,oscillation}$ of ν_e, which are expected under the assumption of full $\nu_\mu \rightarrow \nu_e$ oscillation, is inferred. Except from those efficiencies listed in *Table* 4.2, that are either dependent on the MC-simulation of the new signal or on the π^+-lifetime, all other values remain unchanged thereby. Finally, the full $\nu_\mu \rightarrow \nu_e$ oscillation expectation comes out as:

$$\langle N \rangle^{\nu_\mu \rightarrow \nu_e}_{full\,oscillation} = 397.8 \pm 13.8$$

		for K1 [%]	for K2 [%]
MC-efficiency	ϵ_{MC}	47.11	51.88
prompt time efficiency	$\epsilon_{t_{pr},\,\tau_\pi}$	79.61	79.61
sequential time efficiency	$\epsilon_{t_{seq}}(\epsilon_{MC,\,ECon/off})$		61.22
stack efficiency for prompt event	$\epsilon_{stack,\,pr,\,\tau_\pi}$	91.23	82.00

Table 4.2: Differences in input values for full $\nu_\mu \rightarrow \nu_e$ oscillation expectation compared to the $^{12}\text{C}\,(\,\nu_e\,,\text{e}^-\,)\,^{12}\text{N}_{\text{g.s.}}$ analysis in *Chapter* 3.1: Efficiencies depending either on the MC-simulation of the new signal or on the π^+-lifetime (*see also Appendix* D).

4.3.3 Exclusion Limit for $\nu_\mu \rightarrow \nu_e$ Appearance with Bayesian Method

KARMEN shows no evidence for $\nu_\mu \rightarrow \nu_e$ appearance in the LSND-region of squared-mass differences. The number of 4 ν_e-like sequences found by searching for $\nu_\mu \rightarrow \nu_e$ appearance is well in agreement with the background expectation of 3.93 ν_e-like sequences. Thus, in the following an exclusion limit for an oscillation signal at a given confidence level (CL) will be inferred in an appropriate Bayesian approach. A possible small oscillation signal strength s could come on top of the small number of expected background b, which is known very accurately in this case. Thereby, the observed discrete number of events is a random variable of the Poisson type.

The Poisson distribution $P(r|\mu)$ for the discrete variable r, with the parameter $\mu = \langle P(r) \rangle$ (mean value) is defined as:

$$P(r|\mu) = \frac{\mu^r \cdot e^{-\mu}}{r!} \qquad r = 0, 1, 2, \ldots \ ; \mu > 0 \tag{4.17}$$

This distribution is evidently correctly normalized. Furthermore, the Poisson distribution possesses the property that the mean value μ equals the variance. For small μ the Poisson distribution is very asymmetric and has a tail to the right of the mean. Asymptotically, when μ goes towards infinity, the Poisson distribution becomes identical to the normal distribution. The similarity between these two distributions is rather close[2] already at $\mu = 20$. The maximum probability is at $r = [\mu]$, and with an equal, adjacent maximum at $\mu - 1$ if μ is an integer.

In order to determine the excluded oscillation signal strength s, which can be added to the number of expected background b at a given confidence level CL for N_{obs} observed events, the following background subtraction method is utilized according to *Bayes' theorem* [CER00]:

$$CL = 1 - \frac{\mathcal{P}_1(r_{b+s} \leq N_{obs})}{\mathcal{P}_2(r_b \leq N_{obs})} \tag{4.18}$$

Thus, test statistics for r (sample sizes $\geq$ 10.000) are generated according to the Poisson distributions $P(r|\mu = b + s)$ and $P(r|\mu = b)$, respectively. Herewith, the ratio of the two probabilities $\mathcal{P}_1$ and $\mathcal{P}_2$ in *Eq.* 4.18 is computed, simply by counting the occurrences of $r \leq N_{obs}$ and comparing this sum to the entire number of simulated experiments. The requested ratio of the probabilities, fixed by the value of CL, is derived in an iterative process: The oscillation signal strength s is varied until *Eq.* 4.18 is fulfilled sufficiently enough. Hence, an oscillation signal strength $s_{90\%CL} = 4.81$ can be excluded at 90%CL for the expected background $b = 3.93$ and the number of observed ν_e-like sequences $N_{obs} = 4$. The upper limit on the oscillation probability is then given by the quotient of the excluded oscillation signal strength $s_{90\%CL} = 4.81$ and the full oscillation expectation

---

[2] For $\mu > 60$ the normal distribution was taken in any case whilst computing.

$\langle N \rangle^{\nu_\mu \rightarrow \nu_e}_{full\,oscillation} = 397.80$. Thus, at 90%CL this Bayesian upper limit on the $\nu_\mu \rightarrow \nu_e$ oscillation probability $\mathcal{P}^{\nu_\mu \rightarrow \nu_e}_{90\%CL}$ (in the Δm^2_{LSND}-region) states:

$$\mathcal{P}(\nu_\mu \rightarrow \nu_e) \, < \, 1.21 \cdot 10^{-2} \; (90\%CL)$$

In analogy to *Section* 4.2.1, the oscillation-amplitude $\sin^2(2\Theta)$ can be finally calculated as function of Δm^2 (within the 2-flavor-formalism), by using the same distance-weight-functions $w_{L,main}$ and $w_{L,\mu SR}$ as well as the same ratio $r_{\mu SR}$ of neutrinos from the μSR-pre-target:

$$\begin{aligned} \mathcal{P}^{\nu_\mu \rightarrow \nu_e}_{90\%CL} \quad = \quad & \sin^2(2\Theta) \cdot \left[\, r_{main} \cdot \int\limits_{L'} w_{L,main}(L) \cdot \sin^2\left(\frac{1.27 \cdot \Delta m^2 \cdot L}{E_\nu} \right) \, dL \right. \\ & \left. + \, r_{\mu SR} \cdot \int\limits_{L'} w_{L,\mu SR}(L) \cdot \sin^2\left(\frac{1.27 \cdot \Delta m^2 \cdot L}{E_\nu} \right) \, dL \right] \end{aligned} \tag{4.19}$$

Contrary to *Eq.* 4.15 in *Section* 4.2.1, the energy-weight-function $w_{\Phi,\sigma,\epsilon}(E_\nu)$ is not incorporated, because the ν-energy is fixed at 29.8 MeV from π^+-decay at rest. *Fig.* 4.7 shows the resulting $90\%CL$ exclusion curve for $\nu_\mu \rightarrow \nu_e$ appearance. Regions on the right hand side of the curve are excluded at $90\%CL$. KARMEN attains maximal sensitivity for $\nu_\mu \rightarrow \nu_e$ appearance at $2\,eV^2$ ($\simeq 29.8\,[MeV]/17.7\,[m]$). For large Δm^2 the following upper limit is derived for $\boxed{\nu_\mu \rightarrow \nu_e}$ appearance:

$$\boxed{\sin^2(2\Theta) \, < \, 2.4 \cdot 10^{-2} \; (90\%CL)}$$

This corresponds to an improvement of the old K1 limit [Eit95] by almost a factor of two, due to doubled statistics and the utilization of the measured $^{12}\mathrm{C}\,(\,\nu_e\,,\mathrm{e}^-\,)\,^{12}\mathrm{N}_{\mathrm{g.s.}}$ cross section at 29.8 MeV, which eliminates the theoretical uncertainty. KARMEN is more sensitive to $\nu_\mu \rightarrow \nu_e$ appearance than the NuTeV-experiment in the range of Δm^2 from $0.1\,eV^2$ to $10\,eV^2$ [Avv02].
In a (3+1) scenario ($\Delta m^2 = \Delta m^2_{41} \simeq \Delta m^2_{42} \simeq \Delta m^2_{43}$) this oscillation-amplitude $\sin^2(2\Theta)$ for $\nu_\mu \rightarrow \nu_e$ appearance is then, under the assumption of CP-invariance, given by $\sin^2(2\Theta) = 4 \cdot U^2_{e4} \cdot U^2_{\mu 4}$ (*compare Eq.* 4.4) [Sor03].
Hence, the search for $\nu_\mu \rightarrow \nu_e$ appearance in KARMEN does neither deliver evidence for heavy sterile neutrinos nor for CP-violation in the LSND-region of squared-mass differences.

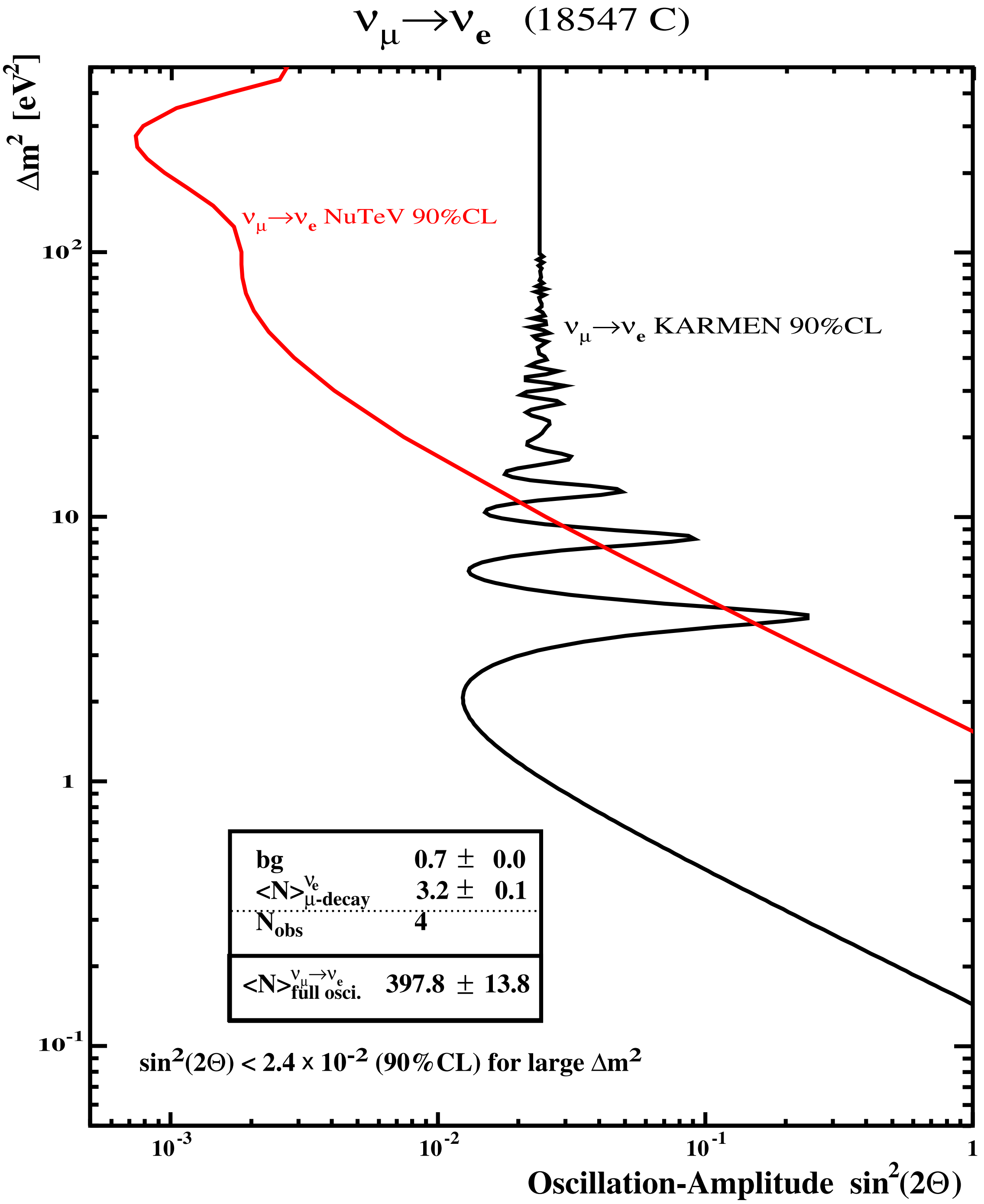

Figure 4.7: Exclusion curve for $\nu_\mu \rightarrow \nu_e$ appearance in KARMEN (dark curve) compared to the result from NuTeV [Avv02] (areas on the right hand side of each curve are excluded at $90\% CL$).

4.4 Search for $\bar{\nu}_\mu \rightarrow \bar{\nu}_e$ Appearance (LSND–Oscillation)

In the following the results from two other complementary methods for the $\bar{\nu}_\mu \rightarrow \bar{\nu}_e$ oscillation search will be introduced in detail. The first method, using sequences for the $\bar{\nu}_\mu \rightarrow \bar{\nu}_e$ appearance search, is basically the same method, which has been chosen for the final KARMEN2 result in [Arm02], apart from the statistical approach. A complementary intuitive window-method will be presented with the application of the Bayesian approach, which has already been introduced in *Section* 4.3.3. The second method, using single-events for the $\bar{\nu}_\mu \rightarrow \bar{\nu}_e$ appearance search, delivers a new independent probe of the LSND evidence region with KARMEN2.

4.4.1 Method using Sequences for $\bar{\nu}_\mu \rightarrow \bar{\nu}_e$ Appearance Search

The predominant reaction for detecting $\bar{\nu}_e$ with KARMEN is the inverse β-decay p($\bar{\nu}_e$,e^+)n on the free protons of the organic scintillator (cross section[3] $\langle\sigma_1\rangle = 93.5 \cdot 10^{-42}\,cm^2$):

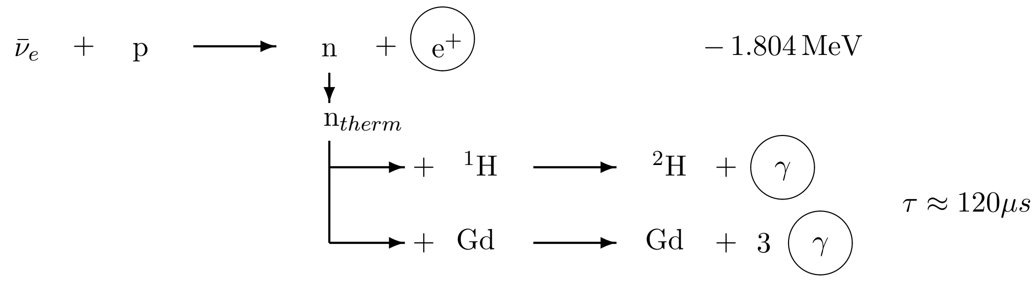

In a dedicated sequence analysis one searches for a prompt e^+ followed in time by a spatially correlated neutron from the CC-reaction above. The prompt e^+ possesses continuous visible energies up to roughly 50 MeV, due to the small Q-value of 1.8 MeV for this CC-reaction and the maximum ν-energy of 52.8 MeV from μ^+-decay at rest. Moreover, the lifetime of the muons ($\tau_\mu = 2.2\,\mu$s) determines the exponentially decreasing time distribution of the prompt positrons. A delayed signal can be observed in the vicinity of the prompt e^+, with a time distribution according to the thermalization and diffusion time of the sequential neutron inside the liquid scintillator ($\tau = 120\,\mu$s). The sequential neutron is detected via (n,γ)-capture, either on the free protons of the organic scintillator or on the gadolinium of the coated paper inside the module walls. Thus, the delayed signal has continuous visible energies up to 8 MeV from neutron capture on Gd as well as a peak at around 2.2 MeV from neutron capture on protons. The detection efficiency of the sequential neutron can be independently measured with another sequence analysis investigating stopped cosmic ray muons inside the KARMEN-detector [Arm02]:

$$\mu^- + {}^{12}C \rightarrow {}^{12-x}B + x \cdot n + \nu_\mu \qquad (4.20)$$

This capture reaction produces neutrons with kinetic energies in the few MeV-range, comparable to the energy of the neutrons from the p($\bar{\nu}_e$,e^+)n process. Additionally, it

---

[3] Total cross section averaged over the $\bar{\nu}_\mu$-energy spectrum.

is demonstrated that such neutrons can be well detected inside a coincidence volume of $V_c \approx 1\,m^3$ ($|\Delta X| \leq 80\,\mathrm{cm}$, $|\Delta ROW| \leq 2.5$, $|\Delta COL| \leq 2.5$) around the endpoint of the muon track. By requiring furthermore that the delayed signal occurs within a coincidence time of $5\,\mu\mathrm{s} \leq \Delta T \leq 300\,\mu\mathrm{s}$ and possesses visible energies $E_{seq,\,vis} \leq 8\,\mathrm{MeV}$, the overall neutron detection efficiency comes out as [Arm02], [Jan95]:

$$\epsilon_n = (42 \pm 3)\% \tag{4.21}$$

The unique signature of the sequential detection of $\bar{\nu}_e$ strongly suppresses background reactions and it is possible to set the lower boundary on the prompt visible e^+-energy down to 16 MeV. Therefore, another exclusive CC-reaction with a minor contribution to the detection of $\bar{\nu}_e$ has to be taken into account. Beside of the process p($\bar{\nu}_e$,e^+)n ($-Q = -1.8\,\mathrm{MeV}$), the inverse β-decay ^{12}C($\bar{\nu}_e$,e^+n)^{11}B ($-Q = -16.8\,\mathrm{MeV}$) on carbon nuclei of the organic scintillator makes the same sequential neutron detection applicable:

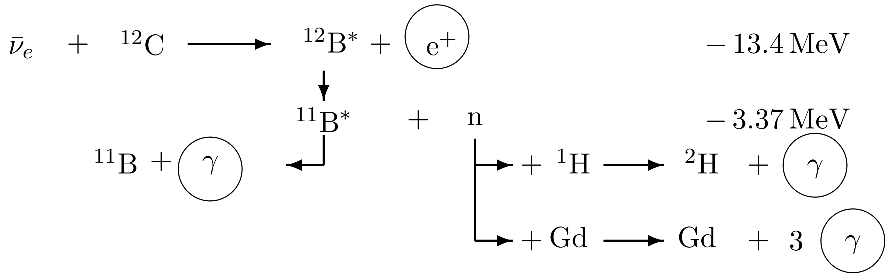

This second process ^{12}C($\bar{\nu}_e$,e^+n)^{11}B contributes roughly 5% to the entire $\bar{\nu}_e$ sequential detection, in consideration of the smaller cross section[4] for the ^{12}C($\bar{\nu}_e$,e^+n)^{11}B reaction ($\langle\sigma_2\rangle = 8.5 \cdot 10^{-42}\,cm^2$ compared to $\langle\sigma_1\rangle = 93.5 \cdot 10^{-42}\,cm^2$ for p($\bar{\nu}_e$,e^+)n) and the smaller number of ^{12}C-nuclei in the organic scintillator ($N_C = 2.54 \cdot 10^{30}$ compared to $N_p = 4.52 \cdot 10^{30}$).

In order to search for $\bar{\nu}_\mu \rightarrow \bar{\nu}_e$ oscillation candidate sequences, the following cuts and general event requirements are applied to the KARMEN2 data, which was taken after the upgrade of the detector with an additional veto-counter:

0.6 μs	$\leq$	T_{pr}	$\leq$	10.6 μs	*; prompt time*
5 μs	$\leq$	ΔT	$\leq$	300 μs	*; time-difference*
16 MeV	$\leq$	$E_{pr,\,vis}$	$\leq$	50 MeV	*; prompt visible energy*
0 MeV	$\leq$	$E_{seq,\,vis}$	$\leq$	8 MeV	*; sequential vis. energy*
−175 cm	$\leq$	X_{pr}	$\leq$	175 cm	*; prompt x-position*
0	$\leq$	ROW_{pr}	$\leq$	32.5	*; prompt row*
0	$\leq$	COL_{pr}	$\leq$	16.5	*; prompt column*
		$\lvert\Delta X\rvert$	$\leq$	80 cm	*; x-position-difference*
		$\lvert\Delta ROW\rvert$	$\leq$	2.5	*; row-difference*
		$\lvert\Delta COL\rvert$	$\leq$	2.5	*; column-difference*

---

[4] Total cross sections averaged over the $\bar{\nu}_\mu$-energy spectrum.

no Veto hit			*; prompt event*
M_{pr}	$\leq$	10	*; prompt multiplicity*
N_{seq}	$=$	1	*; no. of sequences*
Thresh	$=$	30 chn.	*; prompt threshold cut (if* $M_{pr} = 1$*)*
		24 μs	*; pr. dead-time after stack-entry*
		14 μs	*; pr. dead-time after veto-only VO*
T_{REL}	$\leq$	50 ns	*; rel. time between modules*
SMU-reduction			*; see Chapter 3.1.2*

The sequence analysis of the KARMEN2 data, which was acquired from the year 1997 until 2001, delivers 15 $\bar{\nu}_\mu \rightarrow \bar{\nu}_e$ oscillation candidate sequences satisfying all cuts and general event requirements. *Fig.* 4.8 shows the time, visible energy and spatial distributions of the prompt events and the concatenated delayed events, respectively. The remaining background components after the upgrade for the sequential $\bar{\nu}_\mu \rightarrow \bar{\nu}_e$ appearance search will be evaluated in the following section.

4.4.1.1 Background for Sequential $\bar{\nu}_\mu \rightarrow \bar{\nu}_e$ Appearance Search

Apart from the simulated $\bar{\nu}_e$-contamination, the background sources for the performed (e^+,n)-sequence search can be measured very precisely: The cosmic ray induced background, the exclusive CC-reaction $^{12}\mathrm{C}\,(\,\nu_e\,,\mathrm{e}^-\,)\,^{12}\mathrm{N}_{\mathrm{g.s.}}$ and the ν_e-induced random background.

Cosmic Ray Induced Background

The majority of the cosmic induced background is already rejected by the dead-time applied after every stack-entry or veto-only entry (VO), the stopped muons (SMU) reduction and other general event requirements (*see Chapter* 3.1 and [Arm98]).
The remaining dominant cosmic ray induced background is due to muon interactions in the 7000 t steel shielding blockhouse, which generate high-energy neutrons. Two different reaction mechanisms can be distinguished [Arm02]:

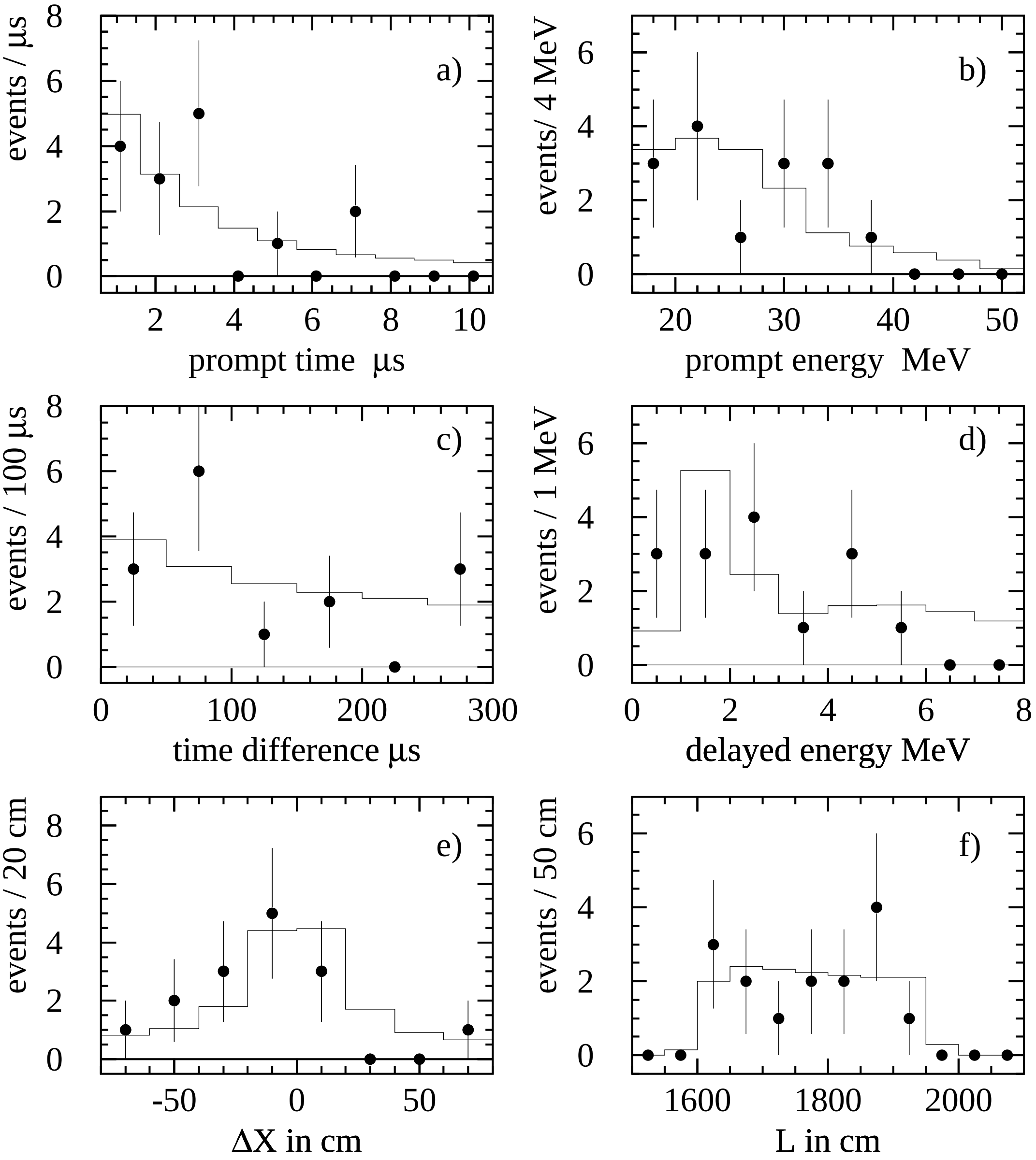

Figure 4.8: Final KARMEN2 $\bar{\nu}_\mu \rightarrow \bar{\nu}_e$ oscillation candidate sequences [Arm02]: a) time and b) visible energy of prompt event, c) time-difference between prompt and delayed sequential event, d) visible energy of sequential event, e) spatial correlation between prompt and sequential event and f) distance of prompt event from main-target. The 15 $\bar{\nu}_\mu \rightarrow \bar{\nu}_e$ oscillation candidate sequences are in very good agreement with the background expectation of 15.8 (solid line).

- μ^- capture on ^{56}Fe:

$$\mu^- + {}^{56}Fe \rightarrow {}^{56-x}Mn + x \cdot n + \nu_\mu \tag{4.22}$$

  Negative charged muons being stopped in iron are predominantly captured and neutrons with energies up to 20 MeV can be emitted by the nucleus.

- Deep inelastic scattering (DIS) of muons on ^{56}Fe:

$$\mu^\pm + {}^{56}Fe \rightarrow X + y \cdot n + \mu^\pm \tag{4.23}$$

  Virtual photons radiated by cosmic muons interact with the iron nuclei and can produce spallation neutrons with energies up to a few GeV.

High-energy neutrons from those processes can penetrate into the liquid scintillator causing prompt signals with visible energies up to 200 MeV via elastic n-p scattering. After thermalization and diffusion, the neutrons can then be captured either on the free protons or on the gadolinium by producing a sequential signal. Thus, the high-energy neutrons, originating from cosmic ray interactions inside the iron blockhouse, cause delayed coincidences which cannot be distinguished from the $\bar{\nu}_e$ sequential signature. The crucial identification of the high-energy neutrons is achieved by the new third system of veto-counters placed inside the steel shielding and thus tagging the initial cosmic muons [Arm98], [Rei98]. The KARMEN-upgrade with a new system of veto-counters reduced the cosmic background for the sequential $\bar{\nu}_\mu \rightarrow \bar{\nu}_e$ appearance search by a factor of 35 [Arm02]. Therefore, only data taken in KARMEN2 was considered for the final evaluation.

The cosmic background expectation for $\bar{\nu}_\mu \rightarrow \bar{\nu}_e$ appearance can be measured very precisely by analyzing the pre-beam time window, which is 19 times longer than the 10 μs short neutrino time window[5]. The portion of cosmic background being due to random sequences is not subtracted thereby. Hence, the expectation of the cosmic induced background for $\bar{\nu}_\mu \rightarrow \bar{\nu}_e$ appearance in K2 is found to be:

$$\langle N_{cos} \rangle^{K2}_{\bar{\nu}_\mu \rightarrow \bar{\nu}_e} = 3.9 \pm 0.2$$

The ν_e-Induced Exclusive CC-Reaction ^{12}C (ν_e , e$^-$) ^{12}N$_{\text{g.s.}}$

After the suppression of the cosmic background with the new system of veto-counters, the exclusive CC-reaction ^{12}C (ν_e , e$^-$) ^{12}N$_{\text{g.s.}}$ constitutes the largest background component for $\bar{\nu}_\mu \rightarrow \bar{\nu}_e$ appearance in K2. (e^-,e^+)-sequences from ^{12}C (ν_e , e$^-$) ^{12}N$_{\text{g.s.}}$, which satisfy all cuts and event requirements for the $\bar{\nu}_\mu \rightarrow \bar{\nu}_e$ appearance search, are indistinguishable from (e^+,n)-sequences from e.g. p($\bar{\nu}_e$,e^+)n. This ambiguity affects only less than 2% of all detected (e^-,e^+)-sequences, primarily due to the small fraction of ^{12}N$_{\text{g.s.}}$ (τ = 15.9 ms) decaying within the first 300 μs and depositing visible energies of less than 8 MeV. The expected number $\langle N_{CC} \rangle^{K2}_{\bar{\nu}_\mu \rightarrow \bar{\nu}_e}$ of (e^-,e^+)-sequences, which contribute to the background

---

[5] The decreasing stack-efficiency in the neutrino time window has to be taken into account, with respect to the applied dead-time (*see Appendix* D).

for the $\bar{\nu}_\mu \rightarrow \bar{\nu}_e$ appearance search in K2, can be calculated in analogy to *Chapter* 3.1 from the definition of the cross section for $^{12}\mathrm{C}\,(\,\nu_e\,,\mathrm{e}^-\,)\,^{12}\mathrm{N}_{\mathrm{g.s.}}$:

$$\begin{aligned}\langle N_{CC}\rangle^{K2}_{\bar{\nu}_\mu \rightarrow \bar{\nu}_e} &= \langle \sigma(^{12}\mathrm{C}\,(\,\nu_e\,,\mathrm{e}^-\,)\,^{12}\mathrm{N}_{\mathrm{g.s.}})\rangle \cdot \Omega_{eff} \cdot N_C \cdot \\ &\cdot \left[\,\epsilon^{K2}_{MC,\,ECoff} \cdot \epsilon_{t_{pr},\,\tau_\mu} \cdot \epsilon^{K2}_{t_{seq}}(\epsilon_{MC,\,ECon/off}) \cdot \epsilon^{K2}_{stack,\,pr,\,\tau_\mu} \cdot \epsilon^{K2}_{stack,\,seq} \cdot \epsilon^{K2}_{SMU} \cdot \Phi^{K2}_{\nu}\right]\end{aligned}$$

The cross section for $^{12}\mathrm{C}\,(\,\nu_e\,,\mathrm{e}^-\,)\,^{12}\mathrm{N}_{\mathrm{g.s.}}$ has been precisely measured with KARMEN and is very well understood. The values of the efficiencies differ from the corresponding values in *Chapter* 3.1 (apart from the SMU-efficiency ϵ^{K2}_{SMU}), due to different event cuts and applied dead-times (*see Appendix* D). Taking the value of $(9.4 \pm 0.4(stat.) \pm 0.8(syst.)) \cdot 10^{-42} cm^2$ for the $^{12}\mathrm{C}\,(\,\nu_e\,,\mathrm{e}^-\,)\,^{12}\mathrm{N}_{\mathrm{g.s.}}$ cross section[6], the expectation of the herefrom ν_e-induced background for $\bar{\nu}_\mu \rightarrow \bar{\nu}_e$ appearance in K2 amounts to:

$$\langle N_{CC}\rangle^{K2}_{\bar{\nu}_\mu \rightarrow \bar{\nu}_e} = 5.1 \pm 0.2$$

ν_e-Induced Random Background

The random background expectation for the sequential $\bar{\nu}_\mu \rightarrow \bar{\nu}_e$ appearance search can be determined in the known way at high precision from the entire data (*see Chapter* 3.1). A prompt event satisfying all cuts is simulated for every recorded beam-period. The data search for a sequential event is then performed for each beam-period as well, in order to measure the random probability for observing a $\bar{\nu}_e$-like sequence. Hence, the number of expected random background sequences is given by the product of the measured random probability and the measured number of prompt single-events[7] (after subtraction of the cosmic background expectation from pre-beam). The portion of cosmic induced random background is already accounted for in the expectation $\langle N_{cos}\rangle^{K2}_{\bar{\nu}_\mu \rightarrow \bar{\nu}_e}$ of the cosmic ray induced background. Due to the requirement that prompt visible energies have to be larger than 16 MeV, $\bar{\nu}_\mu$ do not contribute via the NC-reaction $^{12}\mathrm{C}\,(\,\nu\,,\nu'\,)\,^{12}\mathrm{C}^*(\,1^+\,,1\,;15{,}11$ MeV) to the random background. Thus, the expectation of the purely ν_e-induced random background is found to be:

$$\langle N_{rnd}\rangle^{K2}_{\bar{\nu}_\mu \rightarrow \bar{\nu}_e} = 4.8 \pm 0.3$$

---

[6] Value taken from [Arm98b] is 2% less than the final value of $(9.6 \pm 0.3(stat.) \pm 0.7(syst.)) \cdot 10^{-42} cm^2$ for the $^{12}\mathrm{C}\,(\,\nu_e\,,\mathrm{e}^-\,)\,^{12}\mathrm{N}_{\mathrm{g.s.}}$ cross section, which has been measured in this thesis.

[7] Number of prompt single-events (solely neutrinos) with respect to different cuts and corrected according to different dead-times for single-events and $\bar{\nu}_e$-like sequences (*see Appendix* D).

$\bar{\nu}_e$-Contamination

The only background source, which can not be directly extracted from the data, is the contamination of the neutrino beam with $\bar{\nu}_e$ produced in the π^--μ^--decay chain. Detailed MC-simulations of the ISIS target section are utilized in order to obtain the fraction of π^- and μ^- decaying before they undergo capture on nuclei of the target materials [Bur95]. The simulated ratio of $\bar{\nu}_e$ to $\bar{\nu}_\mu$ being produced within the prompt time interval amounts to $5 \cdot 10^{-4}$. Taking into account as well the smaller value of the overall $\bar{\nu}_e$ cross section of $\langle\sigma\rangle = 72 \cdot 10^{-42}\,cm^2$ for p($\bar{\nu}_e$,e^+)n, which is averaged over the $\bar{\nu}_e$-energy spectrum from μ^--decay at rest, the intrinsic $\bar{\nu}_e$ contamination leads to the smallest background contribution in the sequential $\bar{\nu}_\mu \rightarrow \bar{\nu}_e$ appearance search:

$$\langle N_{conta}\rangle^{K2}_{\bar{\nu}_\mu \rightarrow \bar{\nu}_e} = 2.0 \pm 0.2$$

Hence, the entire expectation of the background for the sequential $\bar{\nu}_\mu \rightarrow \bar{\nu}_e$ appearance search amounts to:

$$\langle N_{cos,\,CC,\,rnd,\,conta}\rangle^{K2}_{\bar{\nu}_\mu \rightarrow \bar{\nu}_e} = 15.8 \pm 0.5$$

4.4.1.2 Exclusion Limit for $\bar{\nu}_\mu \rightarrow \bar{\nu}_e$ Appearance

Due to a strongly suppressed cosmic background rate after the upgrade, KARMEN2 shows no evidence for $\bar{\nu}_\mu \rightarrow \bar{\nu}_e$ appearance in the LSND-region of squared-mass differences. The number of 15 $\bar{\nu}_e$-like sequences, found by the sequential search for $\bar{\nu}_\mu \rightarrow \bar{\nu}_e$ appearance, is in perfect agreement with the background expectation of 15.8 $\bar{\nu}_e$-like sequences. Hence, an oscillation signal strength $s_{90\%CL}$ of 7.4 $\bar{\nu}_e$ can be excluded at 90%CL, according to the Bayesian approach introduced in *Section* 4.3.3. The number $\langle N\rangle^{\bar{\nu}_\mu \rightarrow \bar{\nu}_e}_{full\,oscillation}$ of $\bar{\nu}_e$-sequences, which are expected under the assumption of full $\bar{\nu}_\mu \rightarrow \bar{\nu}_e$ oscillation, is inferred as follows:

$$\begin{aligned}\langle N\rangle^{\bar{\nu}_\mu \rightarrow \bar{\nu}_e}_{full\,oscillation} &= \left[\langle\sigma_1(p(\bar{\nu}_e, e^+)n)\rangle \cdot N_p \;+\; \langle\sigma_2(^{12}\mathrm{C}(\bar{\nu}_e, e^+n)^{11}\mathrm{B})\rangle \cdot N_C \right] \cdot \Omega_{eff} \;\cdot \\ &\quad \cdot \left[\bar{\epsilon}^{K2}_{MC,\,pr} \cdot \epsilon_{t_{pr},\,\tau_\mu} \cdot \epsilon^{K2}_{n} \cdot \epsilon^{K2}_{stack,\,pr,\,\tau_\mu} \cdot \epsilon^{K2}_{SMU} \cdot \Phi^{K2}_{\nu} \right]\end{aligned}$$

The total efficiency amounts to $(19.2 \pm 1.5)\%$ and thus the full $\bar{\nu}_\mu \rightarrow \bar{\nu}_e$ oscillation expectation comes out as (*see Table* 4.3 *and* 4.4 *as well as Chapter* 3.1):

$$\langle N\rangle^{\bar{\nu}_\mu \rightarrow \bar{\nu}_e}_{full\,oscillation} = 5826 \pm 538$$

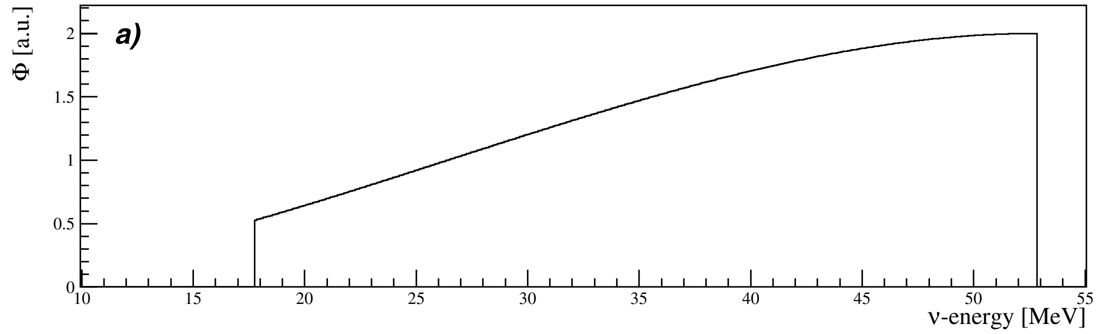

effective differential $\bar{\nu}_\mu$-source-flux from DAR

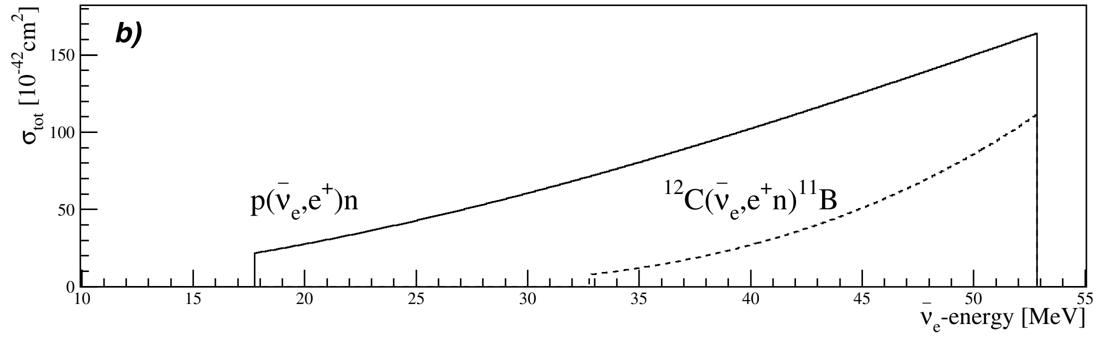

effective differential cross sections

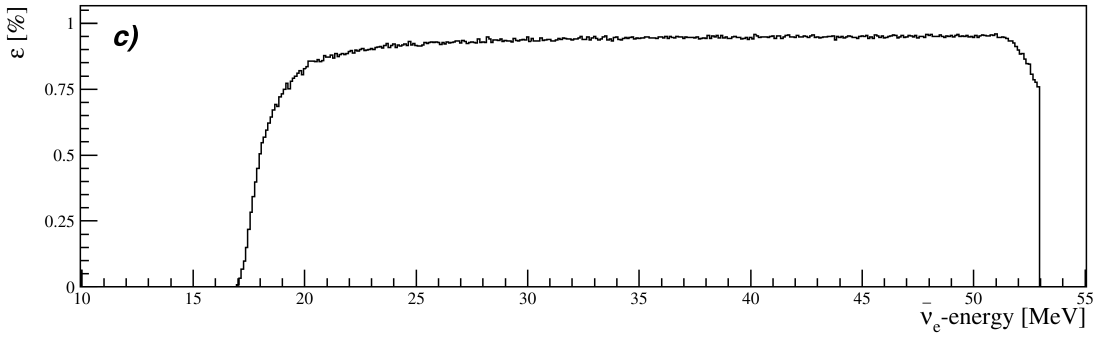

relative efficiency

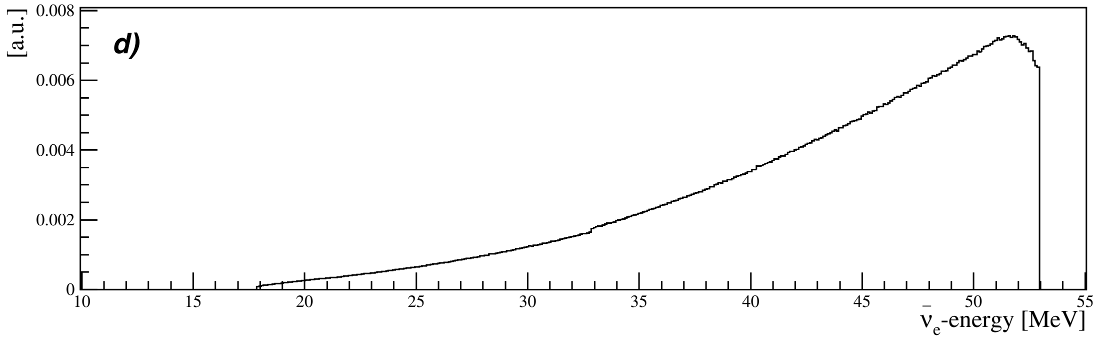

weighted energy spectrum

Figure 4.9: Neutrino energy dependent input distributions needed for the calculation of the oscillation-amplitude $\sin^2(2\Theta)$ as function of Δm^2 (for $\bar{\nu}_\mu \rightarrow \bar{\nu}_e$ appearance in KARMEN2):
a) effective differential $\bar{\nu}_\mu$-source-flux from μ^+-decay at rest (DAR), b) effective differential cross sections for $p(\bar{\nu}_e,e^+)n$ and $^{12}C(\bar{\nu}_e,e^+n)^{11}B$, c) relative detection efficiency and d) overall energy-weight-function $w_{\Phi,\sigma,\epsilon}(E_\nu)$, accounting as well for the different numbers of target nuclei.

The upper limit on the oscillation probability is then given by the quotient of the excluded oscillation signal strength $s_{90\%CL} = 7.4$ and the full oscillation expectation $\langle N\rangle^{\bar{\nu}_\mu \rightarrow \bar{\nu}_e}_{full\,oscillation} = 5826$. Thus, at 90%CL this Bayesian upper limit on the $\bar{\nu}_\mu \rightarrow \bar{\nu}_e$ oscillation probability $\mathcal{P}^{\bar{\nu}_\mu \rightarrow \bar{\nu}_e}_{90\%CL}$ (in the Δm^2_{LSND}-region) states:

$$\mathcal{P}(\bar{\nu}_\mu \rightarrow \bar{\nu}_e) \; < \; 1.27 \cdot 10^{-3} \; (90\%CL)$$

In analogy to *Section* 4.2.1, the oscillation-amplitude $\sin^2(2\Theta)$ can be finally calculated as function of Δm^2 (within the 2-flavor-formalism), by using the same distance-weight-functions $w_{L,main}$ and $w_{L,\mu SR}$ but a different energy-weight-function $w_{\Phi,\sigma,\epsilon}(E_\nu)$ (*see Fig.* 4.9) as well as a different ratio $r_{\mu SR} = 2.8\%$ of neutrinos originating from the thicker μSR-pre-target in K2 ($\overline{d}_{\mu SR} = 8.09\,\text{mm}$):

$$\begin{aligned} \mathcal{P}^{\bar{\nu}_\mu \rightarrow \bar{\nu}_e}_{90\%CL} \quad = \quad \sin^2(2\Theta) \cdot \Bigg[\, r_{main} \cdot \int\limits_{L'} w_{L,main}(L) \cdot \int\limits_{E'_\nu} w_{\Phi,\sigma,\epsilon}(E_\nu) \cdot \sin^2\left(\frac{1.27 \cdot \Delta m^2 \cdot L}{E_\nu}\right) \, dE_\nu \, dL \\ + \, r_{\mu SR} \cdot \int\limits_{L'} w_{L,\mu SR}(L) \cdot \int\limits_{E'_\nu} w_{\Phi,\sigma,\epsilon}(E_\nu) \cdot \sin^2\left(\frac{1.27 \cdot \Delta m^2 \cdot L}{E_\nu}\right) \, dE_\nu \, dL \Bigg] \end{aligned} \tag{4.24}$$

Fig. 4.10 b) shows the obtained $90\%CL$ exclusion curve in comparison with results from other experiments. Regions on the right hand side of the curve are excluded at $90\%CL$. KARMEN attains maximal sensitivity for $\bar{\nu}_\mu \rightarrow \bar{\nu}_e$ appearance at $3\,eV^2$ ($\simeq 52\,[MeV]/17.7\,[m]$ *compare Fig.* 4.9 d) *and Fig.* 4.4 e). For large Δm^2 the following upper limit is derived for $\boxed{\bar{\nu}_\mu \rightarrow \bar{\nu}_e}$ appearance from the sequence analysis:

$$\boxed{\sin^2(2\Theta) \; < \; 2.5 \cdot 10^{-3} \; (90\%CL)}$$

For $\Delta m^2 \; > \; 1\,eV^2$ most parts of the LSND favored evidence region can be excluded at $90\%CL$ due to this KARMEN2 result. A more stringent exclusion limit from the sequence analysis of KARMEN2 is derived from the final maximum likelihood analysis, which is described in [Arm02] and makes additionally use out of the full available spectral information (*compare Fig.* 4.10 a+b). For large Δm^2 the final upper limit of $\sin^2(2\Theta) \; < \; 1.7 \cdot 10^{-3}$ ($90\%CL$) is deduced from a unified approach for the sequential $\bar{\nu}_\mu \rightarrow \bar{\nu}_e$ appearance search.
In a (3+1) scenario ($\Delta m^2 = \Delta m^2_{41} \simeq \Delta m^2_{42} \simeq \Delta m^2_{43}$) this oscillation-amplitude $\sin^2(2\Theta)$ for $\bar{\nu}_\mu \rightarrow \bar{\nu}_e$ appearance is then given by $\sin^2(2\Theta) = 4 \cdot U^2_{e4} \cdot U^2_{\mu 4}$ (*compare Eq.* 4.4) [Sor03]. Hence, the sequential $\bar{\nu}_\mu \rightarrow \bar{\nu}_e$ appearance search in KARMEN2 does not deliver evidence for heavy sterile neutrinos in the LSND-region of squared-mass differences.

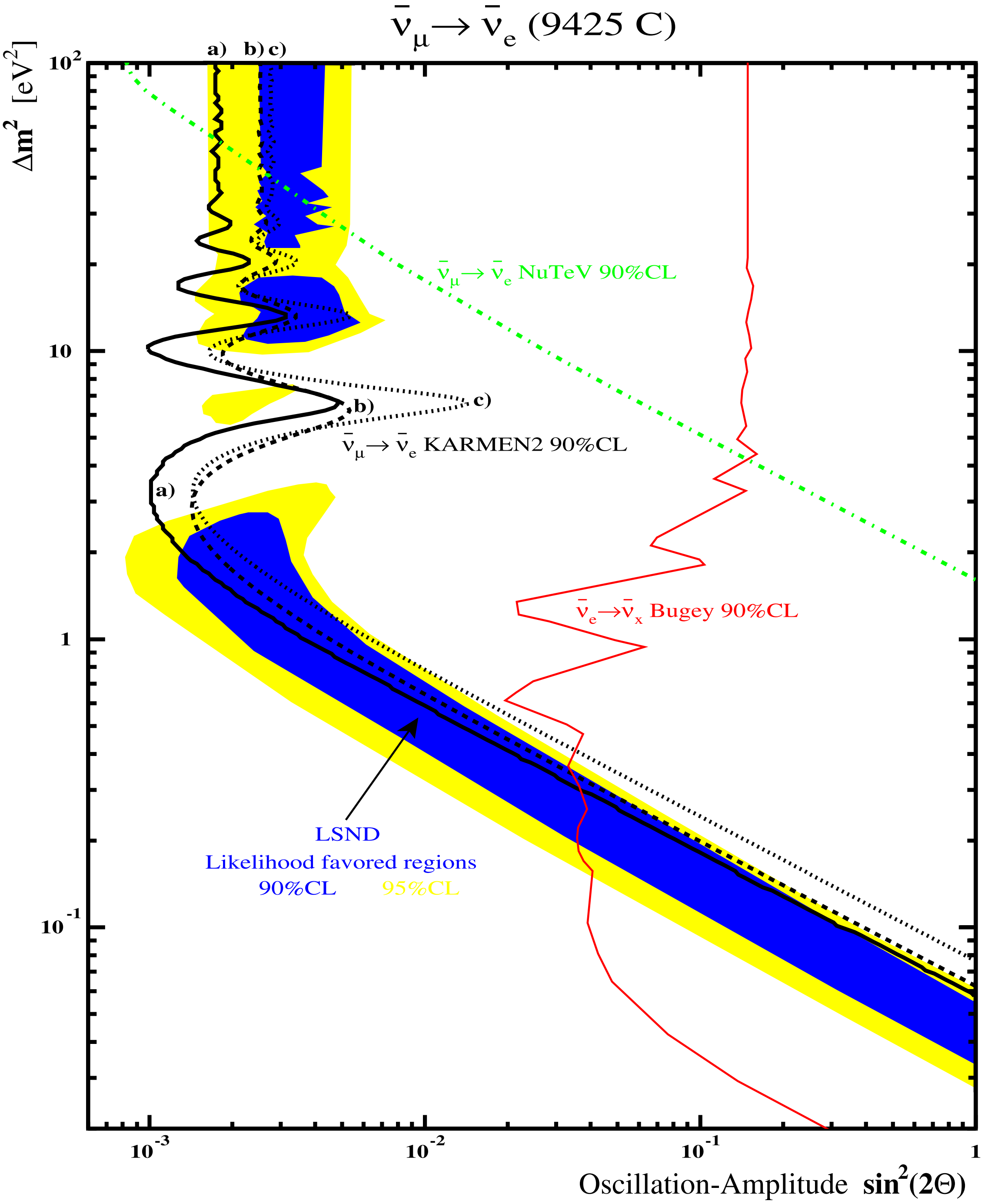

Figure 4.10: Oscillation plot showing the LSND evidence region for $\bar{\nu}_\mu \rightarrow \bar{\nu}_e$ oscillation in comparison with exclusion curves from KARMEN and other short baseline experiments: a) Final KARMEN2 likelihood method [Arm02], b) KARMEN2 sequential window method, c) KARMEN2 single-event analysis, as well as the results from NuTeV [Avv02] and from Bugey ($\bar{\nu}_e \rightarrow \bar{\nu}_x$ disappearance of reactor anti-neutrinos) [Ach95]. Areas on the right hand side of each curve are excluded at $90\% CL$.

4.4.2 Method using Single–Events for $\bar{\nu}_\mu \rightarrow \bar{\nu}_e$ Appearance Search

The measured cross section for the inclusive CC-reaction $^{13}\mathrm{C}\,(\,\nu_e\,,\mathrm{e}^-\,)\,^{13}\mathrm{N}$ in KARMEN2 is in agreement with theoretical calculations (*see Chapter* 3.2.1). $\bar{\nu}_e$ from $\bar{\nu}_\mu \rightarrow \bar{\nu}_e$ oscillations in the LSND-region of squared-mass differences would be detected via the well-known inverse β-decay p($\bar{\nu}_e$,e^+)n on the free protons of the organic scintillator. From this, an unconsidered background component, with prompt visible energies up to around 50 MeV, would increase the measured cross section for the reaction $^{13}\mathrm{C}\,(\,\nu_e\,,\mathrm{e}^-\,)\,^{13}\mathrm{N}$. The measured value is not larger than expected from any of the models, and no additional signal can be observed in the corresponding prompt visible energy spectrum of the 14 single-events (*see Chapter* 3.2.1). Hence, no evidence for $\bar{\nu}_\mu \rightarrow \bar{\nu}_e$ appearance can be deduced from the single-events in KARMEN2. From this new independent probe of the LSND evidence region, another KARMEN2 exclusion limit for $\bar{\nu}_\mu \rightarrow \bar{\nu}_e$ appearance will be derived in the following.

The search of single-events for $\bar{\nu}_\mu \rightarrow \bar{\nu}_e$ appearance is based on the evaluation of the cross section for the inclusive CC-reaction $^{13}\mathrm{C}\,(\,\nu_e\,,\mathrm{e}^-\,)\,^{13}\mathrm{N}$ in KARMEN2 (*see Chapter* 3.2.1). For this window-method, the observed prompt visible energy is required to be above 38 MeV, in contrast to the sequential $\bar{\nu}_\mu \rightarrow \bar{\nu}_e$ appearance search. Thus, the $\bar{\nu}_e$ detection reaction ^{12}C($\bar{\nu}_e$,e^+n)^{11}B on carbon nuclei of the organic scintillator does not contribute, due to the large corresponding Q-value of 16.8 MeV and the maximum ν-energy of 52.8 MeV from μ^+-decay at rest. Solely the inverse β-decay p($\bar{\nu}_e$,e^+)n on the free protons of the organic scintillator was taken into account for the detection of $\bar{\nu}_e$. The background for the $\bar{\nu}_\mu \rightarrow \bar{\nu}_e$ appearance search of single-events is caused by cosmic ray muons, ν-e^--scattering and the inclusive CC-reaction $^{13}\mathrm{C}\,(\,\nu_e\,,\mathrm{e}^-\,)\,^{13}\mathrm{N}$ on ^{13}C nuclei of the organic scintillator. The inclusive CC-reaction $^{56}\mathrm{Fe}\,(\,\nu_e\,,\mathrm{e}^-\,)\,\mathrm{X}$ on iron nuclei of the steel, which surrounds the detector, does not contribute, due to the restriction of the x-position in the applied window-method, which requires $|X| \leq 130\,\mathrm{cm}$.

4.4.2.1 Background in Single–Events for $\bar{\nu}_\mu \rightarrow \bar{\nu}_e$ Appearance Search

Cosmic Ray Induced Background

The cosmic background expectation for the $\bar{\nu}_\mu \rightarrow \bar{\nu}_e$ appearance search in the single-events of KARMEN2 can be measured very precisely in analogy to *Chapter* 3.2.1 by analyzing the pre-beam time window, which is 19 times longer than the 10 μs short neutrino time window[8]. Hence, the expectation of the cosmic induced background for the $\bar{\nu}_\mu \rightarrow \bar{\nu}_e$ appearance search in the single-events of K2 comes out as:

$$\langle N_{cos} \rangle^{K2}_{\bar{\nu}_\mu \rightarrow \bar{\nu}_e} = 2.06 \pm 0.32$$

---

[8] The decreasing stack-efficiency in the neutrino time window has to be taken into account, with respect to the applied dead-time for single-events (*see Appendix* D).

The ν-e^--Scattering $\mathrm{e}^-\,(\,\nu\,,\nu'\,)\,\mathrm{e}^{-\prime}$

The expectation of ν-e^--scattering background for the $\bar{\nu}_\mu\!\rightarrow\bar{\nu}_e$ appearance search in the single-events of KARMEN2 can be calculated very precisely. In analogy to *Chapter* 3.2.1 the analytically calculated and over the ν-energy spectra averaged cross section $\langle\sigma\rangle = (0.347 \pm 0.002)\cdot 10^{-42} cm^2$ for $\mathrm{e}^-\,(\,\nu\,,\nu'\,)\,\mathrm{e}^{-\prime}$ is taken. Herewith, the expected number $\langle N_{ES}\rangle^{K2}_{\bar{\nu}_\mu\rightarrow\,\bar{\nu}_e}$ of single-events from ν-e^--scattering is derived straightforward from the definition of the cross section:

$$\langle N_{ES}\rangle^{K2}_{\bar{\nu}_\mu\rightarrow\,\bar{\nu}_e} \;=\; \langle\sigma(\mathrm{e}^-\,(\,\nu\,,\,\nu'\,)\,\mathrm{e}^{-\prime})\rangle\cdot\Omega_{eff}\cdot N_e\cdot\;\epsilon^{K2}_{MC}\cdot\epsilon_{t_{pr},\,\tau_\mu}\cdot\epsilon^{K2}_{stack,\,pr,\,\tau_\mu}\cdot\epsilon^{K2}_{SMU}\cdot\Phi^{K2}_{\nu}$$

Thus, the expectation of ν-e^--scattering background for the $\bar{\nu}_\mu\!\rightarrow\bar{\nu}_e$ appearance search in the single-events of K2 amounts to (*see Chapter* 3.2.1):

$$\langle N_{ES}\rangle^{K2}_{\bar{\nu}_\mu\rightarrow\,\bar{\nu}_e} = 4.43 \pm 0.03$$

The ν_e-Induced Inclusive CC-Reaction $^{13}\mathrm{C}\,(\,\nu_e\,,\mathrm{e}^-\,)\,^{13}\mathrm{N}$

The expectation of ν_e-induced background from the CC-reaction $^{13}\mathrm{C}\,(\,\nu_e\,,\mathrm{e}^-\,)\,^{13}\mathrm{N}$ for the $\bar{\nu}_\mu\!\rightarrow\bar{\nu}_e$ appearance search in the single-events of KARMEN2 can not be calculated precisely and is strongly dependent of the ν-nucleus-interaction model. Conservatively, the smallest cross section value, averaged over the ν_e-energy spectrum, is chosen from all microscopic model calculations (*see Chapter* 3.2.1):

$\langle\sigma_{theo}(^{13}\mathrm{C}\,(\,\nu_e\,,\,\mathrm{e}^-\,)\,^{13}\mathrm{N})\rangle \;=\; 52.8\cdot 10^{-42} cm^2$ [Kub93]

The measured cross section for the inclusive CC-reaction $^{13}\mathrm{C}\,(\,\nu_e\,,\mathrm{e}^-\,)\,^{13}\mathrm{N}$ derived from the single-events in K2 is found to be (*see Chapter* 3.2.1):

$\langle\sigma_{K2}(^{13}\mathrm{C}\,(\,\nu_e\,,\,\mathrm{e}^-\,)\,^{13}\mathrm{N})\rangle \;=\; (50 \pm 25(stat.) \pm 4(syst.))\cdot 10^{-42} cm^2$

This measured cross section value corresponds to 14 observed single-events including the very precisely known cosmic and ν-e^--scattering background portions. Thus a conservative estimate of the expected background from the CC-reaction $^{13}\mathrm{C}\,(\,\nu_e\,,\mathrm{e}^-\,)\,^{13}\mathrm{N}$ for the $\bar{\nu}_\mu\!\rightarrow\bar{\nu}_e$ appearance search in the single-events of K2 is given as follows:

$$\langle N_{C13}\rangle^{K2}_{\bar{\nu}_\mu\rightarrow\,\bar{\nu}_e} \;=\; 7.9$$

Hence, the conservative expectation of the entire background for the $\bar{\nu}_\mu\!\rightarrow\bar{\nu}_e$ appearance search in the single-events of K2 comes out as[9]:

---

[9] The uncertainty from $\langle\sigma_{theo}(^{13}\mathrm{C}\,(\,\nu_e\,,\,\mathrm{e}^-\,)\,^{13}\mathrm{N})\rangle$ was not accounted for in the value of the error.

$$\langle N_{cos,\,ES,\,C13}\rangle^{K2}_{\bar{\nu}_\mu \rightarrow \bar{\nu}_e} = 14.4 \pm 0.3$$

4.4.2.2 Result from Single–Events for $\bar{\nu}_\mu \rightarrow \bar{\nu}_e$ Appearance Search

The window-method applied to the single-events in KARMEN2, using a strongly suppressed cosmic background rate due to the upgrade, delivers likewise no evidence for $\bar{\nu}_\mu \rightarrow \bar{\nu}_e$ appearance in the LSND-region of squared-mass differences. The number of 14 single-events, which satisfy all cuts and event requirements, is well in agreement with the background expectation of 14.4 single-events. Hence, an oscillation signal strength $s_{90\%CL}$ of 7.4 $\bar{\nu}_e$ can be excluded at 90%CL, according to the Bayesian approach introduced in *Section* 4.3.3. The number $\langle N\rangle^{\bar{\nu}_\mu \rightarrow \bar{\nu}_e}_{full\,oscillation}$ of single-events, which are expected under the assumption of full $\bar{\nu}_\mu \rightarrow \bar{\nu}_e$ oscillation, is inferred as follows:

$$\begin{aligned}\langle N\rangle^{\bar{\nu}_\mu \rightarrow \bar{\nu}_e}_{full\,oscillation} &= \langle \sigma(p(\bar{\nu}_e, e^+)n)\rangle \cdot N_p \cdot \Omega_{eff} \cdot \\ &\quad \cdot \epsilon^{K2}_{MC,\,pr} \cdot \epsilon^{K2}_{x-pos,\,pr} \cdot \epsilon^{K2}_{E_{vis},\,pr} \cdot \epsilon_{t_{pr},\,\tau_\mu} \cdot \epsilon^{K2}_{stack,\,pr,\,\tau_\mu} \cdot \epsilon^{K2}_{SMU} \cdot \Phi^{K2}_{\nu}\end{aligned}$$

Mainly due to the required high threshold of the visible energy and the restriction of the x-position, the total efficiency comes out at approximately the same value as for the sequential $\bar{\nu}_\mu \rightarrow \bar{\nu}_e$ appearance search, which additionally has to consider the neutron detection efficiency (*see Table* 4.3). Hence, the full $\bar{\nu}_\mu \rightarrow \bar{\nu}_e$ oscillation expectation differs only slightly from the value in the previous sequential search (*see Table* 4.4 *and Section* 4.4.1.2). Again, the upper limit on the oscillation probability is then given by the quotient of the excluded oscillation signal strength $s_{90\%CL} = 7.4$ and the full oscillation expectation $\langle N\rangle^{\bar{\nu}_\mu \rightarrow \bar{\nu}_e}_{full\,oscillation} = 5313$. Thus, at 90%CL the Bayesian upper limit on the $\bar{\nu}_\mu \rightarrow \bar{\nu}_e$ oscillation probability $\mathcal{P}^{\bar{\nu}_\mu \rightarrow \bar{\nu}_e}_{90\%CL}$ (in the Δm^2_{LSND}-region) amounts to $1.38 \cdot 10^{-3}$ $(90\%CL)$. In analogy to the previous sequential search in *Section* 4.4.1.2, the oscillation-amplitude

Type of Efficiency	*Single-Event Search*	*Sequential Search*
$\epsilon_{stack} \cdot \epsilon_{SMU}$	0.680	0.709
$\epsilon_{neutron}$	1	0.416
$\epsilon_{x-position}$	0.778	1
$\epsilon_{prompt\,visible\,energy}$	0.532	1
$\epsilon_{prompt\,time}$	0.840	0.840
ϵ_{MC}	0.775	0.775
ϵ_{tot}	0.183	0.192

Table 4.3: Comparison of efficiencies for the $\bar{\nu}_\mu \rightarrow \bar{\nu}_e$ appearance search using single-events and sequences, respectively.

Reaction $\sigma[10^{-42}cm^2]$	N_{full}	$N_T[10^{30}]$
p($\bar{\nu}_e$,e^+)n $\rightarrow$ (n,γ) 93.5	5576	4.52
p($\bar{\nu}_e$,e^+)n 93.5	5313	4.52
^{12}C($\bar{\nu}_e$,e^+n)^{11}B$\rightarrow$ (n,γ) 8.5	250	2.54

Table 4.4: Under the assumption of full $\bar{\nu}_\mu \rightarrow \bar{\nu}_e$ oscillation expected number of $\bar{\nu}_e$ for the different detection reactions (sequential and single-event method, respectively). The corresponding cross sections of the detection reactions and the number of target nuclei are listed as well.

$\sin^2(2\Theta)$ can be finally calculated as function of Δm^2 (within the 2-flavor-formalism) with *Eq.* 4.24. A different energy-weight-function $w_{\Phi,\sigma,\epsilon}(E_\nu)$, accounting for the restricted range of visible energies, has to be taken (*compare Fig.* 4.9). The reaction ^{12}C($\bar{\nu}_e$,e^+n)^{11}B on carbon nuclei of the organic scintillator does not contribute to the $\bar{\nu}_e$ detection, which simplifies matters. *Fig.* 4.10 c) shows the obtained $90\%CL$ exclusion curve in comparison with results from other experiments. Regions on the right hand side of the curve are excluded at $90\%CL$. The shape of the obtained $90\%CL$ exclusion curve differs from the one derived from the sequential $\bar{\nu}_\mu \rightarrow \bar{\nu}_e$ appearance search, primarily due to the restricted range of accessible neutrino energies (*compare Fig.* 4.10 b+c). Again, KARMEN attains maximal sensitivity for $\bar{\nu}_\mu \rightarrow \bar{\nu}_e$ appearance at $3\,eV^2$ ($\simeq 52\,[MeV]/17.7\,[m]$ *compare Fig.* 4.9 d) *and Fig.* 4.4 e). For large Δm^2 the following upper limit is derived for $\boxed{\bar{\nu}_\mu \rightarrow \bar{\nu}_e}$ appearance from the single-event analysis:

$$\boxed{\sin^2(2\Theta) \; < \; 2.8 \cdot 10^{-3} \; (90\%CL)}$$

Again, for $\Delta m^2 > 1\,eV^2$ most parts of the LSND favored evidence region can be excluded at $90\%CL$, due to this new independent KARMEN2 result. However, the most stringent exclusion limit is derived from the sequential final maximum likelihood analysis of KARMEN2, which is described in [Arm02] (*compare Fig.* 4.10 a+c). For large Δm^2 the final upper limit of $\sin^2(2\Theta) < 1.7 \cdot 10^{-3}$ ($90\%CL$) is deduced from a unified approach for the sequential $\bar{\nu}_\mu \rightarrow \bar{\nu}_e$ appearance search.

In a (3+1) scenario ($\Delta m^2 = \Delta m^2_{41} \simeq \Delta m^2_{42} \simeq \Delta m^2_{43}$) this oscillation-amplitude $\sin^2(2\Theta)$ for $\bar{\nu}_\mu \rightarrow \bar{\nu}_e$ appearance is then given by $\sin^2(2\Theta) = 4 \cdot U^2_{e4} \cdot U^2_{\mu 4}$ (*compare Eq.* 4.4) [Sor03]. Hence, in all of the three methods for $\bar{\nu}_\mu \rightarrow \bar{\nu}_e$ appearance search, KARMEN does not show evidence for the existence of an additional heavy sterile neutrino in the LSND-region of squared-mass differences (LSND-scenario).

In a further investigation with KARMEN, $\bar{\nu}_e$-emission from lepton-flavor-violating μ^+-decays can be ruled out as possible alternative explanation of the LSND-excess [Arm03].

Chapter 5

Time–Anomaly

In KARMEN1 an anomaly in the time distribution of single-events was observed between 3μs and 4μs (*see Fig.* 5.1 and E.4). As possible explanation of this KARMEN-Time-Anomaly the pion-decay beyond standard model ($\pi^+ \rightarrow \mu^+ + X$) into a new weakly-interacting 33.9 MeV massive X-particle was intensely discussed [Zei95] [Oeh99]. In the following it will be shown that the KARMEN-Time-Anomaly can be plausibly resolved by intermediate-energy neutrons inducing beam correlated background.

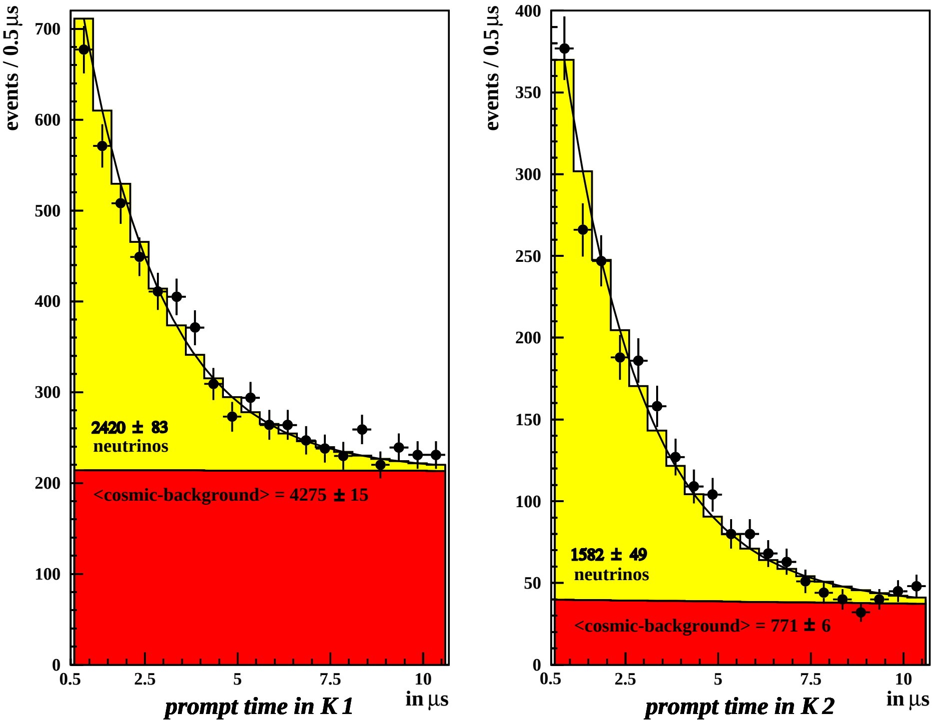

Figure 5.1: Time distribution of single-events in KARMEN1 (K1) before and KARMEN2 (K2) after the upgrade. The portion of cosmic background is drawn-in for each (according to expectation from pre-beam).

5.1 Hypothesis of Intermediate–Energy Neutrons Inducing Beam Correlated Background

The energy dependent total neutron cross section on iron in the region of resonances (1 keV - 2 MeV) is plotted in *Fig.* 5.2a). The distinct minima in the neutron cross section can be clearly seen. Some of those numbered minima are even lower than 100 mbarn. In *Fig.* 5.2b) the energy dependent neutron cross section is now graphed as function of the average time-of-flight from the ISIS main-target to the KARMEN-detector (average distance 17.7 m). Contemplating the deep double minimum in the cross section (no.3 + 4), it can be seen that those neutrons, with kinetic energies of 129 keV and 137 keV, respectively, will reach the KARMEN-detector after roughly 3.5 μs: within the region of the time-anomaly. Via a prompt (n,γ)-reaction within the steel that closely surrounds the detector, those intermediate-energy neutrons could produce indirectly a prompt single-event signature. γ-rays from e.g. ^{57}Fe(n,γ)-reactions have an energy of 10 MeV and can penetrate the detector as deep as 0.5 m. The natural abundance of ^{57}Fe is 2.2 %. In *Table* 5.1 the most common isotopes of iron and chrome are listed. The steel slabs for passive shielding contain mainly iron, whereas the stainless steel of the support structure of the detector contains chrome as well (roughly to a third). γ-rays from Cr(n,γ)-reactions have also energies up to 10 MeV. Moreover, the thermal neutron cross section on ^{50}Cr and ^{53}Cr is by one order of magnitude larger than the ones on iron. If the intermediate-energy neutrons from ISIS are moderated within the stainless steel (very close to the detector), they are more likely to be captured on ^{50}Cr and ^{53}Cr, respectively. Those two isotopes add up to an abundance of 14% in chrome and the resulting γ-energies from neutron capture are 9.3 MeV and 9.7 MeV, respectively. Because of a finite energy resolution of the detector, visible energies above 10 MeV are possible for such (n,γ)-events. The visible energy spectrum of single-events in KARMEN1 show intelligibly an overspill at low threshold between 10 MeV and 12 MeV (*see Fig.* 3.13). After the mounting of the 5 cm thick veto-counters, made out of plastic scintillator with additional 4 cm thick boron treated PE-slabs, the majority of those intermediate-energy neutrons were moderated and captured inside the PE-slabs via a ^{10}B(n,α)-reaction. The time-anomaly between 3μs and 4μs cannot be observed anymore in K2 (*see Fig.* 5.1).

In K2 the pre-target was up to 10 mm thick and thus per average almost twice as thick as in K1. The iron-shielding to the sides, pointing towards the pre-target in the ISIS beam-line, amounts to only 2 m compared with 7 m of shielding towards the main-target. Therefore, a possible signal from the pre-target is more likely to be observed in K2. Corresponding to the larger distance of the pre-target (29.1 m compared with 17.7 m from main-target) the neutrons produced there, with kinetic energies of 129 keV and 137 keV, respectively, will reach the detector not until 5.8μs (*see no.*$3 + 4$ *in Fig.* 5.2c).

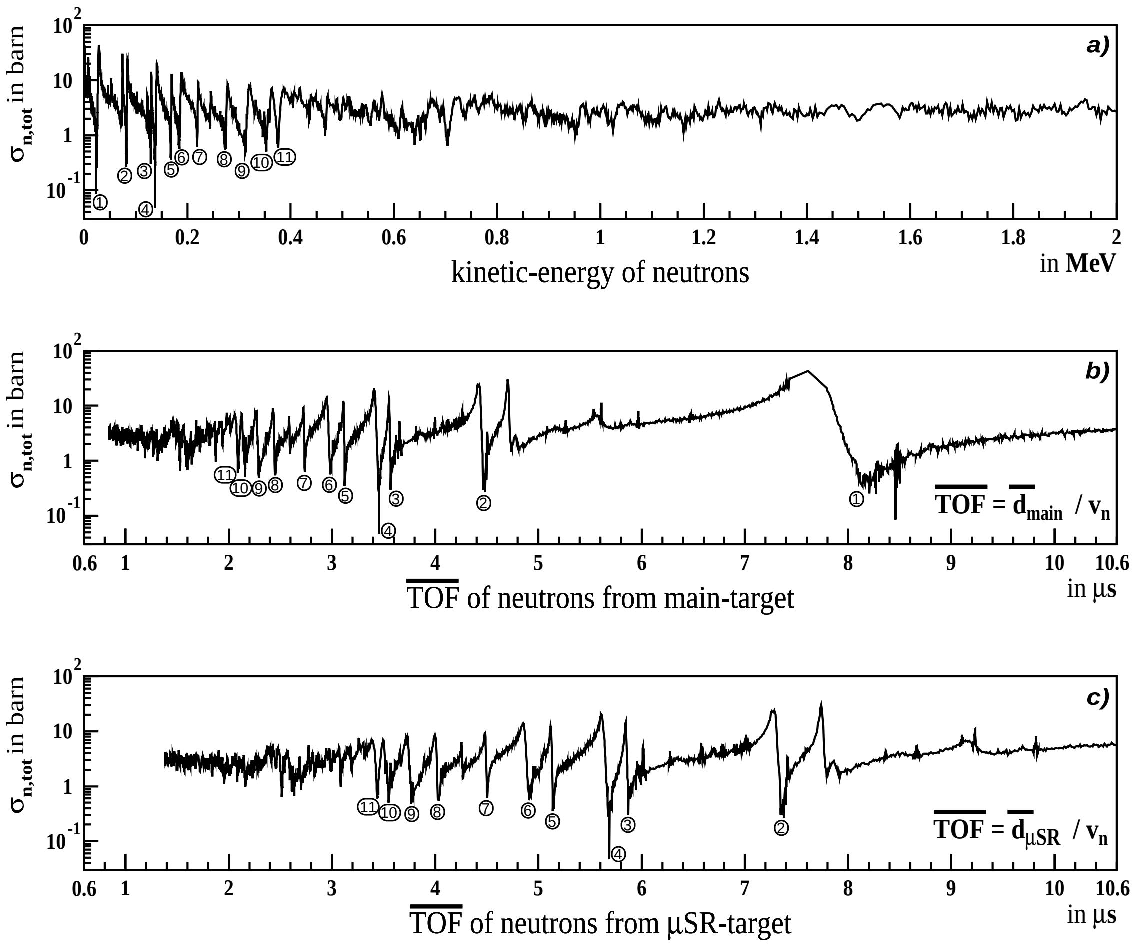

Figure 5.2: Total cross section of neutrons on iron in the region of resonances (1 keV - 2 MeV) [Har84]. Shown in dependence of a) kinetic energy of neutrons, b) average time-of-flight from main-target and c) average time-of-flight from μSR-pre-target. The 11 deepest minima of the cross section are marked for orientation.

Isotope	E_γ [MeV]	Natural Abundance [%]	$\sigma_{therm}(n,\gamma)$ [barn]
^{54}Fe	9.3	5.8	2.3
^{56}Fe	7.7	91.7	2.6
^{57}Fe	10.0	2.2	2.5
^{50}Cr	9.3	4.4	15.9
^{52}Cr	7.9	83.8	0.8
^{53}Cr	9.7	9.5	18.2

Table 5.1: Thermal neutron cross section $\sigma(n,\gamma)$ and resulting γ-energy for the most common isotopes in iron and chrome [BNL73]

5.2 Velocity Analysis

In a dedicated velocity analysis of the single-events, it will be fleshed out with a maximum likelihood method, that the KARMEN-time-anomaly is plausibly explained by beam correlated neutron background. In addition the portion of this background will be quantified. For this purpose the number of (n,γ)-events in the single-events of K1 and K2, respectively, is varied over the neutron-velocity. The intermediate-energy neutrons are generated in the main-target and in the pre-target, respectively, according to the time distribution of the parabola-shaped proton double pulses. The different time-of-flight for the protons, in the section of beam-line inbetween the two targets, has to be taken into account as well.

The velocity v of a single-event is defined as the quotient of measured distance L over prompt time T'. T_0 is the earliest point of time neutrinos can be measured in the detector after being produced in the main-target. Therefore the prompt time T needs to be redefined: $T'_{main} \;=\; T \,+\, 53\,\mathrm{ns}$ and $T'_{pre} \;=\; T \,+\, (53+111)\,\mathrm{ns}$, respectively. *Fig.* 5.3 demonstrates the simulated velocity-resolution for both targets. The velocity-resolution regarding the pre-target is better, corresponding to the larger distance. For a given spatial-resolution, the relative uncertainty of distance improves with increasing distance. Furthermore, for both targets the velocity-resolution degrades with increasing velocity, due to a limited time-resolution.

5.2.1 Maximum Likelihood Approach

There are three probability density functions defined (according to applied cuts for single-events and spatial-resolution of the detector): $f_{cos}(v)$ for cosmic background, $f_{\nu}(v)$ for neutrinos and $f_n(v\,|\,v_n)$ for neutron-induced events with neutron-velocity v_n. All probability density functions are normalized as follows:

$$\int_{vmin}^{vmax} f_i(v)\,dv \;=\; 1 \tag{5.1}$$

The ratios of all components satisfy:

$$r_{cos,best,prebeam} \;+\; r_{\nu} \;+\; r_n \;=\; 1 \tag{5.2}$$

The number of cosmic background events is given by its best fit within 2σ of the expectation value from pre-beam. Together with the observed number of single-events, the ratio of cosmic background is then fixed. Hence, the ratio of neutron-induced events is solely subtracted from the ratio of neutrinos. The probability $\mathcal{P}(v)$ for N_n neutron-induced events at neutron-velocity v_n is given by:

$$\mathcal{P}(v\,|\,v_n, N_n) \;=\; r_{cos}\cdot f_{cos}(v) \;+\; r_{\nu}\cdot f_{\nu}(v) \;+\; r_n\cdot f_n(v\,|\,v_n) \tag{5.3}$$

In *Fig.* 5.4 the probability density functions in dependence of velocity v and their projections on time T are shown for neutrinos, cosmic background and for three exemplary neutron-velocities. The separation in velocity of the double pulses increases with velocity.

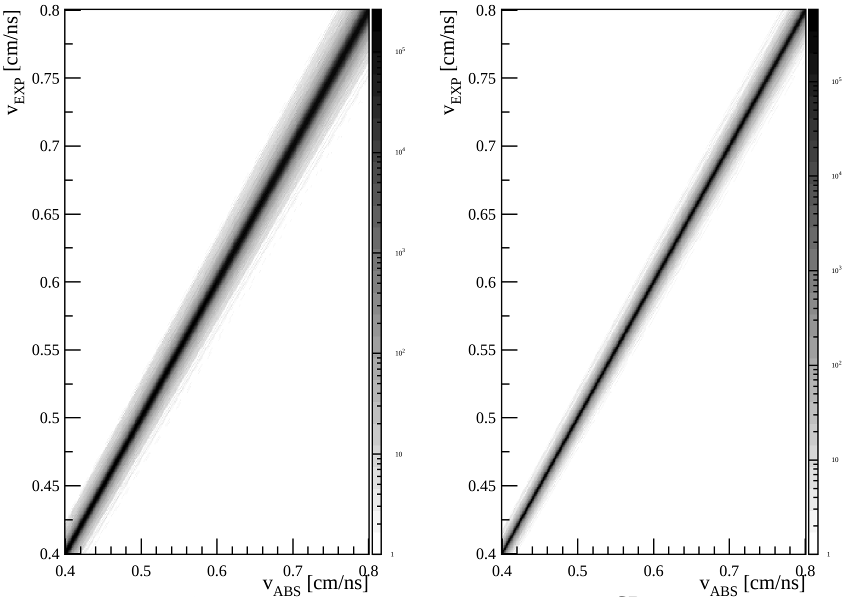

main-target µSR-target

Figure 5.3: Simulated velocity-resolution: observed v_{exp} vs. true v_{abs} (for both targets).

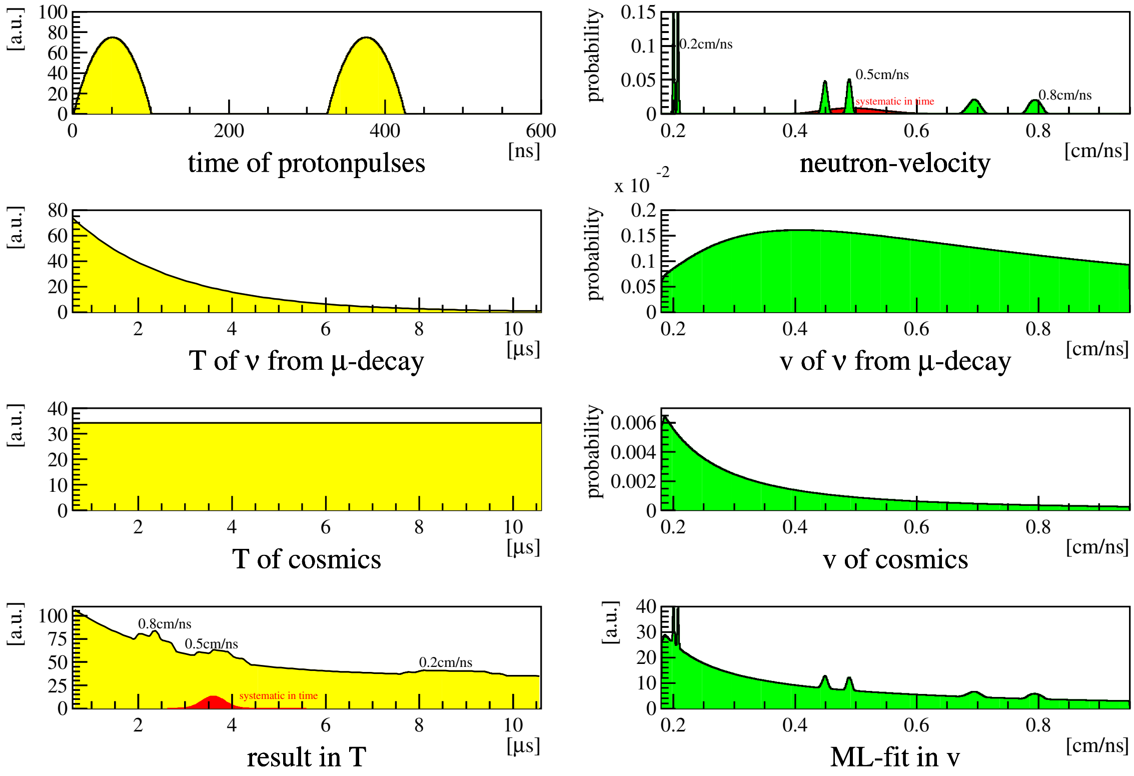

Figure 5.4: Probability density functions in dependence of time T and velocity v for neutrinos, cosmic background and for three exemplary neutron-velocities.

The likelihood function $\mathcal{L}$ in dependence of neutron-velocity v_n and N_n neutron-induced events is defined as follows:

$$\mathcal{L}(v_n, N_n) \;=\; \prod_{sample} \mathcal{P}(v_{event}\,|\,v_n, N_n) \tag{5.4}$$

5.2.2 Results of Maximum Likelihood Analyses

Fig. 5.5 shows the results of the maximum likelihood analyses, related to either the main-target or the pre-target (each for K1 and K2, respectively). Graphed versus velocity is the negative logarithmic maximum likelihood ratio $-ln\mathcal{L}_{ratio}$ of the maximum likelihood function $\mathcal{L}$ over the likelihood function $\mathcal{L}^0$ for null hypothesis. The values of $-ln\mathcal{L}_{ratio}$ are normalized to the global minimum in each set (in order to simplify matters). Consequently, the velocity-values of distinct minima of $-ln\mathcal{L}_{ratio}$ can be compared with minima of the velocity dependent neutron cross section on iron, plotted in C). Regarding the main-target in K1, the deep double minima of the neutron cross section can be assigned statistically significantly to the found neutron-velocities in $-ln\mathcal{L}_{ratio}$ (no.$3+4$ in A1). Those minima, corresponding to the time-anomaly, are not significant anymore in K2 after the upgrade (no.$3+4$ in A2). Now, regarding the thicker pre-target in K2, the cross section minimum (no.3 in B2) is therefor found at the same velocity and with the same significance as in K1 from the main-target.
With regard to ambiguities of $-ln\mathcal{L}_{ratio}$, it is possible to assign more statistical significant minima. The ambiguousness evolves from having always two side minima (double pulse structure; see no.3a,3b in A1) and furthermore two different production targets (2× no.3,3a,3b in A1+B1). For all uniquely assigned minima a benchmark is set to $68\%CL$.
Fig. 5.6 shows the linear likelihood function $\mathcal{L}$ in dependence of neutron-velocity v_n and number of events N_n (exemplarily for $v_n \approx 0.5\,cm/ns$ from main-target in K1). Due to the binormal shape of the linear likelihood function, it is justified to derive errors for the fitted values v_n and N_n with $68\%CL$ by taking the values corresponding to $1.15\,|\Delta ln\mathcal{L}|$ in $-ln\mathcal{L}_{ratio}$ [Fro79]. The likewise plotted evidence region demonstrates that the parameters v_n and N_n can be assumed uncorrelated: The ellipse, derived from a Bayesian approach, is not slant. Assigning all significant and unique minima in the four velocity analyses, the neutron-induced number of single-events can be derived for K1 and K2. *Table* 5.2 lists all statistically significantly ($68\%CL$) assigned numbers of (n,γ)-events. Herewith, the entire number of neutron-induced single-events is found to be:

$$\begin{array}{rl} 125 \pm 43 & \text{(n,}\gamma\text{)-events in K1} \\ 48 \pm 20 & \text{(n,}\gamma\text{)-events in K2} \end{array}$$

Fig. 5.7 shows the likelihood fit results in comparison with the measured velocity spectra of single-events. The agreement is excellent and the double pulse structure with accurate time separation is reflected in the data.

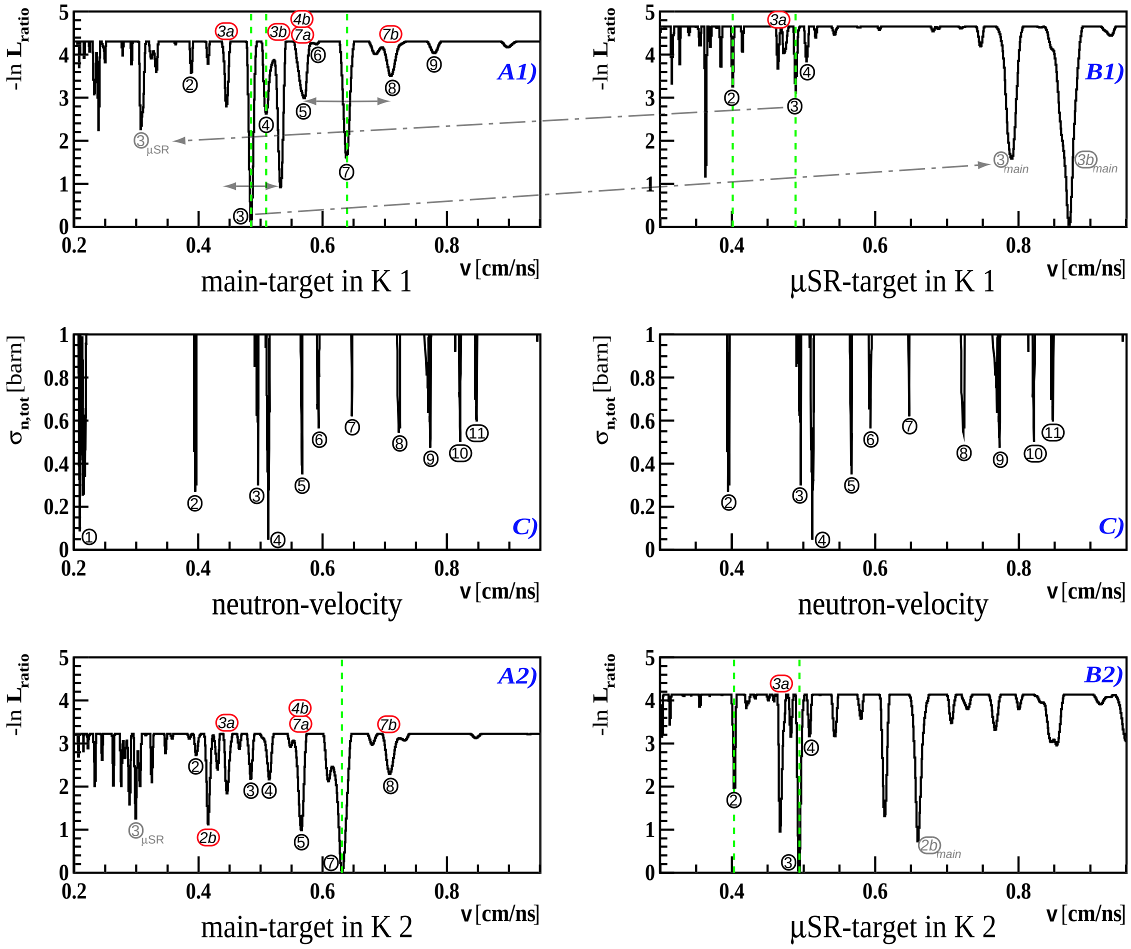

Figure 5.5: Velocity analysis of single-events in KARMEN: Comparison of minima of the velocity dependent neutron cross section in iron C) with the likelihood functions A1),B1) before the upgrade and A2),B2) afterwards. The likelihood functions A1),A2) on the left are related to the main-target, whereas B1),B2) on the right refer to the μSR-pre-target. All uniquely identified and significant minima of the likelihood functions are emphasized with a dashed vertical line. In addition to that the ambiguities of the likelihood functions are visualized in A1),B1). Those evolve by having always two side minima (double pulse structure) and furthermore two production targets.

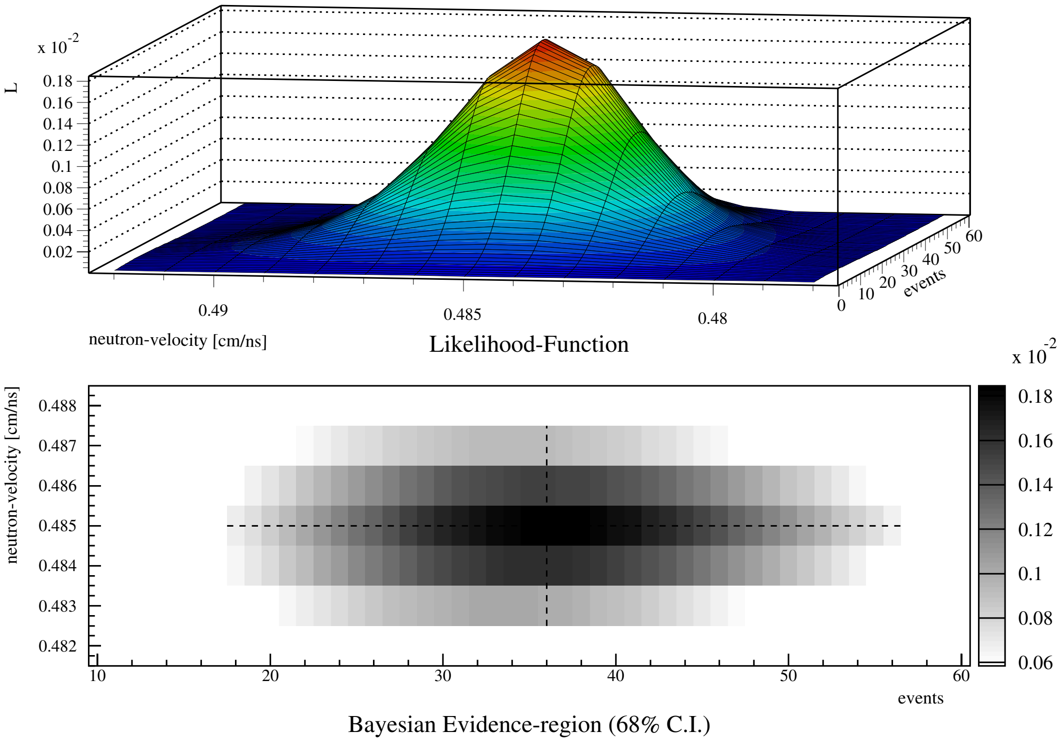

Figure 5.6: *On top*: Exemplary likelihood function in dependence of neutron-velocity and numbers of events (for $v_{neutron} \approx 0.5\, cm/ns$ from main-target in K1). *On bottom*: Derived $68\% CI$ Bayesian evidence region.

	v_n [cm/ns]	(n,γ)-events		v_n [cm/ns]	(n,γ)-events
			$K1$ μSR-target	0.401 ± 0.001	17 ± 16
$K1$ main-target	0.485 ± 0.002	36 ± 21	$K1$ μSR-target	0.489 ± 0.002	18 ± 16
$K1$ main-target	0.509 ± 0.006	23 ± 20			
$K1$ main-target	0.639 ± 0.005	31 ± 21			
			$K2$ μSR-target	0.403 ± 0.002	11 ± 10
			$K2$ μSR-target	0.494 ± 0.002	16 ± 10
$K2$ main-target	0.631 ± 0.006	21 ± 14			

Table 5.2: Statistically significantly ($68\% CL$) assigned numbers of (n,γ)-events derived from velocity analyses

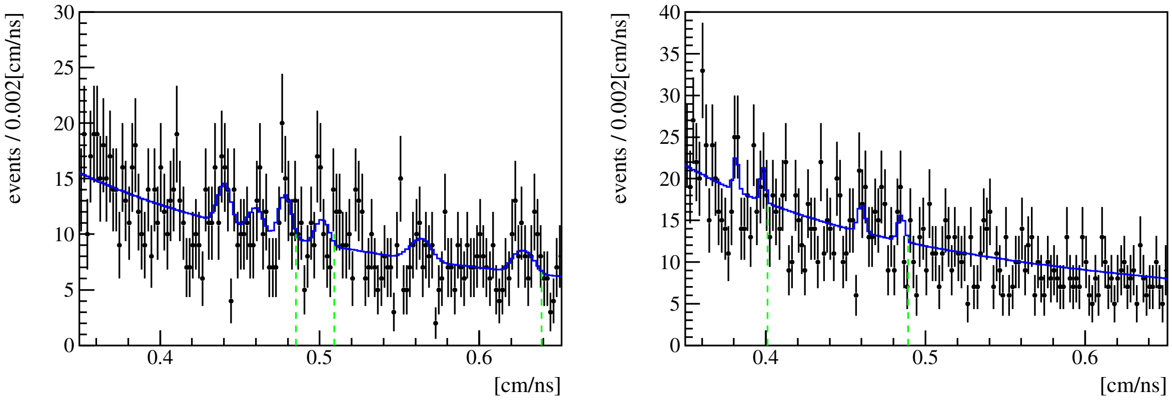

main-target in K 1 µSR-target in K 1

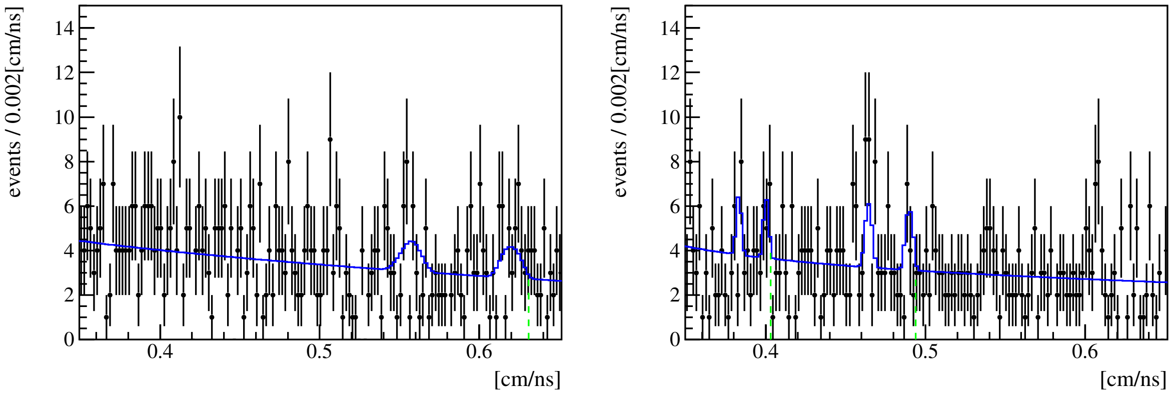

main-target in K 2 µSR-target in K 2

Figure 5.7: Comparison of likelihood results with measured velocity spectra of single-events (significant velocities of neutrons are marked with a dashed vertical line).

5.2.3 Interpretation of Results

From an overall velocity analysis, an entire probability for the hypothesis of beam correlated neutron background can be derived of roughly 1 milliard : 1 compared to the null hypothesis ($\cong -20\, ln\mathcal{L}_{ratio}$). Consequently, the hypothesis of beam correlated neutron background is by 5 orders of magnitude more likely than the X-particle hypothesis with $-7.3\, ln\mathcal{L}_{ratio}$ [Oeh99]. From a statistical point of view it is justifiable to conclude, that intermediate-energy neutrons inducing beam correlated background give a plausible resolution to the KARMEN-time-anomaly.

Descriptively, the massive iron shielding acts as filter for intermediate-energy neutrons coming from the ISIS target. Only neutrons with particular intermediate energies can pass through (due to the minima of the neutron cross section on iron in the resonance region). Having the appropriate time-of-flight within 0.6μs and 10.6μs, those intermediate-energy neutrons can evoke a single-event in the time-window of ν's from μ^+-decay. The higher the energy of those neutrons the less likely they are moderated inside the veto-counters and PE-slabs. But if the neutron-energy is too high, the time-of-flight will be less than 0.6μs. Moreover, the distinct minima of the neutron cross section on iron become less deep for higher neutron energies (*see Fig.* 5.5C). Taking all of that into account, there is an optimum probability of intermediate-energy neutrons inducing beam correlated background between 3μs and 4μs, corresponding to the deep double minimum of the neutron cross section on iron (no.$3+4$ related to main-target in *Fig.* 5.2b).

Prompt visible energies above 10 MeV are possible via (n,γ)-reaction on iron or chrome. But it has to be mentioned that it is not fully understood how those (n,γ)-events can produce prompt visible energies even above 16 MeV, what must have occurred to some extent, especially in K2. There is still an intelligible overspill at prompt visible energies below 13 MeV, accounting for roughly half of those excess-events [Oeh99]. The overall energy resolution of the detector cannot entirely explain the observed ratios. But after the upgrade the number of defective modules increased in K2 and consecutively the description of the energy resolution became less accurate (especially in the outer regions of the detector, due to the lightoutput-curves that are exponentially rising towards the ends of the modules).

Last but not least it is very conclusive that a substantial part of the time anomaly originates from the first quarter of the K1 data, before the extension of shielding with additional steel and boron treated PE-slabs was finished [Ebe92]. The arrangements aimed primarily at neutrons with energies around 25 keV (well-known broad minimum no.1 in *Fig.* 5.2), corresponding to a time-of-flight from main-target of roughly 8μs. Additionally, those later (n,γ)-events can be monitored more distinct in the time distribution of single-events, due to the shorter μ-lifetime of 2.2μs.

5.2.4 Implications on ν Cross Sections Determined from Single-Events

Fig. 5.8 demonstrates the two time distributions of single-events (K1/K2) including the portion of all (n,γ)-events determined as above from the velocity analyses. *Fig.* 5.9 shows the same spectra but using the appropriate standard binning (*Figures* E.5 and E.6 exclude sequences from CC-reactions $^{12}\mathrm{C}\,(\,\nu_e\,,\mathrm{e}^-\,)\,^{12}\mathrm{N}_{\mathrm{g.s.}}$).
The fraction of (n,γ)-events relative to the numbers of neutrinos amounts to 5% in K1 and 3% in K2. The statistical errors of the ν cross sections, determined from single-events in K2, are much larger. Additionally, the absolute number of (n,γ)-events in K2 scales down to less than half. Therefore, possible corrections due to (n,γ)-events can be neglected for K2. Because of the very characteristic peak structure in the visible energy of the NC-reaction $^{12}\mathrm{C}\,(\,\nu\,,\nu'\,)\,^{12}\mathrm{C}^*$, the (n,$\gamma$)-events in K1 can be disregarded for this cross section as well. Considering all worst case scenarios, in which the entire (n,γ)-events are associated in the χ^2-fit with only one of the less distinct CC-reactions, it has to be pointed out that the reactions $^{12}\mathrm{C}\,(\,\nu_e\,,\mathrm{e}^-\,)\,^{12}\mathrm{N}^*$ and $^{56}\mathrm{Fe}\,(\,\nu_e\,,\mathrm{e}^-\,)\,\mathrm{X}$ cannot be evaluated reliably enough for K1. There are only 120 events expected in K1 from $^{56}\mathrm{Fe}\,(\,\nu_e\,,\mathrm{e}^-\,)\,\mathrm{X}$ (taking the value of the measured ν cross section from K2: $217\cdot 10^{-42}\,cm^2$). That are even less than the 125 (n,γ)-events derived from the velocity analyses for K1. The statistical error of the cross section for $^{12}\mathrm{C}\,(\,\nu_e\,,\mathrm{e}^-\,)\,^{12}\mathrm{N}^*$ in K1 is as well intelligibly exceeded by the systematic error due to 125 (n,γ)-events in the worst case: 480 ± 27 events are measured, corresponding to a value of the cross section for $^{12}\mathrm{C}\,(\,\nu_e\,,\mathrm{e}^-\,)\,^{12}\mathrm{N}^*$ in K1 of $(5.4\pm0.3)\cdot 10^{-42}\,cm^2$ (*see Tab.* 3.8).

Neutron-sequences, correlated in time and space with a prompt single-event, must not be excluded from the data set ($0.6\mu s \leq T \leq 10.6\mu s$), because they are due to random background from intermediate-energy neutrons.

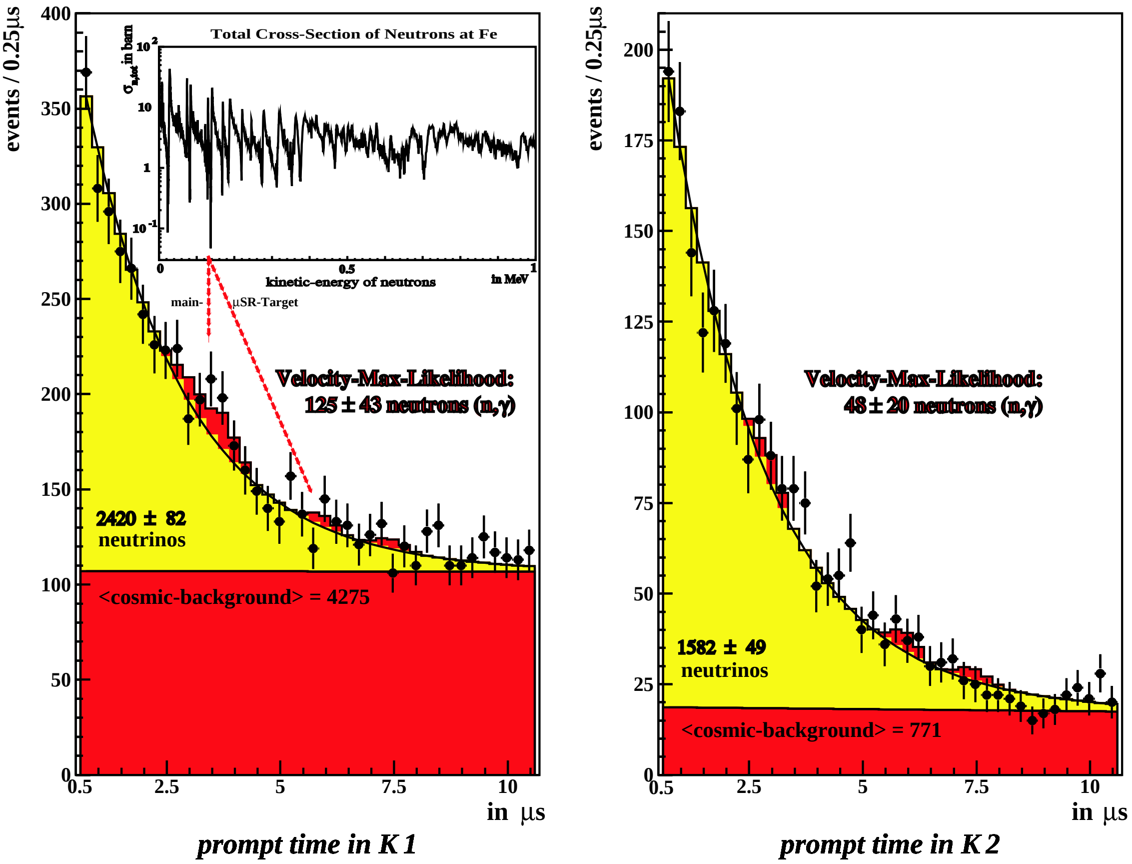

Figure 5.8: Time distribution of single-events in KARMEN1 (K1) before and KARMEN2 (K2) after the upgrade. From the velocity analysis derived portions of neutron-induced beam correlated (n,γ)-events are drawn-in (as well as the almost flat cosmic background expectation from pre-beam). The concatenation of an exemplary minimum of the neutron cross section with the plotted time distribution is shown for K1 (from main-target and μSR-pre-target, respectively).

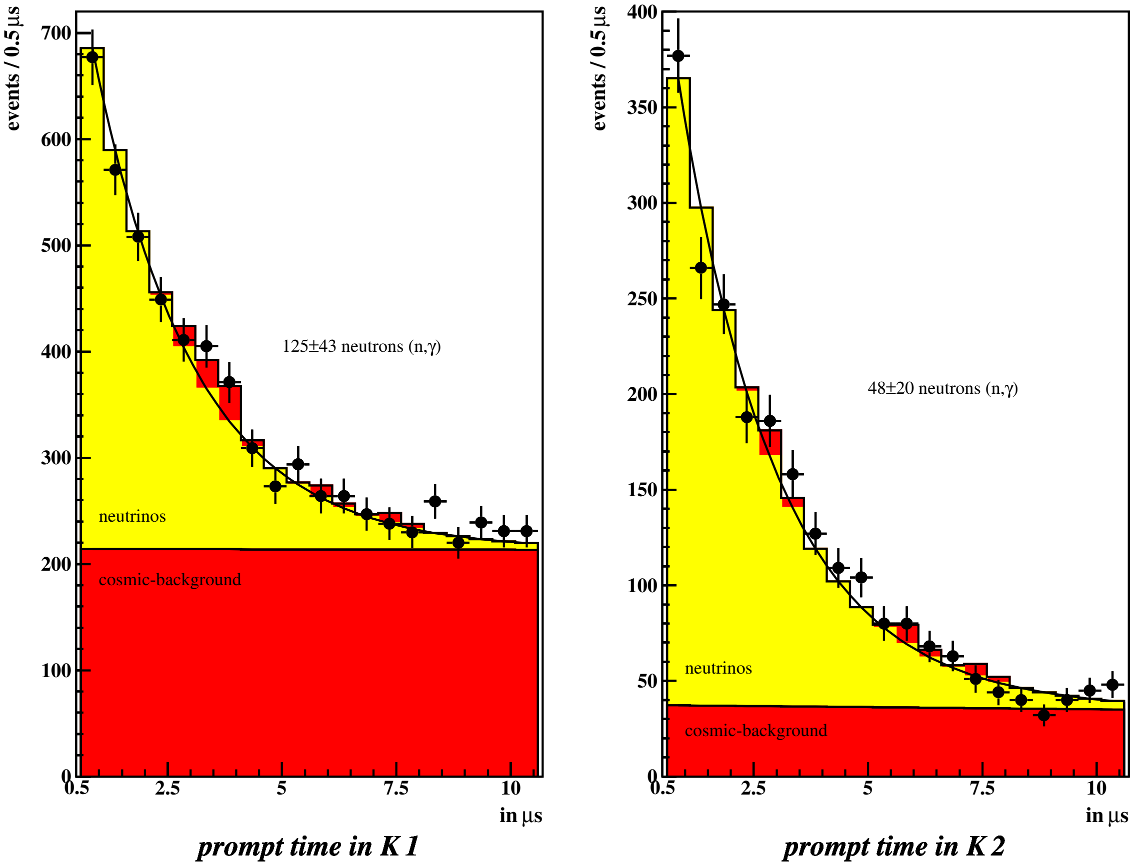

Figure 5.9: Time distribution of single-events in KARMEN1 (K1) before and KARMEN2 (K2) after the upgrade. From the velocity analysis derived portions of neutron-induced beam correlated (n,γ)-events are drawn-in (as well as the almost flat cosmic background expectation from pre-beam).

5.2.5 Implications on $\bar{\nu}_\mu \rightarrow \bar{\nu}_e$ Appearance and LSND

The (e^+,n)-sequence search[1] for $\bar{\nu}_\mu \rightarrow \bar{\nu}_e$ appearance with prompt visible energies from 10 MeV to 50 MeV finds significantly more sequences in K1 than expected. The cosmic background expectation from pre-beam plus the ν-induced random background expectation amount to 198 ± 14 sequences for K1. 258 sequences have been observed, i.e. more than 4σ above expectation[2]. After the upgrade the observed number of sequences is found to be 49, within the expectation of 34 ± 6 for K2. It is concluded that beam correlated intermediate-energy neutrons, penetrating the KARMEN-detector, increase the sequential random background rate. At the beginning of K1 the efficiency of tagging neutrons was less than half of the value towards the end of K1. The overall random background expectation for K1 was underestimated, due to lower statistics at the beginning of K1 and less neutron shielding.

---

[1] Most important other applied cuts: $\Delta T \leq 500\,\mu$s, $\Delta X \leq 80$ cm and $E_{seq,\,vis} \leq 8.4$ MeV

[2] Neglecting approximately 10 sequences from ^{12}C (ν_e , e$^-$) ^{12}N$_{\mathrm{g.s.}}$ and $\bar{\nu}_e$ -contamination

LSND features a comparably thick iron shielding towards the LAMPF target. But a possible time-anomaly cannot be observed there, due to the 600 μs long proton bunches of the LAMPF accelerator and a typical time-of-flight for neutrons on a μs-scale. Therefore, it is not feasible to apply a velocity analysis. Nevertheless, beam correlated intermediate-energy neutrons could increase the sequential random background rate for the (e^+,n)-sequence search. After a prompt neutrino reaction was observed, beam correlated neutrons, penetrating the LSND-detector and being consecutively moderated, could evoke randomly a sequential event. Despite of the particle identification for (e^+,n)-sequences, those neutrons could be interpreted as signal by coincidence: If the sequential random background portion is mainly determined from beam-off data (roughly 90 % according to the duty-factor), the overall background portion could be underestimated for the LSND search of $\bar{\nu}_\mu \rightarrow \bar{\nu}_e$ appearance (LSND-oscillation).

5.3 Exclusion Limit for a Weakly-Interacting 33.9 MeV Massive X-Particle from $\pi^+ \rightarrow \mu^+ + X$

It was suggested that KARMEN has a tentative indication for pion-decays beyond the standard model ($\pi^+ \rightarrow \mu^+ + X$) into a new weakly-interacting 33.9 MeV massive X-particle ([Zei95] and [Oeh99]). This hypothesis of the KARMEN-Time-Anomaly being due to such a new weakly-interacting 33.9 MeV massive X-particle, decaying in the detector with visible energies from 10 MeV to 36 MeV, will be excluded in the following.
The velocity analysis, described as above and slightly modified by the lifetime of pions, is utilized in order to search for such weakly-interacting massive X-particles from $\pi^+ \rightarrow \mu^+ + X$. Therfor the two 100 ns long proton pulses are accessorily folded with an exponential curve according to the 26 ns short lifetime of the pions (*compare with Fig.* 5.4 and 2.2b). A global velocity analysis of K1+K2, regarding exclusively the main-target, delivers 52 ± 27 X-particles ($68\% CL$) at $v_X = (0.641 \pm 0.004)$ cm/ns with $-4.4\, ln\mathcal{L}_{ratio}$ (*Fig.* 5.10). On the one hand this is 80 times more likely than the null hypothesis, but on the other hand it is seven orders of magnitude less likely than the neutron hypothesis described previously. The x-t-analysis in [Oeh99], utilized to search for decaying X-particles, delivers 58 ± 24 X-particles ($68\% CL$) at $v_X = (0.49 \pm 0.01)$ cm/ns with $-7.3\, ln\mathcal{L}_{ratio}$ (using roughly three quarters of the entire data). The resolution in x-position is less accurate than the resolution in the distance L from the target. The x-position is the projection of distance L onto module-axis. The intrinsically more sensitive velocity analysis ($v = L/t$) finds only 46 ± 25 X-particles ($68\% CL$) at $v_X = (0.487 \pm 0.003)$ cm/ns with $-4.3\, ln\mathcal{L}_{ratio}$ in the entire data[3].

---

[3] The much larger significance in the x-t-analysis of [Oeh99] can be partially explained by a binning effect. The bin-widths chosen in [Oeh99] for the probability density functions in the x-t-plane are not small enough, because herefrom calculated corresponding probability density functions in the velocity are not smooth.

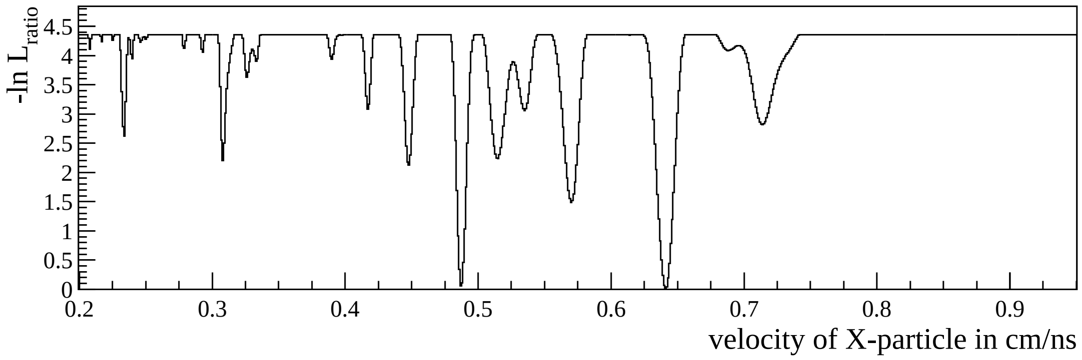

Figure 5.10: From velocity analysis of single-events in KARMEN derived likelihood function for a weakly-interacting massive X-particle from $\pi^+ \rightarrow \mu^+ + X$.

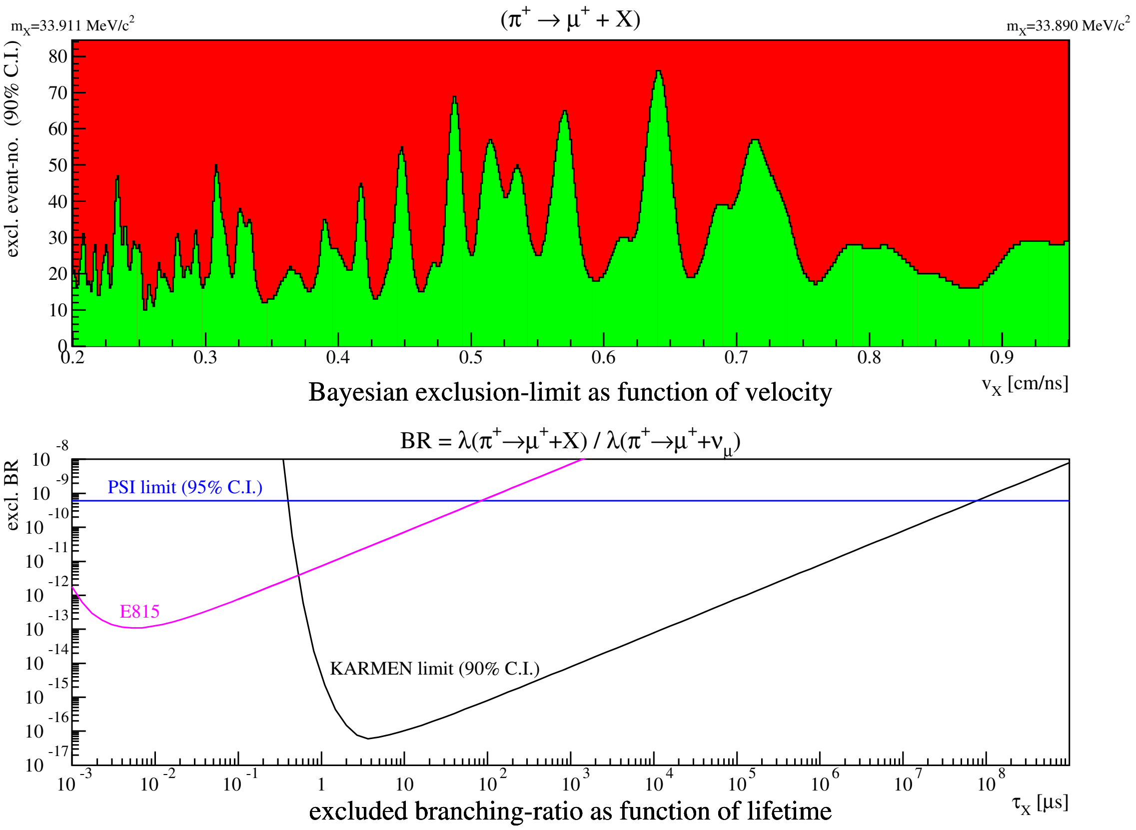

Figure 5.11: Exclusion limits ($90\% CL$) for a weakly-interacting massive X-particle from $\pi^+ \rightarrow \mu^+ + X$ (rest mass in the range from 33.890 MeV to 33.911 MeV). On top: Excluded number of X-particles from KARMEN as a function of velocity. On bottom: Excluded branching ratios versus lifetime from KARMEN, PSI [Dau00] and NuTeV(E815) [For99].

The pion-decay beyond standard model ($\pi^+ \rightarrow \mu^+ + X$) into a new weakly-interacting 33.9 MeV massive X-particle is consequently not observed in KARMEN, and thus a branching ratio down to $6 \cdot 10^{-17}$ is ruled out at $90\% CL$ in a Bayesian approach (for lifetimes on a μs-scale). *Fig.* 5.11 (on top) shows the excluded number of X-particles ($90\% CL$) in dependence of velocity. The values of velocity correspond to a rest mass of the X-particle in the range from 33.890 MeV to 33.911 MeV. An effective total pion flux of $36.5 \cdot 10^{20}$ is calculated by taking into account all efficiencies in K1 and K2. With respect to the geometry of the KARMEN-detector, a branching ratio $\lambda(\pi^+ \rightarrow \mu^+ + X) \,/\, \lambda(\pi^+ \rightarrow \mu^+ + \nu_\mu)$ can be excluded at $90\% CL$ as a function of the lifetime of the X-particle. Over the entire range of velocities different numbers of excluded X-particles ($90\% CL$) are incorporated as well. *Fig.* 5.11 (on bottom) shows the overall excluded branching ratio ($90\% CL$) versus the lifetime of the X-particle in comparison with the results of two other, less sensitive experiments.

The interpretation of the hypothetical X-particle as the lightest neutralino in the framework of a supersymmetric model with violation of R-parity [Cho99] shows, that this hypothesis contradicts the optical observations from supernova SN1987A [Kac00]. Combined with the KARMEN exclusion limit stringent boundaries on the mass of the lightest supersymmetric particle can be derived in the context of this MSSM model [Dre03].
Moreover, the time distribution of single-events in KARMEN can be used to determine boundaries on parameters for brane-world models with extra-dimensions [Luk00].
Most recently, quantized vibrations in models of dibaryons, pentaquarks and Z^* resonances have been proposed to account for a 35 MeV quantum [Ake04], which can be restricted with the KARMEN exclusion limit.

Chapter 6

Conclusion

In the framework of this thesis neutrino-induced neutral- and charged-current-reactions on ^{12}C, ^{13}C and ^{56}Fe nuclei were measured precisely with KARMEN in the energy regime of supernovae. It was possible to derive the corresponding cross sections model-independently and consistently from the first combined analysis of all neutrino-nucleus-interactions, which could be studied with KARMEN. The entire KARMEN data, which was acquired from 1990-2001 and represented 18547 C of accumulated proton-on-target charge, was evaluated globally for the first time. In addition, it was the first analysis of neutrino-nucleus-interactions using the entire KARMEN2 data (with a strongly suppressed cosmic background rate due to the upgrade).

It was feasible to measure 846 ν_e-sequences from exclusive CC-reactions $^{12}\mathrm{C}\,(\,\nu_e\,,\mathrm{e}^-\,)\,^{12}\mathrm{N}_{\mathrm{g.s.}}$ in spectroscopic quality and almost free of background (signal to background ratio of 61 : 1). This measurement demonstrated that the properties of the KARMEN-detector are very well understood. The following cross section, averaged over the ν_e-energy spectrum, was deduced from the global data set (K1+K2):

$$\boxed{\langle\sigma(^{12}\mathrm{C}\,(\,\nu_e\,,\mathrm{e}^-\,)\,^{12}\mathrm{N}_{\mathrm{g.s.}})\rangle = (9.6 \pm 0.3(stat.) \pm 0.7(syst.)) \cdot 10^{-42} cm^2}$$

The measured value is well in agreement with all theoretical EPT, SM and (C)RPA calculations, as well as with the corresponding LSND measurement of $(8.9 \pm 0.3(stat.) \pm 0.9(syst.)) \cdot 10^{-42} cm^2$ [Aue01].

Moreover, it was possible to determine 3826 ν-induced single-events with a χ^2-method, in which all unknown cross sections were varied freely and without relying on results from a particular model for neutrino-nucleus-interactions. Thus, for the NC-reaction $^{12}\mathrm{C}\,(\,\nu\,,\nu'\,)\,^{12}\mathrm{C}^*(\,1^+\,,1\ 15.11\ \mathrm{MeV}\,)$ the following total cross section, averaged over the ν_e- and $\bar{\nu}_\mu$-energy spectrum, was derived from the global data set (K1+K2):

$$\boxed{\langle\sigma(^{12}\mathrm{C}\,(\,\nu\,,\nu'\,)\,^{12}\mathrm{C}^*)\rangle = (10.2 \pm 0.4(stat.) \pm 0.8(syst.)) \cdot 10^{-42} cm^2}$$

Independently from the errors, the measured value is smaller than the former K1 value of $(10.9 \pm 0.7(stat.)) \cdot 10^{-42} cm^2$ [Sch96], mainly due to the fiducial volume, which had caused extra systematics for the MC-efficiency.

The uncertainty of the ν-flux, dominating the systematic errors of the ν cross sections, was eliminated by determining the ratio $R = \langle\sigma^{NC}\rangle/\langle\sigma^{CC}_{gs}\rangle$ of the measured ν cross sections for the neutral-current- and the exclusive charged-current reaction on ^{12}C:

$$\boxed{R = \langle\sigma^{NC}\rangle/\langle\sigma^{CC}_{gs}\rangle = 1.07 \pm 0.06(stat.) \pm 0.01(syst.)}$$

Within the achieved experimental accuracy of 5%, it was feasible to verify the μ-e-universality of neutral and charged weak currents and thus confirming the assumption of the V-A standard model. Furthermore, the unprecedented accuracy of the ratio R (former K1 value: $1.17 \pm 0.1(stat.)$ [Sch96]) has given rise to a more stringent comparison of various theoretical models for ν-interactions with light and medium-heavy nuclei. Despite of the good results from the CRPA, which is also one of the most utilized microscopic models in calculations for neutrino-nucleus-syntheses and supernova-explosions, there remains a discrepancy in R ($R^{CRPA} = 1.18$).

Moreover, it was feasible to derive the following total cross sections for the inclusive CC-reactions on ^{12}C and ^{13}C from KARMEN2 (averaged over the ν_e-energy spectrum):

$$\boxed{\langle\sigma(^{12}\mathrm{C}\,(\,\nu_e\,,\mathrm{e}^-\,)\,^{12}\mathrm{N}^*)\rangle = (4.8 \pm 0.6(stat.)\,^{+\,0.4}_{-\,0.5}(syst.)) \cdot 10^{-42}cm^2}$$

$$\boxed{\langle\sigma(^{13}\mathrm{C}\,(\,\nu_e\,,\mathrm{e}^-\,)\,^{13}\mathrm{N})\rangle = (50 \pm 25(stat.)\,^{+\,4}_{-\,6}(syst.)) \cdot 10^{-42}cm^2}$$

The worldwide first measurement of the cross section for $^{13}\mathrm{C}\,(\,\nu_e\,,\mathrm{e}^-\,)\,^{13}\mathrm{N}$ indicated, that the Gamow-Teller transition into the $^{13}\mathrm{N}^*(3/2^-)$-state is strongly quenched.
The measured value of the cross section for $^{12}\mathrm{C}\,(\,\nu_e\,,\mathrm{e}^-\,)\,^{12}\mathrm{N}^*$ is well in agreement with the final LSND-value of $(4.3 \pm 0.4(stat.) \pm 0.6(syst.)) \cdot 10^{-42}cm^2$ [Aue01].
An exact knowledge of all measured ν cross sections on carbon nuclei is essential for future supernova experiments, using organic scintillator, like KamLAND and Borexino: The observed rates for each neutrino-flavor will enable a discrimination of the discussed supernova-models.

Furthermore, the CC-reaction $^{56}\mathrm{Fe}\,(\,\nu_e\,,\mathrm{e}^-\,)\,\mathrm{X}$ was studied in detail and the following total cross section, averaged over the ν_e-energy spectrum, was derived from KARMEN2:

$$\boxed{\langle\sigma(^{56}\mathrm{Fe}\,(\,\nu_e\,,\mathrm{e}^-\,)\,\mathrm{X})\rangle = (217 \pm 135(stat.)\,^{+\,27}_{-\,65}(syst.)) \cdot 10^{-42}cm^2}$$

Consequently, events from this neutrino-nucleus-reaction on iron were observed at $90\%CL$ in KARMEN2 (disregarding the systematic error). With the derived value for the ν cross section on iron nuclei, the mean free path-length of neutrinos inside the core of a type II supernova amounts to 40 km during the collapse and just 20 m right at the beginning of the explosion [Sch97].

Fundamental new properties of neutrinos are concatenated with the LSND-oscillation ($\bar{\nu}_\mu \!\rightarrow \bar{\nu}_e$). The KARMEN-experiment is sensitive to neutrino-oscillations in an assimilable region of squared-mass differences as LSND. The final KARMEN2 result for $\bar{\nu}_\mu \!\rightarrow \bar{\nu}_e$ oscillation search, gained by evaluations and substantial parts of the data, taken within the framework of this thesis, excludes major parts of the LSND evidence region [Arm02]. Within this dissertation two other complementary methods for $\bar{\nu}_\mu \!\rightarrow \bar{\nu}_e$ oscillation search have been introduced in detail. Both of them strongly support the final KARMEN2 result.

The first method, using sequences for the $\bar{\nu}_\mu \rightarrow \bar{\nu}_e$ appearance search, was basically the same method, which has been chosen for the final KARMEN2 result in [Arm02], apart from the statistical approach. In a complementary intuitive window-method it was possible to exclude straightforward large parts of the LSND favored evidence region. The number of 15 $\bar{\nu}_e$-like sequences, found by the sequential search for $\bar{\nu}_\mu \rightarrow \bar{\nu}_e$ appearance, was well in agreement with the background expectation of 15.8 $\bar{\nu}_e$-like sequences. According to a Bayesian approach, the following upper limit for large Δm^2 was derived for $\boxed{\bar{\nu}_\mu \rightarrow \bar{\nu}_e}$ appearance from the sequence analysis:

$$\boxed{\sin^2(2\Theta) \;<\; 2.5 \cdot 10^{-3}\ (90\% CL)}$$

For $\Delta m^2 > 1\,eV^2$ most parts of the LSND favored evidence region can be excluded at $90\% CL$, due to this KARMEN2 result.

The second method, using single-events for the $\bar{\nu}_\mu \rightarrow \bar{\nu}_e$ appearance search, delivered a new independent probe of the LSND evidence region with KARMEN2. The single-events in KARMEN2 -with a strongly suppressed cosmic background portion due to the upgrade- showed likewise no evidence for $\bar{\nu}_\mu \rightarrow \bar{\nu}_e$ appearance in the LSND-region of squared-mass differences. The number of 14 single-event candidates, found by the applied window-method, was well in agreement with the background expectation of 14.4 single-events. According to a Bayesian approach, the following upper limit for large Δm^2 was derived for $\boxed{\bar{\nu}_\mu \rightarrow \bar{\nu}_e}$ appearance from the single-event analysis:

$$\boxed{\sin^2(2\Theta) \;<\; 2.8 \cdot 10^{-3}\ (90\% CL)}$$

Again, for $\Delta m^2 > 1\,eV^2$ most parts of the LSND favored evidence region can be excluded at $90\% CL$, due to this new independent KARMEN2 result. However, the most stringent exclusion limit is still provided by the final KARMEN2 result, using a maximum likelihood analysis of the $\bar{\nu}_e$-like sequences and an unified statistical approach ($\sin^2(2\Theta) < 1.7 \cdot 10^{-3}$ $(90\% CL)$ for large Δm^2).

Hence, in all of the three methods for $\bar{\nu}_\mu \rightarrow \bar{\nu}_e$ appearance search, KARMEN did not show evidence for the existence of an additional heavy sterile neutrino in the LSND-region of squared-mass differences (LSND-scenario).

Moreover, it was crucial, in the more dimensional context of neutrino-oscillations, to check if other neutrino-oscillations and CP-violation, respectively, occur in the LSND-region of squared-mass differences.

The cross section of the exclusive CC-reaction ${}^{12}\mathrm{C}\,(\,\nu_e\,,\mathrm{e}^-\,)\,{}^{12}\mathrm{N}_{\mathrm{g.s.}}$ as well as the flux-independent ratio $R = \langle\sigma^{NC}\rangle/\langle\sigma_{gs}^{CC}\rangle$, which have been measured very precisely using the entire KARMEN data set, were both in good agreement with theoretical predictions. There was neither evidence for the disappearance of ν_e nor evidence for the appearance of any other active neutrinos. The (860 ± 29.3) ν_e-sequences from ${}^{12}\mathrm{C}\,(\,\nu_e\,,\mathrm{e}^-\,)\,{}^{12}\mathrm{N}_{\mathrm{g.s.}}$, which have been measured, met the theoretical expectation of (806.2 ± 66.1) electron-neutrinos. For large Δm^2 the following upper limit was deduced for $\boxed{\nu_e \rightarrow \nu_{sterile}}$ disappearance:

$$\boxed{\sin^2(2\Theta) \;<\; 0.13\ (90\% CL)}$$

With the derived KARMEN result on $\nu_e \rightarrow \nu_{sterile}$ disappearance, it was feasible to exclude almost the entire region that has been proposed as possible explanation of the Weinberg-angle-anomaly reported by the NuTeV-experiment [Giu02]. KARMEN did not show evidence for such heavy sterile neutrinos being suggested.

With the KARMEN-experiment it was not only possible to search for $\nu_e \rightarrow \nu_{sterile}$ disappearance or $\bar{\nu}_\mu \rightarrow \bar{\nu}_e$ appearance by analyzing the late time window of μ^+-decay, but also to search for $\nu_\mu \rightarrow \nu_e$ appearance by investigating the two early time windows of π^+-decays. The number of 4 ν_e-like sequences, found by searching for $\nu_\mu \rightarrow \nu_e$ appearance, was well in agreement with the background expectation of 3.93 ν_e-like sequences. For large Δm^2 the following upper limit was derived for $\boxed{\nu_\mu \rightarrow \nu_e}$ appearance:

$$\boxed{\sin^2(2\Theta) \; < \; 2.4 \cdot 10^{-2} \; (90\% CL)}$$

This corresponds to an improvement of the old K1 limit [Eit95] by almost a factor of two, due to doubled statistics and the utilization of the measured $^{12}\mathrm{C}\,(\,\nu_e\,,\mathrm{e}^-\,)\,^{12}\mathrm{N}_{\mathrm{g.s.}}$ cross section at 29.8 MeV, which eliminated the theoretical uncertainty. The derived KARMEN-limit on $\nu_\mu \rightarrow \nu_e$ appearance is more stringent in the range of Δm^2 from $0.1\,eV^2$ to $10\,eV^2$ than the corresponding limit from the NuTeV-experiment [Avv02].
In the more dimensional context of neutrino-oscillations, the performed search for $\nu_\mu \rightarrow \nu_e$ appearance in KARMEN did neither deliver evidence for heavy sterile neutrinos nor for CP-violation in the LSND-region of squared-mass differences.

Last but not least, it was shown in the framework of this thesis that the KARMEN-time-anomaly can be explained with a high probability of occurrence by intermediate-energy neutrons inducing beam correlated background from the ISIS accelerator. Descriptively, the massive iron shielding acted as filter for intermediate-energy neutrons coming from the ISIS target, due to the distinct minima of the neutron cross section on iron in the resonance region. There was an optimum probability of intermediate-energy neutrons evoking a single-event in the late time-window of ν's from μ^+-decay between 3μs and 4μs, corresponding to the time-of-flight for neutrons at kinetic energies of the deep double minimum of the neutron cross section on iron (129 keV and 137 keV, respectively). Prompt visible energies above 10 MeV were possible via (n,γ)-reaction on iron or chrome within the steel, that closely surrounded the detector. But it has to be mentioned that it is not fully understood, in the framework of the energy resolution, how those (n,γ)-events produced visible energies even above 16 MeV, what must have occurred to some extent. There was still an intelligible overspill at visible energies below 13 MeV, accounting for approximately half of those (n,γ)-events.
From an overall maximum likelihood velocity analysis, an entire probability for the hypothesis of beam correlated neutron background was derived of roughly 1 milliard : 1 compared to the null hypothesis ($\cong\ -20\,ln\mathcal{L}_{ratio}$). Consequently, the hypothesis of beam correlated neutron background is by 5 orders of magnitude more likely than the former X-particle hypothesis ($\pi^+ \rightarrow \mu^+ + X$) with $-7.3\,ln\mathcal{L}_{ratio}$ [Oeh99]. From a statistical point of view it is justifiable to conclude, that intermediate-energy neutrons inducing beam correlated (n,γ)-events give a very plausible resolution to the KARMEN-time-anomaly.
The pion-decay beyond standard model ($\pi^+ \rightarrow \mu^+ + X$) into a new weakly-interacting 33.9 MeV massive X-particle was not observed in KARMEN, and thus a branching ratio down to $6 \cdot 10^{-17}$ was ruled out at $90\% CL$ in a Bayesian approach (for lifetimes on a μs-scale).

Appendix A

Refinement of Energy–Calibration

The quality of the energy-calibration was affected in KARMEN2, when the number of defective modules increased drastically. Therefore, a refinement of the energy-calibration was performed using stopped cosmic muons, which are recorded with a rate of approximately 170 Hz in every data RUN.

Stopped cosmic muons (SMU) inside the central detector can cause spatially correlated events, mainly on the time scale of a few microseconds. Whereas all μ^+ stopping in the detector will decay, a fraction of $\alpha_c = 7.8\%$ of the stopped μ^- undergo nuclear capture reactions in the scintillator. The muon-decay produces a spatially correlated Michel electron or positron with an energy up to $E_{max} = 52.83$ MeV. The time correlation is defined by the lifetime of μ^+ ($\tau = 2.197\,\mu$s) and μ^- ($\tau = 2.026\,\mu$s). The energy distribution of the Michel electrons or positrons can be calculated analytically from the 3-body-decay of muons at rest. Hence, the stopped muons being recorded every beam-period (since RUN 31), give rise to an *in situ* refinement of the energy-calibration. For each recorded RUN the measured Michel energy spectrum is compared with the corresponding MC-simulation, which accounts for the detector response and calibration. Despite of the excellent energy-calibration, small mismatches occurred up to a 5% level, especially towards the end of KARMEN, when the number of defective modules increased drastically. The small mismatches are corrected by adjusting the 50%-value of the falling edge near the endpoint of the visible Michel energy spectrum of each RUN. Thus, scaling factors for the visible energy of each RUN are deduced. Herewith, it is feasible to refine the energy-calibration RUN-wise. *Fig.* A.1 shows the RUN-wise determined 50%-value of the Michel energy-edge (before and after the refinement) in dependence of the accumulated proton-on-target charge in KARMEN. All modules have been considered for the final adjustment (without any fiducial cut). After the refinement, the remaining fluctuations of the found values for the Michel energy-edge are all within the errors, obtained from the fit.

Fig. A.2 shows the Michel energy spectra before and after the refinement of the energy-calibration in comparison with the expectation from the MC-simulation. Before the refinement in K2, the mismatches between the MC-simulation and the data can be clearly seen. After the refinement of the energy-calibration the agreement with the MC-simulation is excellent for both K1 and K2, regardless if all modules have been selected or only good modules in a full fiducial volume.

Fig. A.3 demonstrates the influence of the refinement of the energy-calibration on the

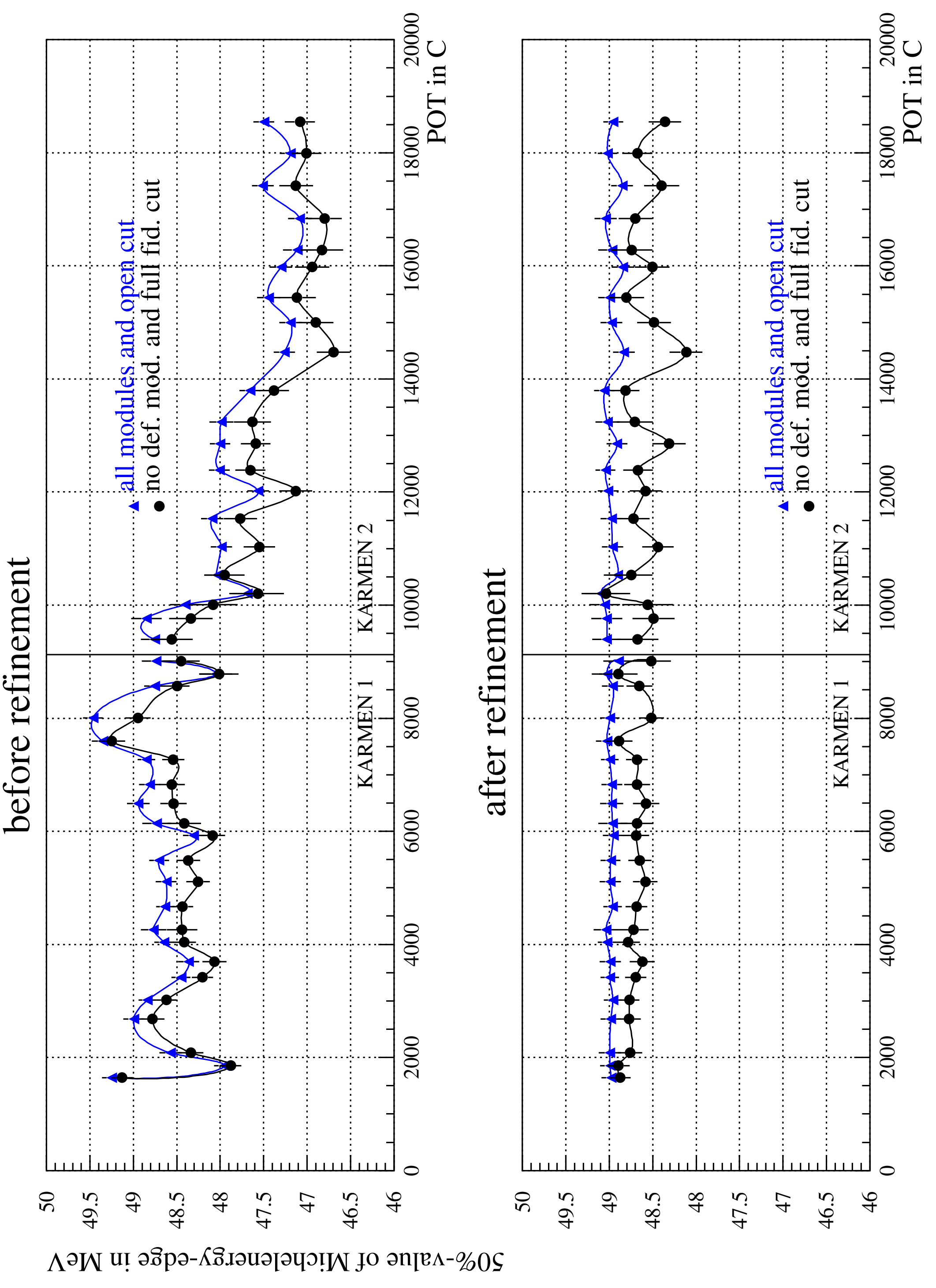

Figure A.1: RUN-wise determined 50%-value of the Michel energy-edge (before and after the refinement) in dependence of the accumulated proton-on-target (POT) charge in KARMEN. All modules have been considered for the final adjustment (without any fiducial cut).

prompt visible energy of single-events (in the late time window $0.6\,\mu\text{s} \leq T_{pr} \leq 10.6\,\mu\text{s}$ for neutrinos from μ^+-decays). Before the refinement in K2, the agreement was not sufficient enough for the determination of the neutrino nucleus cross sections ($\chi^2/ndf = 2.2$), in particular for the NC-reaction $^{12}\text{C}\,(\,\nu\,,\nu'\,)\,^{12}\text{C}^*$ with its characteristic peak structure in the visible energy (*see Chapter* 3.2). After the refinement in K1 and K2, the fitted energy spectra of single-events are in very good agreement with the data ($\chi^2/ndf = 1.2$ for [10 MeV, 30 MeV]).

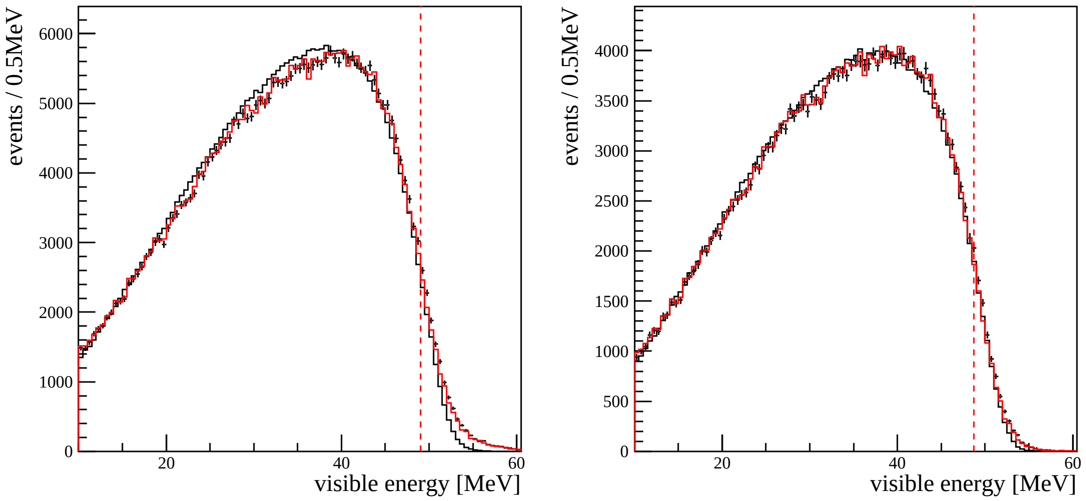

all modules in K1 good mod. & full fid.vol. in K1

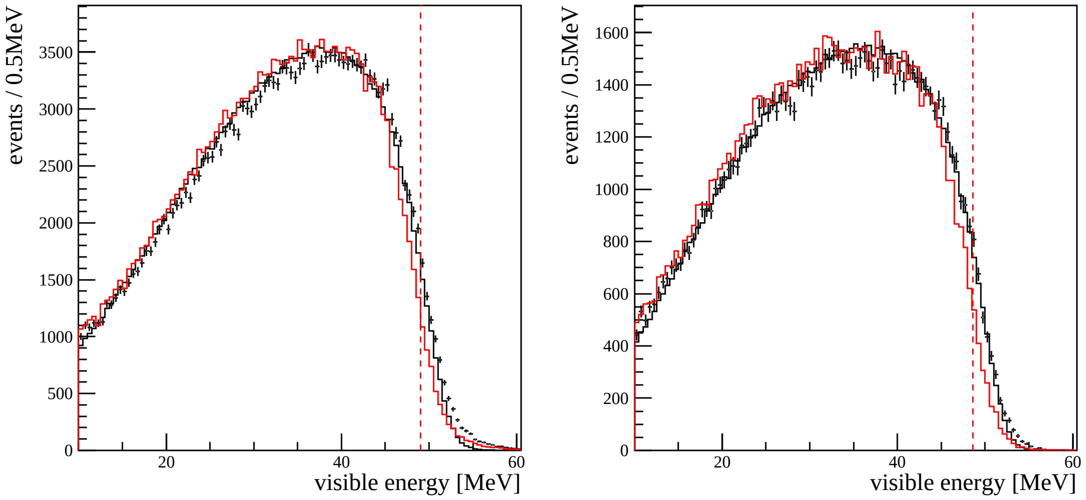

all modules in K2 good mod. & full fid.vol. in K2

Figure A.2: Each histogram shows the Michel energy spectra before refinement (red solid line) and after refinement of the energy-calibration (points with error bars) in comparison with the expectation from the MC-simulation (black solid line). Either all modules in K1 and K2, respectively, have been selected or only good modules in a full fiducial volume for K1 and K2. The corresponding mean 50%-value of the Michel energy-edge, derived from the data after refinement, is marked with a red dashed line in each spectrum. Only stopped cosmic muon (SMU) data have been evaluated, which passed the pre-reduction level of the KARMEN data selection.

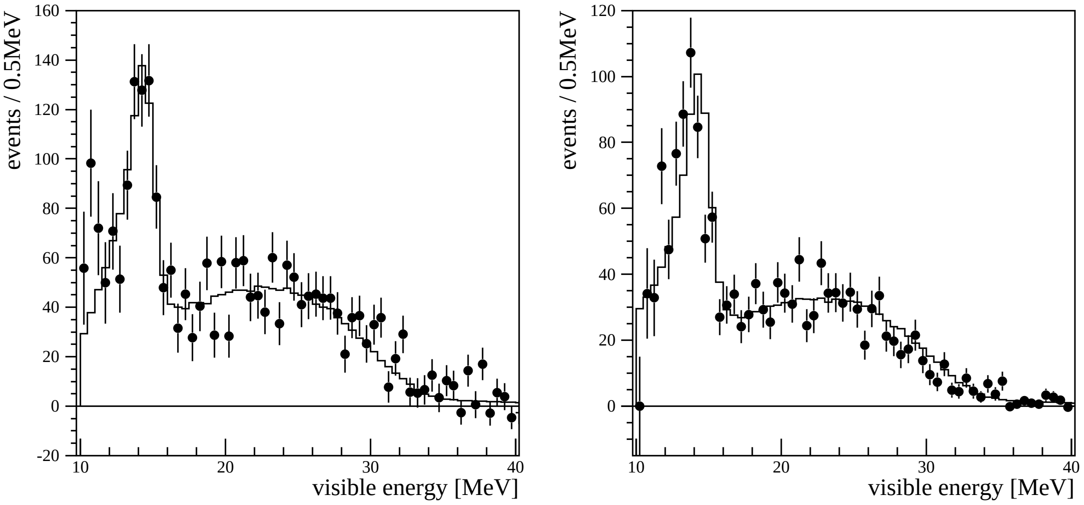

K1 before refinement K2 before refinement

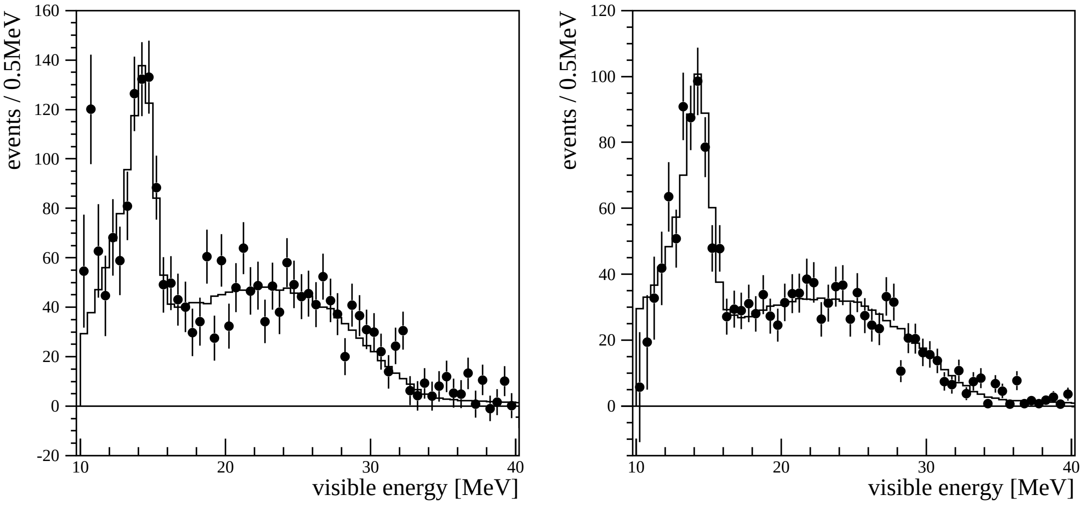

K1 after refinement K2 after refinement

Figure A.3: Prompt visible energy spectra of single-events before and after refinement of the energy-calibration in K1 and K2. For comparison the final single-event energy spectra of K1 and K2, respectively, derived from the χ^2-method in *Chapter* 3.2, are drawn-in as well (solid line in each spectrum). $\chi^2/ndf = 1.2$ for [10 MeV, 30 MeV], apart from K2 before refinement ($\chi^2/ndf = 2.2$ for [10 MeV, 30 MeV]). The portion of cosmic background is already subtracted in the energy spectra (according to the corresponding expectation from pre-beam).

Appendix B

Buzzing–Modules

Single buzzing-modules, producing arbitrarily an electronic noise, can cause a substantial part of the background for the single-events in KARMEN. The electronic noise in a buzzing-module does not vary over its entire x-position, it is restricted to a very narrow range of the x-position instead. Therefore, it is feasible to apply an appropriate spatial cut to the identified buzzing-module and still use the remaining part of the module, without having a significant rise of the overall background rate for the single-events in KARMEN. Buzzing-modules can be easily identified by selecting single-events in the pre-beam time window ($T_{pr} < 0\,\mu$s) with a multiplicity of one and crude energies of larger than 20 ADC-channels for either module-side. Thus, every recorded RUN can be checked for new buzzing-modules. *Fig.* B.1 (on left) displays the determined number of single-events in dependence of the RUN-number in K2 and the module-address. Thus, the new buzzing-modules can be easily spotted in every RUN. *Fig.* B.1 (on right) shows the corresponding module-addresses. For an identified buzzing-module, an appropriate spatial cut can be derived from the spatial distribution of the selected single-events, which occurred in this module since its malfunction. Exemplarily for one identified buzzing-module, *Fig.* B.2 shows the spatial distribution of the counts before and after the appropriate spatial cut was applied. Each of the identified buzzing-modules is marked in the calibration list with its appropriate spatial cut. *Fig.* B.3 (on left) displays the determined counts, after the update of the calibration, in dependence of the RUN-number in K2 and the module-address. After the update, no more buzzing-modules can be spotted. Hence, the background arising from buzzing-modules is minimized successfully in K2.

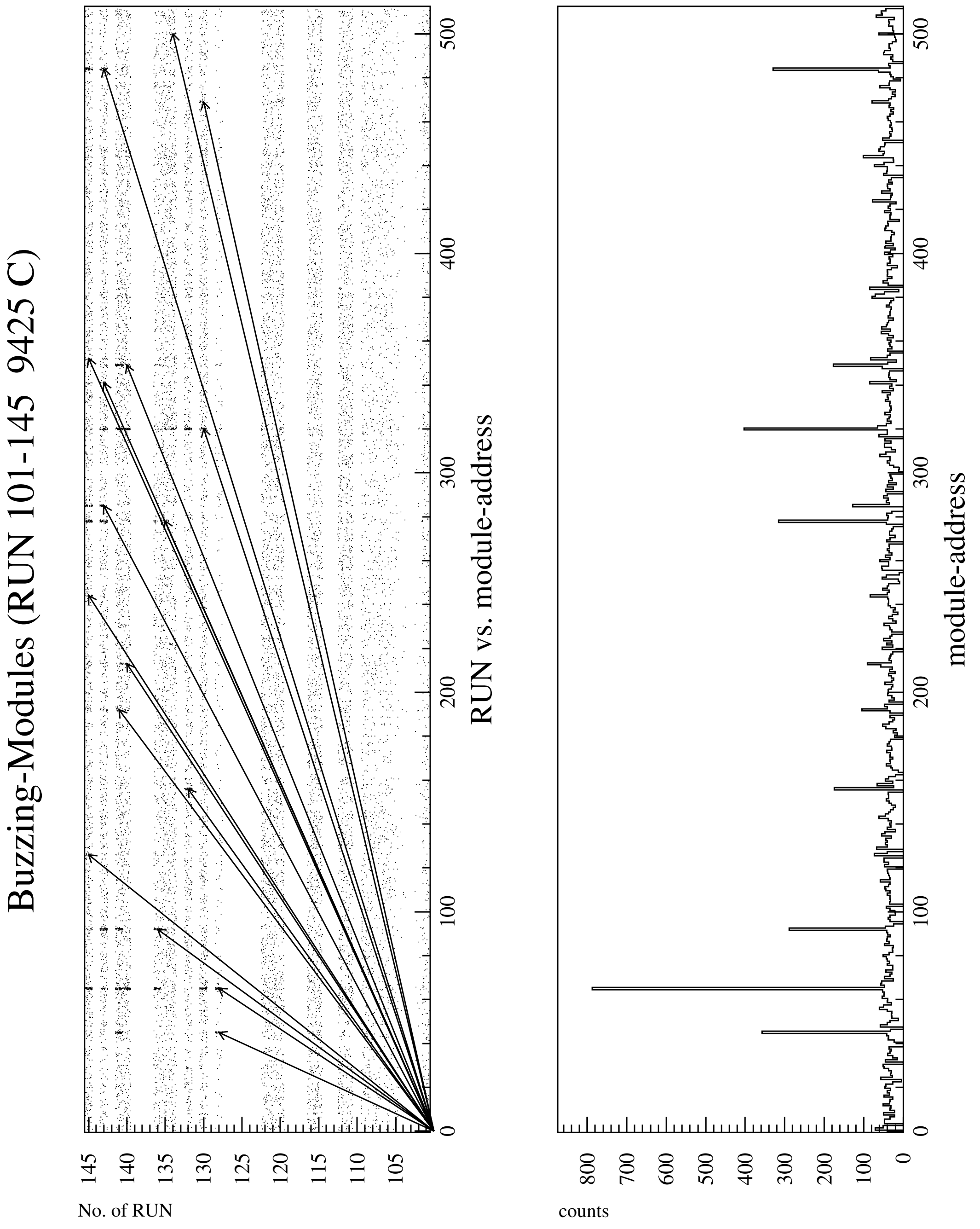

Figure B.1: On left: Number of pre-beam single-events in dependence of the RUN-number in K2 and the module-address (new identified buzzing-modules are marked with an arrow). On right: Number of pre-beam single-events in dependence of the corresponding module-address.

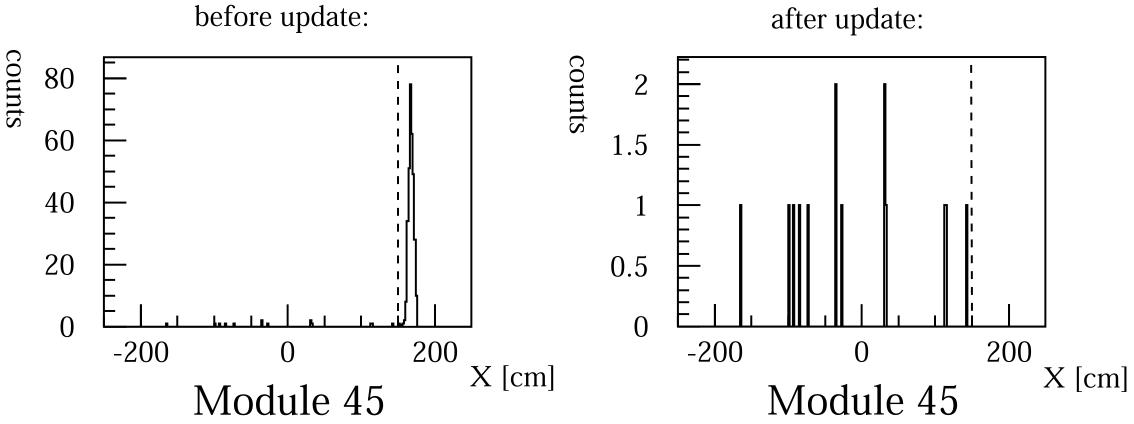

Figure B.2: Spatial distributions of pre-beam single-events before and after the appropriate spatial cut was applied to an exemplary buzzing-module (the appropriate spatial cut is marked with a dashed line).

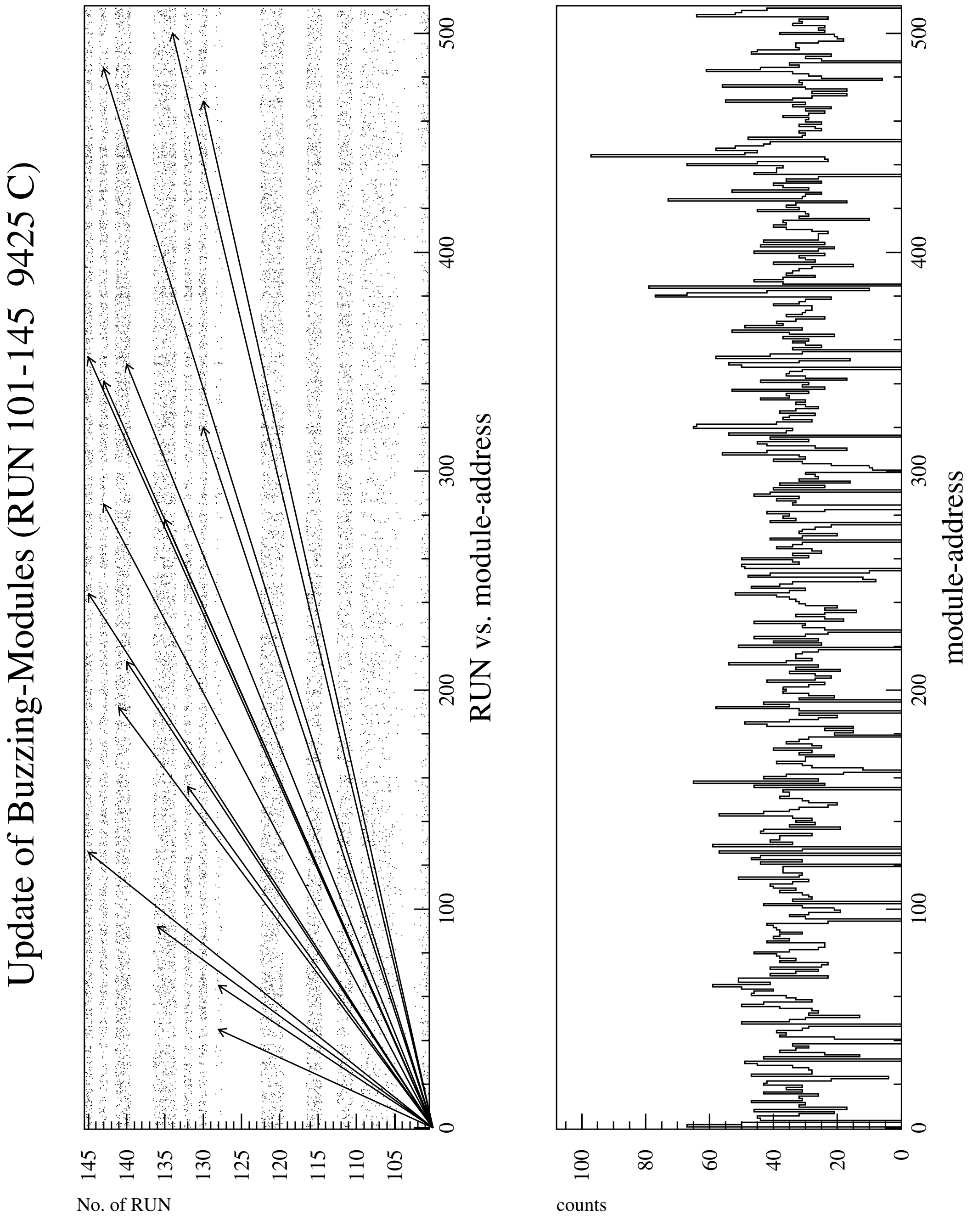

Figure B.3: On left: Number of pre-beam single-events, after the update of calibration, in dependence of the RUN-number in K2 and the module-address (new identified and corrected buzzing-modules are marked with an arrow). On right: Number of pre-beam single-events in dependence of the corresponding module-address.

Appendix C

Rejection of Events in Outer Regions of Defective Modules (X-Cut)

Especially after the upgrade, the number of defective detector modules increased and consecutively the description of the energy resolution became less accurate, predominantly in the outer regions of bad modules (due to the lightoutput-curves that are exponentially rising towards the ends of the modules, which makes the correction of light-leakage more difficult). In addition, the statistics for vertical and horizontal calibration cosmic muons are not sufficient enough for the correction of light-leakage in the outer 76.5 cm of defective modules. Therefore, a spatial X-cut is always applied to defective modules: Single-Events in the outer regions of defective modules ($|X_{pr}| > 100\,\mathrm{cm}$) are rejected, in order to keep up the quality of the energy-calibration. This is essential for a χ^2-fit to the visible energy of the single-events. For statistical reasons, it is not possible to evaluate only good modules, because the fraction of single-events, occurring in defective modules, amounts to roughly a third in K2.

Fig. C.1 *and* C.2 show the prompt visible energies and spatial distributions of the single-events for KARMEN1 before the upgrade and KARMEN2 afterwards in comparison with the cut-out events (X-cut applied). In KARMEN2 the peak in the visible energy of the NC-reaction $^{12}\mathrm{C}\,(\,\nu\,,\nu'\,)\,^{12}\mathrm{C}^{*}$ is evidently degraded for the cut-out events by almost a factor of three compared to the final single-events (*compare Fig.* C.2 *top left and bottom left*).

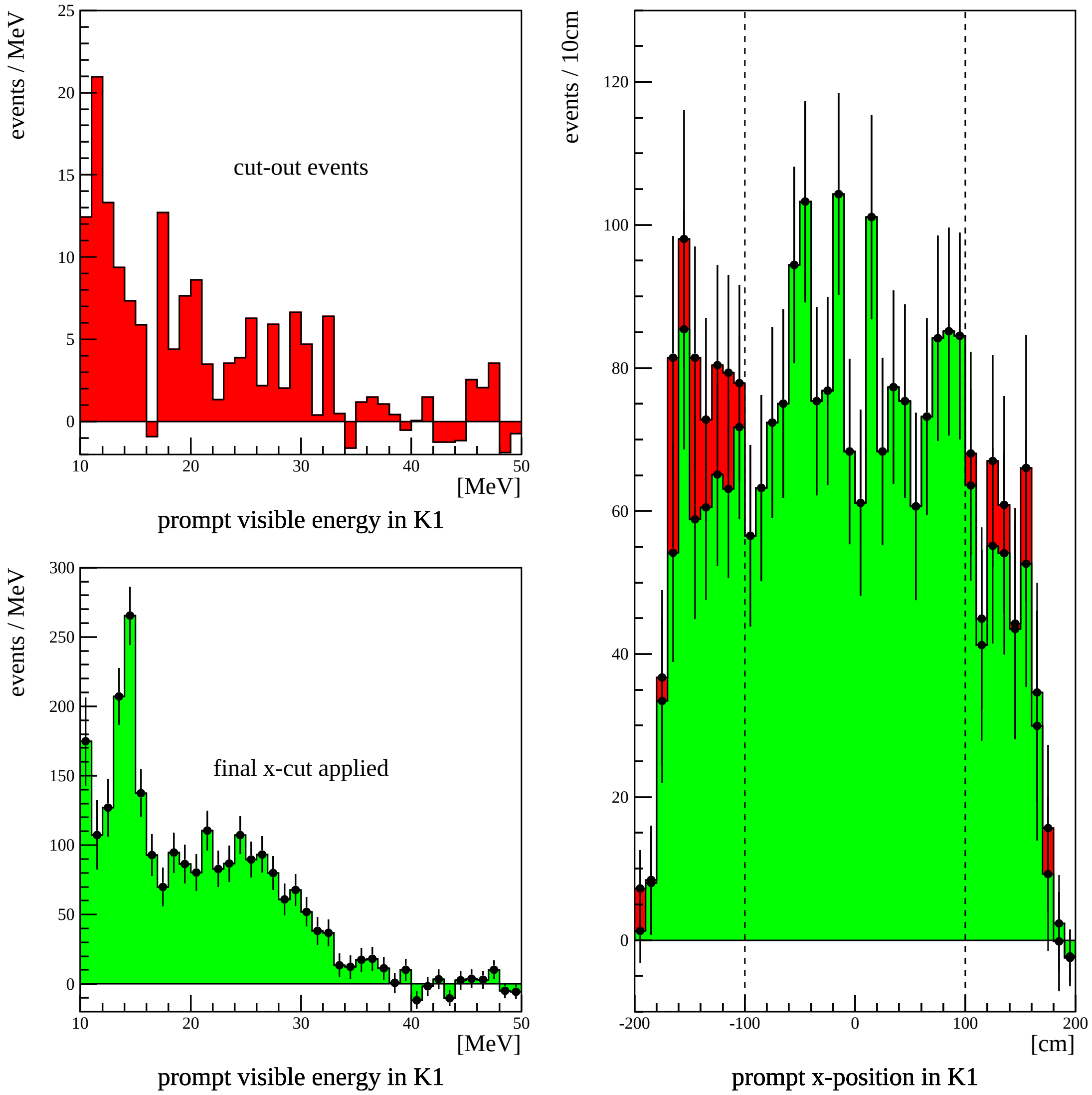

Figure C.1: Prompt visible energies and x-positions of the final (light green area) single-events in KARMEN1 (K1) in comparison with the rejected (dark red area) single-events (X-cut applied). The portion of cosmic background is already subtracted in the spectra (according to the corresponding expectation from pre-beam).

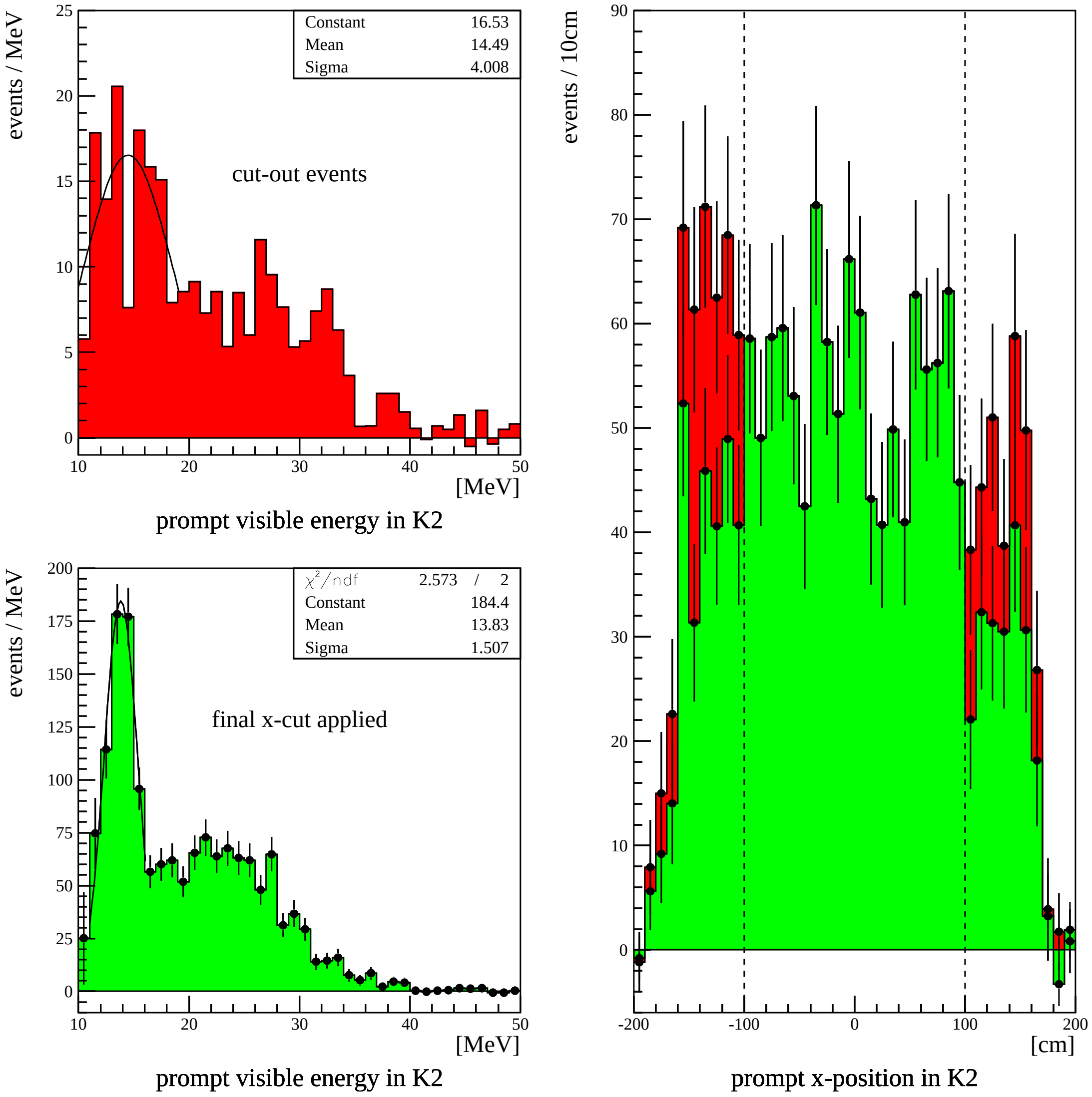

Figure C.2: Prompt visible energies and x-positions of the final (light green area) single-events in KARMEN2 (K2) in comparison with the rejected (dark red area) single-events (X-cut applied). The portion of cosmic background is already subtracted in the spectra (according to the corresponding expectation from pre-beam).

Appendix D

Efficiencies

Stack-Efficiencies

In order to reduce the cosmic background, optimized software dead-times are applied after every stack-entry (and veto-only VO in K2). This stack-reduction minimizes the background from unrecognized muons stopping and decaying ($\overline{\tau} \approx 2.2\,\mu$s) close or inside the central detector and thus mainly producing delayed Michel electrons or positrons with an energy up to $E_{max} = 52.83$ MeV. Although, the efficiency of the anti-counter-system for tagging stopped muons is approximately 99.8%, a background rate for single events remains, which is 10^5 times higher than the neutrino rate. Therefore, after every event, being processed by the MLU[1] and thus obtaining a stack-entry, an optimized software dead-time in the order of $20\,\mu$s is applied [Arm98]. On the one hand this reduces drastically the cosmic background rate, but on the other hand the stack-reduction is causing an efficiency loss of up to 37%, depending on the applied dead-time and the rate of events. The stack-efficiency for each applied software dead-time can be derived precisely from the recorded data: After every stack-entry, the following period of time is marked as paralyzed, according to the applied dead-time. This is done for every recorded beam-period, which was enabled as a second beam-period, in order to avoid an off-set. Finally, the paralyzed time distribution is divided by the entire number of second beam-periods. Thus, the time distribution of the stack-efficiency is derived. This procedure is performed for any of the applied dead-times and for every single recorded RUN. Finally, the time distributions are added RUN-wise flux-weighted in each case, in order to determine the appropriate time dependent stack-efficiencies for K1 and K2. *Fig.* D.1 shows the time dependent stack-efficiencies in K1 and K2 for single-events, for prompt and sequential events from $^{12}\mathrm{C}\,(\,\nu_e\,,\mathrm{e}^-\,)\,^{12}\mathrm{N}_{\mathrm{g.s.}}$ as well as for prompt events from the sequential $\bar{\nu}_\mu \rightarrow \bar{\nu}_e$ appearance search.

---

[1] Memory Lookup Unit

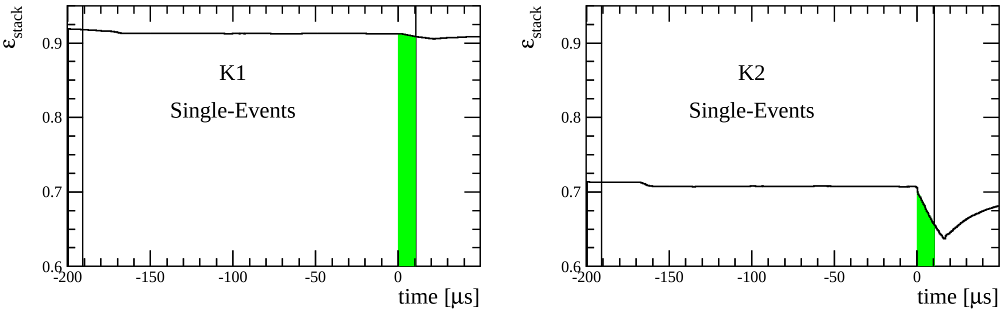

ε_{st} (20µs,0µs VO) K1

ε_{st} (28µs,17µs VO) K2

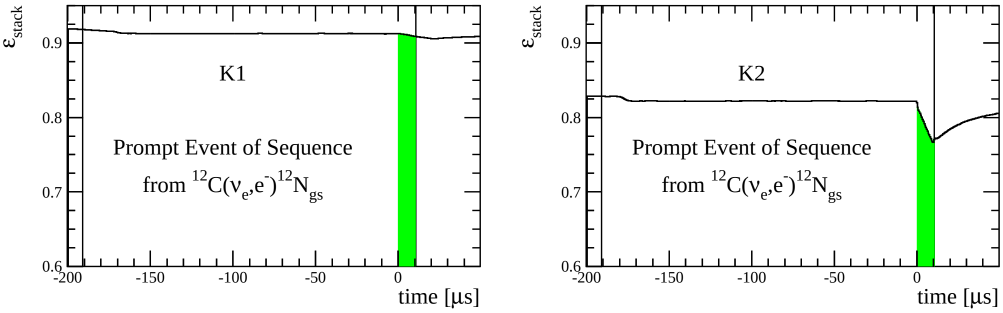

ε_{st} (20µs,0µs VO) K1

ε_{st} (15µs,10µs VO) K2

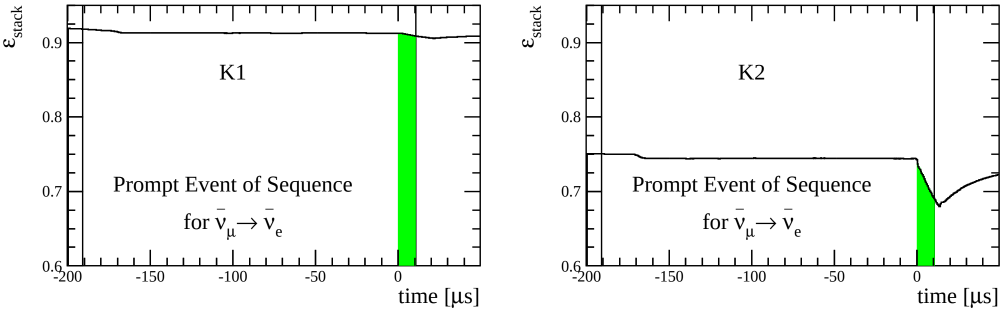

ε_{st} (20µs,0µs VO) K1

ε_{st} (24µs,14µs VO) K2

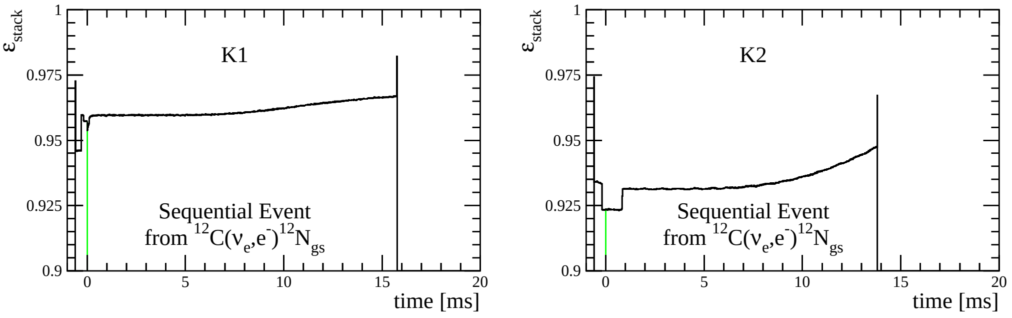

ε_{stack} (10µs) K1

ε_{stack} (10µs) K2

Figure D.1: Time dependent stack-efficiencies in K1 and K2 for single-events, for prompt and sequential events from $^{12}\mathrm{C}\,(\,\nu_e\,,\mathrm{e}^-\,)\,^{12}\mathrm{N}_{\mathrm{g.s.}}$ as well as for prompt events from the sequential $\bar{\nu}_\mu \rightarrow \bar{\nu}_e$ appearance search (the late time window $0.6\,\mu\mathrm{s} \leq T_{pr} \leq 10.6\,\mu\mathrm{s}$ for neutrinos from μ^+-decays is emphasized with a green filled area in every spectrum and the start of the pre-beam time window $T_{pr} = -191\,\mu\mathrm{s}$ is marked with a solid line in either of the prompt time windows).

SMU-Efficiencies

Stopped cosmic muons (SMU) inside the central detector can cause spatially correlated events on the time scale of a few microseconds up to several milliseconds (*see Chapter* 3.1.2). In order to eliminate most of the background originating from stopped muons, events are rejected if a preceding stopped muon is found within the following time-differences and coincidence volumes (SMU-reduction since RUN 31):

$$^{12}\mathrm{B}_{\mathrm{g.s.}} \rightarrow {}^{12}\mathrm{C} + \mathrm{e}^- + \bar{\nu}_e$$

$$\begin{array}{llllll}
500\ \mu\mathrm{s} & \leq & \Delta T & < & 100\ \mathrm{ms} & ;\ \textit{time-difference} \\
 & & |\Delta X| & < & 60\ \mathrm{cm} & ;\ \textit{x-position-difference} \\
 & & |\Delta ROW| & < & 0.5 & ;\ \textit{row-difference} \\
 & & |\Delta COL| & < & 0.5 & ;\ \textit{column-difference}
\end{array}$$

$$\mu^- + {}^{12}\mathrm{C} \rightarrow {}^{12-x}\mathrm{B} + \mathrm{x} \cdot \mathrm{n} + \nu_\mu$$

$$\begin{array}{llllll}
40\ \mu\mathrm{s} & \leq & \Delta T & < & 500\ \mu\mathrm{s} & ;\ \textit{time-difference} \\
 & & |\Delta X| & < & 80\ \mathrm{cm} & ;\ \textit{x-position-difference} \\
 & & |\Delta ROW| & < & 2.5 & ;\ \textit{row-difference} \\
 & & |\Delta COL| & < & 2.5 & ;\ \textit{column-difference}
\end{array}$$

$$\begin{array}{llll}
\Delta T & < & 40\ \mu\mathrm{s} & ;\ \textit{time-difference} \\
\text{entire detector} & & &
\end{array}$$

The SMU-efficiency can be derived precisely from the recorded data, in analogy to the stack-efficiency, apart from the fact that the applied dead-time has to be weighted with the fraction of the applied dead-volume. In order to cover the time-period of 100 ms, a segmented buffer over five beam-periods is utilized. If the system is already paralyzed due to the applied stack-dead-time, the SMU-dead-time must not be counted additionally. For computing time reasons, this is done solely for the prompt time window, which is relevant for the value of the SMU-efficiency, needed as input for the evaluations. *Fig.* D.2 shows the time dependent SMU-efficiencies in K1 and K2 for an entire beam-period as well as for the prompt time window. It can be clearly seen, that the reduction of β-decays from $^{12}\mathrm{B}_{\mathrm{g.s.}}$ ($\tau = 29.1\,\mathrm{ms}$), which leads to the longest time-difference of 100 ms, is predominantly responsible for the efficiency loss.

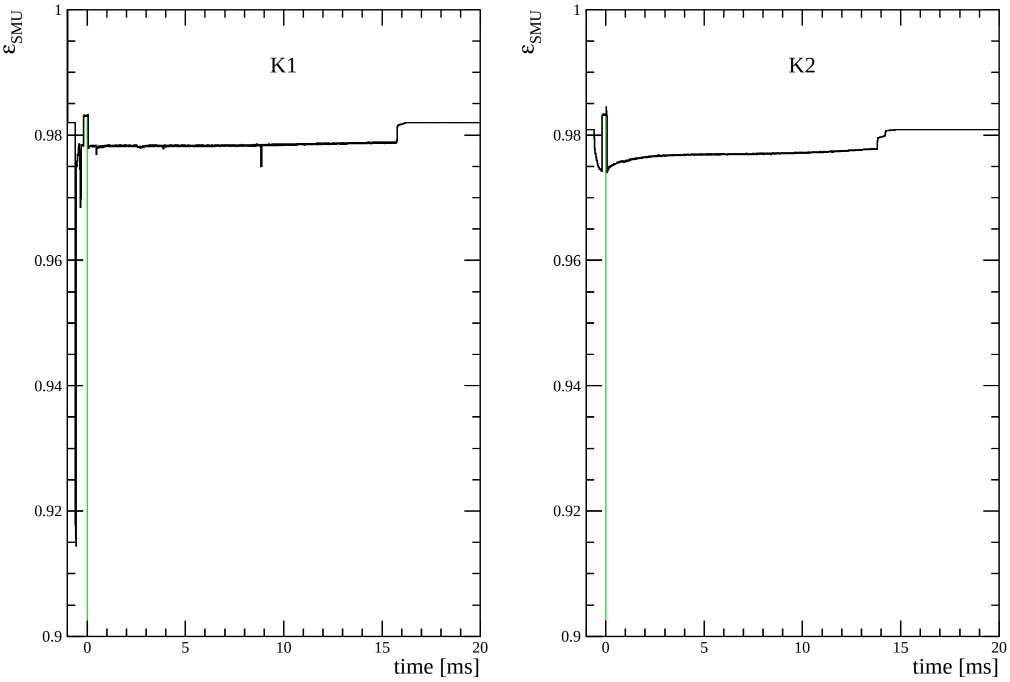

ε_{SMU} in K1 ε_{SMU} in K2

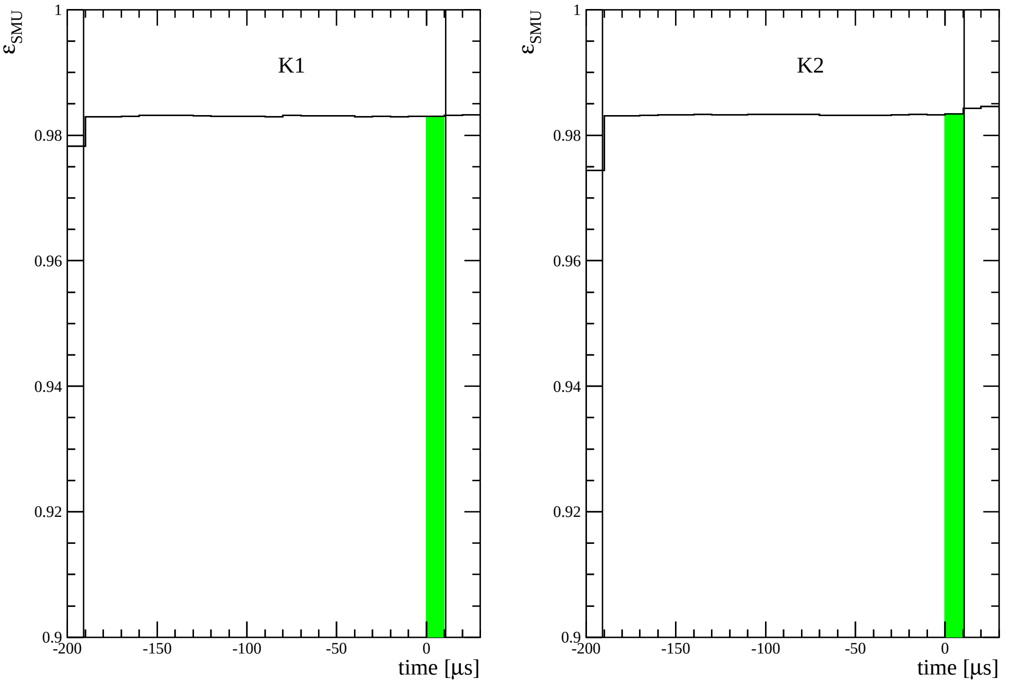

ε_{SMU} K1 ε_{SMU} K2

Figure D.2: Time dependence of SMU-efficiencies in K1 and K2 for an entire beam-period as well as for the prompt time window (the late time window $0.6\,\mu\text{s} \leq T_{pr} \leq 10.6\,\mu\text{s}$ for neutrinos from μ^+-decays is emphasized with a green filled area in every spectrum and the start of the pre-beam time window $T_{pr} = -191\,\mu\text{s}$ is marked with a solid line in either of the prompt time windows).

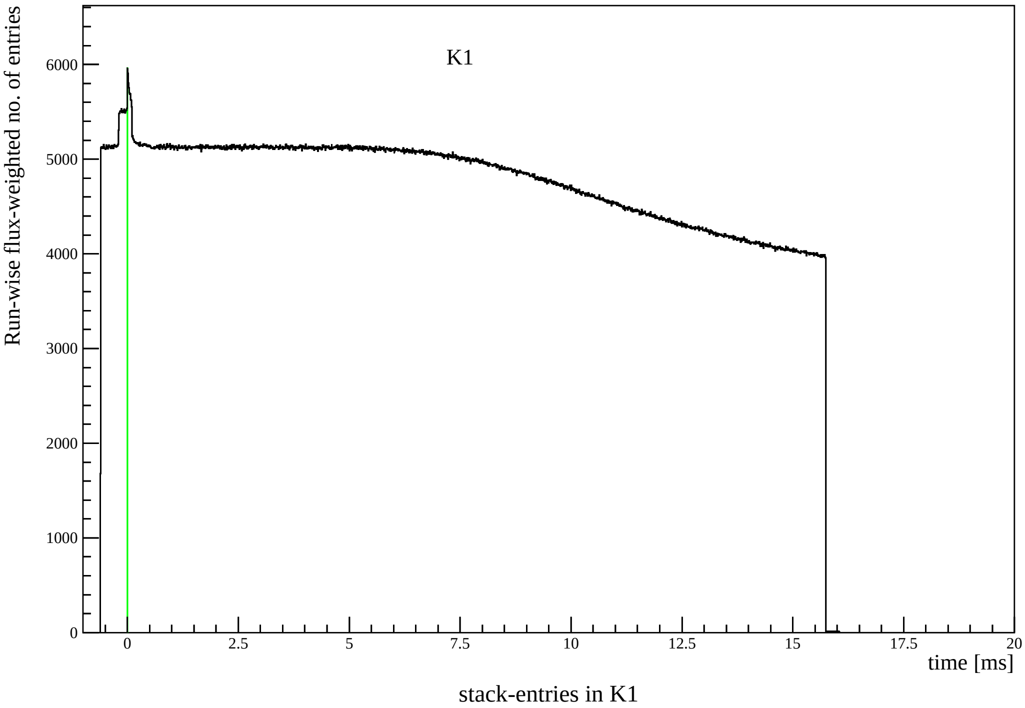

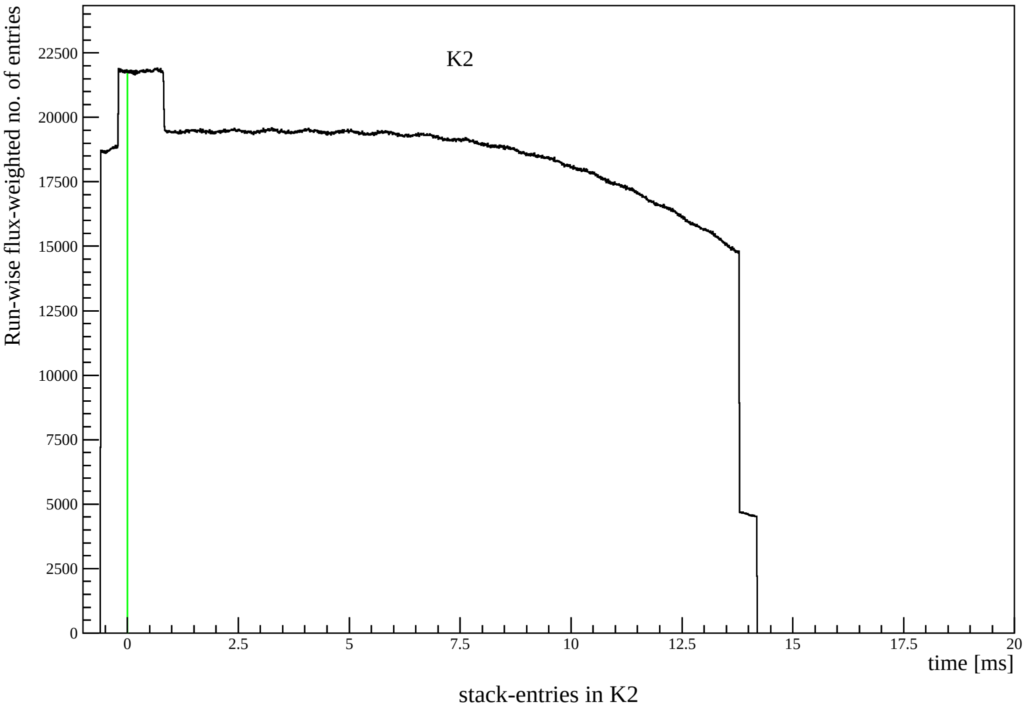

Figure D.3: Time distribution of stack-entries in K1 and K2 for an entire beam-period. For this, the number of entries is added RUN-wise flux-weighted. The late time window $0.6\,\mu\text{s} \leq T_{pr} \leq 10.6\,\mu\text{s}$ for neutrinos from μ^+-decays is emphasized with a green filled area in each spectrum.

Data-Stack

Every event, being processed by the MLU[2] obtains an entry in the data-stack. *Fig.* D.3 shows the time distribution of the stack-entries in K1 and K2 for an entire beam-period. Thus, the structure of a beam-period in K1 and K2, respectively, can be monitored precisely (*compare Fig.* 2.6). The maximum number of 16 events, which can be recorded every beam-period, is causing a time dependent efficiency loss (mainly in K2, due to lower threshold values and a higher rate of events).

Sequential Time Efficiency for $^{12}\mathbf{C}\,(\,\nu_e\,,\mathbf{e}^-\,)\,^{12}\mathbf{N}_{\mathrm{g.s.}}$

The time-difference distribution of the sequential events from $^{12}\mathrm{C}\,(\,\nu_e\,,\mathrm{e}^-\,)\,^{12}\mathrm{N}_{\mathrm{g.s.}}$ in KARMEN does not reflect directly the lifetime of $^{12}\mathrm{N}_{\mathrm{g.s.}}$ ($\tau = 15.9\,\mathrm{ms}$). Corrections, caused by the electronics, have to be taken into account. These corrections are due to: a) the read-out gap at the end of every beam-period, b) the maximum number of 16 events, which can be recorded every beam-period (*compare Fig.* D.3), c) the variable EC1-threshold in K2 (for $T > 800\mu\mathrm{s}$), which switches again to a $600\,\mu\mathrm{s}$ long period of low threshold (EC1 off) after an event above MLU-threshold occurred (*see Fig.* 2.6) as well as d) failures of the enabling of the second beam-period mode for the following beam-period. All of these corrections, modifying the observed sequential time spectrum of positrons from β^+-decays of $^{12}\mathrm{N}_{\mathrm{g.s.}}$ ($\tau = 15.9\,\mathrm{ms}$), can be derived precisely from the recorded data (*see Table* 3.2 *in Chapter* 3.1). For this, the only input parameters in K2 are the simulated values of the MC-efficiencies with EC1-threshold on and off. *Fig.* D.4 shows the expected time-difference distribution of the sequential events from $^{12}\mathrm{C}\,(\,\nu_e\,,\mathrm{e}^-\,)\,^{12}\mathrm{N}_{\mathrm{g.s.}}$ for K1 and for K2, with respect to all corrections caused by the electronics (rate added RUN-wise flux-weighted).

---

[2] Memory Lookup Unit

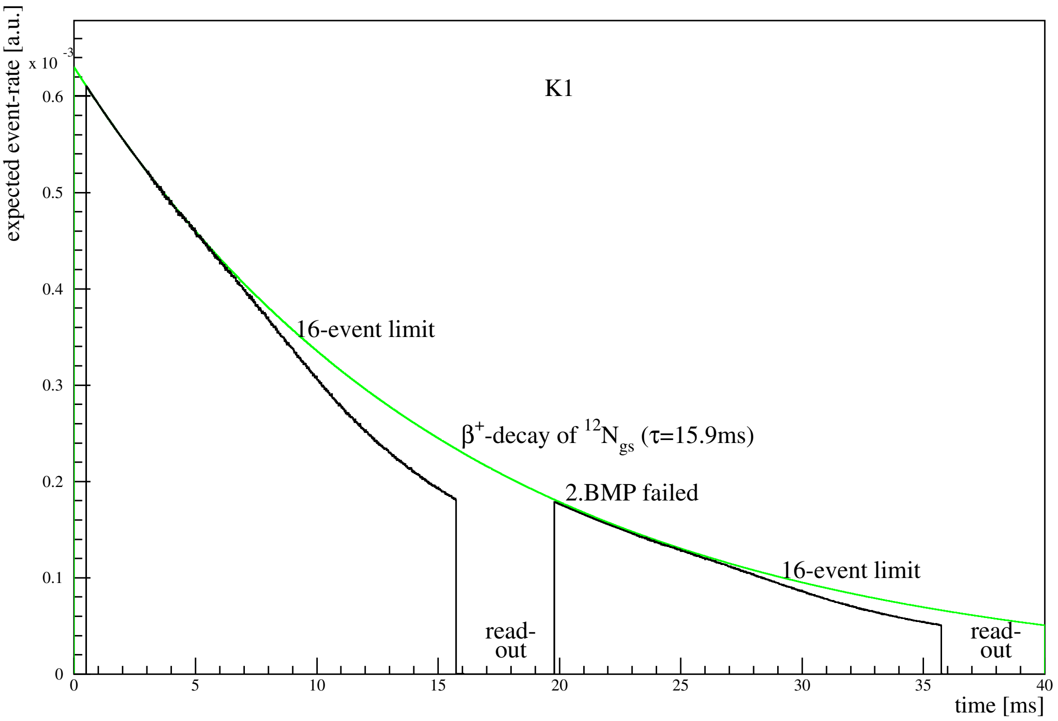

Sequential Event from $^{12}C(\nu_e,e^-)^{12}N_{gs}$ in K1

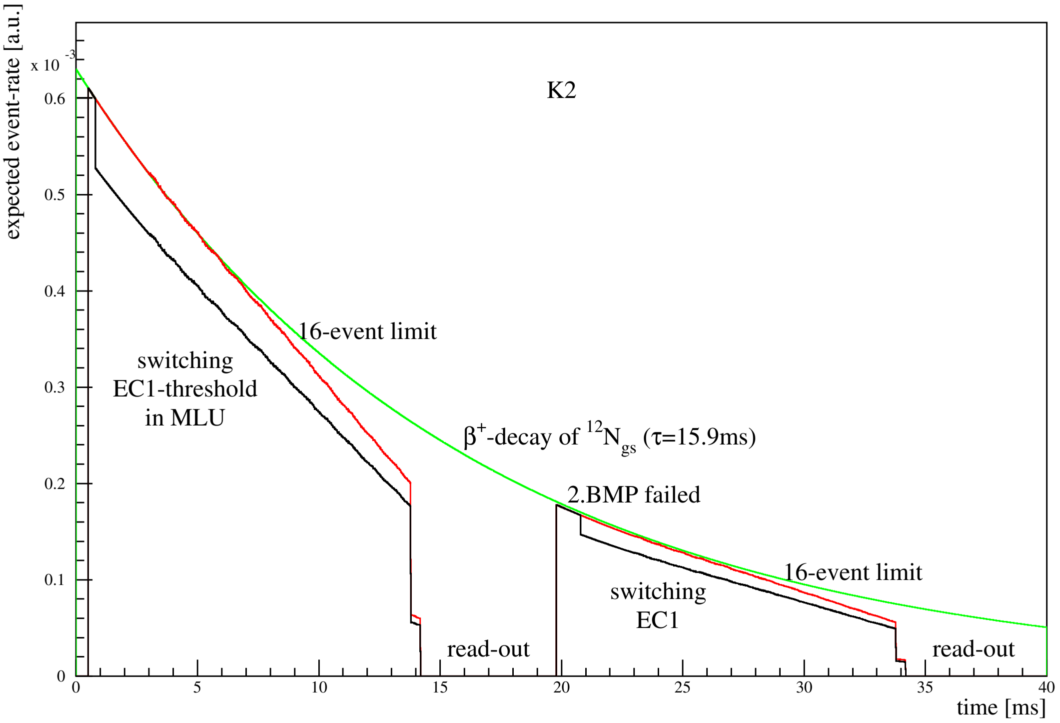

Sequential Event from $^{12}C(\nu_e,e^-)^{12}N_{gs}$ in K2

Figure D.4: The expected time-difference distribution of the sequential events from $^{12}\mathrm{C}\,(\,\nu_e$-$,\mathrm{e}^-\,)\,^{12}\mathrm{N}_{\mathrm{g.s.}}$ in K1 and K2, with respect to corrections caused by the electronics (black solid line). Drawn-in, for comparison, is the unmodified exponential curve (green solid line) according to the lifetime of $^{12}\mathrm{N}_{\mathrm{g.s.}}$ ($\tau = 15.9\,\mathrm{ms}$). For K2 the time-difference distribution, disregarding the variable EC1-threshold in K2, is visualized as well (red solid line).

Appendix E

Single–Events Excluding Sequences from CC–Reaction $^{12}\mathrm{C}\,(\,\nu_e\,,\mathrm{e}^-\,)\,^{12}\mathrm{N}_{\mathrm{g.s.}}$

The following figures show energy-, time- and spatial distributions of the single-events in KARMEN, excluding identified sequences from $^{12}\mathrm{C}\,(\,\nu_e\,,\mathrm{e}^-\,)\,^{12}\mathrm{N}_{\mathrm{g.s.}}$. These measured spectra are all in excellent agreement (within the errors) with the drawn-in corresponding expectation according to the final results. The spatial distribution possesses the expected $1/(distance)^2$-dependance in each of the three regions (separation due to the rejection of defective modules in the outer 76.5 cm). The time distribution reflects clearly the sum of the almost flat cosmic background expectation and the expected exponential function of the neutrinos according to the lifetime of muons ($\tau = 2.2\,\mu$s). From the velocity analysis derived portions of neutron-induced beam correlated (n,γ)-events are drawn-in as well in Fig. E.5 *and* E.6.

The numbers of identified sequences from $^{12}\mathrm{C}\,(\,\nu_e\,,\mathrm{e}^-\,)\,^{12}\mathrm{N}_{\rm g.s.}$ in the sample of single-events for K1 and K2, respectively, give rise to an independent cross check of the evaluation of the overall detection efficiencies. Especially for the exclusive CC-reaction $^{12}\mathrm{C}\,(\,\nu_e\,,\mathrm{e}^-\,)\,^{12}\mathrm{N}_{\rm g.s.}$ in K2, most efficiency components deviated strongly from the corresponding ones before the upgrade. Thus, the number of 278 identified and excluded sequences for K2, which is well in agreement with the expectation of 263.1 ± 16.2, demonstrates impressively that the treatment of the overall efficiencies is correct, both for the sequential detection and for the single-events (*compare Table* E.1 *with* 3.8 *and see Table* 3.1). So does the number of 475 identified and excluded sequences for K1, which is also well in agreement with the corresponding expectation of 465.8 ± 21.5.

Reaction		N	$N_{target}[10^{30}]$	$\epsilon_{overall}[\%]$
$^{12}\mathrm{C}\,(\,\nu\,,\nu'\,)\,^{12}\mathrm{C}^*$	*K1*	604.2 ± 20.9	2.54	36.2
$^{12}\mathrm{C}\,(\,\nu\,,\nu'\,)\,^{12}\mathrm{C}^*$	*K2*	451.7 ± 34.7	2.54	26.0
$^{12}\mathrm{C}\,(\,\nu_e\,,\mathrm{e}^-\,)\,^{12}\mathrm{N}_{\rm g.s.}$	*K1*	$\langle 409.2 \pm 18.8 \rangle$	2.54	25.7
$^{12}\mathrm{C}\,(\,\nu_e\,,\mathrm{e}^-\,)\,^{12}\mathrm{N}_{\rm g.s.}$	*K2*	$\langle 324.5 \pm 17.5 \rangle$	2.54	20.4
$^{12}\mathrm{C}\,(\,\nu_e\,,\mathrm{e}^-\,)\,^{12}\mathrm{N}^*$	*K1*	$\langle 430.7 \pm 52.5 \rangle$	2.54	55.5
$^{12}\mathrm{C}\,(\,\nu_e\,,\mathrm{e}^-\,)\,^{12}\mathrm{N}^*$	*K2*	313.2 ± 38.2	2.54	37.3
$^{13}\mathrm{C}\,(\,\nu_e\,,\mathrm{e}^-\,)\,^{13}\mathrm{N}$	*K1*	$\langle 49.7 \pm 24.9 \rangle$	0.0282	55.5
$^{13}\mathrm{C}\,(\,\nu_e\,,\mathrm{e}^-\,)\,^{13}\mathrm{N}$	*K2*	$\langle 35.1 \pm 17.6 \rangle$	0.0282	36.2
$^{56}\mathrm{Fe}\,(\,\nu_e\,,\mathrm{e}^-\,)\,\mathrm{X}$	*K1*	$\langle 120.4 \pm 74.8 \rangle$	2.34	0.37
$^{56}\mathrm{Fe}\,(\,\nu_e\,,\mathrm{e}^-\,)\,\mathrm{X}$	*K2*	88.7 ± 55.1	2.34	0.25
$\mathrm{e}^-\,(\,\nu\,,\nu'\,)\,\mathrm{e}^{-\prime}$	*K1*	$\langle 158.6 \pm 1.0 \rangle$	20.2	35.7
$\mathrm{e}^-\,(\,\nu\,,\nu'\,)\,\mathrm{e}^{-\prime}$	*K2*	$\langle 117.4 \pm 0.7 \rangle$	20.2	24.4

Table E.1: Fitted (or ⟨expected⟩) number of events, effective number of target-nuclei and overall detection efficiency for either of the single-event reactions in K1 and K2 (excluding identified sequences from $^{12}\mathrm{C}\,(\,\nu_e\,,\mathrm{e}^-\,)\,^{12}\mathrm{N}_{\rm g.s.}$).

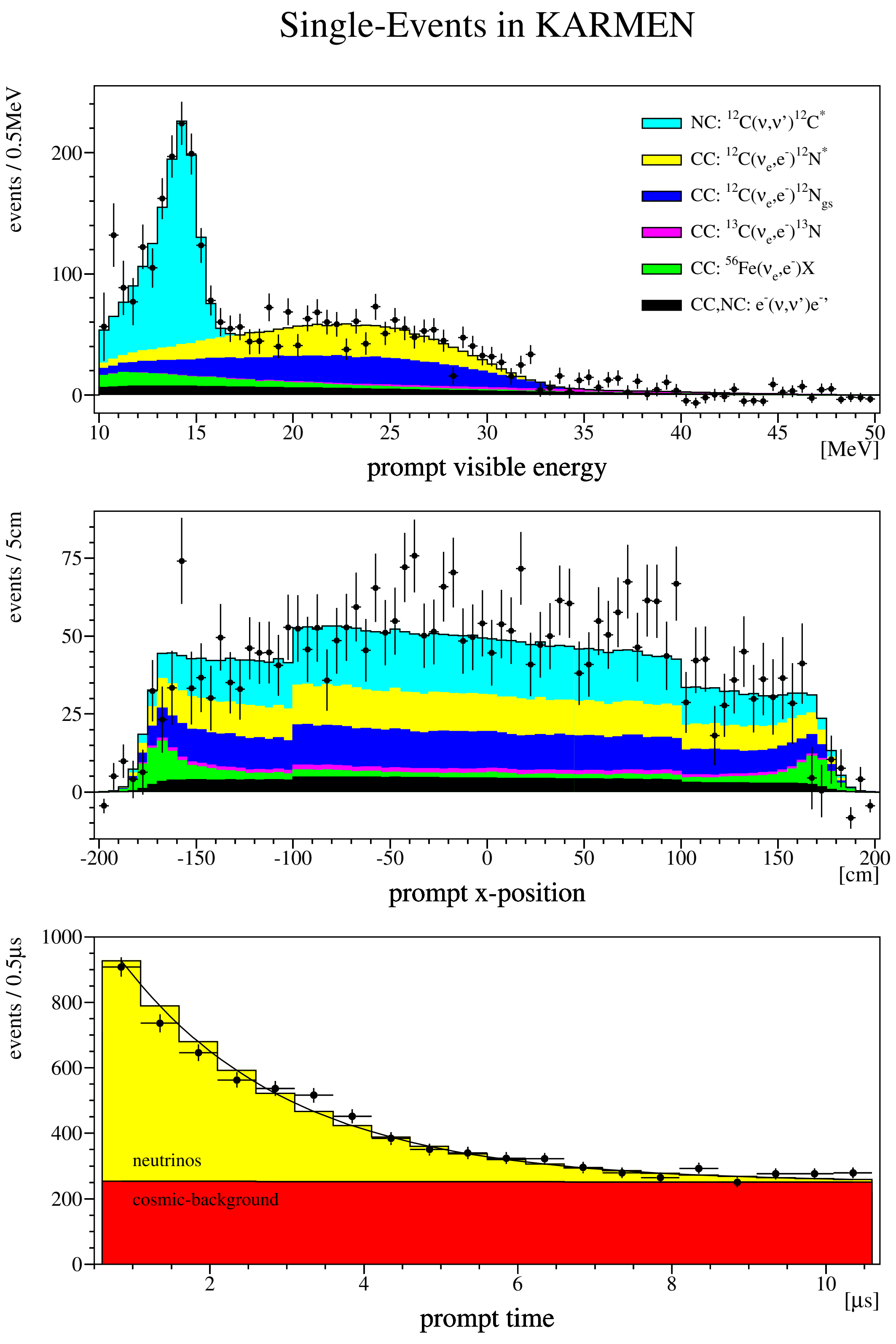

Figure E.1: In KARMEN (K1 + K2) measured energy-, spatial- and time distribution of single-events excluding observed sequences from $^{12}\mathrm{C}\,(\,\nu_e\,,\mathrm{e}^-\,)\,^{12}\mathrm{N}_{\mathrm{g.s.}}$. The portion of cosmic background is already subtracted in the energy- and spatial spectrum (according to the expectation from pre-beam). Plotted into the measured energy- and spatial spectrum are the expected portions for each single-event reaction derived from the combined analysis and MC-simulations (solid line for overall expectation).

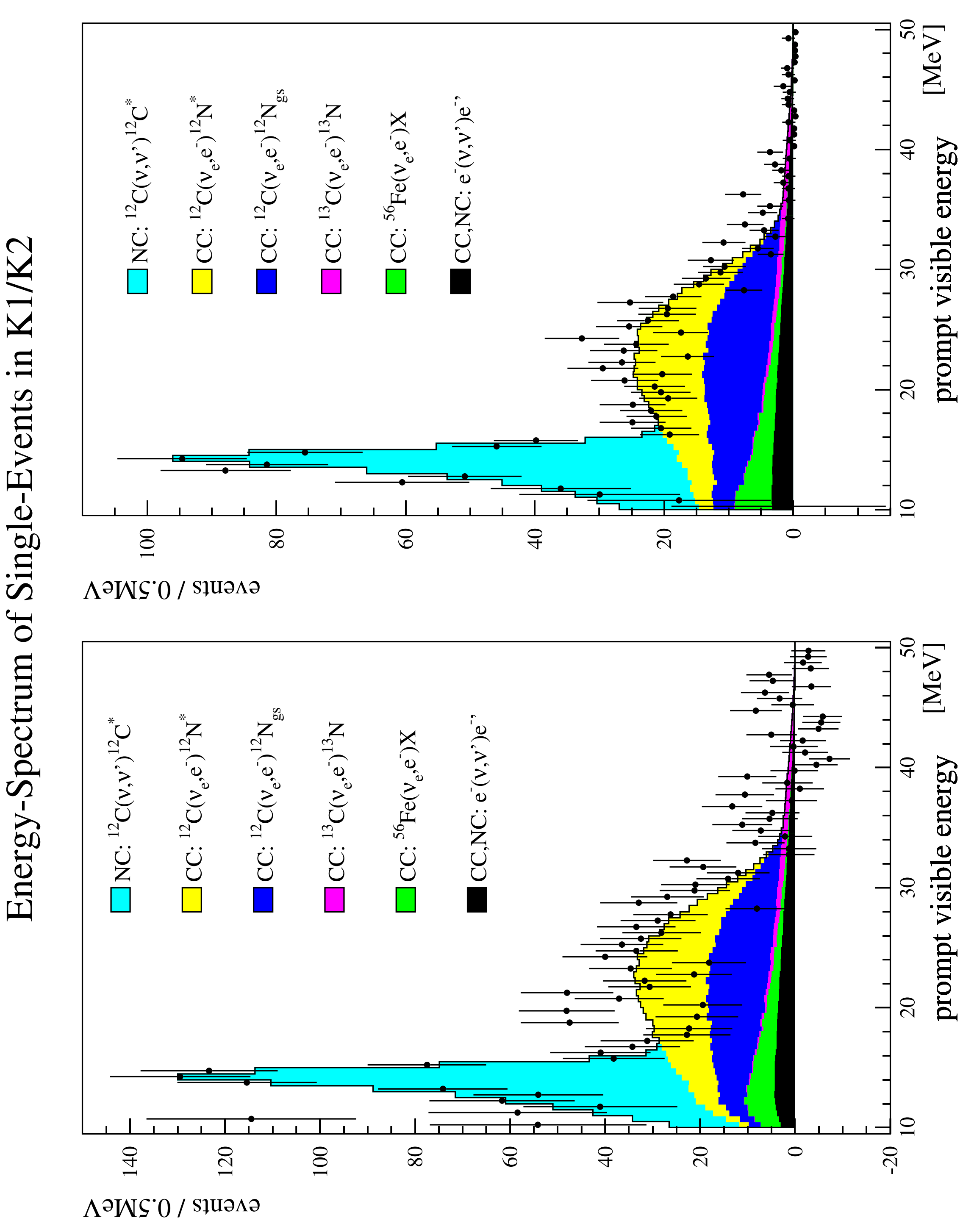

Figure E.2: Measured visible energy spectra of single-events excluding observed sequences from $^{12}\mathrm{C}\,(\,\nu_e\,,\mathrm{e}^-\,)\,^{12}\mathrm{N}_{\mathrm{g.s.}}$ in KARMEN1 (left) and KARMEN2 (right). The portion of cosmic background is already subtracted in the energy spectra (according to the corresponding expectation from pre-beam). Also drawn-in are the expected portions for each single-event reaction derived from the combined analysis and MC-simulations (solid line for overall expectation).

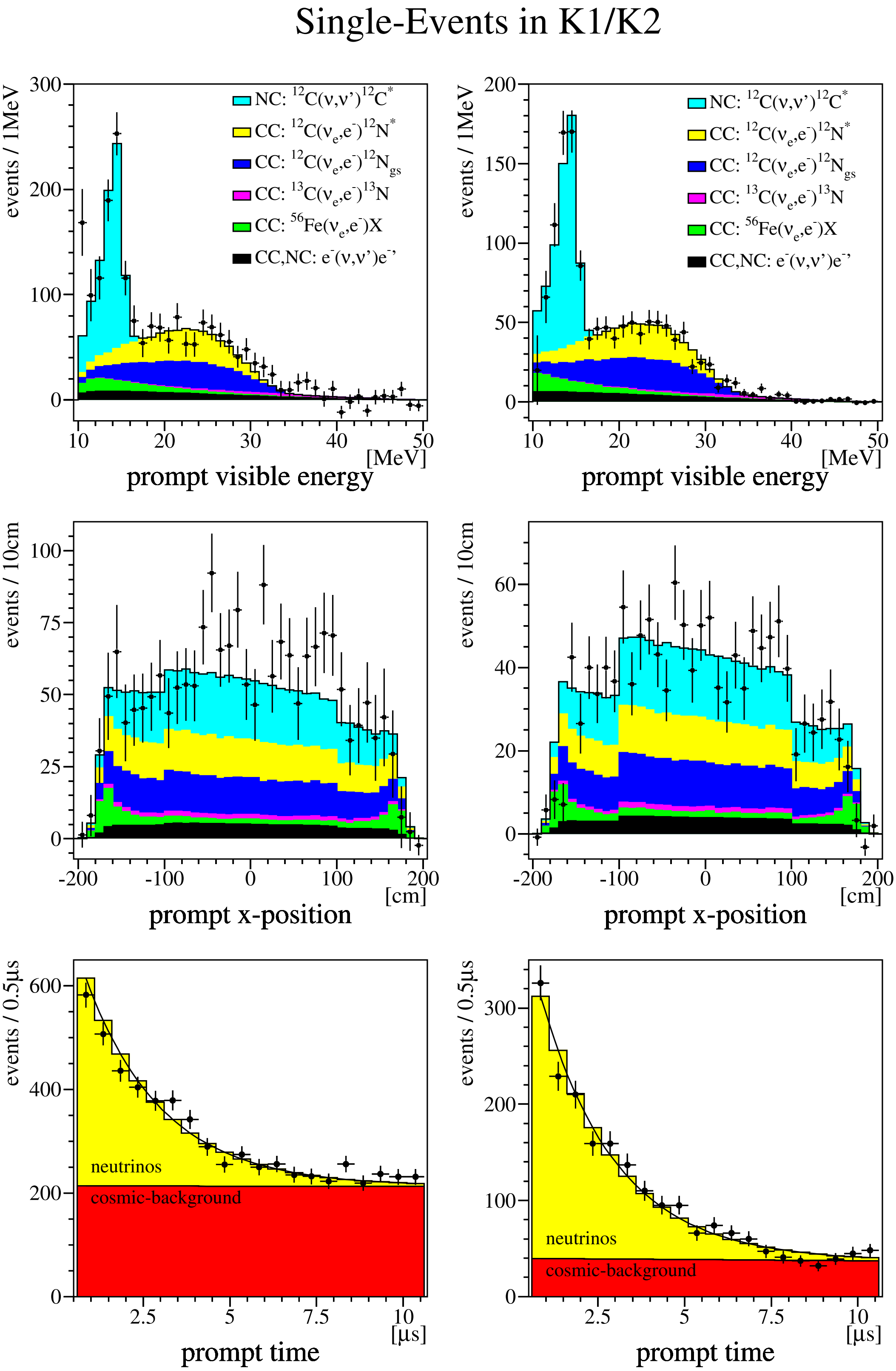

Figure E.3: Measured energy-, spatial- and time distributions of single-events excluding observed sequences from ^{12}C (ν_e , e$^-$) ^{12}N$_{\text{g.s.}}$ in KARMEN1 (left) and KARMEN2 (right). The portion of cosmic background is already subtracted in the energy- and spatial spectra (according to the corresponding expectation from pre-beam). Plotted into the measured energy- and spatial spectra are the expected portions for each single-event reaction derived from the combined analysis and MC-simulations (solid line for overall expectation).

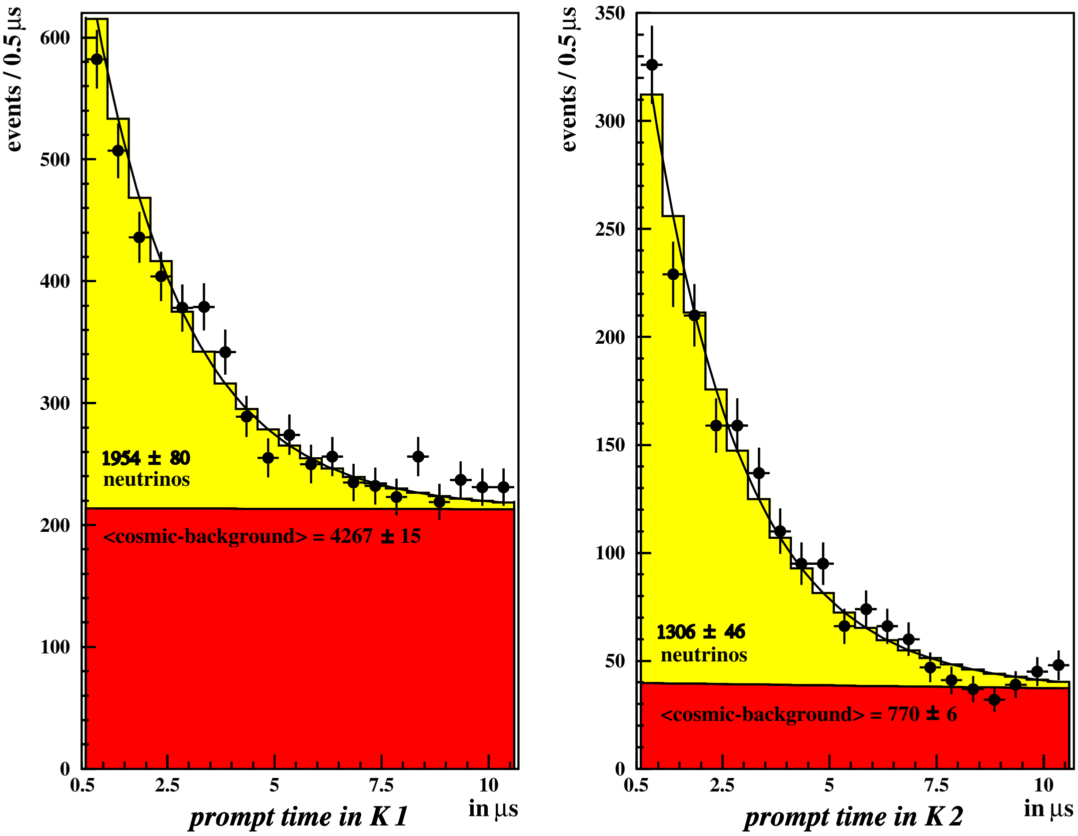

Figure E.4: Time distribution of single-events excluding observed sequences from $^{12}\mathrm{C}\,(\,\nu_e\,,\mathrm{e}^-\,)\,^{12}\mathrm{N}_{\rm g.s.}$. On the left for KARMEN1 (K1) before the upgrade and on the right for KARMEN2 (K2) afterwards. The portion of cosmic background is drawn-in for each (according to expectation from pre-beam).

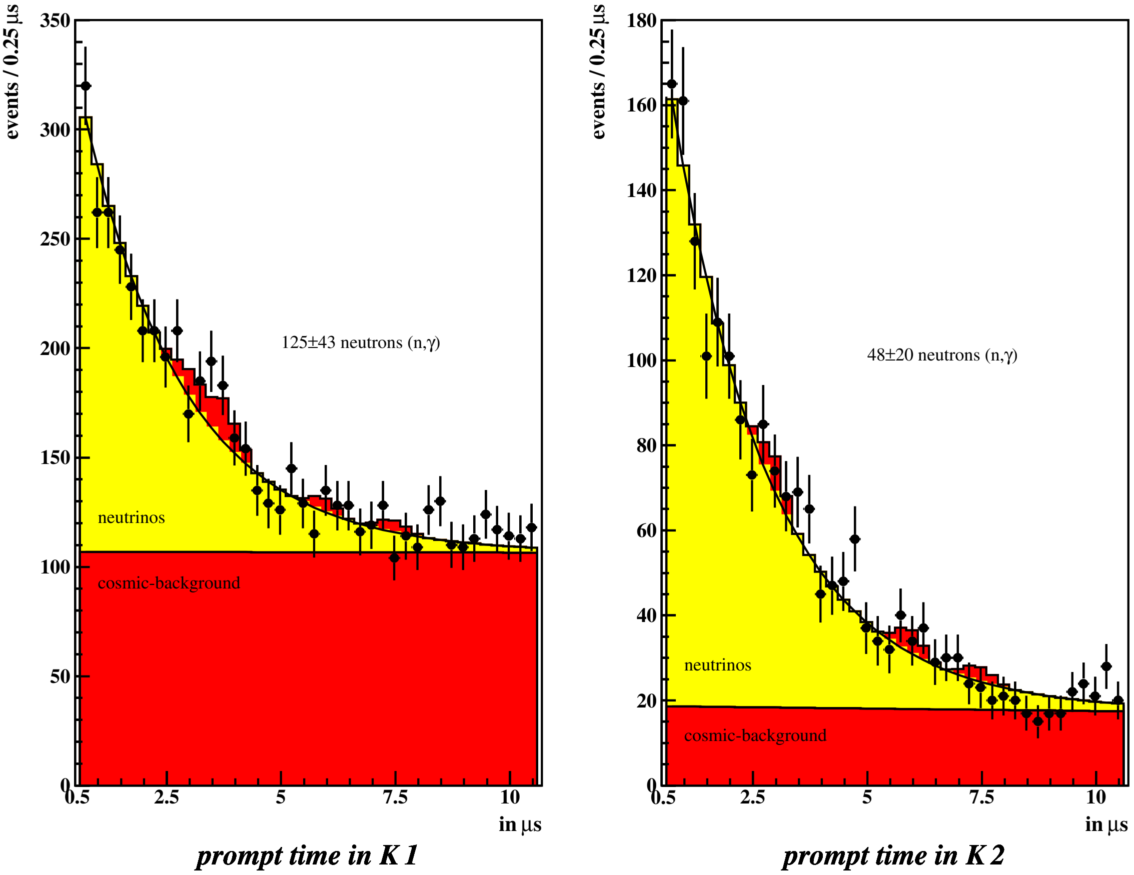

Figure E.5: Time distribution of single-events excluding observed sequences from $^{12}\mathrm{C}\,(\,\nu_e\,,\mathrm{e}^-\,)\,^{12}\mathrm{N}_{\mathrm{g.s.}}$. On the left for KARMEN1 (K1) before the upgrade and on the right for KARMEN2 (K2) afterwards. From the velocity analysis derived portions of neutron-induced beam correlated (n,γ)-events are drawn-in (as well as the almost flat cosmic background expectation from pre-beam).

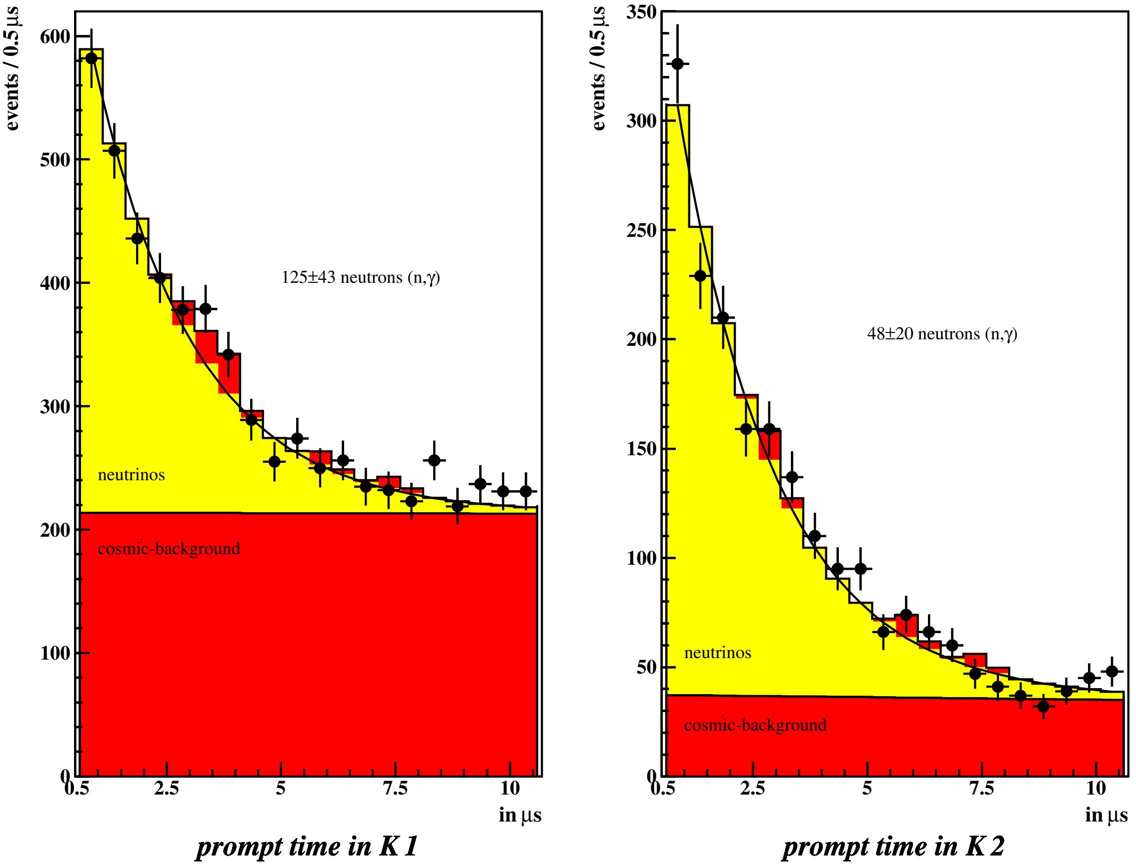

Figure E.6: Time distribution of single-events excluding observed sequences from $^{12}\mathrm{C}\,(\,\nu_e\,,\mathrm{e}^-\,)\,^{12}\mathrm{N}_{\mathrm{g.s.}}$. On the left for KARMEN1 (K1) before the upgrade and on the right for KARMEN2 (K2) afterwards. From the velocity analysis derived portions of neutron-induced beam correlated (n,γ)-events are drawn-in (as well as the almost flat cosmic background expectation from pre-beam).

Bibliography

[Ach95] B. Achkar *et al.*, *Search for Neutrino Oscillations at 15-Meters, 40-Meters, and 95-Meters from a Nuclear Power Reactor at Bugey*, Nucl. Phys. B **434** (1995) 503.

[Ahm02a] Q. R. Ahmad *et al.* [SNO Collaboration], *Direct Evidence for Neutrino Flavor Transformation from Neutral-Current Interactions in the Sudbury Neutrino Observatory*, Phys. Rev. Lett. **89** (2002) 011301 [arXiv:nucl-ex/0204008].

[Ahm02b] Q. R. Ahmad *et al.* [SNO Collaboration], *Measurement of Day and Night Neutrino Energy Spectra at SNO and Constraints on Neutrino Mixing Parameters*, Phys. Rev. Lett. **89** (2002) 011302 [arXiv:nucl-ex/0204009].

[Agu01] A. Aguilar *et al.* [LSND Collaboration], *Evidence for Neutrino Oscillations from the Observation of $\bar{\nu}_e$ Appearance in a $\bar{\nu}_\mu$ Beam*, Phys. Rev. D **64** (2001) 112007 [arXiv:hep-ex/0104049].

[Ajz90] F. Ajzenberg-Selove, *Energy Levels of Light Nuclei $A = 11 - 12$*, Nucl. Phys. A **506** (1990) 1.

[Ake04] D. Akers, *Quantized Vibrations in Models of Dibaryons, Pentaquarks and Z^* Resonances*, [arXiv:hep-ph/0403142].

[Alt03] G. Altarelli and K. Winter (Eds.), *Neutrino Mass*, Springer Tracts in Modern Physics Vol. 190 (2003).

[Apo99] M. Apollonio *et al.* [CHOOZ Collaboration], *Limits on Neutrino Oscillations from the CHOOZ Experiment*, Phys. Lett. B **466** (1999) 415 [arXiv:hep-ex/9907037].

[Ara89] J. Arafune, M. Fukugita, Y. Kohyama and K. Kubodera, *C-13 As A Solar Neutrino Detector*, Phys. Lett. B **217** (1989) 186.

[Arm95] B. Armbruster et al, *Anomaly in the Time Distribution of Neutrinos from a pulsed beam stop source*, Phys. Lett. B **348** (1995) 19-28

[Arm98] B. Armbruster, *Der myoninduzierte Untergrund für die Suche nach $\bar{\nu}_\mu \rightarrow \bar{\nu}_e$ Oszillationen und seine Eliminierung durch den KARMEN Upgrade*, PhD-Thesis, University of Karlsruhe (Forschungszentrum Karlsruhe) FZKA-6102 (1998)

[Arm98b] B. Armbruster et al, *Measurement of the Energy Spectrum of ν_e from Muon Decay and Implications for the Lorentz Structure of the Weak Interaction*, Phys. Rev. Lett. **81** (1998) 520

[Arm98c] B. Armbruster *et al.* [KARMEN Collaboration], *Measurement of the Weak Neutral Current Excitation C-12(nu(mu), nu'(mu))C*-12(1+,1,15.1-MeV) at E(nu(mu)) = 29.8-MeV*, Phys. Lett. B **423** (1998) 15.

[Arm02] B. Armbruster *et al.* [KARMEN Collaboration], *Upper Limits for Neutrino Oscillations $\bar{\nu}_\mu \rightarrow \bar{\nu}_e$ from Muon Decay at Rest*, Phys. Rev. D **65** (2002) 112001 [arXiv:hep-ex/0203021].

[Arm03] B. Armbruster *et al.* [KARMEN Collaboration], *Improved Limits on $\bar{\nu}_e$ Emission from μ^+-Decay*, Phys. Rev. Lett. **90** (2003) 181804 [arXiv:hep-ex/0302017].

[Ath95] C. Athanassopoulos *et al.* [LSND Collaboration], *Candidate Events in a Search for $\bar{\nu}_\mu \rightarrow \bar{\nu}_e$ Oscillations*, Phys. Rev. Lett. **75** (1995) 2650 [arXiv:nucl-ex/9504002].

[Ath96] C. Athanassopoulos *et al.* [LSND Collaboration], *The Liquid Scintillator Neutrino Detector and LAMPF Neutrino Source*, Nucl. Instrum. Meth. A **388** (1997) 149 [arXiv:nucl-ex/9605002].

[Aue97] N. Auerbach, N. Van Giai and O. K. Vorov, *Neutrino Scattering from C-12 and O-16*, Phys. Rev. C **56** (1997) 2368 [arXiv:nucl-th/9705003].

[Aue01] L. B. Auerbach *et al.* [LSND Collaboration], *Measurements of Charged Current Reactions of nu/e on C-12*, Phys. Rev. C **64** (2001) 065501 [arXiv:hep-ex/0105068].

[Avv02] S. Avvakumov *et al.*, *A Search for nu/mu → nu/e and anti-nu/mu → anti-nu/e Oscillations at NuTeV*, Phys. Rev. Lett. **89** (2002) 011804 [arXiv:hep-ex/0203018].

[Baz02] A. O. Bazarko [BooNE Collaboration], *Status of MiniBooNE*, [arXiv:hep-ex/0210020].

[BNL73] Brookhaven National Laboratory, *Neutron Cross Sections*, BNL325 third edition vol1

[Bru85] S. W. Bruenn, *Stellar Core Collapse: Numerical Model And Infall Epoch*, Astrophys. J. Suppl. **58** (1985) 771.

[Bug79] E. V. Bugaev, G. S. Bisnovatyi-Kogan, M. A. Rudzsky and Z. F. Seidov, *The Interaction Of Intermediate-Energy Neutrinos With Nuclei*, Nucl. Phys. A **324** (1979) 350.

[Bur95] R. L. Burman, A. C. Dodd, P. Plischke, *Neutrino Flux Calculations for the KARMEN Detector at the ISIS Spallation Neutron Facility*, (Forschungszentrum Karlsruhe) FZKA-5595 (1995), Nucl. Instr. and Meth. A **368** (1996) 416-424

[Cho99] D. Choudhury, H. K. Dreiner, P. Richardson and S. Sarkar, *A Supersymmetric Solution to the KARMEN Time Anomaly*, Phys. Rev. D **61** (2000) 095009 [arXiv:hep-ph/9911365].

[CER00] CERN, *Workshop on Confidence Level (CL)*, P. **103** (1/2000)

[Dau00] M. Daum *et al.*, *The KARMEN Time Anomaly: Search for a Neutral Particle of Mass 33.9-MeV in Pion Decay*, Phys. Rev. Lett. **85** (2000) 1815 [arXiv:hep-ex/0008014].

[Dod93] A. Dodd et al., *The Laser Calibration Monitor of the KARMEN Scintillation Calorimeter*, Nucl. Instr. and Meth. A **336** (1993) 136-145

[Don79] T. W. Donnelly and R. D. Peccei, *Neutral Current Effects in Nuclei*, Phys. Rep. **50** (1979) 1.

[Don91] T. W. Donnelly, *Private Communication: Program NUEE for Calculating Neutrino Cross Sections on Nuclei*, (1991)

[Dre03] H. K. Dreiner, C. Hanhart, U. Langenfeld and D. R. Phillips, *Supernovae and Light Neutralinos: SN1987A Bounds on Supersymmetry Revisited*, Phys. Rev. D **68** (2003) 055004 [arXiv:hep-ph/0304289].

[Dre90] G. Drexlin *et al.*, *The High Resolution Neutrino Calorimeter Karmen*, Nucl. Instrum. Meth. A **289** (1990) 490.

[Dre02] G. Drexlin, *Private Communication*, (2002) April

[Ebe92] V. Eberhard, *Erster Nachweis der inelastischen Neutrino-Kern-Streuung* $\nu+^{12}C \rightarrow \nu'+^{12}C^*$, PhD-Thesis, University of Karlsruhe (Forschungszentrum Karlsruhe) FZKA-5063 (1992)

[Eit95] K. Eitel, *Suche nach Neutrinooszillationen* $\nu_\mu \rightarrow \nu_e$ *und* $\nu_e \rightarrow \nu_x$ *sowie leptonzahlverletzenden Zerfällen des Myons und des Pions mit dem KARMEN Experiment*, PhD-Thesis, University of Karlsruhe (Forschungszentrum Karlsruhe) FZKA-5684 (1995)

[Egu02] K. Eguchi *et al.* [KamLAND Collaboration], *First Results from KamLAND: Evidence for Reactor Anti-Neutrino Disappearance*, Phys. Rev. Lett. **90** (2003) 021802 [arXiv:hep-ex/0212021].

[Fog03] G. L. Fogli, E. Lisi, A. Marrone, D. Montanino, A. Palazzo and A. M. Rotunno, *Solar Neutrino Oscillation Parameters after First KamLAND Results*, Phys. Rev. D **67** (2003) 073002 [arXiv:hep-ph/0212127].

[For99] J. A. Formaggio *et al.* [NuTeV Collaboration], *Search for a 33.9-MeV/c**2 Neutral Particle in Pion Decay*, Phys. Rev. Lett. **84** (2000) 4043 [arXiv:hep-ex/9912062].

[Fuk98] Y. Fukuda *et al.* [Super-Kamiokande Collaboration], *Evidence for Oscillation of Atmospheric Neutrinos*, Phys. Rev. Lett. **81** (1998) 1562 [arXiv:hep-ex/9807003].

[Fuk88] M. Fukugita, Y. Kohyama and K. Kubodera, *Neutrino Reaction Cross-Sections On C-12 Target*, Phys. Lett. B **212** (1988) 139.

[Fro79] A. G. Frodesen, O. Skjeggestad and H. Tofte, *Probability and Statistics in Particle Physics*, Universitetsforlaget Oslo (1979)

[Giu02] C. Giunti and M. Laveder, $\nu_e \rightarrow \nu_{sterile}$ *Oscillations with Large Neutrino Mass in NuTeV ?*, arXiv:hep-ph/0202152.

[Han03] S. Hannestad, *Neutrino Masses and the Number of Neutrino Species from WMAP and 2dFGRS*, JCAP **0305** (2003) 004 [arXiv:astro-ph/0303076].

[Har84] J.A. Harvey, F.G. Perey, J.A. Hill, *The 56Fe 1.15 keV Resonance Parameters from Transmission Measurements at ORELA* R,DOE-NDC-33,142 (1984)
Data approved by D. Wiarda (2000)

[Hay00] A. C. Hayes and I. S. Towner, *Shell-model Calculations of Neutrino Scattering from C-12*, Phys. Rev. C **61** (2000) 044603 [arXiv:nucl-th/9907049].

[Heg03] A. Heger, E. Kolbe, W. C. Haxton, K. Langanke, G. Martinez-Pinedo and S. E. Woosley, *Neutrino Nucleosynthesis*, [arXiv:astro-ph/0307546].

[Hil95] J. E. Hill, *An Alternative Analysis of the LSND Neutrino Oscillation Search Data on* $\bar{\nu}_\mu \rightarrow \bar{\nu}_e$, Phys. Rev. Lett. **75** (1995) 2654 [arXiv:hep-ex/9504009].

[Jan95] T. E. Jannakos, *Myoneinfang-Reaktionen an* ^{12}C *und* ^{13}C *im KARMEN Detektor*, Diploma-Thesis, University of Karlsruhe (Forschungszentrum Karlsruhe) FZKA-5520 (1995)

[Kac00] M. Kachelriess, *The KARMEN Anomaly, Light Neutralinos and Supernova SN1987A*, JHEP **0002** (2000) 010 [arXiv:hep-ph/0001160].

[Kan02] K. Kaneyuki [SUPER-KAMIOKANDE Collaboration], *Determination of Neutrino Oscillation Parameters with Atmospheric Neutrinos*, Nucl. Phys. Proc. Suppl. **112** (2002) 24.

[Kat03] I. Kato [K2K Collaboration], *The Results of Oscillation Analysis in K2K Experiment and an Overview of JHF-nu Experiment*, [arXiv:hep-ex/0306043].

[Kla02] H. V. Klapdor-Kleingrothaus, *Is The Neutrino A Majorana Particle?*, Phys. Unserer Zeit **33** (2002) 155.

[Kol99] E. Kolbe, K. Langanke and P. Vogel, *Weak Reactions on 12C within the Continuum Random Phase Approximation with Partial Occupancies*, Nucl. Phys. A **652** (1999) 91 [arXiv:nucl-th/9903022].

[Kol01] E. Kolbe and K. Langanke, *The Role of ν Induced Reactions on Lead and Iron in Neutrino Detectors*, Phys. Rev. C **63** (2001) 025802 [arXiv:nucl-th/0003060].

[Kub93] K. Kubodera and S. Nozawa, *Neutrino–Nucleus Reactions*, Int. J. Mod. Phys. E **3** (1994) 101 [arXiv:nucl-th/9310014].

[Luk00] A. Lukas and A. Romanino, *A Brane-World Explanation of the KARMEN Anomaly* [arXiv:hep-ph/0004130].

[Mak62] Z. Maki, M. Nakagawa and S. Sakata, Prog. Theor. Phys. **28**,870 (1962).

[Min93] M. Pourkaviani and S. L. Mintz, *Inclusive Inelastic Neutral Current Neutrino Reactions In C-12 And The Charged Current Reaction*, Nucl. Phys. A **573** (1994) 501.

[Min00] S. L. Mintz, *Inclusive Neutrino Reactions In C-13*, Nucl. Phys. A **672** (2000) 503.

[Min02] S. L. Mintz, *Inclusive Neutrino And Anti-Neutrino Reactions In Fe-56*, J. Phys. G **28** (2002) 451.

[Neu04a] G. Gratta, *Results from the KamLAND Experiment*, Talk given at NEUTRINO 2004 Conference (Paris)

[Neu04b] E. Kearns, *Atmospheric Neutrino Results from SuperKamiokande*, Talk given at NEUTRINO 2004 Conference (Paris)

[Oeh99] C. Oehler, *Statistische Analyse der KARMEN-Zeitanomalie*, PhD-Thesis, University of Karlsruhe (Forschungszentrum Karlsruhe)

[Par94] R. Parthasarathy, *Neutrino Neutral Current Excitation Of C*-12 (1+, T=1, 15.1-Mev)*, Int. J. Mod. Phys. E **3** (1994) 1195.

[PDG02] Particle Data Group, *Review of Particle Physics*, Phys. Rev. D **66** (2002) 010001 [http://pdg.lbl.gov].

[Rei53] F. Reines, C. Cowan, Phys. Rev. 92, 830 L (1953)

[Rei98] J. Reichenbacher, *Untersuchung der optischen Eigenschaften großflächiger Plastikszintillatoren für den KARMEN-Upgrade*, Diploma-Thesis, University of Karlsruhe (Forschungszentrum Karlsruhe) FZKA-6202 (1998)

[Ruf95] C. Ruf, *Bestimmung des Wirkungsquerschnitts der Reaktionen* $^{56}Fe\,(\nu_e\,,e^-\,)^{56}Co^*$ *und* $^{13}C\,(\nu_e\,,e^-\,)^{13}N$, Diploma-Thesis, University of Karlsruhe (Forschungszentrum Karlsruhe) [1995]

[Sch96] P. Schirrmann, *Analyse der Universalität neutraler Ströme im Niederenergiebereich*, Diploma-Thesis, University of Karlsruhe (Forschungszentrum Karlsruhe) [1996]

[Sch97] N. Schmitz, *Neutrinophysik*, (1997) 369-370

[Sin98] S. K. Singh, N. C. Mukhopadhyay and E. Oset, *Inclusive Neutrino Scattering in C-12: Implications for nu/mu to nu/e Oscillations*, Phys. Rev. C **57** (1998) 2687 [arXiv:nucl-th/9802059].

[Sor03] M. Sorel, J. Conrad and M. Shaevitz, *A Combined Analysis of Short-Baseline Neutrino Experiments in the (3+1) and (3+2) Sterile Neutrino Oscillation Hypotheses*, [arXiv:hep-ph/0305255].

[Ste99] M. Steidl, *Die Suche nach* $\bar{\nu}_\mu \!\rightarrow\! \bar{\nu}_e$ *Oszillationen mit dem KARMEN 2 Experiment.*, PhD-Thesis, University of Karlsruhe (Forschungszentrum Karlsruhe) FZKA-6406 (1999)

[Vog96] J. Engel, E. Kolbe, K. Langanke and P. Vogel, *Neutrino Induced Transitions between the Ground States of the* $A = 12$ *Triad*, Phys. Rev. C **54** (1996) 2740 [arXiv:nucl-th/9606031].

[Vol01] C. Volpe, N. Auerbach, G. Colo, T. Suzuki and N. Van Giai, *Neutrino C-12 Reactions And The Lsnd And Karmen Experiments On Neutrino Oscillations*, Phys. Atom. Nucl. **64** (2001) 1165 [Yad. Fiz. **64** (2001) 1242].

[Wei03] C. Weinheimer, *The Neutrino Mass Direct Measurements*, [arXiv:hep-ex/0306057].

[Wol78] L. Wolfenstein, Phys. Rev. D **17** (1978) 2369; Phys. Rev. D **20** (1979) 2634; S.P. Mikheyev and A.Y. Smirnov, Sov. J. Nucl. Phys. **42** (1985) 913; Nuovo Cim. C **9** (1986) 17.

[Wol95] J. Wolf, *Kalibration des KARMEN Detektors und die Analyse inklusiver Neutrino-Reaktionen mit* ^{12}C, PhD-Thesis, University of Karlsruhe (Forschungszentrum Karlsruhe) FZKA-5636 (1995)

[Zei95] B. Zeitnitz, *Anomalie im Zeitspektrum von beam stop Neutrinos*, Physikalische Blätter **51** (1995) Nr.2

[Zel01] G. P. Zeller *et al.* [NuTeV Collaboration], *A Precise Determination of Electroweak Parameters in Neutrino Nucleon Scattering*, Phys. Rev. Lett. **88** (2002) 091802 [Erratum-ibid. **90** (2003) 239902] [arXiv:hep-ex/0110059].